Dissipative Nanomechanics

Thesis by

Mandar M. Inamdar

Advisor: Rob Phillips

In Partial Fulfillment of the Requirements

for the Degree of

Doctor of Philosophy

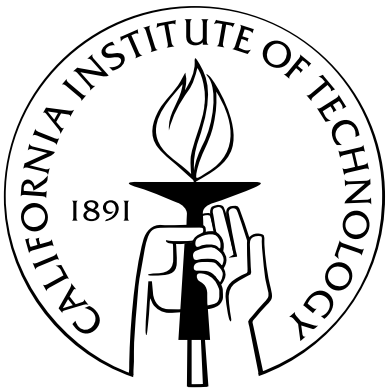

California Institute of Technology

Pasadena, California

2006

(Defended January 23, 2006)

Acknowledgements

I would first like to thank Kaushik Bhattacharya, Ken Dill (thanks, Ken, for flying all the way from SF), Bill Gelbart, Rob Phillips, and Zhen-Gang Wang for agreeing to be part of my committee. I consider them to be first rate scientists and people of integrity. It's my great fortune that I had a chance to interact with them.

A number of people are responsible for making my professional and personal stay at Caltech satisfying. First and foremost, I would like to thank my advisor, Rob Phillips. It was a privilege to be his first student at Caltech, and I feel truly lucky for the opportunity to work with him for the last five years. He gave me a number of new research ideas and provided ample freedom to explore on my own. He slowly built my confidence over these last many years, applauded me for my successes, and corrected me when I was wrong. I felt sheltered under his tutelage and can truly say that he is not just my advisor, but a very good friend.

I am also fortunate to have wonderful collaborators in Ken Dill, Bill Gelbart, and Jané Kondev. They provided me excellent ideas for research and especially taught me the joys of scientific work. It is a real privilege to know these guys. Similarly, I am also very lucky to have good friends, fellow collaborators, and lab-mates at Caltech. I owe a huge debt of gratitude to them. Specifically, I would like to thank Kings Ghosh, Paul Grayson, Prashant Purohit, Frosso Seitaridou, and Dave Wu for being patient collaborators and good friends. Paul Wiggins taught me so many things about physics. I regret that I was not able to write a paper with him.

Finally, but not in the least, I would like to thank my parents and my sister for their love and support.

Abstract

Due to thermal fluctuations, systems at small length scales are remarkably different than their large length scale counterparts. For example, bacterial viruses (phages) have thousands of nanometers of DNA packed inside a hollow capsid of tens of nanometers. This tight compaction leads to large forces on the phage DNA (tens of piconewtons). These forces can be subsequently utilized to instigate the DNA ejection during the infection phase. Developments in optics, biochemistry, microfluidics, etc., have enabled the experimental quantification of these forces, and the rate of DNA packing and ejection. Similarly, eukaryotic genome is compacted into nanometer-size structures called nucleosomes. The conformational changes in the nucleosome due to the thermal fluctuations of the DNA are instrumental in making the DNA accessible for key genomic processes. Developments in FRET, gel electrophoresis, spectroscopy, etc., have made it possible to quantify the equilibrium constant and the rates of these fluctuations. The first part of the thesis involves formulation of simple models for the phage and nucleosome to respond to the existing experimental data and predicts results to stimulate further experimentation.

One of the next frontiers in biology is to understand the "small numbers" problem: how does a biological cell function given that most of its proteins and nucleotide polymers are present in numbers much smaller than Avogadro's number? For example, one of the most important molecules, a cell's DNA, occurs in only a single copy. Also, it is the flow of matter and energy through cells that makes it possible for organisms to maintain a relatively stable form. Hence, cells must be in this stable state far from equilibrium to function. Many problems of current interest thus involve small systems that are out of equilibrium. Unfortunately, there is no general theoretical frame-work to model these dissipative systems. E. T. Jaynes suggested the use of dynamical microtrajectories to write down the trajectory entropy, or caliber, for such systems. Maximization of this trajectory entropy, subject to the external constraints, provides one with the probabilities of the underlying microtrajectories. Jaynes calls this the "principle of maximum caliber." Advances in optics, video-microscopy, etc., have made it possible to experimentally measure these microtrajectories for various systems. In the second part of the thesis we develop simple microtrajectory models for small systems like molecular motors, ion channels, etc., and apply the maximum caliber principle to obtain the probabilities of the underlying microtrajectories. Our goal is to respond to these experiments and make new

predictions.

Contents

List of Figures

List of Tables

Chapter 1

Dissipative Nanomechanics: An Introduction

The basic living organism is a cell, and one of its most important characteristics is the capacity to sustain itself and transmit its legacy by self-reproduction. Multicellular organisms such as humans, have different types of cells, which, in addition to fulfilling their own requirements also interact with each other to ensure the organism's overall well-being. The cell is thus not a static entity, but a dynamic factory teeming with activities at various length-scales [1]. The legacy of a cell is encoded in its genetic material (DNA or RNA) in the form of genes. Each gene has a particular protein associated with it, which itself is composed of amino acids. The genome is thus the blue-print, and the proteins form the building blocks of the cell.

In eukaryotic organisms such as humans, the genome is located in the nucleus of the cell. The total length of the human genome ($\approx 10^{-2}$m) is around four order of magnitudes larger than the size of the nucleus ($\approx 10^{-}6$ m). Hence, in order to pack this large length of genome into the nuclei, the DNA is tightly compacted into structures called nucleosomes ($\approx$ 10 nm)(see Fig. 1.2). This compaction of the genome makes it inaccessible for key processes like replication, gene expression, and repair. Similarly is the case of viruses that infect bacteria (bacteriophage or phage). In this case, a long genome is tightly packed into the relatively small hollow head of the phage. For example, bacteriophage λ has a nearly spherical capsid (head) with a diameter of around 60nm, while the length of its genome is around 16000nm, around two order of magnitudes larger. Hence, similar to the case of the eukaryotic genome the phage genome needs to be tightly compacted so that it can fit inside the capsid. The tight genome compaction is the common thread running through these two problems. In the case of nucleosomes, the tight genome compaction leads to its apparent inaccessibility to the binding proteins, while in the case of bacteriophages the tight genome compaction leads to strong bending and interaction forces (of the order tens of piconewtons) acting on the DNA. The first half of the thesis analyzes the statics and dynamics of DNA under strong compaction. In Chapter 3 we formulate theoretical models to estimate the forces acting on the

DNA inside the phage capsid, and how the force an be utilized for the subsequent DNA ejection. In Chapter 4 we make use of the forces obtained in Chapter 3 to obtain the rate of ejection in bacteriophage. Chapter 5 deals with the DNA accessibility problem in nucleosomes. In this chapter we formulate simple models to make an estimate of the time rate of genome exposure. In short these chapters deal with mechanics of the above mentioned nano-systems.

The second part of the thesis is dedicated exclusively to non-equilibrium systems. A system is said to be in non-equilibrium if there is a macroscopically measurable flux of particles or energy within the system. Such flux has a thermodynamic driving force associated with it and results in production of entropy [2]. In general, entropy production is called dissipation, and all phenomena which are accompanied by entropy production will be called dissipative [3]. Dissipative processes are also called irreversible processes. Thus, non-equilibrium, dissipation, and irreversibility are generally different names for the same thing [4]. Everyday life is irreversible and corresponds to an inescapable increase in entropy. "Life," at its basic level of cells, is sustained by a number of such irreversible processes and is thus essentially dissipative. Due to this prevalence of irreversibility, a general theory for such processes is greatly sought after. Unfortunately, other than description of systems very near to equilibrium, there exists no counterpart of thermodynamics (or equilibrium statistical mechanics) for non-equilibrium systems. On the other hand, if entropy is recognized as related to the macroscopic information of the system, dissipation can be looked at as an information loss. This information-theoretic-approach towards dissipative systems was pioneered by E. T. Jaynes [5, 6, 7, 8]. Jaynes introduced what he called a counterpart of the equilibrium entropy, and called it as the "caliber" of the non-equilibrium system [7, 8] by replacing the microstates in equilibrium statistical mechanics with microtrajectories. In this formalism, the principle of maximum entropy of thermodynamics is replaced by the "principle of maximum caliber." The second part of the thesis involves applying these ideas to simple models and to obtain analytically tractable solutions for the same. In particular, we apply these ideas to analyze particle diffusion, heat diffusion, the dwell times of molecular motors, the voltage dependence of ion-current in ion-channels, etc. We also introduce some novel quantities like potency and bad-actors (Chapter 7), which may serve as a metric to describe the distance of a non-equilibrium system from equilibrium.

1.1 The Devastatingly Beautiful World of Viruses

Viruses are on the border line of living and non-living. Of course, to distinguish between living and non-living one must have a clear cut idea of what life is. Tentatively, we can take a living system to be the one that can, given "proper" environmental conditions, sustain and reproduce itself, just by using the nutrients from the surroundings. Viruses can most definitely sustain themselves under various, but not too harsh environmental conditions, but lack the ability to reproduce without using

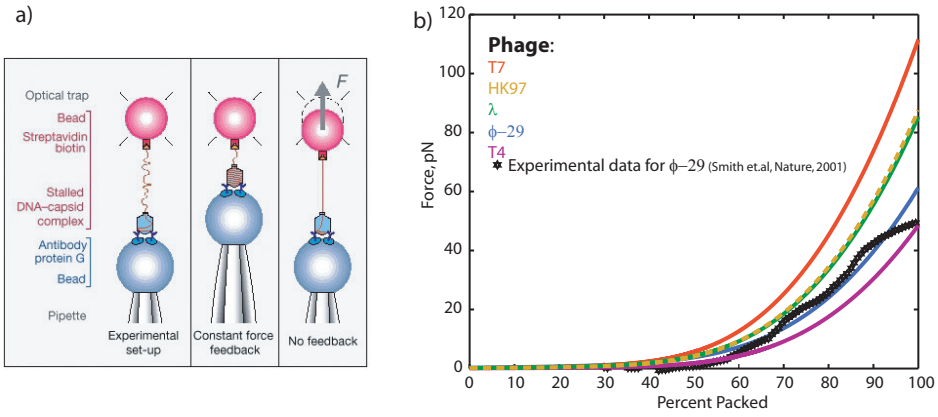

Figure 1.1: Force measurement experiment for DNA packaging in bacteriophage $\phi 29$. a) The experiment by Smith et al. [11] in which a polystyrene bead was attached to one end of the phage genome. Using optical traps, a pulling force was applied to the DNA getting packed inside the phage capsid by the ATP-consuming portal motor. The stall force corresponded to the force exerted by the motor. (b) The theoretical prediction for the internal resisting force on the DNA as a function of amount of DNA packed. The experimental data in Smith et al. [11] was for $\phi 29$. We matched the data for the theoretical prediction and also make predictions for other bacteriophage.

the cellular machinery of other "living" cells.

Viruses come in sizes from tens to hundreds of nanometers [9] and are the smallest known hijackers. A whole gamut of living organisms are infected by viruses [10]. Morphologically speaking, a typical bacterial virus has a head, neck, and a tail. The head (or the capsid) of a virus encapsulates the genetic material (DNA or RNA), which consists of the entire self blue-print. The head may also contain a supporting cast of a few other type of proteins that help the virus transmit its DNA into the host cell and hijack the genetic mechanism of the cell in an efficient manner to transfer its legacy. Speaking anthropomorphically, the phage uses extremely elegant means of taking over the mechanism of the host cells. There is an austere simplicity in this process, and the variation in the mechanisms is stunning (see Chapter 4). This apparent simplicity of the viral mechanisms has instigated and sustained the development of molecular biology [9]. There has always been social and commercial interest in the viruses because of the damage they cause to living organisms, including humans. Recently, viruses have resumed their role as a testing ground for quantitative modeling in biology, and a part of the aim of the present thesis is to apply mechanical modeling to the processes involved in the viral assault on the host cell.

1.1.1 Different Stages in the Phage Life-cycle are Quantitatively Measurable

Briefly speaking, the phage life-cycle consists of four stages: i) adsorption onto the bacterial surface, ii) DNA ejection, iii) gene-replication and the production of proteins, iv) assembly of various components and DNA packaging into the head. In this thesis we are mainly concerned about the DNA ejection from the phage capsid and its subsequent packing into the phage head. DNA is highly compressed inside bacteriophage capsid, and the resulting forces have important effects on the phage life cycle, as revealed in several experiments. Smith et al. [11] reinforced the idea that a strong force builds up during packaging with real-time single-phage packaging experiments (see Fig. 1.1. See also, Chapter 3). They measured the rate of DNA packaging while subjecting the DNA to various resisting forces, quantifying the forces imposed by the packaging motor and the force resisting further packaging as a result of the confined DNA. This experiment give us a picture of DNA packaging in which a strong portal motor consumes ATP and in so doing pushes the DNA into the capsid against an ever-increasing resistive force.

It is believed that the tightly wound DNA stores large energies, resulting in high forces which in some cases could aid DNA ejection into the host cell. Experiments were conducted by Evilevitch et al. [12] and Grayson et al. [13], who coerced λ into ejecting its genome into a solution containing polyethylene glycol (PEG) to create an external osmotic pressure. They found that various osmotic pressures of several tens of atmospheres could halt the ejection process resulting in fractional genome ejection. The fractional ejection reflects a balance of forces between the inside and outside of the capsid. From this experiment it is concluded that forces are still present during ejection at the same high levels as observed during packaging and in static capsids.

There are a variety of impressive *in vitro* experiments which demonstrate pressure-driven ejection of the phage genome [14, 15]. For the *in vivo* case, ejection driven by internal force is only one of several mechanisms that have been hypothesized to participate in transferring the genome of bacteriophage into the host cell. Another mechanism is suggested by Molineux [16] who, on the basis of a wealth of experimental evidence, argues that the DNA of phage T7 is assisted into the cell by DNA-binding proteins. It is likely that different bacteriophage use a combination of these two methods for ejecting their DNA into the host cell (see Chapters 3 and 4).

Finally, recent cryo-electron microscopy (cryo-EM) and X-ray crystallography studies of bacteriophage have revealed their detailed internal structure and, particularly, the ordered state of the packaged DNA. Cerritelli et al. [17] verified the tight packing measured by Earnshaw and Harrison [18] and showed that the DNA is apparently organized into circular rings within capsids. Other structural experiments have revealed the structure of components involved during ejection in T7 [19], the assembly of bacteriophage ϕ29 [20], and the structure of the packaging motor in ϕ29 [21]. This

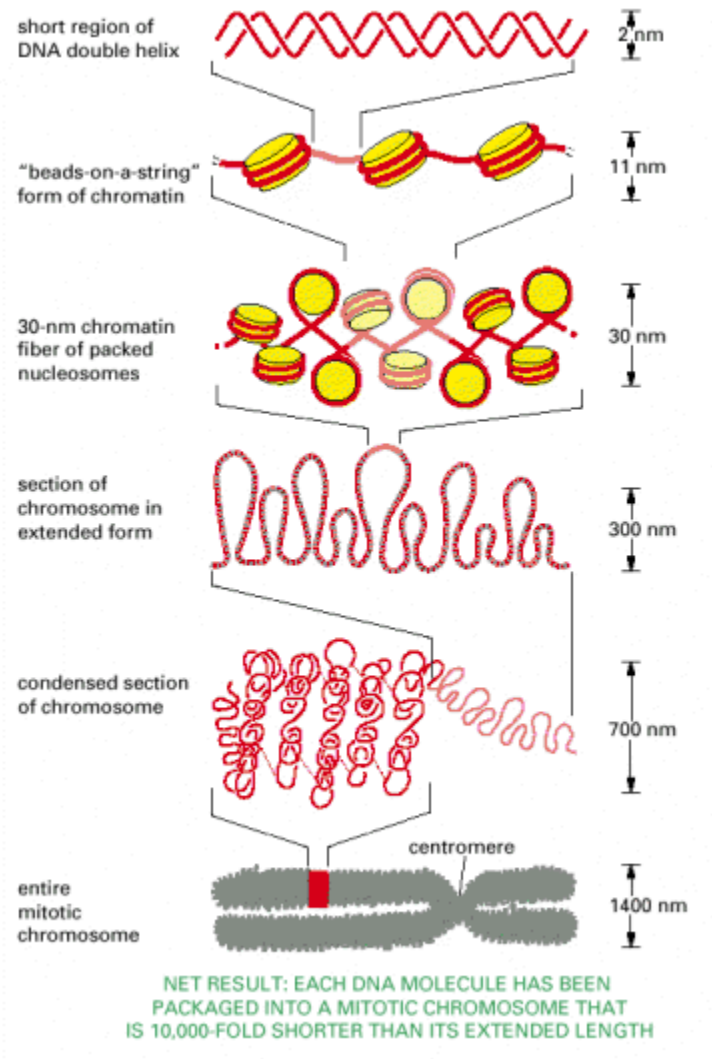

Figure 1.2: Different scales of packing of DNA in eukaryotic nuclei. The human genome is around 1cm long, while the typical eukaryotic nucleus has a size of roughly $2-5\mu$m. The DNA undergoes compaction at various level so as to fit inside the nuclei.

structural information complements the single molecule measurements and will guide us in the construction of a quantitative model of the packaging and ejection processes in Chapters 3 and 4.

1.2 Mechanism of DNA Accessibility in Nucleosomes

Thus far our discussion has concentrated on viruses in which the DNA is tightly packed in the capsid. Here we are going to talk about DNA compaction in a different form that occurs in the nucleus of the eukaryotic cells. The total length of the human genome is around 1 cm, while the typical size of the human nuclei is around 5mum . How can the nuclei hold the complete genome? The answer to this question lies in the fact that the genome is packed tightly into structures called nucleosomes.

The nucleosomes are themselves packed in a super-structure until the final structure formed of the compacted genome is around 1μm (see Fig. 1.2). This raises an apparent paradox: Different parts of the DNA need to be accessible at different times of the cell-cycle for various genomic processes; how is the DNA accessed when it is so tightly packed? This apparent paradox can be resolved by noting that not only do chromosomes globally condense in accord with the cell cycle, but that different regions of the chromosomes condense and decondense as the cells gain access to specific DNA sequences for gene expression, DNA repair, and replication.

1.2.1 The Spontaneous Fluctuations of the Nucleosomal DNA Exposes its Sequences

As seen in Fig. 1.2, the genomic DNA in eukaryotes is organized in a repeating array of nucleosomes in which short stretches of DNA are wrapped twice around spools of histone proteins. DNA wrapped in nucleosomes is sterically occluded from proteins, which are essential for gene expression, gene repair, and gene replication. The access to the buried sites in nucleosomes can be facilitated by ATP-dependent remodeling factors than can actively move or unwrap the nucleosome [22, 23]. However, such remodeling factors may not be always required. It has been shown [24, 22, 23] that the DNA can spontaneously unwrap from the nucleosomes due to the thermal fluctuations. The partial unwrapping of the wrapped nucleosomal DNA exposes buried sites for various proteins. When the buried site is exposed the proteins can bind on to them and carry out their required activity (see Fig. 1.3a). These two broad mechanisms for accessing DNA that is–via active ATP-dependent remodeling factors, or via passive binding–are not exclusive. The experimental finding of Li and Widom [22] show that nucleosomes inherently facilitate both of these mechanisms through spontaneous large-scale conformational changes.

1.2.2 Quantitative Measurements of DNA Accessibility in Nucleosomes

As mentioned in the previous section nucleosomal DNA undergoes large scale spontaneous unwrapping. Fluorescence Resonance Energy Transfer (FRET) experiments performed by Li and Widom [22] (see Fig. 1.3) have quantified DNA unwrapping and the subsequent re-wrapping process in the nucleosomes. The equilibrium constant, in general, depends on the depth of the binding site from the free end. Polach and Widom [24] have characterized the equilibrium constant as a function of the burial depth (see Fig. 1.3). Another set of FRET experiments performed by Li et al. [23] have also characterized the rate of unwrapping and re-wrapping of the DNA from the nucleosome (see Fig. 1.3b). In Chapter 5 we formulate a simple theoretical model based on statistical mechanics to account for these experiments and also make predictions for future experimentation.

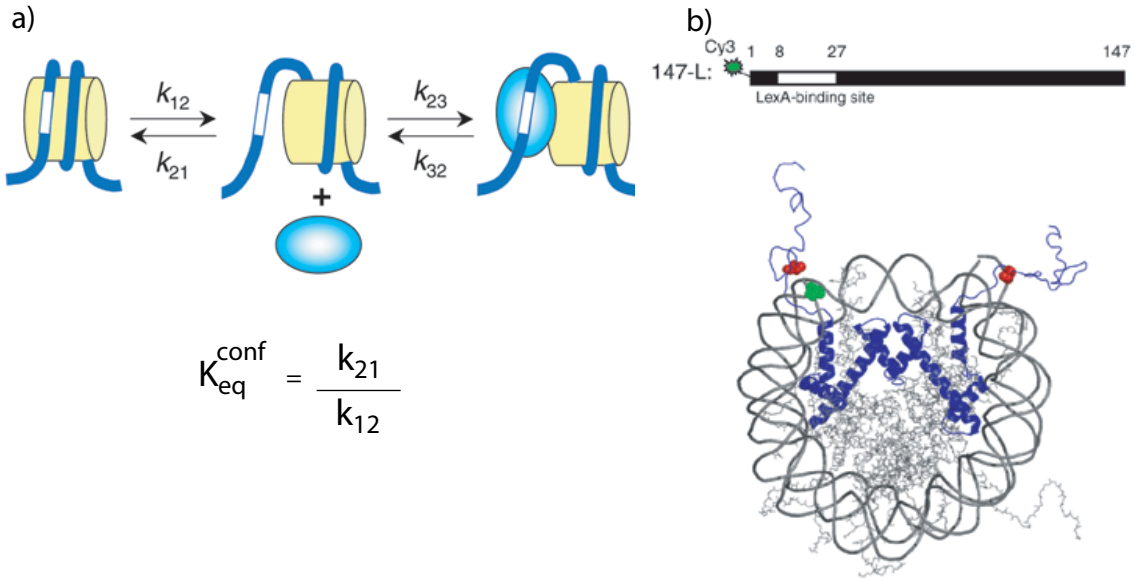

Figure 1.3: The measurement of thermal fluctuations of nucleosomal DNA. a)The nucleosomal DNA spontaneously unwraps at a rate of k_{12} exposing the binding site for the binding protein LexA. b) The donor cy3 and the acceptor cy5 are attached at the beginning of the nucleosomal DNA and on the histone protein, respectively. When the DNA unwraps, the donor and the acceptor are separated at a distance farther than the characteristic FRET distance R_0. This reduces the FRET efficiency.

1.3 Irreversible Processes and Non-equilibrium Systems

Consider a large system composed of $N_A \approx 10^{23}$ particles. At some time t_1, take a measurement of a given macroscopic quantity, say, volume of the system on length scales much larger than the spacing between atoms, and on time scales much larger than the vibrational frequency of the atoms. Call this measurement $V(t_1)$. Now, repeat the same measurement after another time t_2 to obtain $V(t_2)$. If within the experimental errors, $V(t_1) \approx V(t_2)$, we say the system is stationary. Now, in addition to the above property, if there is no energy or particle flux on those time-scales, the system is said to in thermodynamic equilibrium. That there is a well developed theory of thermostatics and equilibrium statistical mechanics [25, 26] is a major attraction of trying to model systems that are in equilibrium. On the other hand, many important problems in physical and chemical systems, and almost all interesting biological systems are in a non-equilibrium state. Life at its most fundamental level is governed by processes at the cellular level. [27] Since a process by definition implies some spatio-temporal change, non-equilibrium is the signature of life [2]. With this clarification we will turn towards what is meant by thermodynamic non-equilibrium.

1.3.1 Life and Non-equilibrium

Living systems are far from thermodynamic equilibrium. This means that there is a constant influx of energy and particles within the cells, between different cells, and between the cell and the

environment. There is a constant flurry of activities like gene replication, gene regulation, protein translation, cargo transport, ion-channel activity, etc., [27] happening in the cell almost always. Since the concept of time is not built in them, ideas of equilibrium statistical mechanics fall short of describing these processes. One has to resort to various different ideas like the master equation, Fokker-Planck equations, etc., as described in Chapter 6, to model such processes. Unlike the well-established theory of statistical equilibrium, founded on the thermodynamic extremum principle of the second law, there is no unanimously accepted or demonstrated general theory of non-equilibrium. The "principle of maximum caliber" introduced by E. T. Jaynes [7], developed from his previous work [5, 6], has been claimed to be such a general theory for thermodynamics. In equilibrium statistical mechanics, one writes down the entropy of the system by counting all possible *microstates*. The "principle of maximum caliber" is also a maximum entropy (maxent) principle, which involves maximizing the entropy over dynamical *macrotrajectories* as opposed to microstates (more details in Chapter 6). One of the central themes of this thesis is to make simple models for biological systems and apply the maximum caliber principle to these models to make new predictions and instigate new experiments (see Chapter 7 and Chapter 8).

1.3.2 Time-scales, Length-scales, and the Interplay Between Equilibrium and Non-equilibrium

We have discussed when a system is equilibrium or non-equilibrium. In real life the situation is not always this simple. For example, a system may have processes happening at different time-scales and length-scales. If the separation between the time and length scales of these processes is large, then for all practical purposes, it is reasonable the consider the process happening at fast-time scales to be happening in a steady background of slow processes. For example, the gene regulation in the nucleus of eukaryotic cells happens on the order of minutes, while cell-division happens in the order of hours. [27]. Hence, while considering the process of gene regulation, we may, for all practical purposes, assume that the cell has a constant volume. This condition is called local equilibrium. If there is no proper separation between the time and the length scales, then the assumption of local equilibrium breaks down, and one is forced to use a complete non-equilibrium description of the system. [3]

1.4 Thesis Outline

As seen earlier, the goal of this thesis is to apply statistical mechanics to dissipative or non-dissipative biological systems that are small in size. The outline of the thesis is as follows.

Chapter 2: In this chapter we provide a brief introduction to equilibrium statistical mechanics the way it is conventionally taught. We use the ideas in Chapter 3 to obtain the forces during

DNA packaging and ejection in bacteriophage and later in Chapter 5 to obtain the equilibrium constant for the DNA fluctuations in nucleosomes. We then outline a brief description of few of the prevalent ideas when the system of interest is far from equilibrium. We give a quick derivation of the 1-D Fokker-Planck (or Smoluchowski's) equation, which is used to model the diffusion of a Brownian particle on an energy landscape. This equation is used in Chapter 4 to make estimates of the kinetics of DNA ejection from bacteriophage and later in Chapter 5 to obtain rates of DNA unwrapping and re-wrapping in nucleosomes. Later in Chapter 2 we introduce the ideas of non-equilibrium thermodynamics with special emphasis on Onsager reciprocal relations, linear-response theory, the fluctuation-dissipation theorem, and the Kubo relations. Since this thesis places special emphasis on dissipative systems, we introduce the famous Jarzynski's equality, which relates the non-equilibrium work with the equilibrium free energies, and the Fluctuation theorem, which quantifies the probability of violation of second law of thermodynamics.

Chapter 3: This chapter addresses physical processes in the viral life cycle through a quantitative framework based on insights from structural biology, single molecule biophysics, electron microscopy, and solution biochemistry. The models are motivated by specific experiments on $\phi 29$ [11] and λ [12, 13], but their applicability extends to all dsDNA bacteriophages. In the case of DNA packaging, we obtain the force on the DNA inside the phage capsid as a function of the genome length packed, for a wide-range of bacteriophages. The theoretical results obtained match very well with the experimental results from Smith et al. [11] on $\phi 29$ (see Fig. 1.1). We then make predictions for the amount of DNA ejected in λ phage as a function of the external resistive force. Our predictions give good fit to the experimental results obtained by Evilevitch et al. [12] and Grayson et al. [13].

The work completed in this chapter was done collaboration with P. Grayson, J. Kondev, R. Phillips, P. Purohit, and T. Squires. A large portion of this work is published in Purohit et al. [28].

Chapter 4: The force on the DNA inside the phage capsid can be as high as 60pN [11] (see also Fig. 1.1) and can be utilized to drive the DNA ejection in bacteriophage. In this chapter we obtain the kinetics of DNA ejection due to this force by using a Fokker-Planck description. We also model the DNA ejection from a phage into lipid vesicles [14, 15] and obtain the time required to complete ejection as a function of the size of vesicles (see Fig. 1.4). Finally, we investigate the role of DNA binding proteins for the DNA ejection in phage and conclude that they can speed-up the ejection process.

The work in this chapter was done in collaboration with W. Gelbart and R. Phillips. Majority of this work will be published in Inamdar et al. [29].

Chapter 5: The eukaryotic genome is organized in compact structures called nucleosomes. The nucleosomes undergo spontaneous conformational changes, thereby transiently exposing their genome to the binding proteins [24, 22, 23]. In this chapter we formulate a simple model by taking into account the DNA bending energy and the DNA-histone interaction to obtain the equilibrium constant

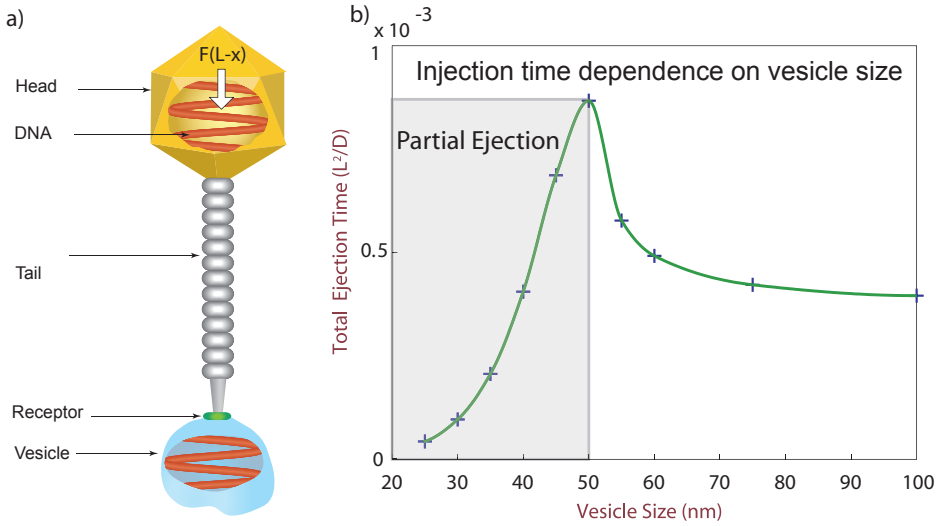

Figure 1.4: The theoretical modeling of DNA ejection into vesicles. (a) Lipid vesicles can be made by reconstituting the receptor for the particular phage [14, 15]. The bacteriophage adsorbs onto the receptor on the vesicle and eject its DNA. (b) The time for DNA ejection as a function of vesicle size. As the vesicle size increases, the amount of DNA ejected into the vesicle increases. At an optimal size, the phage ejects its complete genome into the host cell. When the vesicle size is increased further, the time-required eject its genome decreases.

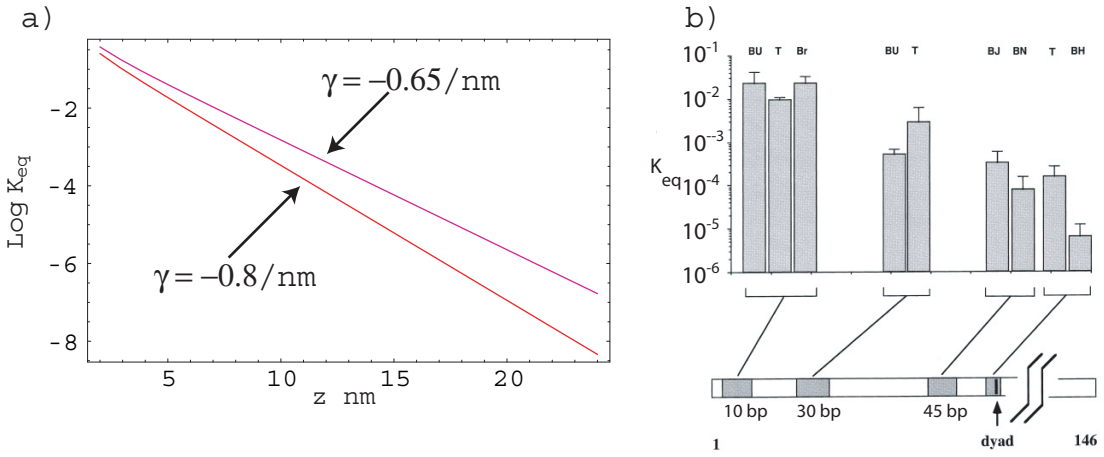

Figure 1.5: Thermal fluctuations of the nucleosomal DNA. a) The nucleosomal DNA undergoes spontaneous unwrapping and rewrapping around the histone core. Polach and Widom [24] measured the equilibrium constant for the unwrapping and the rewrapping processes. b) The theoretical result for equilibrium constant from a simple model based on statistical mechanics (see Chapter 5).

for the spontaneous thermal fluctuations of the DNA (see Fig. 1.5). We then use a Fokker-Planck description to obtain the rate of unwrapping and re-wrapping.

This work is in progress in collaboration with J. Kondev, R. Phillips, T. Rimachala, and J. Widom.

Chapter 6: From Chapter 6 onwards we focus on the application of the information-theoretic-methods to model systems that are far from equilibrium. When the system is in equilibrium its behavior is governed by the underlying microstates of the system. On the other hand, when the system is far from equilibrium its evolution is dictated by the underlying microtrajectories. The entropy of equilibrium system is obtained by a a summation over all microstates. E. T. Jaynes [6, 7, 8] extended this to non-equilibrium systems where the "trajectory entropy" is obtained by summation over all possible microtrajectories. Subject to proper constraints, the maximization of this "trajectory entropy" provides the probabilities of the microtrajectories. This method is called the "maximum caliber principle," and its rationale is described in Chapter 6.

Chapter 7: Phenomena like Fick's Law of diffusion and chemical decay processes belong to the domain of non-equilibrium thermodynamics. In this chapter we formulate a simple dog-flea model for dynamical processes like particle diffusion, heat diffusion, and chemical kinetics. Following the maximum caliber principle, we identify the phase trajectories in each case and write down the corresponding entropy. We then maximize this entropy, subject to the physical/chemical constraints involved in the process, to obtain the probability distribution for its trajectories. From this probability distribution we can get the mean value and fluctuations for the variables of interest. We also introduce new quantities, potency, and bad-actors which may serve as a metric to measure the distance of the system of interest from equilibrium. Finally, we use a modification of the dog-flea model to give a demonstration of Onsager reciprocal relations.

This work was done in collaboration in K. Dill, K. Ghosh, R. Phillips, and E. Seitaridou.

Chapter 8: In Chapter 8 we discuss the application of the maximum caliber principle to two state systems. Specifically, we apply the maximum caliber principle to two classes of microtrajectories (see Fig. 1.6). We use the class of trajectories shown in Fig. 1.6a to describe the dynamics of processive molecular motors. The second class of trajectories in Fig. 1.6b is used to describe the dynamics of ion channels and their analogs. We also propose experiments using a Brownian particle trapped in dual-laser-traps, currently underway in our lab, to verify the predictions of these theoretical results.

This work is in progress in collaboration with K. Dill, K. Ghosh, R Phillips, E. Seitaridou, and D. Wu.

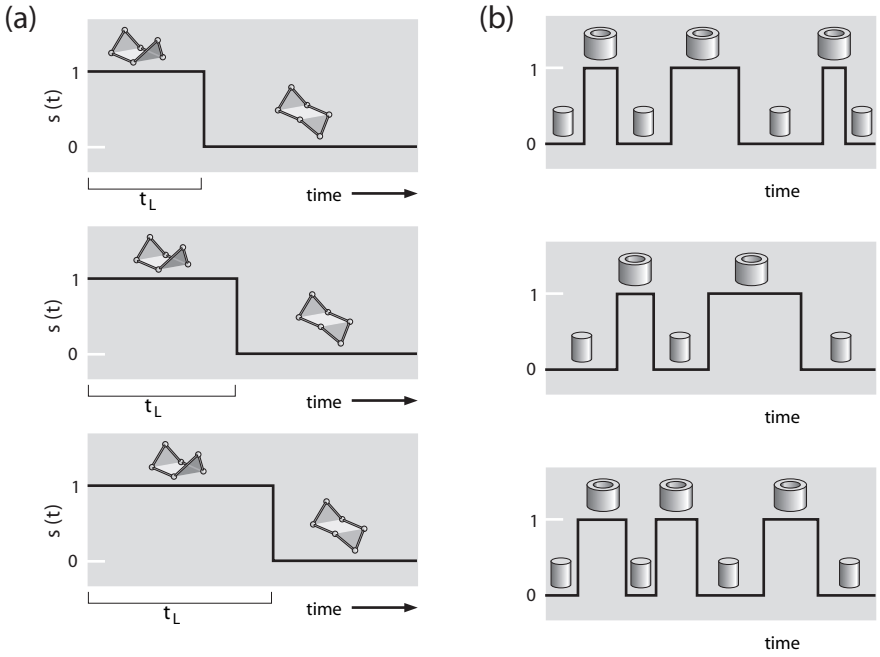

Figure 1.6: Two class of microtrajectories for two-state systems. a) This class of trajectories is to model processes of form $A \rightarrow B$. We use them to model the dynamics of processive motors. b) This class of trajectories is to model processes of form $A \leftrightharpoons B$. We use them to model the dynamics of ion-channels.

Chapter 2

Introduction to Non-Equilibrium Statistical Mechanics

Our primary interface with nature is through the properties of macroscopic matter. Classically speaking, macroscopic matter is composed of particles. The dynamics of these constituent particles that are acted upon by forces are governed by Newton's laws, while the dynamics of the fields that mediate these forces are governed by Maxwell's laws. Thermodynamics does not introduce any such fundamental laws. On the other hand, it is applicable to all systems in macroscopic aggregation. In brief, thermodynamics is the study of the restrictions on the possible properties of matter that follow from the symmetry properties of the fundamental laws of physics [25]. The connection between the symmetries of the fundamental laws and the macroscopic properties of matter is not trivially evident. Instead of deriving the latter from the former, thermodynamics is usually formulated in terms of postulates [25]. The drawback of thermodynamics is in the fact that because it is universally applicability to any system, in order to get actual numbers for a particular system one needs to specify some empirical results whose relationship with the underlying microscopic dynamics is not apparent. Statistical thermodynamics is precisely to get over this limitation and establish thermodynamics on a more fundamental footing.

Since this thesis mainly involves the use of equilibrium and non-equilibrium statistical mechanics to small scale system we would like to discuss the basics of thermodynamics and equilibrium statistical mechanics and some of the prevalent approaches when the system is far from equilibrium. In Chapter 1 we briefly discussed about equilibrium and non-equilibrium thermodynamics. In this chapter we will give a brief description of equilibrium statistical mechanics from the traditional point of view. We will then provide a brief review of the different methods for non-equilibrium systems that are used in the literature.

2.1 Thermostatics and Equilibrium Statistical Mechanics

Equilibrium thermodynamics is a contradiction; the more appropriate name is thermostatics, but until and unless the tag of non-equilibrium precedes thermodynamics, we will take it to mean thermostatics. A system which (i) does not change with time, (ii) does not have particle or energy flux, and (iii) whose properties do not depend on the history of preparation of the system is said to be in equilibrium. Like any well-established scientific theory, thermodynamics is based on postulates [25, 3]. The first postulate states that given sufficient time an isolated system will attain an equilibrium state that is independent of its past history and characterized by its own intrinsic properties such as volume V, energy E, and numbers $N^{(i)}$ of molecules of different types. The second postulate is a variation of the famous *second law of thermodynamics*. It postulates the existence of the entropy function, S, and states that for any process, the entropy of an isolated system cannot decrease. The third postulate is related to low temperatures and states that when the temperature of a system tends to absolute zero, the entropy per unit volume reaches a constant value S_0 which is independent of the type of the system. For more details one is referred to the delightful exposition of thermodynamics by H. B. Callen [25]. A more terse but concise explanation is given in Chapter 1 of Le Bellac et al. [3]. Just using these postulates (especially postulates one and two) combined with phenomenological observations, it is possible to deduce relations between seemingly unrelated quantities. If these postulates are combined by the empirically observed so-called state function, specific to a particular system, one can get exact values of many quantities of interest for the system. As mentioned earlier, the drawback of this postulational approach is that the relationship between the macro properties of the system and its underlying fundamental micro properties is not at all apparent. This is where equilibrium statistical mechanics comes into play. What statistical mechanics does is simply use all the postulates of thermostatics but connect the entropy of the system with the underlying microscopic behavior. It states that the entropy of an isolated system is the logarithm of the total number of underlying stationary microstates, Ω, of the system at a given value of energy E, volume V, and number of moles N. In mathematical language,

$$S(E, V, N) = k \ln \Omega(E, V, N). \tag{2.1}$$

This is the famous Boltzmann equation, which is engraved on Boltzmann's tombstone in Vienna. This particular description of entropy is supplemented with three other assumptions:

1. For an isolated system with a given value of energy E, each microstate is equally likely.

2. Given enough time the system will pass through each and every microstate.

3. The time average of a given quantity is equal to the ensemble average of that quantity.

The second assumption is called the ergodic hypothesis and has been a subject of rigorous investigation and debate since the inception of statistical mechanics. This ergodic hypothesis combined with the first assumption implies that the system stays in all microstates for an equal amount of time. The third assumption introduces what is called the ensemble average. The ensemble average of a quantity A is given by

$$\langle A \rangle = \sum_{\text{microstates} \equiv \nu} A_\nu p_\nu, \tag{2.2}$$

where ν stands for a particular microstate of the system and p_ν is the probability that the system is in that microstate. Conventionally, p_ν is interpreted as $\lim_{T\to\infty} \frac{T_\nu}{T} = p_\nu$, where T_ν is the time spent by the system in state ν. The three assumptions combined together imply that

$$\begin{aligned} \langle A \rangle &= \sum_\nu A_\nu p_\nu, \\ &= \lim_{T\to\infty} \frac{1}{T} \sum_\nu A_\nu T_\nu, \\ &= \lim_{T\to\infty} \frac{1}{\Omega} \sum_\nu A_\nu. \end{aligned}$$

It is very difficult to prove the validity of the ergodic hypothesis, even for very simple systems. It will be seen in Chapter 6 that if the entropy is viewed from an information theoretic point of view, and the probabilities are considered as the reflection of our information, it will be possible to bypass the notion of ergodicity.

Until now we have talked only about isolated systems. On the other hand, if we have a system in contact with heat bath at a given temperature T, the system plus the heat bath is an isolated system. Using the methods for an isolated system, one can project out the degrees of freedom for the thermal bath and get expressions for p_ν just for the system as

$$p_\nu = \frac{\exp(-\beta E_\nu)}{Z(\beta)}, \tag{2.3}$$

where $\beta = 1/k_B T$ and $Z(\beta)$ is the partition function of the system and is given by

$$Z(\beta) = \sum_\nu \exp(-\beta E_\nu). \tag{2.4}$$

The entropy of the system $S(E, V, N)$ will be replaced by the corresponding free energy $F(T, V, N)$ (which is the Legendre transform of the entropy). The free energy of the system $F(T, V, N) = U(S, V, N) - TS$ is related to partition function as,

$$F = -k_B T \ln Z(\beta). \tag{2.5}$$

The various derivatives of $F(T, V, N)$ will, in accordance with the postulates of thermodynamics, give us the corresponding quantities of interest. In addition to giving us information about the relation of macro quantities with the underlying microstates, statistical mechanics also gives us the thermodynamic fluctuations of equilibrium systems. This precise property of statistical mechanics was brilliantly exploited by Einstein to give his famous theory of photons, leading to the explanation of photoelectric effect, the fluctuation-dissipation theorem associated with the Brownian motion, and later the theory of critical opalescence.

In order to put this section in the perspective of this thesis, it may be noted that the theory of equilibrium statistical mechanics is used in Chapter 3 to estimate the forces during DNA packaging and ejection in bacteriophage. Equilibrium statistical mechanics is also used in Chapter 5 in order to evaluate the probabilities of wrapping and unwrapping of DNA in nucleosomes.

We now proceed from equilibrium systems to the systems that are are close to equilibrium.

2.2 Non-equilibrium Thermodynamics Near Equilibrium

The extension of thermodynamics that has reference to the rates of physical processes is the theory of non-equilibrium, or irreversible thermodynamics. Linear irreversible thermodynamics is based on the postulates of thermodynamics plus the additional postulate of time reversal symmetry of the laws of physics. This additional postulate states that the laws of physics remain unchanged if time t is everywhere replaced by its negative $-t$ and if simultaneously the magnetic field B is replaced by its negative $-B$. Non-equilibrium thermodynamics is based on the Onsager Reciprocity Theorem, formulated by Lars Onsager. Statistical theorems like, the fluctuation-dissipation theorem, the Kubo relations, and the formalism of the linear response theory also exist. In this section we will briefly review these theories.

2.2.1 Notion of Local Equilibrium

A physical system can be so far out of equilibrium that quantities like temperature and pressure cannot be even defined. On the other hand, there are many cases where one can define these quantities. We consider an idealized case where we assume the system to be composed of homogeneous cells, small on the macroscopic scale but large on the microscopic one. We also assume that cells interact weakly with their neighbors so that each cell independently attains a local equilibrium with a microscopic relaxation time, τ_{micro}, which is very small compared to the macroscopic relaxation time, τ_{macro}, needed to achieve global equilibrium. The local equilibrium is said to exist when

1. Each subsystem is at equilibrium independently of the other subsystems.

2. Interactions between neighboring subsystems are weak.

When the system is in local equilibrium, all we need is the local conservation of energy and particles, and the local equation of state. The local equation of state equates the rate of entropy production, $\dot{s}$, with the flux J_i and the corresponding affinity (driving force):

$$\dot{s} = \sum_i \mathcal{F}_i J_i. \tag{2.6}$$

The second step involves the use of phenomenological relations between the affinities $\mathcal{F}_i$ and the corresponding fluxes J_k. For this we need to invoke the famous Onsager's reciprocal theorem. We will discuss that in the next section.

2.2.2 Onsager's Reciprocal Relations

For certain systems the fluxes at a given instant depend only on the values of the affinities at that instant. Such systems are referred to as resistive systems. For a purely resistive system, by definition, each local flux depends only upon the instantaneous local affinities and the local intensive parameters. That is, dropping the indices denoting vector components,

$$J_k = J_k(\mathcal{F}_0, ..., \mathcal{F}_j, ...; F_0, ..., F_j, ...). \tag{2.7}$$

Though it is true that each flux J_i tends to depend most strongly on its own associated affinity $\mathcal{F}_i$, its dependence on other affinities is the source of the most interesting phenomena in the field of irreversibility. Each flux J_i is known to vanish as the affinities vanish, so we can expand J_k in powers of the affinities with no constant term:

$$J_k = \sum_j L_{jk}\mathcal{F}_j + \frac{1}{2!}\sum_i \sum_j L_{ijk}\mathcal{F}_i\mathcal{F}_j + ... \tag{2.8}$$

where

$$L_{jk} = \left(\frac{\partial J_k}{\partial \mathcal{F}_j}\right)_0 \tag{2.9}$$

and

$$L_{ijk} = \left(\frac{\partial^2 J_k}{\partial \mathcal{F}_i \partial \mathcal{F}_j}\right)_0. \tag{2.10}$$

. The functions L_{jk} are called the kinetic coefficients. They are functions of the local extensive parameter. For the purposes of the Onsager theorem, it is convenient to adopt a notation that exhibits the functional dependence of the kinetic coefficients on an externally applied magnetic field

B, suppressing the dependence of other intensive parameters:

$$L_{jk} = L_{jk}(B). \tag{2.11}$$

The Onsager theorem states that

$$L_{jk}(B) = L_{kj}(-B), \tag{2.12}$$

that is, the value of the kinetic coefficient L_{jk} measured in an external magnetic field B is identical to the value of L_{kj} measured in the reversed magnetic field B. The Onsager theorem states a symmetry between the linear effect of the jth affinity on the kth flux and the linear effect of the kth affinity on the jth flux when these effects are measured in opposite magnetic fields. If the affinities are so small that all quadratic and higher order terms in Eq. 2.8 can be neglected and

$$J_k = \sum_j L_{jk}\mathcal{F}_j \tag{2.13}$$

such a process is called a linear purely resistive process. Onsager theorem is a powerful tool for the analysis of such a process.

In this thesis, a simple derivation of Onsager's reciprocal theorems (derived for a more general case by E. T. Jaynes [7, 8]) by the application of maximum entropy methods to a simple model is explained in Chapter 7. The derivation is really simple, and makes one appreciate the beauty and elegance of the maximum entropy methods.

2.2.3 Fluctuation-dissipation Theorem, Green-Kubo Relations, and Linear Response Theory

Consider a system in equilibrium with extensive macroscopic parameters $\mathcal{A}_1, ...\mathcal{A}_m$. Now, if we perturb this system from equilibrium by disturbing the parameter $\mathcal{A}_i$ by $\delta\mathcal{A}_i = \mathcal{A}_i - \langle\mathcal{A}_i\rangle$, the perturbation on the Hamiltonian will be of the form

$$\Delta H = -\sum_j f_j\mathcal{A}_j, \tag{2.14}$$

so that the equilibrium Hamiltonian will be transformed to

$$H \to H_1 = H_0 + \Delta H = H - \sum_j f_j\mathcal{A}_j. \tag{2.15}$$

The f_j's are often called the external forces, or simply the forces. Just as a matter of convention, we denote $\overline{A_i}$ as the average of the quantity $\mathcal{A}_i$ using the modified Hamiltonian (i.e., the modified probability distribution function), while we use $\langle \mathcal{A}_i \rangle$ to imply average using the equilibrium probability distribution function. For small values of forces it can be shown that [3]

$$\begin{aligned} \overline{\delta \mathcal{A}_j}(t) &= \overline{\mathcal{A}_i}(t) - \langle \mathcal{A}_i \rangle, \\ &= \beta \sum_j f_j \langle \delta \mathcal{A}_i(t) \delta \mathcal{A}_j(0) \rangle. \end{aligned} \tag{2.16}$$

The summand in Eq. 2.16 is called the Kubo function and is represented as

$$C_{ij}(t) = \langle \delta \mathcal{A}_i(t) \delta \mathcal{A}_j(0) \rangle. \tag{2.17}$$

The Kubo function is directly related to the dynamical susceptibility $\xi_{ij}(t)$, which is defined by writing the most general formula for the dynamical linear response to an external time-dependent perturbation $\sum_j f_j(t) \mathcal{A}_j$:

$$\overline{\delta \mathcal{A}_i}(t) = \sum_j \int_{-\infty}^{t} dt' \xi_{ij}(t - t') f_j(t'). \tag{2.18}$$

In Fourier space, and supposing that $\xi_{ij}(t - t')$ vanishes for $t' > t$, the convolution in Eq. 2.18 is transformed into a product

$$\overline{\delta \mathcal{A}_i}(\omega) = \sum_j \xi_{ij}(\omega) f_j(\omega). \tag{2.19}$$

Using a few manipulations it can be shown that

$$\xi_{ij}(t) = -\beta \dot{C_{ij}}(t). \tag{2.20}$$

This is most general version of the Kubo formula. This relationship between the equilibrium fluctuations and the dynamic susceptibility can be used to give relationships between transport coefficients and the equilibrium correlation functions. These relationships are called Green-Kubo formulas.

Using the analyticity properties of the susceptibility function and the the notion of causality that $\xi(t) = 0$ if $t < 0$, which reflects the obvious requirement that effect must follow cause, one obtains what is called the fluctuation-dissipation theorem. The classical version of this theorem is

$$\xi''(\omega) = \frac{1}{2} \beta \omega C(\omega), \tag{2.21}$$

where $\xi''(t)$ is defined as

$$\xi''(t) = \frac{i}{2}\beta\dot{C}(t). \tag{2.22}$$

The right hand side (RHS) of this equation is clearly the fluctuation part. It is a priori not clear that the left hand side (LHS) is the dissipation, but it can be shown that it indeed is the dissipation. The linear response theory and the fluctuation-dissipation theorem provide the microscopic basis of Onsager relations, while the Green-Kubo relations give a method to obtain the transport coefficients for non-equilibrium processes by observing the non-equilibrium fluctuations in the system.

2.3 Brownian Motion, Langevin Equation, Master Equation, and Fokker-Planck Equation

We use the Fokker-Planck equation in Chapter 4 to describe the process of DNA ejection in bacteriophage. Later in Chapter 5 we again use the Fokker-Planck equation to elucidate the process of DNA unwrapping in the nucleosomes. In this section we will provide a brief overview of the Langevin and the Fokker-Planck equation.

It was observed by Robert Brown that a pollen grain suspended in water undergoes a jiggling random motion. After its discovery, this phenomenon, later called Brownian motion, was attributed to several different fantastic causes. It required the genius of Einstein to relate the sudden jumps in the motion of the pollen grain to the collective collisions of water molecules on it. Einstein also gave an estimate of Avogadro's number ($N_A \approx 10^{23}$) and provided the impetus for the then controversial theory that matter is composed of constituent atoms. Einstein formulated the theory of Brownian motion by introducing the notion of random walk. An alternative description of Brownian motion was given by P. Langevin. The approach is as follows. Consider a Brownian particle of mass m in a fluid with friction coefficient ζ, subject to a potential field $U(x)$. The particle is buffeted by the fluid molecules. These force acting from the fluid particles is modeled as a random force $g(t)$. The governing equation for the motion of this Brownian particle is the stochastic differential equation [30]:

$$m\frac{d^2x}{dt^2} = -\zeta\frac{dx}{dt} - \frac{\partial U}{\partial x} + g(t). \tag{2.23}$$

Assuming that the velocity fluctuations in the presence of the potential field are the same as when there is no field, the mean and variance of $g(t)$ are as follows:

$$\langle g(t)\rangle = 0; \quad \langle g(t)g(t')\rangle = B\delta(t-t') \tag{2.24}$$

where B is the strength of the force fluctuation. With this governing equation and the above mentioned properties of the random force one can derive the velocity correlation function $v(t)v(t')$, and the position correlation function $x(t)x(t')$. It can be shown that the relaxation time for the velocity, i.e., time after which the velocity distribution reaches the equilibrium distribution, the velocity relaxation time is given by $\tau_{\rm v} = m/\zeta$. If the friction from the fluid ζ is large (the system is over damped), then the inertial terms (terms involving mass and the acceleration) can be neglected, and the equation of motion for the particle will reduce to

$$\zeta \frac{dx}{dt} = \frac{\partial U}{\partial x} + g(t). \tag{2.25}$$

The time evolution of $x(t)$ will be given by the following equation:

$$x(t+\Delta t) = x(t) - \frac{1}{\zeta}\frac{\partial U}{\partial x}\Delta t + \Delta G(t) \tag{2.26}$$

where ΔG is the probability distribution function formed by integrating $g(t)$ from t to $t+\Delta t$:

$$\Delta G = \int_t^{t+\Delta t} dt' g(t'). \tag{2.27}$$

The mean and variance of ΔG are calculated using Eq. 2.24 as follows:

$$\begin{aligned} \langle \Delta G(t) \rangle &= 0, \\ \langle \Delta G(t) \Delta G(t') \rangle &= \int_t^{t+\Delta t} dt_1 \int_{t'}^{t'+\Delta t'} dt_2 2D\delta(t_1 - t - 2), \\ &= B\delta_{t,t'}\Delta t. \end{aligned} \tag{2.28}$$

This would mean that if x evolves according to Eq. 2.26, the probability distribution function $p(x,t)$ of x must satisfy the following master equation [30]:

$$p(x, t+\Delta t) = \int_{-\infty}^{\infty} d\xi p(x-\xi, t) F(\xi; x-\xi, t), \tag{2.29}$$

where $\xi = x(t+\Delta t) - x(t)$ and $F(\xi; x, t)$ is

$$F(\xi; x, t) = (2\pi B \Delta t)^{-1/2} \exp\left(-\frac{(\xi + \frac{1}{\zeta}\frac{\partial U}{\partial x}\Delta t)^2}{2B\Delta t} \right). \tag{2.30}$$

This master equation can be expanded in ξ to give what is called the Fokker-Planck equation [30],

$$\frac{\partial p(x,t)}{\partial t} = \frac{\partial^2 D p(x,t)}{\partial x^2} + \frac{\partial}{\partial x}\left(\frac{1}{\zeta}\frac{\partial U}{\partial x} \right), \tag{2.31}$$

where $D = B/2 = kT/\zeta$ is the diffusion constant. This relationship is called the Stokes-Einstein formula and is the first instance of the generalized fluctuation-dissipation theorem about which we will see more in the next section.

Brownian motion appears in different garbs throughout the literature of non-equilibrium statistical mechanics. The Langevin equation and the corresponding Fokker-Planck equation are the methodologies to describe the Brownian dynamics phenomena. The representation in Eqs. 2.25 and 2.31 is the simplest and the most commonly used form of these equations, but depending on the problem there exist many different forms of these equations [31].

2.4 Jarzynski's Equality and the Fluctuation Theorem

In the previous sections we discussed various approaches for systems that are not in equilibrium. Each approach was based on some assumption or the other. For example, in the case of Onsager relations we had to assume that the assumption of local equilibrium was right and that the system was close to equilibrium. When we use Langevin equation or the modified Langevin equation, we have to assume certain properties of the thermal bath. On the other hand, there exists extremely general results which are true no matter how far from equilibrium the system is. One such results is the non equilibrium work theorem, more popularly know as the Jarzynski's equality. The content of the theorem is as follows.

Consider a system in equilibrium with the heat bath at temperature T. Let λ be the extensive parameter of the system. For example, if the experiment involves pulling on a polymer, then λ will be the distance between the two ends of the polymer. Let us say that the value of this parameter is λ_1 when the system is in equilibrium in state-1. Now, vary parameter λ as a function of time from its initial value $\lambda(0) = \lambda_1$ to its final value $\lambda(T) = \lambda_2$ with a prescribed time-history $\lambda(t)$. Repeat the same procedure, say, N number of times. If the work obtained during ith trial is W_i, Jarzynski's equality [32, 33, 34] states that,

$$\lim_{N\to\infty} \frac{1}{N} \sum_{i=1}^{N} \exp\left(\frac{-W_i}{k_B T}\right) = \left\langle \exp\left(-\frac{W_i}{k_B T}\right)\right\rangle = \exp\left(-\frac{F_2 - F_1}{k_B T}\right). \tag{2.32}$$

Here F_1 and F_2 are the free energies of the system when the values of the extensive parameter λ are λ_1 and λ_2, respectively. This equality is true no matter what the time history of loading $\lambda(t)$ is. Apart from being a really nifty theorem in non-equilibrium statistical mechanics, the major attraction of Jarzynski's equality lies in the fact that it can be utilized to obtain the free energy landscapes of biological systems [35]. Since free energy is an equilibrium quantity, in order to obtain the energy landscape for a system one needs to perform a time-consuming quasi static process. The drift of the optical table, changes in temperature, vibrations, etc., make it difficult to perform

a real experiment on such time-scales. Similarly, the inherent limitations in molecular dynamics computation relative to the amount of time it can simulate makes it almost impossible to perform an equilibrium computational experiment. The Jarzynski's equality, on the other hand, allows any rapid time history for the process $\lambda(t)$. This makes the free energy estimation via real experiment, or by computation much more feasible.

The fluctuation theorems [36, 37] are a group of relations that describe the entropy production of a finite classical system coupled to a constant temperature heat bath, that is driven out of equilibrium by a time dependent work process. Although the type of system, range of applicability, and exact interpretation differ, these theorems have the same general form [36],

$$\frac{P(+\sigma)}{P(-\sigma)} \simeq \exp(\tau\sigma). \tag{2.33}$$

Here, $P(+\sigma)$ is the probability of observing an entropy production rate, σ, measured over a trajectory of time τ. This theorem thus quantifies the probability of violation of the second law of thermodynamics. Entropy production is an extensive quantity and depends on the size of the system, so larger the system, larger is σ, and the probability that entropy production is negative vanishes. Similarly, the larger the time of observation τ, larger is the right hand side of Eq. 2.33, and hence the probability that entropy is consumed becomes negligible. The second law of thermodynamics is, hence, almost deterministically valid for large systems and large observation times.

Chapter 3

DNA Packaging and Ejection in Bacterial Viruses (Bacteriophage)

Most of the work in this chapter is published in Purohit et al. [28], and Grayson et al. [13]

The conjunction of insights from structural biology, solution biochemistry, genetics, and single molecule biophysics has provided a renewed impetus for the construction of quantitative models of biological processes. One area that has been a beneficiary of these experimental techniques is the study of viruses. In this chapter we describe how the insights obtained from such experiments can be utilized to construct physical models of processes in the viral life cycle. We focus on dsDNA bacteriophages and show that the bending elasticity of DNA and its electrostatics in solution can be combined to determine the forces experienced during packaging and ejection of the viral genome.

Furthermore, we quantitatively analyze the effect of fluid viscosity and capsid expansion on the forces experienced during packaging. Finally, we present a model for DNA ejection from bacteriophages based on the hypothesis that the energy stored in the tightly packed genome within the capsid leads to its forceful ejection. The predictions of our model can be tested through experiments *in vitro* where DNA ejection is inhibited by the application of external osmotic pressure.

As shown in Fig. 3.1, a typical phage life cycle consists of adsorption, ejection, genome replication, protein synthesis, self-assembly of capsid proteins, genome packaging inside the capsid, and lysis of the bacterial cell. A wealth of knowledge about various aspects of these processes has been garnered over the last century, with the main focus being on replication and protein-synthesis. However, recent developments in the fields of x-ray crystallography, cryo-electron microscopy, spectroscopy, etc., have helped reveal the structural properties of the viral components [38, 39] involved in ejection, assembly, and packaging, while recent experiments on $\phi 29$ [11] and λ [12] have helped quantify the forces involved in the packaging and ejection processes, respectively. In this chapter we bring together these experimental insights to formulate quantitative models for the packaging and ejection processes. The model is based on what we know about the structural "parts list" of a phage: the shape, size, and strength of the capsid the mechanical and electrostatic properties of DNA and

high-resolution images that reveal the structure of assembled phage particles. Our goal is to create a detailed picture of the forces implicated in DNA packaging and ejection and, most importantly, make quantitative predictions that can be tested experimentally.

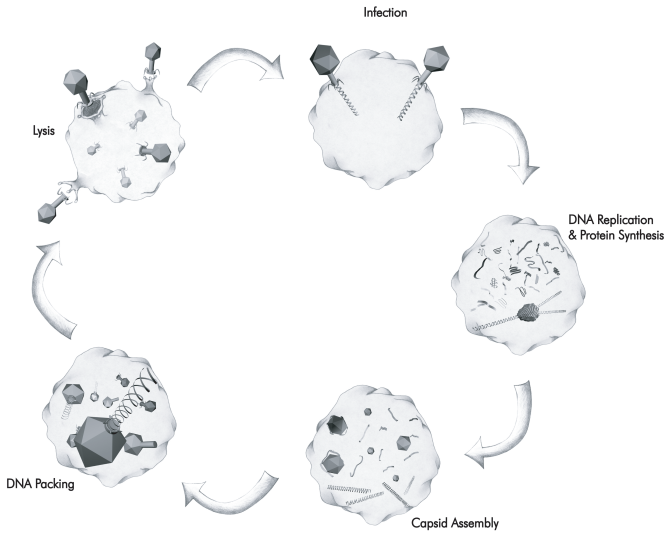

Figure 3.1: Life cycle of a bacterial virus. The ejection of the genome into the host cell happens within a minute for phage like λ and T4 [14, 40]. The eclipse period (time between the viral adsorption and the first appearance of the progeny) is about 10-15 minutes [41]. The packaging of the genome into a single capsid takes about 5 minutes [11]. Lysis of the bacterial cell is completed in less than an hour [41].

The chapter is organized as follows: In Section 5.1 we provide a brief introduction to viruses in general, and bacteriophages in particular. In Section 3.2 we examine dsDNA bacteriophage with the aim of assembling the relevant insights needed to formulate quantitative models of packing and ejection. In Section 3.3 we develop the model by examining the DNA packaging process in detail, and in Section 3.4 we show that it can be used to explain the DNA ejection process as well. In Section 3.5 we take stock of a range of quantitative predictions that can be made on the basis of the model and suggests new experiments.

3.1 Introduction to Viruses

Viruses are the simplest known organisms, with sizes ranging from tens to hundreds of of nanometers. They are on the borderline of living and non-living. Unlike all other living organisms, outside the host cell they show no more sign of living than a piece of rock. But once inside the host cell they show extreme vitality. They take over the cellular mechanism of the host, make multiple copies of themselves, destroy the host cell, and break free to attack more such cells with a replenished garrison.

Despite their evident malice, historically the study of virus has served as both an inspiration and testing ground for the basic theories of genetics and structural biology and has been an object of affection for researchers from various fields. Recently, viruses have resumed their role as a testing ground for quantitative modeling in biology, and a part of the aim of the present thesis is to apply mechanical modeling to the processes involved in the forementioned assault on the host cell.

3.1.1 Major Groups of Viruses

It is customary to subdivide viruses according to the nature of their hosts into plant viruses, animal viruses and bacterial viruses or bacteriophages (*bacteria eater*) [10]. Even such broad divisions can create ambiguities with some plant viruses that can multiply in their insect vectors. Each virus has a range of hosts in which it can reproduce. Viruses are discovered as pathogens, and hence it is logical to classify them in terms of their *major host*, the host whose response to the viruses first came to the attention of man.

1: Animal viruses

The only invertebrates in which virus diseases have been reported are the insects, which are economically the most important and therefore most thoroughly studied class of invertebrates.

Virus diseases are known in fish and in amphibia. In birds one finds many virus diseases, some of them economically very important, like Newcastle disease and laryngotracheitis. Virus diseases have been recognised in most domestic mammals as well as in many wild ones. Virus diseases of humans include such major epidemiological problems as smallpox, yellow fever, mumps, rabies, AIDS, SARS, etc.

2: Plant viruses

There are relatively few known viruses in gymnosperms, ferns, fungi or algae. The flowering plants on the other hand, are hosts to many types of viruses. The viruses rank next to fungi in causing plant diseases of economic importance including diseases of potatoes, beans, beets, tobacco, sugarcane, cocoa, and fruit crops. Historically the importance of plant viruses lie in the fact that the very existence of viruses was discovered by Dutch scientist Martinus Beijerinck while working on the tobacco mosaic disease, which we now say to be caused by the Tobacco Mosaic Virus (TMV) [9].

3: Bacterial viruses or bacteriophages

Bacteriophage literally means *bacteria eater*. There is hardly a group of bacteria for which bacteriophages (phage for short) have not yet been discovered. Bacteria for which no phage has yet been reported are those about which our knowledge is quite limited. The phage specificity in attacking the host may be narrower or broader then the classification boundaries that separate the bacterial genera and species. For example, a phage may multiply only on a certain strain of *Escherichia coli*, whereas another phage reproduces in many strains of *E. coli* and the closely allied genus *Shigella*. Since bacteria can acquire phage resistance by discrete mutational steps, a strain sensitive to several

phages may produce a series of stable mutants resistant to one or more of the phages.

The phage is the simplest viral system. The phage life-cycle is measured in minutes, whereas the infectious cycles of plant and animal viruses occupy hours or days. Phage replicate in bacterial hosts that can be readily obtained by an overnight culture, contrary to the plant or animal cells, which take much longer to grow to concentrations sufficient for infection. Due to these reasons, bacteriophages provide a tractable experimental system for analysis and have expedited the progress in virology in the past and the present [9]. It is precisely because of this simplicity of the phage and the vast experimental literature on it that we shall refer to phage as the model system for our mechanical modeling.

Bacteriophage have served as a historical centerpiece in the development of molecular biology. For example, the classic Hershey-Chase experiment [42, 43] that established nucleic acid to be the carrier of the genetic blueprint was performed using bacteriophage T2. The biology of bacteriophage λ provided a fertile ground for the development of the understanding of gene regulation [44], while the study of virulent T phages (T1 to T7) paved the way for many other advances such as the definition of a gene, the discovery of mRNA, and elucidation of the triplet code by genetic analysis [43]. One of the central themes of the present chapter is that phage are similarly poised to serve as compelling model systems for quantitative analyses of biological systems.

Henceforth we will mostly discuss phages, and if the word virus is used without any additional qualification, it should be taken to mean phage.

3.1.2 Structure of a Typical Bacteriophage

The phage particles are elegant assemblies of viral, and occasionally cellular, macromolecules. They are marvellous examples of architecture on the molecular scale with form beautifully adapted to the functions of the phage. The structure of a typical phage is as shown in Fig. 3.2

1: Genetic Material

The phage genome carries the entire blueprint for its propogation. The phage genome can be one of the following nucleic acids: single-stranded (ss) DNA, double-stranded(ds) DNA, ssRNA, or dsRNA. There is a flurry of diabolic activities once the viral genome gets inside the host cell. The genetic code on the genome is such that the cellular machinery is tricked into synthesizing the enzyme RNA polymerase for the virus, and after that the virus essentially takes over the host cell. The RNA polymerase produces mRNA, which in turn produces all the proteins encoded in the genetic code and makes copies of the genome. The proteins and the genome thus synthesized then assemble to form new viruses, all at the expense of the cellular resources. The host cell breaks open after this attrition and the new virus particles are liberated. The nucleic acid dsDNA being the human genetic material is studied the most among the above mentioned nucleic acids. As a result, its chemical,

structural and, more importantly for us, mechanical properties are better known (explained in Section 3.6.1). We will, hence, investigate only the dsDNA phages.

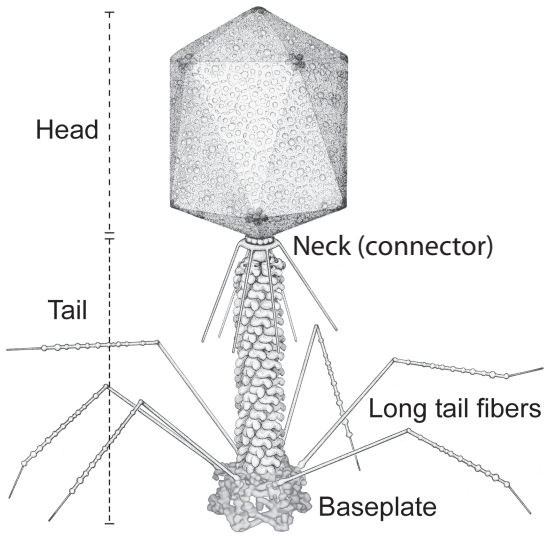

Figure 3.2: Structure of a typical bacteriophage. This is bacteriophage T4 [39]. It has a capsid, neck, tail, base-plate, and tail-fibers. These components are composed of proteins synthesized by the virus inside the host cell. The genetic material is protected inside the capsid.

2: Capsid (Head) and neck

The genetic material is enclosed inside the capsid, which is made up of protein subunits assembled according to relatively simple geometrical principles based on elementary physical considerations. There are only two basic types of capsids, helical and isometric (or quasi-spherical) [10]. Each of these arrangements is reached by the capsid proteins by a process of self-assembly that must be energetically favorable. As can be seen from Fig. 3.3a, the recent advancements in cryoelectron microscopy (CEM) have made it possible to image the structure of viral capsids in amazing detail. The main function of the capsid is to protect the genetic material from large variations in the temperature, pH, or chemical composition of the environment. The DNA is organized in the capsid in a very regular fashion (see Fig. 3.3b).

3: Neck or Connector

The connector is the junction between the head and the tail of the virion and is the point of DNA entry during packaging and exit during the ejection. The connector forms a part of the portal motor that utilizes ATP hydrolyses to drive DNA translocation and package it inside the phage capsid [11].

5: Tail, baseplate and tail fibers

Many but not all phages have tails attached to the phage head. The tail is a hollow tube through which the nucleic acid passes during infection. The size of the tail can vary, and some phages do not even have a tail structure. In the more complex phages like T4 the tail is surrounded by a

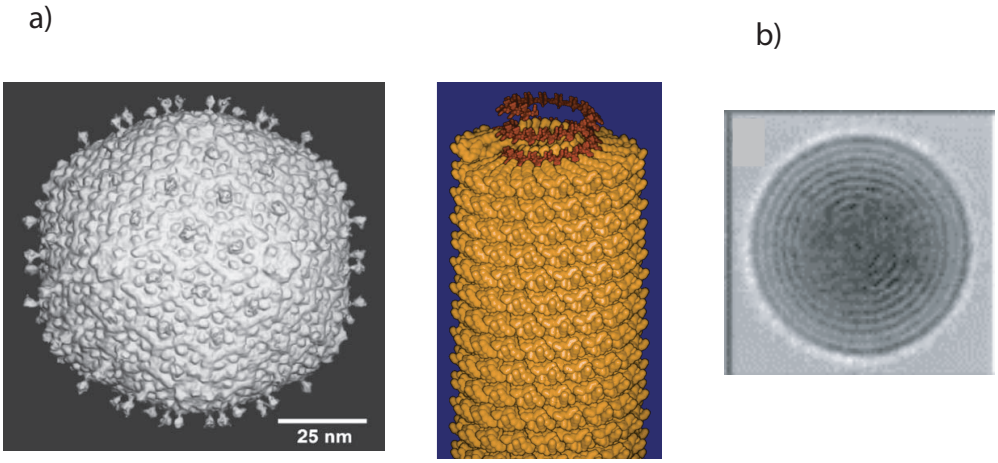

Figure 3.3: The structure of viral capsid and the organisation of the DNA inside. (a) The viral capsid can be either isometric (or quasi-spherical) or organized in a helical fashion (figure taken from Baker et al. [38]). (b) The cryoelectron micrograph (CEM) of the genome inside the capsid of bacteriophage T7. The DNA is arranged in a very regular fashion (figure taken from Cerritelli et al. [17]).

contractile sheath which contracts during infection of the bacterium. At the end of the tail the more complex phages like T4 have a base plate with one or more tail fibers attached to it. The base plate and tail fibers are involved in the adsorption of the phage to the bacterial cell. Not all phages have base plates and tail fibers. In these instances other structures are involved in binding of the phage particle to the bacterium. The tail fibres are used to hold on the outer layer of the host cell while the virus is preparing to launch its genome inside the host-cell.

3.2 Physical Processes in the Bacterial Life-cycle

Since the early measurements of virus size many experiments involving viruses have been of a quantitative character. The emergence of quantitative insight into viruses has come from many quarters including electron microscopy, X-ray crystallography, single molecule biophysics, and a large repertoire of classical methods in biochemistry and genetics. For many viruses these techniques have given us a detailed picture of the structure and function of the entire viral parts list. Many viral genomes have been sequenced, and the structure of many of the proteins coded for in the genome have been solved [38, 45]. Though it is impossible to discuss all of these advances here, we review some of the experimental insights that have informed our model building efforts.

3.2.1 Experimental Background

DNA is highly compressed inside bacteriophage capsids, and the resulting forces have important effects on the phage life cycle, as revealed in several experiments. One early experiment which shed light on the possible role of the forces associated with packaged DNA is that of Earnshaw and Harrison [18], who characterized the tight packaging of DNA in viral capsids by the distance d_s between strands (around 2.8 nm in full capsids), and by Feiss et al. [46], who identified limits on the amount of DNA that can be packaged into a λ capsid. Feiss et al. [46] found an upper limit barely above the wild-type genome length and suggested that adding more DNA makes the capsid unstable. Rau et al. [47] made measurements on large volumes of non-viral DNA that showed that d_s values in the range of 2.5 nm to 3.0 nm correspond to a pressure of several tens of atmospheres.

Since the experiments of Feiss et al. [46] and Earnshaw and Harrison [18], there have been a variety of experiments on DNA packing, several of which stand out because of their relevance to quantifying the internal buildup of force during packaging. Shibata et al. [48] measured the rate of packaging for phage T3 under various temperatures and chemical conditions. Through these experiments they determined that the packaging process was reversible—one third of the genome was ejected back into solution upon early interruption of packaging. Smith et al. [11] reinforced the idea that a strong force builds up during packaging with real time single-phage packaging experiments. They measured the rate of DNA packaging while subjecting the DNA to various resisting forces, quantifying the forces imposed by the packaging motor and the force resisting further packaging as a result of the confined DNA. Taken together, these two experiments give us a picture of DNA packaging in which a strong portal motor consumes ATP and in so doing pushes the DNA into the capsid against an ever-increasing resistive force.

It is believed that the tightly wound DNA stores large energies resulting in high forces, which in some cases could aid DNA ejection into the host cell. Recently, an experiment to test this hypothesis was conducted by Evilevitch et al. [12], who coerced λ into ejecting its genome into a solution containing polyethylene glycol (PEG) to create an external osmotic pressure. They found that various osmotic pressures of several tens of atmospheres could halt the ejection process, resulting in fractional genome ejection. The fractional ejection reflects a balance of forces between the inside and outside of the capsid. From this experiment it is concluded that forces are still present during ejection at the same high levels as were observed during packaging and in static capsids.

There are a variety of impressive *in vitro* experiments which demonstrate pressure-driven ejection of the phage genome [14, 15]. For the *in vivo* case, ejection driven by internal force is only one of several mechanisms that have been hypothesized to participate in transferring the genome of bacteriophage into the host cell. Another mechanism is suggested by Molinuex [16] who, on the basis of a wealth of experimental evidence, argues that the DNA of phage T7 is assisted into the cell by DNA-binding proteins. It is likely that different bacteriophage use a combination of these

two methods for ejecting their DNA into the host cell.

Finally, recent cryo-electron microscopy (cryo-EM) and X-ray crystallography studies of bacteriophage have revealed their detailed internal structure and, particularly, the ordered state of the packaged DNA. Cerritelli et al. [17] verified the tight packing measured by Earnshaw and Harrison [18] and showed that the DNA is apparently organized into circular rings within capsids. Other structural experiments have revealed the structure of components involved during ejection in T7 [19], the assembly of bacteriophage ϕ29[20], and structure of the packaging motor in ϕ29[21]. This structural information complements the single molecule measurements and will guide us in the construction of a quantitative model of the packaging and ejection processes.

3.2.2 Orders of Magnitude in Bacteriophage Biophysics

In the previous section we provided background on some of the experimental advances on bacteriophage which quantify the packaging and ejection processes. It is the aim of the remainder of this chapter to discuss the implications of these experiments in a more quantitative way and to make predictions about the phage life cycle that can be tested experimentally. Before describing our models in precise terms, we first perform estimates of the orders of magnitude of relevant physical properties involved in phage biophysics. Bacteriophage range in size from a few tens of nanometers to several hundred nanometers [38]. The capsids of most are regular icosahedral structures a few tens of nanometers in size. Table 3.1 gives an idea of the typical sizes of bacteriophage, as well as some animal viruses for comparison. These small containers house a genome which is several tens of microns long, a feat that demands extremely efficient utilization of space. In fact, an interesting dimensionless quantity for roughly characterizing the packaging efficiency is

$$\rho_{\text{pack}} = \frac{\Omega_{\text{genome}}}{\Omega_{\text{capsid}}}, \tag{3.1}$$

where Ω_{genome} is the volume of the genetic material and Ω_{capsid} is the volume of the capsid. For double-stranded DNA bacteriophage, this result may be rewritten simply in terms of the number of base pairs in the phage DNA, N_{bp}, using the approximation that DNA is a cylinder of radius 1nm and length 0.34nm per base pair. Note that this estimate is strictly geometrical and is intended to provide a simple feel for the degree of compaction of the genome. Using these approximations, ρ_{pack} can be rewritten as

$$\rho_{\text{pack}} = \frac{0.34\pi N_{\text{bp}}}{\Omega_{\text{capsid}}}\,, \tag{3.2}$$

making the calculation of ρ_{pack} straightforward. Note that in this formula, Ω_{capsid} is computed in units of nm^3.

Virus type	Host type	genome length (kbp)	Diameter (nm)	ρ_{pack}
Bacteriophage T7	Bacteria	40	55	0.490
Bacteriophage $\phi 29$[1]	Bacteria	19.4	47	0.459
Bacteriophage T4	Bacteria	169	92	0.443
Bacteriophage λ[2]	Bacteria	48.5	63	0.419
Bacteriophage P22	Bacteria	41.7	63	0.319
Herpes Simplex Virus 1	Human	152	125	0.159
Human Adenovirus C	Human	36	80	0.143
Smallpox Virus 1[3]	Human	186	220	0.036
Polyoma Virus SV40	Human	5.3	~ 50	0.083
Mimivirus[4]	Amoeba	~ 800	~ 400	0.026
Papillomavirus BPV1	Animal	7.9	60	0.070

Table 3.1: Packaged volume fractions of some bacteriophage and eukaryotic viruses. We have used the outer dimensions of the capsid from Baker et al. [38] in the calculation of ρ_{pack} since these are more readily available than the dimensions of the empty space inside the capsid. The genome lengths are given, for most viruses, in [49]. The DNA in bacteriophage is seen to be significantly more tightly packed than the other viruses, revealing the geometric origin of the large packing forces associated with bacteriophage.

For purposes of examining the significance of this parameter, Table 3.1 shows ρ_{pack} for a number of different viruses. A trend that is evident in the table is that viruses that infect bacteria are more tightly packed than the viruses that infect eukaryotic cells. A likely reason for this difference in degree of genome compaction is the difference in infection strategies employed by the two types of viruses. While eukaryotic viruses are brought into a host cell through processes in which both the genetic material and the capsid are taken into the infected cell, bacteriophage typically attach to the outside of the host and eject their DNA into the cytoplasm through a small channel. In order to transport their DNA quickly into the host, which itself is pressurized at $\sim$ 3atm [53], bacteriophage may power the ejection with a large internal pressure. However, as mentioned earlier, there is experimental evidence in the case of phage T7 that DNA-binding proteins play a role in DNA transport. These experiments raise doubts about the possibility of finding a single mechanism responsible for ejection from all types of phage [16].

The bacteriophage life cycle is a dynamic process and is of interest not only to consider the geometric parameters associated with viral DNA, but to attend to the temporal scales that are involved as well. The first step in the cycle is the adsorption of the phage onto the host cell. The frequency of this event depends on the abundance of available phage particles and their hosts. Since about 50 to 300 new phage particles are released by a single infection, the destruction of the host cell in a culture proceeds exponentially once a cell is infected [54]. After the phage has attached itself to the host, its genome is generally released on time scales ranging from seconds to minutes [40]. Probably concomitantly, the transcription and translocation machinery of the host cell is hijacked,

[1] Since the $\phi 29$ capsids are aspherical, we use an average diameter that gives the correct volume [20].
[2] [50]
[3] Since the smallpox particles are aspherical, we use an average diameter that gives the correct volume [51].
[4] this is the largest virus currently known [52].

and the production of phage proteins and factors required for replication of its genome begins. The time between the adsorption of the phage and the appearance of the first progeny capsids is usually on the order of minutes [9]. This period is known as the "eclipse period" and is the time required to build up the concentration of the phage proteins to a level high enough to initiate self-assembly of the capsid, tail, and motor proteins that constitute a mature phage particle. Self-assembly is a highly concentration-dependent process, but once it starts it proceeds rapidly to completion in a few seconds.

The second step, the packaging process, is completed in about 5–6 minutes [11]. The packaging rate is on the order of 100 bp/s in the initial stages, but it slows down as more of the genome is confined inside the capsid. That is, the rate of packaging depends on the force opposing the motor as it packages the genome. This internal force grows as the amount of genome packaged increases, and the magnitude of the force depends on the solvent conditions. In fact, some biologically important multivalent ions such as spermidine cause spontaneous DNA condensation, resulting in much smaller packaging forces [55]. This will be demonstrated more clearly later in this chapter. After the progeny phage have been completely assembled, enzymes lyse the host cell and a new generation of phage are released. The process of adsorption to lysis is completed in less than an hour [9].

The objective of this section was to highlight some of the opportunities for quantitative analysis provided by processes in the viral life-cycle. Despite the wide range of interesting physical process in the viral life-cycle, the remainder of this chapter focuses on the physical forces associated with packaged dsDNA and the implications of these forces for the packing and ejection processes.

3.3 The DNA Packaging Process

The model we invoke to examine the energetics of packaged DNA is predicated upon two key physical effects: i) the elastic cost to bend DNA so that it will fit in the viral capsid and ii) the interaction energy which results from the proximity of nearby strands of DNA and which derives from charges on both the DNA and in the surrounding solution.

This work is very much inspired by previous theoretical work: The work of Riemer and Bloomfield [56] laid the foundation for subsequent efforts on the energetics of packaged DNA by systematically examining each of the possible contributions to the overall free energy budget. Kindt et al. [57] and Tzlil et al. [58] estimated the forces in packaging of the phage λ. Arsuaga et al. [59] computed conformations of DNA in phage P4 using molecular mechanics models, observing that the conformation of DNA within a capsid depends on its volume, in agreement with our suggestion that the parameter ρ_{pack} characterizes the extent of packing in phage. Odijk [60] has discussed several issues in bacteriophage packaging, including the important problem of deriving an expression for the electrostatic interactions between DNA strands starting from the Poisson-Boltzmann equation with

the added complication of high density of packing and possibly non-hexagonal arrangement. Kindt et al. [57], Purohit et al. [61], and Tzlil et al. [58] do not derive these expressions *apriori*; rather they use results obtained by Rau et al. [47], Parsegian et al. [62], and Rau et al. [63] from osmotic pressure experiments on DNA to characterize these interactions. We have already underlined the importance of electrostatic interactions in solutions as a critical factor in the bacteriophage life cycle. More recently, Odijk and Slok [64] analyze the possibility of a non-uniform density of DNA inside the capsid and compute the size of regions within the capsid that are void. [65] study the effects of the finite thickness of DNA on the forces experienced during packaging within a viral capsid. The aim of this chapter is to take models like those described above and to systematically examine trends from one virus to another as well as for mutants within a given phage type.

3.3.1 Structural Models for the Packaged DNA

In order to construct a quantitative model of DNA packaging and ejection, it is necessary to specify the arrangement of the packaged DNA. One of the earliest successful attempts at determining the structure of DNA packaged in a phage capsid was an X-ray diffraction study by Earnshaw and Harrison [18] on P22 and some mutants of λ. Their studies revealed both long- range and short-range order of the encapsidated DNA. The evidence of long-range order comes from the observation that the diffraction is modulated by a series of ripples, indicating that the phage head is uniformly filled. Short-range order was indicated by a strong peak corresponding to a 25Å spacing. In an earlier study, Richards et al. [66] used electron microscopy to visualize gently disrupted phage particles and found that the DNA close to the capsid boundary has a circumferential orientation. These investigations together suggested a coaxial spool-like arrangement of the DNA inside the capsid. This model was further corroborated by experiments of Booy et al. [67] on HSV-1 and Cerritelli et al. [17], who used cryo-electron microscopy to obtain three dimensional visualizations of the packaged DNA in T7 phage. They consistently found a concentric ring-like geometry in both wild-type and mutant versions of T7 with a spacing of around 25Å in nearly-filled phage heads. However, none of these experiments shed much light on the geometry of packaged DNA in the very early stages of packing nor on the DNA in the central core of the fully packaged capsid.

A well ordered structure of the encapsidated DNA is also suggested by other observations on DNA condensation in the presence of polyvalent cations or other condensing agents such as methanol, ethanol or dilute solutions of spermidine, PEG, and other low molecular weight polymers [see 68, for an extensive overview]. The strands in the condensate are known to have local hexagonal co-ordination, another piece of evidence in favor of the kind of short-range order described above. Simulations by Kindt et al. [57] and theoretical investigations by Odijk [69] point in this direction as well. Evidence in support of this hypothesis is also provided by the simulations of Arsuaga et al. [59], who show that the coaxial spool (or inverse spool) is an energetically favorable configuration,

particularly when the density of packing is high as in bacteriophage. In light of these arguments we *assume* that the DNA is arranged in columns of concentric hoops starting from the inner wall of the capsid. Each of the hoops is surrounded by six similar hoops (hexagonal arrangement), except those at the innermost column and those touching the surface of the capsid. Though we have assumed a limited class of geometries for the packaged DNA, namely spool models, we note that such models are not necessarily the lowest possible free energy structures [70], and other models have been proposed [71]. Further, we remain unclear as to the precise dynamic pathways that would orchestrate such structures during packing and ejection, though simulations are consistent with the dynamical development of such structures [59, 57, 72]

3.3.2 Modeling the Free Energy of Packed DNA

With a specific arrangement of DNA in hand, we can now compute the free energy required to package that DNA. Our efforts to write an expression for the free energy of the DNA packed inside a phage capsid are inspired by the experimental insights described above concerning the configuration of the encapsidated DNA and its behavior in ionic environments. We follow [56], [69], and [57] and break up the energetics of the encapsidated DNA into an elastic term and a DNA-DNA interaction term:

$$G_{\rm tot}(d_{\rm s}, L) = G_{\rm bend} + G_{\rm int}\,. \tag{3.3}$$

We begin with the first term, by asserting that the bending energy in an elastic fragment of length L is given by

$$G(L) = \frac{\xi_p k_{\rm B} T}{2} \int_0^L \frac{dx}{R(s)^2}\,, \tag{3.4}$$

where ξ_p is the persistence length of DNA and $R(s)$ is the radius of curvature at the position with arc length parameter s. This simply reflects the energetic cost $G_{\rm bend} = \xi_p k_{\rm B} T l/2R^2$ to bend an elastic rod of length l into a circular arc of radius of curvature R.

The expression for the bending energy is considerably simplified by a structural insight provided by the experiments described earlier of Earnshaw and Harrison [18], Booy et al. [67], and Cerritelli et al. [17] which showed that the DNA is arranged in the capsid in a series of circular hoops starting close to the surface of the capsid and winding inwards in concentric helices. Therefore, we specialize this expression to a hoop of radius R of length $l = 2\pi R$ and deduce that the bending energy in the hoop is $G_{\rm hoop} = \pi \xi_p k_{\rm B} T/R$. We ignore the pitch of the helix and think of the encapsidated DNA as a series of hoops of different radii [61]. This leads to the following expression for the total bending energy:

$$G_{\rm bend}(L) = \pi \xi_p k_{\rm B} T \sum_i \frac{N(R_i)}{R_i}, \tag{3.5}$$

where $N(R_i)$ is the number of hoops of radius R_i in the capsid. Note that in neglecting the helical

pitch we have also assumed that the successive layers of hoops are parallel to each other. A more realistic model would acknowledge that strands in successive layers form a criss-cross pattern. We drop this complication in favor of the simple model used above that captures the essential physics. The persistence length of DNA depends on solvent conditions [73] and also on the sequence of basepairs [74]. However, $\xi_p = 50$nm is an appropriate number for the solvent conditions in the packaging experiment of Smith et al. [11] and the ejection experiment of Evilevitch et al. [12]. We note here that the size of many bacteriophage capsids is on the order of a few tens of nanometers which is comparable to the the persistence length of double stranded DNA itself. This hints that the bending energy indeed constitutes a significant portion of the free energy of the encapsidated DNA. Note that we have neglected twist and writhe as contributors to the free energy, very much in line with the work of Arsuaga et al. [59], Kindt et al. [57], Tzlil et al. [58], and Odijk [60]. The twisting modulus of DNA is higher than its bending modulus, and the twist would be relaxed if the ends of the DNA are free to rotate. However, there is no conclusive experimental data validating this claim and more work is required on this point. There is a possibility that the DNA packaging motor is a rotational device [21], and investigations elaborating its mode of operation are expected to shed more light on this problem. Given the current lack of information, we neglect the twisting energy of the DNA and simplify the expression for the bending energy by converting the discrete sum in eqn.(3.5) to an integral according to the prescription $\Sigma_i = \frac{2}{\sqrt{3}d_s}\int dR$. In particular, we replace the sum of eqn.(3.5) with

$$G_{\rm bend}(L) = \frac{2\pi\xi_p k_{\rm B}T}{\sqrt{3}d_{\rm s}}\int_R^{R_{\rm out}} \frac{N(R')}{R'}dR', \tag{3.6}$$

where $R_{\rm out}$ is the radius of the inner surface of the capsid and the length L of packaged DNA is given by

$$L = \frac{4\pi}{\sqrt{3}d_{\rm s}}\int_R^{R_{\rm out}} R'N(R')dR'. \tag{3.7}$$

The factor of $\frac{\sqrt{3}}{2}d_{\rm s}$ appears because it is observed [17] that the DNA strands are arranged in a lattice with local hexagonal coordination and spacing $d_{\rm s}$. In other words, each strand has six nearest neighbors except those near the surface of the capsid and the innermost cylindrical space, where there are three nearest neighbors on average. We expect that the interaction of the DNA with the proteins of the capsid would give rise to surface energy terms [58] in the expression for the total free energy, but we neglect these terms in our analysis.

We next turn to the DNA-DNA interaction energy $G_{\rm int}$. DNA has a backbone that is highly negatively charged. As a result, there are large energetic costs associated with bringing DNA fragments close together in solution. These interactions can in turn be screened by counterions which fill the space between DNA strands. From a theoretical perspective it is natural to treat these interactions by applying the Poisson-Boltzmann approximation in which charge is smoothly distributed according to a Boltzmann distribution consistent with the potential it produces [75].

In this approximation the free energy is calculated from a sum of entropy (assuming the ions are locally an ideal gas) and electrostatic energy. Water is modeled as a continuous dielectric. In the limit of extremely close packing, ideal-gas pressure dominates over the relatively constant electrostatic energy, and the correct pressure is predicted. However, the experiments of Rau et al. [47] and Parsegian et al. [62] show that this approximation does not give the correct dependence of the pressure on interstrand spacing as shown in Fig. 3.4. The mismatch between theory and experiment is likely due to effects ignored by the Poisson-Boltzmann treatment, such as the discreteness of ions and of water molecules. However, detailed Monte-Carlo simulations in which the ions are treated as discrete objects but water remains continuous [76] work remarkably well. Though our treatment of the interaction energy, $G_{\rm int}$, will be based upon the experimental data of [47], calculations like those of [76] could be used to construct a "first-principles" model of the interactions, at least for monovalent and divalent counterions. We rely on empirical data for this study but suggest the use of simulated data if experimental data is not available. The experiments of Rau et al. [47] and Rau

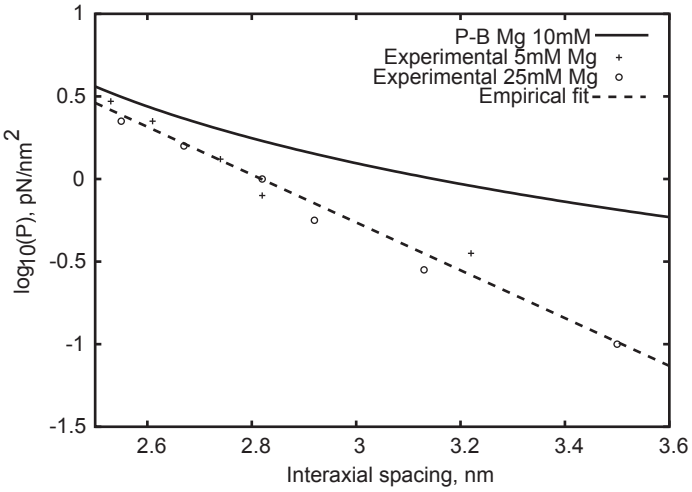

Figure 3.4: Pressure in a hexagonal lattice of DNA, according to experiment and Poisson-Boltzmann theory. Experimental data points are from the data of Rau et al. [47] for 25 mM and 5 mM Mg^{2+} concentrations. Our theoretical calculations follow from a discrete one-dimensional Poisson-Boltzmann solver, assuming cylindrical symmetry. The free energy was calculated as a sum of the Shannon entropy of the ions and the electrostatic energy of ions and DNA, with the zero point for the potential set so that internal and external ionic concentrations were related by a Boltzmann factor. The theoretical predictions differ from the experimental points by a factor of ten, though the slopes are approximately correct and it is difficult to distinguish between the data for the two different concentrations. Also shown is a least-squares fit to the empirical datapoints, resulting in the parameters $c = 0.30$ nm and $F_0 = 1.2 \times 10^4$ pN/nm^2.

et al. [63] provide an empirical formula that relates osmotic pressure p to strand spacing d_s in the

range of two to four nanometers as

$$p(d_{\mathrm{s}}) = F_0 \exp(-\frac{d_{\mathrm{s}}}{c}) \,. \tag{3.8}$$

The value of the pressure is dependent on both the ion concentration and its charge. When working with this formula it is important to remember that a large change in F_0 can be mostly compensated by a small change in c since most data points are in a small region far from the p-axis. Hence, even though c is relatively constant, we state the value used for both c and F_0 together to avoid confusion. Fig. 3.4 shows the experimental data for a solution containing 5 and 25 mM $MgCl_2$ at 298 K in which measurements reveal $c = 0.30$ nm and $F_0 = 1.2{\times}10^4$ pN/nm^2. These values should be appropriate for use whenever Mg^{2+} ions are the dominant species and have a concentration of 5–25 mM, conditions satisfied in solutions commonly used in phage experiments, including, for example, SM buffer and the TM buffer used in [12]. The solution used by [12] also contained the buffering agent TRIS, which we expect resulted in additional monovalent ions at a 10 mM concentration. Since Mg^{2+} is smaller and has a higher charge, we expect that it will still be the dominant ion within the phage capsids. Unfortunately, the buffer used in Smith et al. [11] includes enough sodium to suggest that the effect of Na^+ must be considered in addition to Mg^{2+}. The solutions *in vivo* are far more complex, and F_0 is difficult to determine. Even solutions *in vitro* contain different concentrations of ions, and determining F_0 for each one of them through experiments would be impractical.

The data on the measured pressure in terms of d_{s} can be used to deduce the functional form of energy stored in the electrostatic interactions. We do not go through the details here but refer the reader to Purohit et al. [61] for the full calculation. The calculation rests on the assumption of a pair potential interaction among N parallel strands of length l each packed in a hexagonal array with a spacing d_{s}. The total interaction energy of this arrangement is

$$G_{\mathrm{int}}(L, d_{\mathrm{s}}) = \sqrt{3} F_0 (c^2 + c d_{\mathrm{s}}) L \exp(-\frac{d_{\mathrm{s}}}{c}), \tag{3.9}$$

where $L = Nl$ is the total length of the strands. This is the expression for the interaction energy when the ions in the ambient solution are monovalent or divalent cations. In this regime the interaction between the strands is entirely repulsive, and these interactions decay as the strands are moved farther apart. For trivalent and tetravalent ions the physics is quite different. In this regime there is an attractive interaction with a preferred spacing d_0 between the strands, and the measurements are well fit by

$$G_{\mathrm{int}}(L, d_{\mathrm{s}}) = \sqrt{3} F_0 L \Big[(c^2 + c d_{\mathrm{s}}) \exp(\frac{d_0 - d_{\mathrm{s}}}{c}) - (c^2 + c d_0) - \frac{1}{2}(d_0^2 - d_{\mathrm{s}}^2) \Big], \tag{3.10}$$

where $c = 0.14$nm and $d_0 = 2.8$nm, for example, in the case of cobalt hexamine as the condensing

agent. For $d_{\rm S} < d_0$ the interaction is strongly repulsive and for $d_{\rm S} > d_0$ it is attractive. This expression is a good representation of the free energy of interactions between the DNA molecules for spacings d_s less than or equal to the preferred value d_0 [63]. In viral packaging we encounter interaxial spacings in exactly this range, and hence we will use this free energy to study the effects of repulsive-attractive interactions on encapsidated DNA.

It is important to note that in the experiments of Rau et al. [47] and Rau et al. [63] DNA was confined in the same way (except for the lack of bending) as it is within a phage capsid. This means that the free energy $G_{\rm int}$ obtained from their measurements accounts for multiple effects, including electrostatics, entropy of the DNA [77] and counterions, and any hydration phenomena [78].

Given that we have now examined the separate contributions arising from DNA bending, entropy and interaction terms, we now write the free energy of the encapsidated DNA in the repulsive regime,

$$G_{\rm tot}(L, d_{\rm S}) = \underbrace{\frac{2\pi\xi_p k_{\rm B}T}{\sqrt{3}d_{\rm S}} \int_R^{R_{\rm out}} \frac{N(R')}{R'} dR'}_{\text{Bending}} + \underbrace{\sqrt{3}F_0(c^2 + cd_{\rm S})L\exp(-\frac{d_{\rm S}}{c})}_{\text{Interaction}}. \tag{3.11}$$

An analogous formula holds for the repulsive-attractive regime. Note that this expression reports the free energy of the inverse spool configurations when a length L has been packaged by relating, R to L via (3.7). We will now show that the spacing between the strands varies in a systematic way during the packing process, reflecting the competition between bending and interaction terms.

3.3.3 DNA Spacing in Packed Capsids

Our model makes a concrete prediction for the free energy $G_{\rm tot}$ of packaged DNA in any phage and for a wide range of solution conditions. In order to find $G_{\rm tot}$ for a particular phage, we minimize eqn.(3.11) by varying $d_{\rm S}$ under the constraint that L given by (3.7) is equal to the length of DNA already packaged. The expressions for $N(R')$ will differ for different capsid geometries. Most capsids are icosahedral, and we idealize them as spheres. Some capsids, e.g., ϕ29, have a "waist." We idealize them as cylinders with hemispherical caps. Eventually we will find that the geometry does not affect the overall free energy of packing as long as the internal volume of the idealization is the same for each geometry, once again reflecting the importance of the parameter $\rho_{\rm pack}$ introduced earlier. Before we specialize to particular geometries (see Fig. 3.5)we observe that $N(R') = \frac{z(R')}{d_{\rm S}}$, where $z(R')$ is the height of a column of hoops of DNA situated at radius R'. Using this fact and differentiating (3.7) with respect to $d_{\rm S}$ while holding L constant gives us $\frac{dR}{dd_s} = -\frac{\sqrt{3}Ld_s}{2\pi Rz(R)}$. Minimizing $G_{\rm tot}$ with respect to the interstrand spacing d_s gives

$$\sqrt{3}F_0\exp(-d_{\rm S}/c) = \frac{\xi_p k_{\rm B}T}{R^2 d_{\rm S}^2} - \frac{\xi_p k_{\rm B}T}{d_{\rm S}^2} \frac{\int_R^{R_{\rm out}} \frac{z(R')}{R'} dR'}{\int_R^{R_{\rm out}} R' z(R') dR'}. \tag{3.12}$$

This equation represents a balance between the bending energy terms and the interaction terms. Note that if the size of the capsid is fixed, then longer lengths of packed DNA imply smaller radii of curvature for the hoops since the strands want to be as far away as possible from each other for the case in which the interaction between the adjacent strands is repulsive. On the other hand, smaller radii of curvature eventually lead to large bending energy costs, resulting in a trade-off that is captured mathematically in eqn. (3.12). We now specialize this result to particular geometries

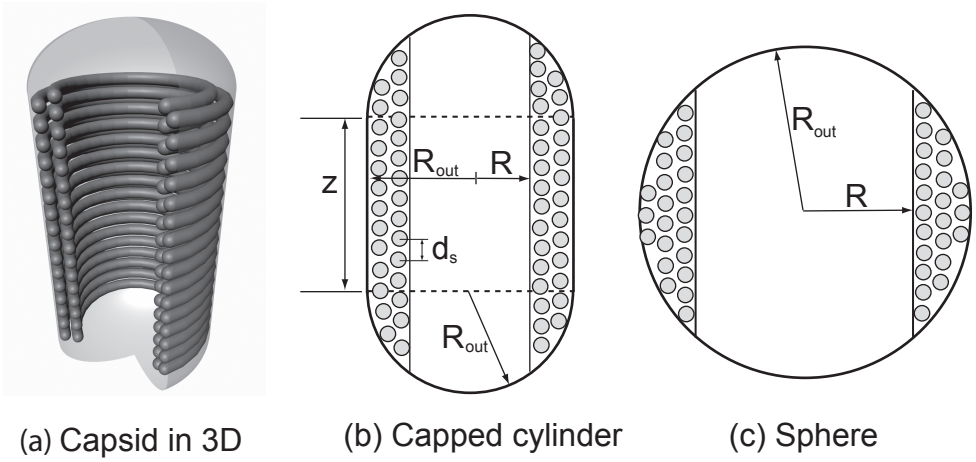

Figure 3.5: Idealized geometries of viral capsids.

(i.e., particular choices of $z(R')$). For a sphere, $z(R') = 2\sqrt{R_{\rm out}^2 - R'^2}$, and the equation which determines the optimal $d_{\rm s}$ reads

$$\begin{aligned}\sqrt{3}F_0 \exp(-d_{\rm s}/c) &= \frac{\xi_p k_{\rm B}T}{R^2 d_{\rm s}^2} + \frac{3\xi_p k_{\rm B}T}{d_{\rm s}^2}\Big(\frac{1}{R_{\rm out}^2 - R^2} \\ &+ \frac{R_{\rm out}}{(R_{\rm out}^2 - R^2)^{3/2}} \log\big(\frac{R_{\rm out} - \sqrt{R_{\rm out}^2 - R^2}}{R}\big)\Big). \end{aligned} \tag{3.13}$$

For a cylinder with hemispherical caps, $z(R') = h + 2\sqrt{R_{\rm out}^2 - R'^2}$, where h is the height of the waist portion and $d_{\rm s}$ is the solution of the following equation:

$$\begin{aligned}\sqrt{3}F_0 \exp(-d_{\rm s}/c) &= \frac{\xi_p k_{\rm B}T}{R^2 d_{\rm s}^2} \\ &+ \frac{\xi_p k_{\rm B}T}{d_{\rm s}^2} \frac{\Big(h \log(\frac{R_{\rm out}}{R}) - \sqrt{R_{\rm out}^2 - R^2} - \log\big(\frac{R_{\rm out} - \sqrt{R_{\rm out}^2 - R^2}}{R}\big)\Big)}{\frac{h}{2}\sqrt{R_{\rm out}^2 - R^2} + \frac{1}{3}(R_{\rm out}^2 - R^2)^{3/2}}. \end{aligned} \tag{3.14}$$

Phage type	Model Geometry	R_{out} (nm)	h (nm)	Genome length (nm)	ρ_{pack}
T4 [79]	Capped cylinder	39.8	29.0	57424	0.442
T7[1] [17]	Sphere	26.6	0	13579	0.541
ϕ29 [20]	Capped cylinder	19.4	12.0	6584	0.461
HK97 [80]	Sphere	27.2	0	13509	0.503
λ [38]	Sphere	29.0	0	16491	0.507

Table 3.2: Idealized geometries of bacteriophage. The radius and height are determined by using the volume available to the DNA. They have been calculated from experimental data about the geometry of capsids from several sources (in parentheses above). ρ_{pack} for some phage in this table is higher than corresponding values in table 3.1 since this table uses internal volumes, whereas table 3.1 uses the outer dimensions that are more readily available.

Fig. 3.6 shows d_{s} as a function of the fraction of the genome packed for five different phage. We assume that all of them are packaged under the same (repulsive) conditions, with $F_0 = 2.3 \times 10^5 \text{pN/nm}^2$ and $c = 0.27\text{nm}$ as in Purohit et al. [61], corresponding to the best visual fit to the data in the experiments of Smith et al. [11] which was performed in a solution containing 5mM $MgCl_2$ and 50mM NaCl. Note that these values are different than the ones found in Section 3.3.2 because the ionic concentrations differ. Table 3.3.3 gives the details of the geometry of the phage used in the calculation. As noted earlier, a sufficient concentration of polyvalent cations suffices to induce

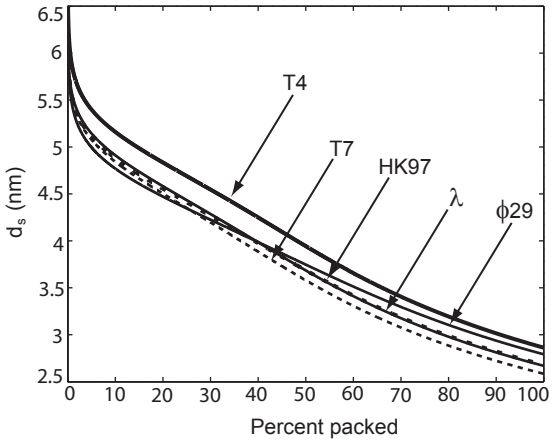

Figure 3.6: The spacing d_{s} in five different phage under fully repulsive conditions with $F_0 = 2.3 \times 10^5 \text{pN/nm}^2$ and $c = 0.27\text{nm}$. These values of F_0 and c result in the best visual fit to the data in the experiment on ϕ29 by Smith et al. [11](5mM $MgCl_2$ and 50mM NaCl). The graphs show d_{s} monotonically decreasing as more of the genome is packaged. T7 is the most tightly packed while T4 is most loosely packed. λ and HK97 show an almost identical history of d_{s} vs. fraction of genome packed since the two are closely related structurally.

[1]The T7 phage is unusual in that a part of its cylindrical tail (radius 9.5nm, height 28.5nm) protrudes into the empty space within the spherical capsid. The space occupied by this tail is not available to the DNA and we exclude it to get an effective radius.

effective attraction between adjacent DNA strands. Under such repulsive-attractive conditions the left hand side of Eqn.(3.12) changes and we get

$$\sqrt{3}F_0(\exp(\frac{d_0 - d_{\rm s}}{c}) - 1) = \frac{\xi_p k_{\rm B}T}{R^2 d_{\rm s}^2} - \frac{\xi_p k_{\rm B}T}{d_{\rm s}^2}\frac{\int_R^{R_{\rm out}} \frac{z(R')}{R'} dR'}{\int_R^{R_{\rm out}} R' z(R') dR'}. \tag{3.15}$$

Here too, the idea is to solve for the optimal $d_{\rm s}$ at each packaged length L. The results with the

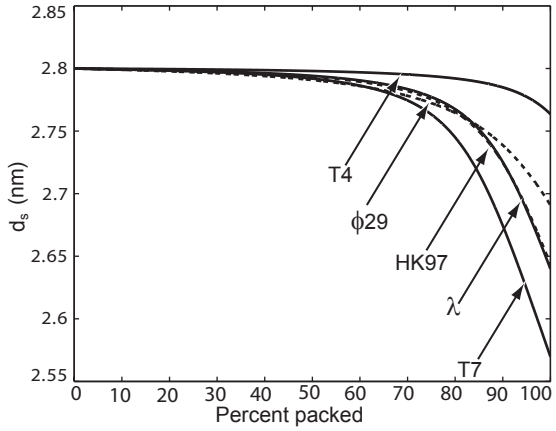

Figure 3.7: The spacing $d_{\rm s}$ under repulsive-attractive conditions. We use $F_0 = 0.5$ pN/nm^2, $d_0 = 2.8$nm and $c = 0.14$nm. This corresponds to a solution containing 5mM $Co(NH_3)_6Cl_3$, 0.1M NaCl, 10mM TrisCl [57, 63]. The spacing remains at the preferred value of 2.8nm for most of the packaging process, except in the end when volumetric constraints lead to smaller spacings as a consequence of high energy costs for maintaining this $d_{\rm s}$.

repulsive-attractive potential for different phage are shown in Fig. 3.7. We note the similarity in the observed trends with the results of Kindt et al. [57] who also study the packaging process with a repulsive-attractive potential. In the presence of surface energy, the encapsidated DNA assumes a toroidal configuration in the early stages of packing [57] much as it would have in solution in the absence of a capsid [81]. At the later stages of packing the inverse spool is the more energetically favorable geometry and the calculations of Kindt et al. [57] show a smooth transition between these configurations. However, we assume that the inverse spool is the optimal geometry throughout the packaging process since we do not have surface energy terms. Note also that the trends in Fig. 3.7 are quite different from those with the fully-repulsive conditions in Fig. 3.6. Most importantly, in the early stages of packing under repulsive-attractive conditions the DNA strands tend to be at the preferred spacing of 2.8nm [57, 58]. Volumetric constraints at the later stages of packing result in tighter packing, and $d_{\rm s}$ decreases to values lower than the preferred 2.8nm. Under fully-repulsive interactions the interstrand spacing decreases monotonically as more DNA is packaged.

For many bacteriophage, even were they to be packaged under conditions in which there was an

effective attraction between adjacent DNA segments, the genome would not be fit into the capsid if the interaxial spacing is at the preferred value of 2.8nm. This would result in repulsive interactions between adjacent DNA segments in the terminal part of the packaging process. Interestingly, in these circumstances $d_{\rm S}$ can be estimated using strictly geometric arguments. In particular, we equate the total volume available in the capsid with the volume of the packaged DNA. In particular, this implies

$$V_{cap} = \frac{\sqrt{3}}{2} d_{\rm S}^2 L, \tag{3.16}$$

where L is the length of the packaged DNA. This in turn implies

$$d_{\rm S} = \sqrt{\frac{2V_{cap}}{\sqrt{3}}} \frac{1}{\sqrt{L}}, \tag{3.17}$$

or, more generally, $d_{\rm S} \propto 1/\sqrt{L}$. In deriving this expression we have assumed that the volume of

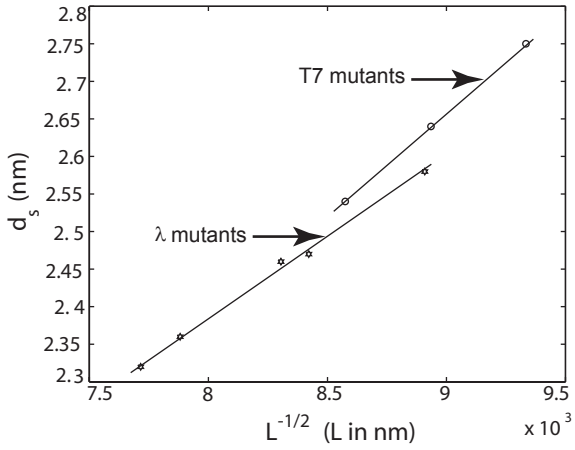

Figure 3.8: Comparison of measured spacings $d_{\rm S}$ with $\frac{1}{\sqrt{L}}$ scaling law. The circles correspond to interstrand spacing in T7 obtained by Cerritelli et al. [17]. The stars represent data from Earnshaw and Harrison [18] for mutants of λ-phage. We fit straight lines to both these data sets to show that the spacing scales with the inverse square root of the packaged length in capsids that are nearly full.

the cylindrical void (unoccupied by the DNA) [69, 57, 59] in the middle of the capsid is negligible in comparison to the volume of the capsid. Equivalently, we may assume that the size of the void is independent of the length packaged in the final stages of packaging. The predicted scaling of $d_{\rm S}$ with DNA length L above can be compared to several different experiments, as shown in Fig. 3.8. In particular, the spacing has been measured both in λ mutants [18] and in the T7 bacteriophage [17]. As seen in the figure, the scaling suggested by the model appears to provide a satisfactory description of the measured trends. More generally, note that the spacing of the packaged DNA is one of the key points of contact between our theory and experiment. In particular, both Fig. 3.6

and Fig. 3.7 are *predictive* in that they suggest how the spacing $d_{\rm s}$ varies from one phage to another for different solution conditions.

3.3.4 Forces During DNA Packing

The phage genome is subject to various resistive forces during the packaging process. As discussed earlier, these forces depend on the size and geometry of the capsid, solvent conditions, and the size of the genome. In this section we calculate those forces using the expressions for the elastic and the interaction energy derived in the previous section.

3.3.4.1 Forces from DNA confinement

To obtain the force we differentiate the total free energy, $G_{\rm tot}$, formulated in Eq. 3.11, with respect to the packaged length L. Since the dependence of the spacing $d_{\rm s}$ on L is already known we substitute it into the expression for $G_{\rm tot}$, rendering it a function of L alone. We then carry out the differentiation and obtain the following expression for the force:

$$F(d_{\rm s}(L), L) = -\frac{dG_{\rm tot}}{dL} = \sqrt{3}F_0 \exp(c^2 + cd_{\rm s}) + \frac{\xi_p k_{\rm B}T}{2R^2}, \tag{3.18}$$

where we assume that the radius R and the spacing $d_{\rm s}$ are known functions of L. In Fig. 3.9, we

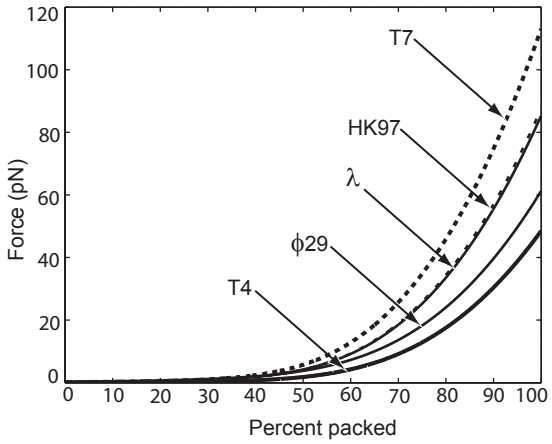

Figure 3.9: Comparison of forces during DNA packing process for different phage under fully repulsive conditions. T7 requires the largest force to package since it is most densely packed. T4 is at the other end of the spectrum, requiring the smallest force. The data above corresponds to $F_0 = 2.3 \times 10^5$ pN/nm^2 and $c = 0.27$nm obtained by a visual fit to the data of [11], who conducted the packaging experiment for phage $\phi 29$ in a solution containing 5mM $MgCl_2$ and 50mM NaCl.

show the result of a series of such calculations for different phage, all done assuming ionic conditions such as those used in the experiments of Smith et al. [11]. The value of F_0 and c corresponding to

these conditions were determined by a fit to the data of [11] for bacteriophage Φ29. In principle more accurate values of these parameters can be obtained by a least-squares fit. The key point of Fig. 3.9 is to illustrate the trends across different phage with particular reference to the way in which the maximum packaging force scales with $\rho_{\rm pack}$. This is shown more clearly in Fig. 3.10. We observe that the maximum resistive force scales roughly linearly with the packing density $\rho_{\rm pack}$ across different phage of varied shapes. We have also plotted the maximum resistive force for $\phi 29$ in Fig. 3.11 for different salt concentrations of the ambient solution. The repulsive interactions between the DNA strands grow progressively larger as the concentration of the Na^+ ions in solution decreases. This results in larger packaging forces as can be seen in Fig. 3.11.

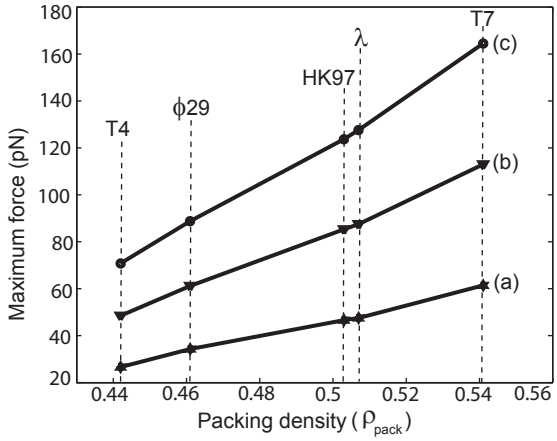

Figure 3.10: Maximum resistive force in different phage under three different repulsive conditions. (a) corresponds to $F_0 = 1.1 \times 10^5$ pN/nm^2 and $c = 0.27$nm, (b) corresponds to $F_0 = 2.3 \times 10^5$ pN/nm^2 and $c = 0.27$nm and (c) corresponds to $F_0 = 3.3 \times 10^5$ pN/nm^2 and $c = 0.27$nm. The forces increase with the packing density $\rho_{\rm pack}$ and also with increasing F_0.

We have also obtained the force required for packaging under repulsive-attractive interactions. The results can be seen in Fig. 3.12. The forces are considerably smaller when the strands are at the preferred spacing $d_0 = 2.8$ nm. As with the DNA spacing discussed earlier, the results in Fig. 3.9 and 3.10 are *predictive* and suggest a wide range of new experiments using both different solution conditions and different phage. Though we have attempted to provide a faithful analysis of the interactions between adjacent DNA strands, these interactions are complicated and involve a variety of different factors which make a "first-principles" analysis of these interactions in the presence of polyvalent cations and bent DNA difficult. However, regardless of the particular choice of interaction, it is clear that adjacent strands repel each other at small interstrand separations and this qualitative behavior and the trends it implies in these calculations are indifferent to these details.

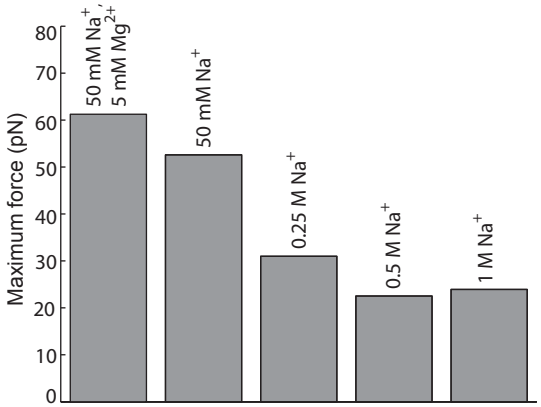

Figure 3.11: Maximum resistive force in $\phi 29$ for different salt concentrations. The maximum force increases as the salt concentration decreases since the DNA interstrand repulsion becomes larger as the solution becomes more dilute. The values of F_0 and c for the salt solutions used in this figure were obtained from fits to the data of [47].

The history of force as a function of packaged length obtained above rested on the assumption that the integral approximation adopted in eqn. (3.6) is an accurate representation of the bending free energy. In principle, the optimal spacing $d_{\rm S}(L)$ and the resistive force $F(L)$ can be obtained by minimizing the free energy without resorting to the integral approximation. This has been carried out in [82], and the results are shown in Fig. 3.13. There are several distinctive features to be noted in this figure. Foremost among them is that the curves for the history of resistive force and interaxial spacing as a function of the length of DNA packed are not monotonic, unlike the curves obtained from the integral (continuum) models. The discrete steps represent the addition of a new stack of hoops during the packaging reaction. More importantly, discreteness of packing implies that at specific lengths packaged there will be sharp changes of the spacing $d_{\rm S}$ due to an increase in the number of hoops per layer. These events might be a mechanical signal of the packaging configuration. In particular, the observation of such steps in an experiment would be evidence in favor of our quasi-static picture of the dynamics of packaging.

3.3.4.2 Forces due to Viscous Dissipation

Thus far we have calculated the free energy stored in the compressed DNA within a bacteriophage capsid, which represents the total amount of work that the motor must do to package the entire genome. We have not yet considered irreversible work that may result from the high rate of packaging. An obvious source of irreversible work is viscous dissipation in the fluid. Here we demonstrate that, in fact, such forces are negligible, as speculated by Smith et al. [11].

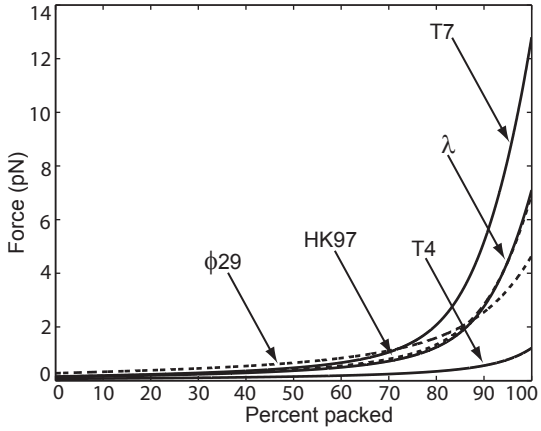

Figure 3.12: Comparison of forces during DNA packing process for different phage under repulsive-attractive conditions with $F_0 = 0.5$ pN/nm^2, $d_0 = 2.8$nm and $c = 0.14$nm. This corresponds to a solution containing 5mM $Co(NH_3)_6Cl_3$, 0.1M NaCl, 10mM TrisCl [57, 63]. The trends seen here are no different from those in the fully repulsive conditions - T7 requires large forces and T4 requires small forces for packaging. The maximum force, however, is significantly smaller than that seen for fully-repulsive conditions.

We identify four sources of viscous dissipation during packaging: drag on (i) the capsid and (ii) the unpackaged genome as each is pulled through the fluid, (iii) viscous dissipation within the sheath (as might be important during ejection), and (iv) dissipation as fluid is extruded through capsid pores. We calculate an upper bound on each to provide an upper bound on fluid dissipation in general and conclude that such forces are negligible. Note, however, that we assume water to behave as a continuum material throughout this analysis. Non-continuum effects, which could affect our conclusions, are not treated here. In what follows, we use values from Table 3.3.

R	Capsid radius	30 nm
t_c	Capsid thickness	2 nm
R_p	Pore radius	2 nm
N	Number of pores	10
X	Sheath length	50 nm
D	Inner sheath radius	1.3 nm
d	DNA radius	1.0 nm
V	DNA velocity	100 bp/s $\approx$ 30 nm/s
R_G	Unpackaged genome radius of gyration	300 nm

Table 3.3: Physical numbers for DNA packing in ϕ29, taken from Tao et al. [20].

First, as DNA is pushed into the capsid, equal and opposite forces pull both the unpackaged genome and the capsid through the surrounding fluid. Although the (smaller) capsid certainly moves more quickly than the genome, as an upper bound, we assume each to move at the full translocation velocity V. Furthermore, an upper bound can be obtained using the Stokes drag $F = 6\pi\mu R_b V$ on a

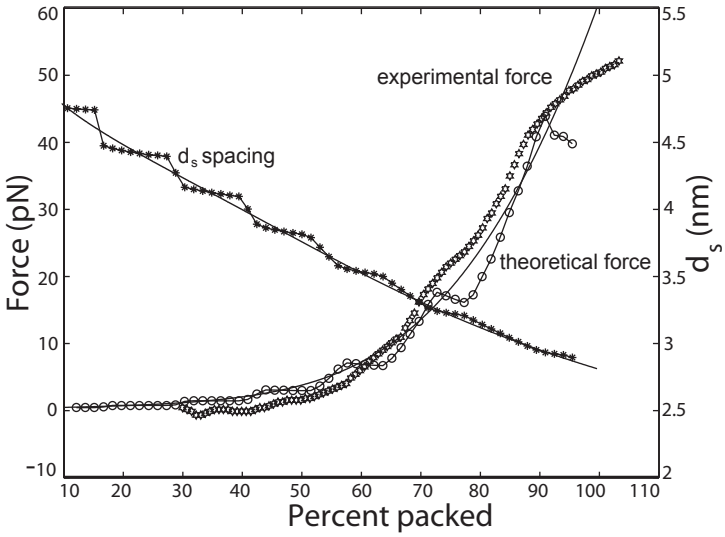

Figure 3.13: Force and interaxial spacing as functions of the amount of DNA packed in bacteriophage ϕ29. The hexagons correspond to the experimental data of Smith et al. [11]. The thick lines are results of the continuum model and the circles connected with the thin line are obtained from the discrete model.

solid sphere of radius R_b bounding each. Using $R_b \sim R$ for the capsid and $R_b = R_G$ for the genome, we obtain

$$F_{\text{capsid}} \approx 2 \times 10^{-5}\,\text{pN} \;\text{ and }\; F_{\text{genome}} \approx 2 \times 10^{-4}\,\text{pN}, \tag{3.19}$$

giving power dissipation

$$U_{\text{capsid}} \approx 1.5 \times 10^{-4}\,k_{\text{B}}T/\text{s} \;\text{ and }\; U_{\text{genome}} \approx 1.5 \times 10^{-3}\,k_{\text{B}}T/\text{s}. \tag{3.20}$$

Second, to estimate the dissipation within the sheath, we consider the fluid drag on a DNA molecule (modelled as a cylinder) of radius d moving at velocity V through a cylindrical sheath of inner radius D and length X into or out of a viral capsid. The fluid between the DNA and the sheath is assumed to obey the Stokes equations subject to the no-slip boundary conditions. Packaging or ejecting DNA requires an equal volume of fluid to be expelled from or injected into the capsid, which can occur either through pores in the capsid, or back through the sheath. Below we treat the fluid dissipation in both cases.

This is a textbook problem in fluid mechanics [83], giving a fluid velocity profile (with radial coordinate r)

$$u = \frac{V}{\ln d/D}\ln(r/D) + \frac{\Delta P}{4\mu X}\left(r^2 - d^2 - \frac{(D^2-d^2)}{\ln D/d}\ln r/d\right). \tag{3.21}$$

The pressure ΔP depends on the nature of the capsid. If the capsid is impermeable to water, the

volume of DNA $\pi d^2 V$ entering the capsid must exactly equal the fluid volume $2\pi \int_d^D urdr$ leaving the capsid, which gives

$$\Delta P = \frac{4\mu V X}{((d^2+D^2)\ln(D/d) + d^2 - D^2)} \tag{3.22}$$

of order 10^2 Pa. The total power dissipated comes from shear stress on the DNA, $U_{\text{shear}} = 2\pi d X V \partial_r u|_{r=d}$, and from $p - V$ work, driving a volume flux of DNA against a pressure ΔP, $U_{\text{pressure}} = \pi d^2 V \Delta P$. These two give a total dissipation

$$U_{\text{sheath}} = 2\pi\mu V^2 X \frac{D^2 + d^2}{d^2 - D^2 + (d^2+D^2)\ln D/d} \approx 10^{-2} k_{\text{B}} T/\text{s}, \tag{3.23}$$

which represents an upper bound for dissipation within the sheath.

If, as we assume below, it is easier for the fluid to flow through capsid pores than through the sheath, the "backflow" in Eq. 3.21, proportional to ΔP, disappears [84]. In that case, only shear stresses occur and give a total dissipation

$$U'_{\text{sheath}} = 2\pi X \frac{\mu V^2}{\ln(D/d)} \sim 3 \times 10^{-4} k_{\text{B}} T/\text{s}. \tag{3.24}$$

Finally, we estimate the power dissipated for fluid extruded through capsid pores, rather than the sheath. These pores occur at N symmetry points on the capsid shell. A crude estimate for the dissipation through each is obtained by assuming Poiseuille flow through each pore. Entrance and exit effects contribute, at most, a term of comparable magnitude. The flow rate through N pores due to a pressure ΔP inside the capsid is

$$Q_p \sim \frac{N \Delta P \pi R_p^4}{8\mu t_c}. \tag{3.25}$$

Requiring the DNA volume entering the capsid $\pi d^2 V$ to equal the fluid flux Q_p out of the capsid determines ΔP to be

$$\Delta P \sim \frac{8\mu t_c d^2 V}{N R_p^4}, \tag{3.26}$$

giving rise to a viscous dissipation

$$U_p = \Delta P \pi d^2 V \sim \frac{8\pi\mu t_c d^4 V^2}{N R_p^4} \sim 10^{-7} k_{\text{B}} T/\text{s}. \tag{3.27}$$

Since the dissipation through the pores is so much lower than that through the sheath, one expects most fluid extrusion to occur primarily through the pores. All of these effects are negligible in comparison with the power supplied by the motor, which consumes roughly $\sim 10 k_{\text{B}} T$ per 2 base pairs, giving $W_{\text{motor}} \sim 400 k_{\text{B}} T/\text{s}$.

Lastly, we note that if viscous forces from the flow of water into the capsid represent the primary

damping mechanism during ejection, the DNA ejection velocity can be obtained using the above results. If fluid must flow through the sheath to replace the volume lost by ejecting DNA, the ejection rate is $V_e \sim 6\mu$m/s per atmosphere of applied pressure, which implies an ejection time of less than 1 s; whereas if fluid can flow freely through capsid pores, higher ejection rates, $V_e \sim 300\mu$m/s per atmosphere of applied pressure, are obtained, resulting in a 1/50 s ejection time.

3.3.5 Capsid Mechanics

In all the calculations above we have assumed the capsid to be rigid. In this section we will be concerned with the elastic properties of the capsid, in an effort to understand the interplay between the forces exerted by the packaged DNA and the elastic deformation of the capsid. We will not consider the inelastic changes of the capsid geometry occurring during the early stages of packaging, referred to in the literature under the general heading of *capsid maturation* or *prohead expansion* [71, 80].

The mature capsid of bacteriophages such as λ, T7, and HK97 is made up of copies of a few proteins arranged on an icosahedral shell. For the purposes of this analysis we model the capsid as an elastic sphere and assume that the protein sub-units making up the capsids undergo only small deformations so that the elastic energy stored in a capsid expanded to a radius $R_{\rm out}$ is given by

$$G_{\rm cap}(R_{\rm out}) = \kappa(R_{\rm out} - R_0)^2\,, \tag{3.28}$$

where R_0 is the equilibrium radius of an empty capsid and κ is a constant measuring the capsid stiffness. An example of such an energy emerges from the simulations of Tama and Brooks [85], who perturb the positions of atoms in the capsid of a plant virus (CCMV) and measure its energy as a function of radius. They fit a quadratic polynomial in $R_{\rm out}$ to the energy obtained from their simulations and find

$$\kappa = 5.0 \times 10^5 \text{pN/nm}\,. \tag{3.29}$$

The capsid can be described as a thin shell of radius $R_{\rm out}$. In the presence of an internal pressure p, the free energy is minimized [58, 61] when

$$-4\pi R_{\rm out}^2 p + 2\kappa(R_{\rm out} - R_0) = 0\,, \tag{3.30}$$

which implies

$$R_{\rm out} - R_0 = \frac{2\pi R_{\rm out}^2 p}{\kappa}\,. \tag{3.31}$$

Using eqn.(3.29) and parameters from a typical phage capsid, $p = 40$atm and $R_{\rm out} = 30$nm, we

find

$$R_{\text{out}} - R_0 = 4.6 \times 10^{-2}\,\text{nm}\,. \tag{3.32}$$

This change is negligible in comparison to R_{out}, implying that a phage capsid can be treated as a rigid shell.

The analysis given above estimates the deformation of the capsid in response to the forces exerted by the packaged DNA. It is also of interest to determine the maximum pressure that a capsid can sustain, particularly in view of the osmotic shock experiments on these systems [86]. We approach this problem by modeling the capsid as an assemblage of proteins interacting through weak forces such as van der Waal's forces and hydrogen bonds. We note that capsids have thin walls compared to their diameter. For example, the capsid of $\phi 29$ is about 1.5nm thick, while its linear dimensions are of the order of 40-50nm [see 20, for data on $\phi 29$]. We use these ideas in conjunction with a coarse-grained model for the cohesive energies between protein subunits [45] and estimate the maximum pressure sustainable for a capsid to be in excess of 100atm. The details of the calculations can be found in Purohit et al. [61].

3.4 The DNA Ejection Process

We saw in the previous sections that packaged bacteriophage capsids are pressurized with pressures as high as 60atm. This has led to the speculation that the high pressure in the bacteriophage provides the driving force for DNA ejection into the host cell [11, 57, 58]. In this section, we examine the feasibility of this hypothesis. Specifically, we show that internal forces explain the results in Evilevitch et al. [12] and Grayson et al. [13] on the inhibition of DNA ejection from phage λ and allow us to make predictions for bacteriophages with varying genome lengths.

Any experiment in which we can control the amount of DNA ejected from a bacteriophage by the application of external pressure can help us understand whether internal forces drive ejection. In an experiment by Evilevitch et al. [12], mutant of λ bacteriophage EMBL3 with genome size of 48.5kbp were coerced into ejecting their DNA *in vitro* with the help of a protein called LamB or maltoporin. This protein, found on the outer membrane of *E. coli*, is the natural receptor for λ. When the phage binds to this protein it ejects its cargo of DNA. The DNA was ejected into solutions of polyethylene glycol 8000 (PEG) of various concentrations, which applied known osmotic pressures to the capsid. Evilevitch et al. [12] found that osmotic pressures of 20 atm were sufficient to prevent any DNA from leaving the capsid, whereas DNA was partially ejected at lower external pressures.

We can use our model for the forces associated with the packaged DNA to analyze the experiments of [12]. To that end we consider the system of bacteriophage, ejected DNA, and the PEG solution at equilibrium. The energetics of the DNA inside the phage capsid remains the same as discussed earlier in this chapter. The extra feature we add is the free energy of the ejected DNA-PEG system. Since

the persistence length of the DNA (50nm) is much larger than the persistence length of the PEG molecule ($\approx$ 1 nm), we model the insertion of the DNA inside the PEG solution as being equivalent to the insertion of a rigid cylindrical rod of radius R inside a solution which exerts osmotic pressure Π_0 on the rod. This problem has been studied by Castelnovo et al. [87] and Evilevitch et al. [88], who estimate the work of insertion of rigid rod (DNA) into a polymer (PEG 8000) solution as a combination of pressure-volume work, energy associated with creating new surfaces, and the entropic effects associated with polymer in solution. In particular, depletion effects result in a correction term [89, 90] that may be significant in this case because the diameter of DNA (1 nm) is comparable to the size of PEG ($R_g \approx 0.4$ nm). Here, however, we resort to a simple approximation where we retain only the term associated with the pressure-volume work (we take up the correction term in Appendix 3.6.2). Hence, the work expended to insert length $L_0 - L$ of DNA of radius R into the

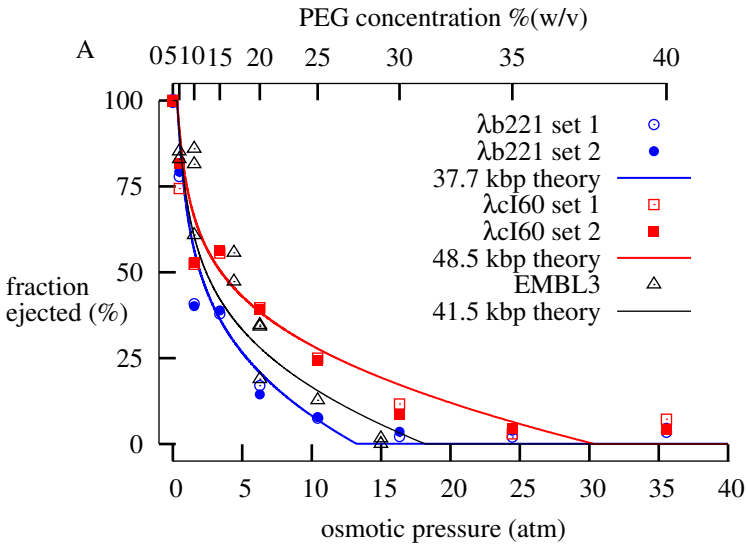

Figure 3.14: Fractional DNA ejection in λ-phage as a function of osmotic pressure. The experiment was performed in a TM buffer maintained at a pH of 7.4 and consisting of 50 mM TRIS and 10mM $MgSO_4$ [12, 13]. Experiment by Evilevitch was done on a mutant $EMBL3$ of λ phage and has a genome length of 41.5 kbp. The experiment by Grayson et al. [13] was performed on wild-type λ phage λI60 with a genome length of 48.5kbp and on a mutant λB221 with a genome length of 37.4 kbp. We see a very good match between the experimental findings and the theoretical results.

PEG solution is given by

$$w(L_0 - L) = \Pi_0(L_0 - L)\pi R_{\mathrm{DNA}}^2, \tag{3.33}$$

where R_{DNA} is the effective radius of DNA. The effective radius is the smallest possible distance between the center of a PEG monomer and the center of DNA, so that $((L_0 - L)\pi R_{\mathrm{DNA}}^2$ gives is the total volume excluded to PEG because of the DNA. We take R_{DNA} as 1.0nm (bare DNA) plus 0.2 nm, half the PEG monomer length found experimentally [91]. The total free energy of the system

is the sum of the free energy of the DNA inside the phage capsid and the work of insertion and is given by

$$G_{\rm tot}(d_s(L), L) + \Pi_0(L_0 - L)\pi R^2. \tag{3.34}$$

We already know that the free energy of the DNA inside the capsid depends on the parameters F_0 and c, which in turn depend on the ionic strength of the buffer used in the ejection reaction. The experiment by Evilevitch et al. [12] involved a buffer of 10 mM $MgSO_4$. Thus, we can use the empirical values $c = 0.30$ nm and $F_0 = 1.2 \times 10^4$ pN/nm^2 for Mg^{2+} solutions as determined earlier. We will use these values for all the fits to the experimental data and for further predictions.

In order to find find $L_0 - L$, the ejected length, we need to minimize the free energy $G_{\rm tot}$ with respect to L. Differentiating eqn.(3.34), we get, at equilibrium,

$$\frac{\partial G_{\rm tot}(d_s(L), L)}{\partial L} - \Pi_o \pi R^2 = 0. \tag{3.35}$$

The first term in the above expression is merely the resisting force $F(d(L), L)$ derived earlier. Consequently, equation(3.35) becomes

$$F(d_s(L), L) = \Pi_o \pi R^2. \tag{3.36}$$

This equation is solved for L for several values of Π_0 and the results for the percentage of DNA ejected as a function of osmotic pressure are given in Fig. 3.14 for different total DNA lengths L_0. Grayson et al. [13] improved significantly upon the experimental techniques by Evilevitch et al. [12] and performed ejection inhibition experiments on wild-type λ phage λCI60 with 48.5kbp long genome and a mutant λ221 with 37.4kbp genome. These new improved experimental results [13] combined with the older results [12] show a conclusive match with the theoretical predictions (see Fig. 3.14). It must be noted that this is a completely parameter-free prediction in the sense that all the theoretical parameters are obtained from some independent experimental source. It is, hence, all the more satisfying to see such a good match between the experiment and the theory. Figure. 3.15 shows how the model applies to the ejection behavior of other phage under the same solvent conditions as in Evilevitch et al. [12].

3.5 Discussions and Conclusions

This chapter addresses physical processes in the viral life cycle through a quantitative framework based on insights from structural biology, single molecule biophysics, electron microscopy, and solution biochemistry. The models were motivated by specific experiments on ϕ29 [11] and λ [12] but their applicability extends to all dsDNA bacteriophages. In fact, we use our models to predict

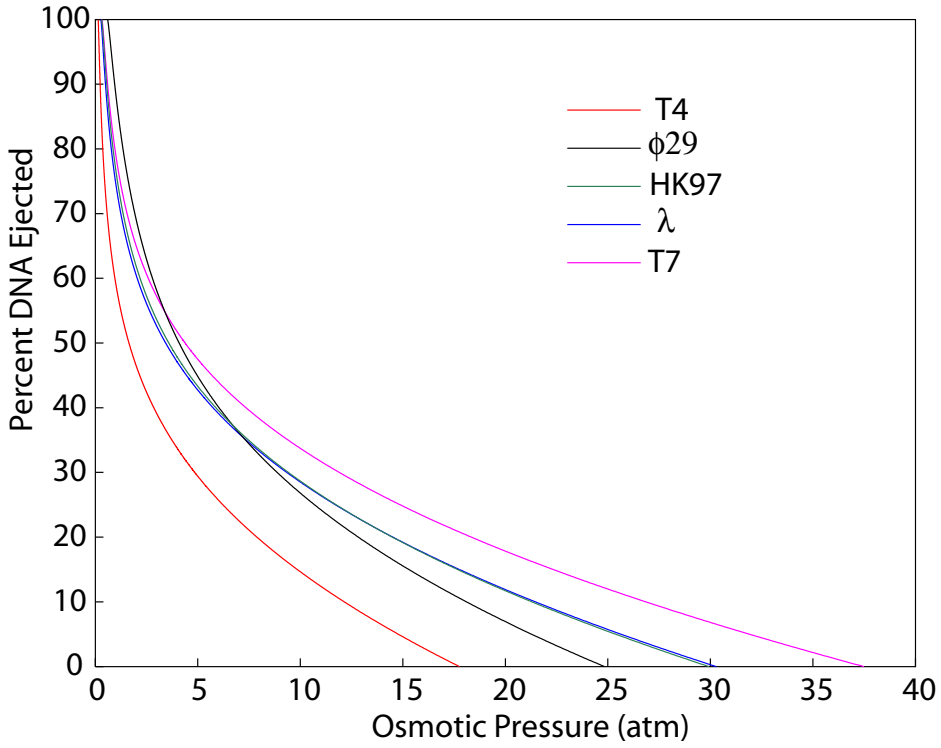

Figure 3.15: DNA ejection as a function of osmotic pressure for various wild-type species of bacteriophage for ionic conditions similar to the experiment of [12] (10mM $MgSO_4$). The lines show the DNA ejection behavior for T4, HK97, ϕ29, T7, and λ. Osmotic pressures as high as 35-55atm are required to inhibit ejection in these bacteriophage (figure taken from Grayson et al. [13]).

important features of the packaging and ejection processes in phages other than ϕ29 and λ.

The key predictions arising from the modeling efforts described here are:

- *Dependence of Forces and Spacing on Ionic Strength.* As shown in Fig. 3.6, Fig. 3.7, Fig. 3.9 and Fig. 3.12, there is a strong dependence of both the spacing of the packaged DNA as well as the forces that build up due to packing on the ionic conditions during the packaging reaction. We suggest systematic experiments to explore these effects.

- *Dependence of Forces and Spacing on Phage Identity.* As shown in Fig. 3.9 and Fig.3.10, we find a systematic and strong dependence of the packing forces on the particular phage species of interest. In particular, had the experiment of Smith *et al.* been carried out in phage T7, we predict a maximum packing force in excess of 100pN, rather than the 57pN found in ϕ29. A simple parameter for developing intuition concerning the forces associated with different phage is ρ_{pack}, the ratio of the volume of the genome to the volume of the capsid.

- *Force Steps During Packaging.* One of the weakest points of the analysis described in this chapter is the uncertainties that attend the particular structural arrangements of the DNA on the way to the fully packaged state. In particular, we have *assumed* a sequence of structural

states which are all of the inverse spool form, and one consequence of this structural picture which might be testable is the presence of steps in both the DNA spacing and forces as shown in Fig. 9.

- *Dependence of ejection inhibition on genome length, virus type, and solution conditions.* The beautiful experiments of Evilevitch et al. [12, 13] provide a direct window on the forces associated with the packaged DNA. Fig. 3.14 and Fig. 3.15 represent a wide range of parameter-free predictions for the fractional ejection inhibition that should be seen in such experiments. We can see from Fig. 3.14 that the theoretical predictions give an excellent match to the experimental observations.

Finally, a cautionary note. Experiments have shown that some bacteriophage, such as T7 [16] may rely on a different mechanism for delivering their genome into the host cell. This is a possibility worthy of further exploration, but we emphasize that viruses may use many different methods or combinations thereof to propagate themselves.

3.6 Appendix

3.6.1 The Genetic Material dsDNA

In this chapter we worked with bacteriophages with dsDNA as the genetic material. It would be useful to briefly review the genetic material in this section. Without doubt, the mechanical properties of dsDNA depend primarily on its chemical composition and structure. In this section we will briefly touch upon this aspect and try to argue a bit if the entire details of the structure are relevant for the mechanical behavior we are out to describe.

3.6.1.1 DNA Composition and Structure

DNA stands for deoxyribonucleic acid. It is constructed from individual monomeric units to form an unbranched chain. The elementary monomeric unit of DNA(also RNA), nucleotides, are a troika of phosphate, sugar, and organic base, with the phosphate and sugar units alternating along the backbone. The two different sugars found in the nucleotides, ribose in RNA and deoxyriboses in DNA, are five membered rings differing from each other by only one atom. In either molecule, the OH^{-1} groups are potential reaction sites for addition of a base. Five organic bases are found in nucleotides, and they fall into two chemically similar groups: purines and pyrimidines. Only four of the five bases are present in a given DNA or RNA molecule, and the one *missing* base is different for each:

1) RNA: adenine, guanine, cytosine, uracil.

2) DNA: adenine, guanine, cytosine, thymine.

The reaction of a sugar with a base releases water (an -OH from the sugar plus an H from the base)

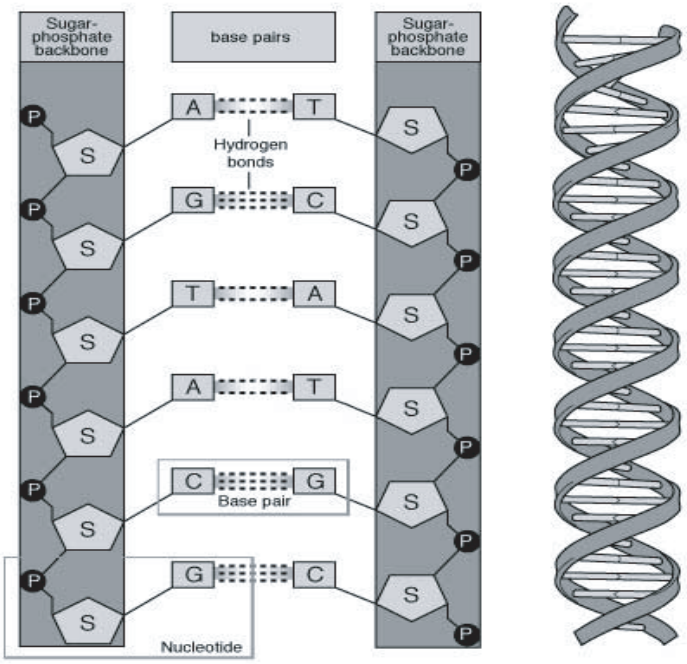

Figure 3.16: DNA structure and composition

and produces a sugar-base combination called a nucleoside. Addition of a phosphate to the nucleoside releases water and produces a nucleotide. The nucleotides themselves can polymerize to form DNA and RNA, through linkage between a sugar from one nucleotide and a phosphate from another. In the double-stranded helix of DNA, the bases lie in the interior of the helix and hold the helix together through the hydrogen bonding between base-pairs. As illustrated in Fig. 3.16, each matching base pair on the opposing strands consists of one purine and one pyrimidine: adanine/thymine and guanine/cytosine.

The dsDNA is roughly a cylindrical molecule of diameter 2nm. It consists of a stack of roughly flat plates (the basepairs), each about 0.34nm thick. But the genome total length of $\lambda -$ phage is 16.5nm, still far bigger than the diameter. Hence, we may hope that the behavior of DNA on such long length scales may not depend very much on the entire details of its structure.

3.6.1.2 Persistence Length and the Elastic Energy of DNA

In the previous section we had a brief argument as to why the entire structural details of the chain may be irrelevant in describing the mechanical properties of DNA. In this section we will model DNA as an elastic rod and introduce the concept of persistence length. If we bend an elastic rod of length L and bending-modulus κ into an arc of a circle of radius R, the elastic energy of the rod is

given by

$$E_{\text{arc}} = \frac{1}{2}\frac{\kappa L}{R^2}, \tag{3.37}$$

$\kappa = YI$, where Y is the Young's modulus, a material property, and I is the area moment of inertia (larger for larger bending cross-section and proportional to R^4 for circular cross-section), a geometrical property. The energy of an object in thermal equilibrium fluctuates with time with the thermal energy scale set by k_BT ($k_B = 1.38 \times 10^{-23}$ J/K is the Boltzmann constant, and T is the absolute temperature). At room temperature the value of k_BT in units of pN-nm is approximately 4.1. One way of quantifying the amplitude of the shape fluctuations at finite temperature is finding the typical distance along the rod over which it loses its tangent-tangent correlation. This length scale must be directly proportional to the bending rigidity κ and inversely proportional to T. The combination κ/k_BT has units of length and is called the persistence length.

$$\xi_p = \frac{\kappa}{k_BT} \tag{3.38}$$

So long as its persistence length is large compared to its contour length i.e. $\xi_p \gg L$, a filament appears relatively straight.

If the polymer is bent into a curve parametrized by arc length parameter s, as in Fig. 3.17 then the following relationships hold.

$$\partial\mathbf{t}/\partial s = C\mathbf{n} \tag{3.39}$$

$$C\mathbf{n} = \partial^2\mathbf{r}/\partial s^2. \tag{3.40}$$

where C is the curvature at that point and is given by $1/R_c$ where R_c is the local radius of curvature. Equation(3.37) gave us an expression for energy per unit length of an elastic rod bent into a circular arc. So the energy of any arbitary curve will be,

$$E_{\text{bend}} = (\kappa/2)\int_0^L 1/R_c^2 ds = (\kappa/2)\int_0^L (\partial t/\partial s)^2 ds = (\kappa/2)\int_0^L (\partial^2\mathbf{r}/\partial s^2)^2 \tag{3.41}$$

If we assume that the chain is laterally isotropic, i.e., any rotation perpendicular to the lateral plane does not change its energy, then it can be shown that [92]

$$\langle \mathbf{t}(0).\mathbf{t}(s)\rangle = \exp(-s/\xi_p). \tag{3.42}$$

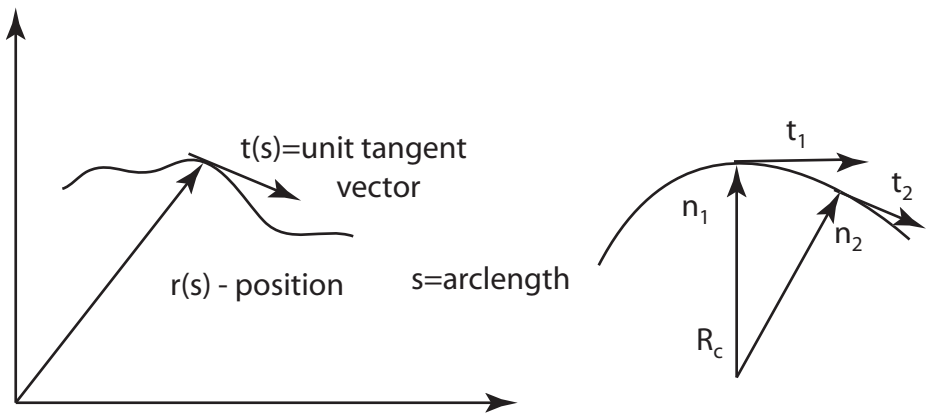

Figure 3.17: The schematic of an idealized curve describing DNA bending. (a)A point on the curve at arc length s is described by position vector $\mathbf{r}(s)$ and a unit tangent vector $\mathbf{t}_s$ (b) Two locations are seperated by an arc length Δs subtending an angle $\Delta\theta$ as a vertex formed by extensions of the unit normals $\mathbf{n}_1$and $\mathbf{n}_2$and intersect at a distance R_c from the curve.

The length ξ_p in the exponential of the above equation is called persistence length. The persistence length can be related to bending moduli κ as [92]

$$\kappa = \xi_p k_B T. \tag{3.43}$$

Similarly, we can also prove that the end-end distance of such a chain is given by

$$\langle \mathbf{r}_{ee}^2 \rangle = 2\xi_p L - 2\xi_p^2(1 - \exp(-L/\xi_p)). \tag{3.44}$$

Hence, we can say that

$$\langle \mathbf{r}_{ee}^2 \rangle = \begin{cases} 2\xi_p L \text{ (if } L \gg \xi_p) \\ L^2 \text{ (if } L \ll \xi_p) \end{cases} \tag{3.45}$$

The persistence length of DNA is observed to be 50nm [74] under physiological conditions. The typical phage capsid size is around tens to hundreds of nanometers. Thus, the DNA has to be tightly bent inside the phage capsid, and thus it should cost a large amount of bending energy to pack the DNA inside the phage capsid.

3.6.2 Fitting the Experimental Data on DNA Ejection with the Theory

In the previous sections we did not use any "fitting" parameters to evaluate either the internal force on the DNA or the external osmotic force resisting the DNA ejection. The values for phage capsid radius (R_{out}), the empirical parameters F_0 and c for the interaction forces (see Eq. 3.9), and the

radius of DNA (R_{DNA}) were obtained from various experimental observations. It is very likely that there were some experimental errors in obtaining these parameters. It is also possible that these various parameters were obtained under different experimental conditions, and hence it is not strictly legal to use them together. Similarly, in order to obtain the resisting osmotic force on the DNA in Section 3.4, we simply multiplied the effective cross-section area of the DNA with the osmotic pressure. But since the radius of the DNA is comparable to the radius of the osmolyte PEG-8000, as will be seen later, there will be an additional term contributing to the resisting force with a free parameter α associated with it. Hence, in this section we take these parameters as "free," obtain the values that give a best least-square fit to the DNA ejection data from Grayson et al. [13], and compare them with the results obtained without fitting. The goal of this analysis is to examine how sensitive our results are to the choice of parameters.

As seen in earlier sections, the theory for the amount of force on the DNA within the capsid has three parameters that require external determination. As explained in the introductory paragraph of this section, they are F_0, c, and R_{out}. The effect of the external osmotic pressure also has three parameters. They are R_{DNA}, the Kuhn length b for the flexible polymer PEG-8000, and the proportionality constant α that goes with the correction term. If we assume PEG-8000 to be a flexible polymer, the osmotic pressure exerted by the PEG as a function of the *volume* fraction ϕ of the PEG in water is given by [93]

$$\Pi_{\mathrm{Osmotic}} = k_{\mathrm{B}}T\frac{\phi^{9/4}}{b^3}. \tag{3.46}$$

The osmotic pressure exerted by PEG-8000 is obtained by using the empirical result [62]

$$\Pi_{\mathrm{Osmotic}} = -1.29G^2T + 140G^2 + 4G, \tag{3.47}$$

where G is the weight of PEG per gram of water and T is the temperature. This quantity G is one of the quantities controlled experimentally by Grayson et al. [13], and the empirical result mentioned above is used to obtain the osmotic pressure. The volume fraction ϕ is related to G by [94]

$$\phi = \frac{w}{w + 1.335(1-w)}, \tag{3.48}$$

where $w = G/(G+1)$. Since we now have a connection between the volume fraction ϕ and the weight fraction G, we can relate the theoretical results for osmotic pressure (Eq. 3.46) with the empirical result (Eq. 3.47). If we use a value of the Kuhn length (the approximate monomer size) b to be approximately equal to 0.45 nm, we get a very good agreement between these two results. The size $b \approx 0.45$ nm is also close to the theoretical values of $b = 0.4$ nm used in the literature [91].

The bare radius of the DNA (1.0 nm) is comparable to the radius of gyration, R_g, of PEG-8000,

which is approximately 0.4 nm. So it is not correct to assume DNA to be a wide rod working against just the osmotic pressure. It is important to add the effects coming from the excluded volume effects due to the interpenetration of DNA and PEG [87, 89, 88]. This correction can be taken into account by addition of an extra term to the force from the osmotic pressure. The total external force due to the osmolyte becomes

$$F_{\text{External}} = \Pi_{\text{Osmotic}} \pi R_{\text{DNA}}^2 + \alpha k_{\text{B}} T \phi \frac{R_{\text{DNA}}^{1/3}}{b^{4/3}}. \tag{3.49}$$

We, hence, have five parameters needed to fit the experimental data with the theoretical result. To define the goodness of a fit, we need to define a positive definite function for the discrepancy between the experimental data and the theoretical prediction. We define our error metric as follows. The experiment by Grayson et al. [13] obtains two data sets each for 37.4 kbp and 48.5 kbp phage that involve the osmotic pressure Π_{Osmotic} and the corresponding fraction of DNA ejected from the phage (see Section 3.4). The fraction of DNA ejected is equal to $1 - L/L_0$, where L is the length of the DNA inside the phage capsid and L_0 is the total genome length of the phage. As seen in Section 3.4, the basic governing equation for the DNA ejection equilibrium is the force balance between the internal force on the DNA and the external force on the DNA:

$$F_{\text{Internal}}(F_0, c, R_{\text{out}}, L) = F_{\text{External}}(R_{\text{DNA}}, \alpha, \Pi_{\text{Osmotic}}). \tag{3.50}$$

Of all these quantities, Π_{Osmotic} is the quantity that is controlled in the experiment. If L_0 is the total length of the phage genome and L is the amount of DNA left in the capsid, $L_0 - L$ is the ejected length, the measured quantity, and the remainder are the parameters. Supposed that we have a set of data points for both types of phage all combined and given by $\{(\Pi_{\text{Osmotic}}^{(1)}, L^{(1)}), ...(\Pi_{\text{Osmotic}}^{(M)}, L^{(M)})\}$. Solving Eq. (3.50) will give us $L = L(F_0, c, R_{\text{out}}, L, R_{\text{DNA}}, \Pi_{\text{Osmotic}}, \alpha)$. It may be noted that we are writing the equation in this form because Π_{Osmotic} is the controlled quantity and L is the derived quantity. We thus have experimentally controlled values of $\Pi_{\text{Osmotic}}^{(i)}$, and observed values of $L^{(i)}$. Also, for every $\Pi_{\text{Osmotic}}^{(i)}$ we will have a theoretically calculated value $L_{\text{Theory}}^{(i)}$. We hence write down the error function $\Xi(F_0, c, R_{\text{out}}, R_{\text{DNA}}, \alpha)$ as

$$\Xi(F_0, c, R_{\text{out}}, R_{\text{DNA}}, \alpha) = \frac{1}{L_{\text{Total}}} \sqrt{\frac{1}{M} \sum_{i=1}^{M} (L_{\text{Theory}}^{(i)} - L^{(i)})^2}, \tag{3.51}$$

where $L_{\text{Total}} = 48500 * 0.34$ nm, the total genome length of the wild-type phage, is just a normalizing term. We wish to minimize this complicated function, and since there is no closed form expression for L_{Theory}, we have to resort to numerical calculations. We gather a set of values for each parameter close to its value obtained from various sources and choose those values which give a minimum

error as given in Eq. 3.51. The different parameters used in Section 3.4 are $F_0 = 12000\text{pN/nm}^2$, $c = 0.3$ nm [47], $R_{\text{DNA}} = 1.0$ nm, $R_{\text{out}} = 29$ nm [18], and $\alpha \approx 1.0$. We then estimate the error $\Xi(F_0, c, R_{\text{out}}, R_{\text{DNA}}, \alpha)$ over a range of values for these parameters:

$$F_0 = 7000, 8000, 9000, 10000, 11000, 12000, 13000, 14000, 15000, 16000, \tag{3.52}$$

$$c = 0.26, 0.27, 0.28, 0.29, 0.30, 0.31, 0.32, 0.33, 0.34, 0.35, \tag{3.53}$$

$$R_{\text{out}} = 27, 28, 29, 30, 31 \tag{3.54}$$

$$R_{\text{DNA}} = 1.0, 1.2, 1.5, \tag{3.55}$$

$$\alpha = 0.0, 1.0, 1.5, 2.0. \tag{3.56}$$

It may be noted that when $\alpha = 0$ we recover back the simple case of "only osmotic pressure" that we have used in Section 3.4. The set of parameters giving us the minimum error is, of course, the best fit. In order to perform the required error analysis, we will broadly divide the entire set of parameters into two cases. The first case is when we do not have the correction term, i.e., $\alpha = 0$, while the second case is with positive values of α.

1: No Correction Terms, i.e., α equals 0

If we do not have the correction term in Eq. 3.49, the equation for force-balance becomes,

$$F_{\text{Internal}}(F_0, c, R_{\text{out}}, L) = \Pi_{\text{Osmotic}} \pi R_{\text{DNA}}^2. \tag{3.57}$$

Upon inversion (numerical, of course) we will obtain $L = L(F_0, c, R_{\text{out}}, R_{\text{DNA}}, \Pi_{\text{Osmotic}})$. Π_{Osmotic} is an experimentally given quantity, while the remaining variables are the unknown parameters. We will, hence, minimize the error $\Xi(F_0, c, R_{\text{out}}, R_{\text{DNA}}, \alpha)$ on the parameter space, of F_0, c, R_{out}, and R_{DNA}. There could be many variants, even in this case. For example, the values of F_0 and c used in Section 3.4 to address the experimental conditions of Evilevitch et al. [12] and Grayson et al. [13] were obtained from the data of Rau et al. [47] for 10mM Mg^{2+} ions. But these DNA ejection experiments also have positively charged TRIS ions in addition to the Mg^{+2} ions. Since there is no experimental data for this additional ionic condition, the values of F_0 and c used are not exact. Hence, we can first start by using F_0 and c as the fitting parameters. Taking R_{DNA} equal to 1.0 nm is a decent approximation. Also, the capsid-size is known to be around 29 nm [18]. So we will begin by fitting over the parameters F_0 and c, and estimating the error over the already choosen range of values of F_0 and c in Eqs. 3.53 and 3.54, respectively. Over this range of values of F_0 and c we obtain the least error when $F_0 = 12000\text{pN/nm}^2$ and $c = 0.27$ (see the black curve in Fig. 3.18(a), and (b)).

The second case will be to vary the capsid size because Earnshaw and Harrison [18] find the internal radius of the capsid R_{out} to be around 29 nm, while Dokland and Murialdo [50] get an

estimate of around 27.5 ± 1.5 nm. Hence, keeping the diameter of DNA as 1.0 nm, we vary the capsid size around the standard size of 29 nm and get the best estimate of the parameters F_0, c, and R_{out}. The best estimates are when $F_0 = 10000\text{pN/nm}^2$, $c = 0.3$ nm, and $R_{\text{out}} = 31$ nm (see the red curve in Fig. 3.18(a), and (b)).

The third case is by varying F_0, c, R_{out}, and R_{DNA}. The bare radius of the DNA cylinder is estimated to be 1.0 nm, but since the DNA is surrounded by the polymer with Kuhn length $b \approx 0.4$ nm, there may an addition of upto 0.4 nm in the DNA radius due to this excluded-volume effect. We will hence vary the DNA radius from 1.0 nm to 1.5 nm and see which radius gives us the best fit to the experimental data. Upon performing the calculation over the range of values of parameters in Eqs. 3.53, 3.54, 3.55, and 3.56, the minimum error $\Xi(F_0, c, R_{\text{out}}, R_{\text{DNA}}, \alpha)$ is obtained when $F_0 = 7000\text{pN/nm}^2$, $c = 0.32$nm , $R_{\text{out}} = 29$nm, and $R_{\text{DNA}} = 1.5$nm (see the cyan curve in Fig. 3.18(a) and (b)).

2: Error analysis when the correction term α is not zero. We saw earlier that the bare radius of the DNA (1.0 nm) is comparable to the radius of gyration of PEG-8000, $R_{\text{g}} \approx 3.4$ nm. So it is important to add the contribution coming from the excluded volume effects due to the interpenetration of DNA and PEG. After addition of the correction term as shown in Eq. 3.49 the force balance between the internal and the external force on the DNA will be

$$F_{\text{Internal}}(L, R_{\text{out}}, F_0, C) = \Pi_{\text{Osmotic}} \pi R_{\text{DNA}}^2 + \alpha k_{\text{B}} T \phi \frac{R_{\text{DNA}}^{1/3}}{b^{4/3}}. \tag{3.58}$$

Hence, we can solve Eq. (3.58) to obtain L in terms of volume fraction ϕ and other parameters. But since there is a one-to-one relation between ϕ and Π_{Osmotic} (Eq. 3.46), L can be expressed as $L(F_0, c, R_{\text{out}}, R_{\text{DNA}}, \alpha, \Pi_{\text{Osmotic}})$. We now vary the parameter α as shown before to obtain the error $\Xi(F_0, c, R_{\text{out}}, R_{\text{DNA}}, \alpha)$. The minimization of the error $\Xi(F_0, c, R_{\text{out}}, R_{\text{DNA}}, \alpha)$ gives us $F_0 = 7000\text{pN/nm}^2$, $c = 0.32$nm, $R_{\text{out}} = 29$nm, $R_{\text{DNA}} = 1.5$ nm and $\alpha = 0$. Since we have included all possible parameters in this error minimization, this is the best fit for the range of values choosen in Eqs. 3.53– 3.56. Also observe that in the the best fit there is no need to have a correction term α! We make a plot of the fraction DNA ejected and the osmotic pressure with these parameters and show it in Fig. (3.18). We can see from the figure that the best fit matches very well with the experimental data.

As can be seen from Eq. 3.53– 3.56, we choose a discrete range of values for the set of parameters F_0, c, R_{DNA}, R_{out}, and α. The values of these parameters may, hence, not really be the ones that give a best fit by minizing the error metric in Eq. 3.51. On the other hand, as can be seen from Fig. 3.18, the "no parameter" fit is not really too far off for relatively small perturbations in the corresponding parameters. Thus the "no parameter" solution in Section 3.4 can be considered as a good prediction to the experimental data in Grayson et al. [13].

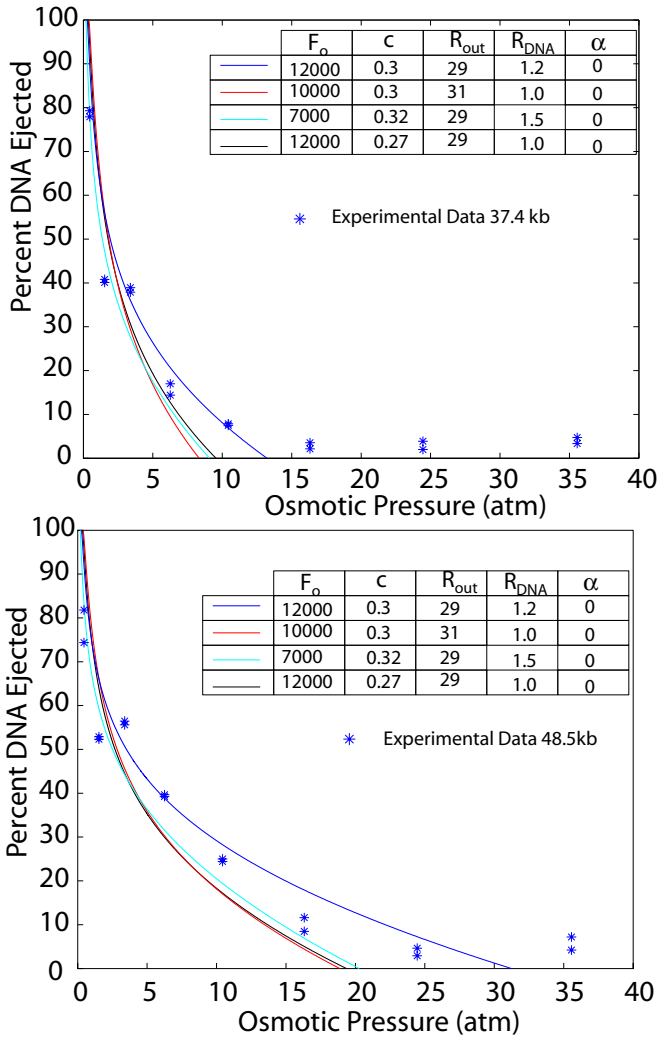

Figure 3.18: The percent DNA ejected vs osmotic pressure for different values of the parameters F_0, c, R_{out}, R_{DNA}, and α, which minimize the error metric obtained by comparing the experimental data from [13] with the theoretical predictions. Parts (a) and (b) correspond to λ phage with genome lengths 37.4kbp and 48.5kbp, respectively. The table in parts (a) and (b) of the figure correspond to various cases discussed in the main text of Appendix 3.6.2. It can be seen that these various cases give almost the same quality of fit to the experimental data points. The blue curve corresponds to a "no fit" result as used in Section 3.4. The least metric of error (Eq. 3.51) over the range of values of parameters in Eqs. 3.53– 3.56 is obtained when F_0 is 7000pN/nm^2, c is 0.32nm , R_{out} is 29nm, and R_{DNA} equals 1.5nm. It can be observed that the "no parameter" (blue curve) is within $10-30\%$ of the "best fit" curve (cyan) curve.

Chapter 4

Kinetics of DNA Ejection in Bacteriophage

[*Most of the work in this chapter is from Inamdar et al.[29]*]

The ejection of DNA from a bacterial virus ("phage") into its host cell is a biologically important example of the translocation of a macromolecular chain along its length through a membrane. The simplest mechanism for this motion is diffusion, but in the case of phage ejection a significant driving force derives from the high degree of stress to which the DNA is subjected in the viral capsid. The translocation is further sped up by the ratcheting and entropic forces associated with proteins that bind to the viral DNA in the host cell cytoplasm. We formulate a generalized diffusion equation that includes these various pushing and pulling effects and make estimates of the corresponding speed-ups in the overall translocation process. Stress in the capsid is the dominant factor throughout early ejection, with the pull due to binding particles taking over at later stages. Confinement effects are also investigated in the case where the phage injects its DNA into a volume comparable to the capsid size. Our results suggest a series of *in vitro* experiments involving the ejection of DNA into vesicles filled with varying amounts of binding proteins from phage whose state of stress is controlled by ambient salt conditions or by tuning genome length.

4.1 Introduction

A crucial first step in the life cycle of most bacterial viruses involves binding of the virion to a receptor protein in the host cell membrane followed by injection of the phage DNA. The viral genome is typically about 10 microns long, and its translocation from outside to inside the host cell is accomplished over times that vary from seconds to minutes. The wide range of mechanisms responsible for injection of phage genomes has recently been systematically reviewed [16, 40, 95], including many references to the last few decades of relevant literature. In the present paper we

formulate a general theory of chain translocation that takes into account many of the physical phenomena involved in actual phage life cycles. These phenomena include diffusion of the DNA chain along its length; driving forces due to stress on the DNA inside the viral capsid; resisting forces associated with osmotic pressure in the host cell; cell confinement effects that constrain the injected chain; and ratcheting and pulling forces associated with DNA-binding proteins in the host cell cytoplasm.

Considerable effort has been focused on the energetics of packaging and ejecting DNA in phage. In particular, theoretical work [56, 69, 57, 61, 58, 96, 97, 28] has shown that the dominant source of stress on the DNA in the capsid results from strong repulsive interactions between neighboring portions of double helix that are confined at average interaxial spacings as small as 2.5 nm. Another major contribution comes from the bending stress that arises from the capsid radius being smaller than the DNA persistence length. The force needed to package the genome against this resistance is provided by a virally encoded motor protein that pushes in the DNA along its length. Recent laser tweezer measurements [11] have confirmed that this force increases progressively as packaging proceeds, i.e., as the chain becomes more crowded and bent, reaching values as large as 50 pN upon completion. Conversely, the force *ejecting* the DNA upon binding of the phage to its membrane receptor has been shown [12, 13] to *decrease* monotonically from tens of piconewtons to zero as crowding and bending stress are progressively relieved. In the current paper we consider the *dynamics* of phage ejection and attempt to distinguish the relative importance of these large, varying, "internal" forces and the binding particles in the external solution (bacterial cytoplasm).

It is useful at the outset to consider the simple diffusion limit of the translocation process. More explicitly, consider the case in which a chain is threaded through a hole in a membrane, dividing one solution from another. If the chain is free, i.e., in the absence of pushing or pulling forces and of binding particles, it will simply diffuse along its length, experiencing a friction associated with its passage through the membrane and the viscosity of the solution. The time required for its translocation from, say, the left to the right will be $L^2/2D = \tau_d$, where L is the length of the chain and D is its effective translational diffusion coefficient.

Suppose now that particles are added to the right-hand solution which bind *irreversibly* to the chain at regularly spaced sites as soon as they diffuse into the solution. Then, if s is the spacing between these binding sites, the diffusion of the chain will be *ratcheted* each time another length s has entered the solution [98, 99, 75], corresponding to the fact that the chain cannot move backwards through the hole at a site where a particle is bound. Accordingly, the time it takes for the entire chain to appear on the right is simply given by $s^2/2D$ – the time required for diffusion between a pair of neighboring binding sites – times the total number of sites, L/s. It follows that the overall translocation time in the presence of perfect ratcheting is reduced by a factor of s/L over that for free diffusion. When the binding of particles is *reversible* – they do not remain bound indefinitely, thereby

allowing some sites to diffuse backwards through the hole – the translocation time is increased by a factor of $(1 + 2K)$ compared to perfect ratcheting, where K is the ratio of "off" and "on" rates for particle binding [98, 99]. Finally, note that the ideal ratcheting time of $Ls/2D$ corresponds to a velocity of $2D/s$ and hence, by the Stokes-Einstein relation, to a *force* of $2k_BT/s$ pulling the chain into the particle-containing solution [100].

When the particle binding is reversible, however, it turns out that there can be a different mechanism from the ratcheting dynamics, one that can significantly *shorten* the translocation time below $Ls/2D = \tau_{\rm idealratchet}$. This effect requires that the diffusive motion of the chain is slow enough and is due to the fact that the entropy of reversibly bound particles increases when there is more chain for them to explore. As a result, the entropy is an increasing function of chain length available in the right-hand solution. Indeed, in the limit of fully equilibrated binding, the system is equivalent to a one-dimensional Langmuir adsorption problem [100, 101](P. G. de Gennes, personal communication. Also, see Section 4.4.2) . More explicitly, the $1D$ Langmuir pressure can be written in the form $P_{1D} = (k_BT/s)\ln\{1 + \exp[(\epsilon + \mu)/k_BT]\}$, where $\epsilon > 0$ is the energy lowering of the adsorbing particles upon binding and μ is their chemical potential in solution. Note that in the limit of large binding energy ($(\epsilon+\mu)/k_BT \gg 1$) this pressure reduces simply to $(\epsilon+\mu)/s$, which – *because pressure is force in a* $1D$ *system* – can be directly interpreted as the force pulling on the chain due to the reversible binding of particles. Note further, in the large binding energy limit, that this force is necessarily large compared to the ideal ratcheting force, $2k_BT/s$ [100].

Ambjornsson and Metzler [101] have recently clarified the various timescales that determine the different regimes of chain translocation in the presence of "chaperones", i.e., binding particles. The first, τ_0, is the time needed for the chain to diffuse a distance of order s, the separation between binding sites. The second and third are $\tau_{\rm occ}$ and $\tau_{\rm unocc}$, the characteristic times that a binding site remains occupied and unoccupied, respectively. $\tau_{\rm occ}$ and $\tau_{\rm unocc}$ are related by the equilibrium relation

$$\frac{\tau_{\rm occ}}{\tau_{\rm unocc}} = \exp\left(\frac{\epsilon+\mu}{k_BT}\right). \tag{4.1}$$

Finally, $\tau_{\rm unocc}$ can be approximated by the typical time it takes for a particle to diffuse a distance of order R ($\simeq c_0^{-1/3}$) between binding free particles:

$$\tau_{\rm unocc} = \frac{R^2}{2D_0} \simeq \frac{1}{D_0 c_0^{2/3}}, \tag{4.2}$$

where D_0 is the diffusion coefficient of the particles. One can then distinguish between three different regimes:

1. Diffusive regime: $\tau_0 \ll \tau_{\rm unocc}, \tau_{\rm occ}$. Here the binding particles are irrelevant to the chain

translocation because the chain diffuses its full length in a time too short for the particles to bind.

2. Irreversible binding regime: $\tau_{\rm unocc} \ll \tau_0 \ll \tau_{\rm occ}$. Here particles bind essentially irreversibly on a time scale short compared to the time it takes for the chain to diffuse a distance between binding sites. We shall refer to this as the "ratcheting" regime.

3. Reversible binding regime: $\tau_{\rm unocc}, \tau_{\rm occ} \ll \tau_0$. Here diffusion of the chain along its length is slow compared to the time required for an "on"/"off" equilibrium of the binding particles to be achieved. We shall refer to this as the "Langmuir" regime.

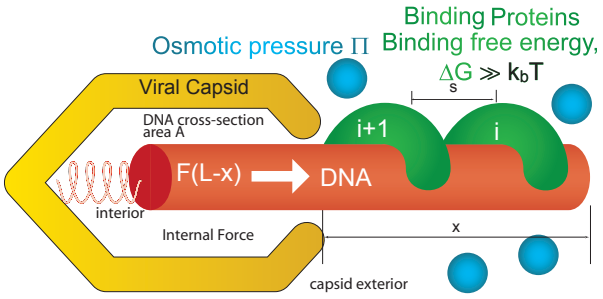

Figure 4.1: Schematic showing the various physical effects which assist bare diffusion in the process of phage DNA ejection. The DNA cross-section is not shown to scale: its diameter is $2-4$ nm, as compared with a capsid interior diameter that is ten times larger. The spring denotes schematically the stored energy density resulting in a force F acting along the length $L-x$ of chain remaining in the capsid. The small spheres denote particles giving rise to an "external" (cytoplasmic) osmotic pressure $\Pi_{\rm Osmotic}$, while the green particles labeled i and $i+1$ are successive binding particles. (The schematic inspired from Fig.10.10 in [75].)

It is also important to clarify some relevant *length* scales involved in the problem. Specifically, we distinguish between two extremes of how the separation, s, between binding sites compares with the range, δ, of the attractive interaction between binding particle and the chain. Pure and "perfect" ratcheting will arise when $\tau_{\rm unocc} \ll \tau_0 \ll \tau_{\rm occ}$, independent of the relative values of δ and s. "Imperfect" ratcheting will arise when $\tau_{\rm unocc}, \tau_{\rm occ} \ll \tau_0$, but $\delta \ll s$. The translocation time for the "imperfect" ratchet is higher than the "perfect" ratchet by a factor of $(1+2K)$. Finally, when $\tau_{\rm unocc}, \tau_{\rm occ} \ll \tau_0$, and $\delta \approx s$, we will have a Langmuir force acting on the chain. Note that if the binding free energy between DNA and the binding proteins is very large, then $K \ll 1$, and the imperfect ratchet is no different than the perfect one. In this paper we will always take this limit. A schematic of the role of these various effects is shown in Fig. 4.1.

Before proceeding further it is instructive to make some numerical estimates. Within this simple translocation model all time scales are naturally referenced to that for pure translational diffusion of a chain along its length and, hence, to the diffusion coefficient D introduced earlier. In reality, however,

the DNA ejection process is enormously more complicated since the chain moving through the tail of the phage is feeling not only the friction associated with the few hydration layers surrounding it but also the viscous effects arising from interaction with the inner surface of the tail just nanometers away. Furthermore, this chain portion is connected to the lengths of chain inside the capsid and outside in the cell cytoplasm. The chain remaining inside the capsid moves by reptating through neighboring portions of still-packaged chain and/or by overall rotation of the packaged chain. All of these latter motions involve viscous dissipation that is insufficiently well-characterized to enable realistic estimates of diffusion time scales, even though one can distinguish between different dependence on chain length for each of these dynamical processes [96, 84]. As a result, in pursuing the simple translocation picture as a model for overall phage ejection kinetics, we resort to using an effective diffusion coefficient D to define the unit of time, $\tau_d = L^2/2D$.

A strong upper bound for D can be obtained by considering the part of the dissipation arising as the chain moves through the tail portion of the virus. Taking into account only the friction between the DNA and the fluid in the tail we have, for example [84, 83], $\zeta = 2\pi l\eta/\ln(\Delta/d)$. Here ζ is the friction coefficient, l is the length of the tail, η is the viscosity of water, Δ is the inner diameter of the tail, and d is the diameter of the double-stranded DNA. Taking $l = 100$nm, $\eta = 10^{-9}$pN-s/nm^2, $\Delta = 4$nm [20], and $d = 2$nm, we find $\zeta = 9 \times 10^{-7}$pN-s/nm and hence a diffusion coefficient ($D = k_BT/\zeta$) of 5×10^6nm^2/s. For a typical phage genome length (L) of 10μm, this in turn leads to a diffusional translocation time ($\tau_d = L^2/2D$) of about 10 seconds, not unlike ejection times measured for phage λ [14](P. Grayson, personal communication). Recall, however, that this estimate is based on a value for D which is a strong *upper* bound because of all the viscous dissipation contributions that were neglected, suggesting that the actual unassisted diffusional time is likely several orders of magnitude larger than this 10 seconds estimate. Indeed, the outcome of the work presented below is that the translocation time is shortened beyond τ_d by several orders of magnitude by a combination of effects dominated by pressure in the capsid and binding particles in the external solution. This simple estimate provides us with an interesting insight into the dissipation mechanisms. It brings forth two possibilities: 1) The friction of water (and hence, dissipation) is much larger at such short length scales or 2) as mentioned above, there are several other dissipation mechanisms which are not taken into account. It is hence a useful pointer towards the dissipation mechanism(s) during DNA ejection from phage.

The outline of this chapter is as follows. In the next section we include the effect of capsid pressure by formulating a Fokker-Planck description of translocation driven by a combination of diffusion and spatially varying force, i.e., a force pushing the chain from one side that depends on the length of chain remaining on that side (corresponding to the portion still in the capsid and hence experiencing stress due to crowding and bending). We evaluate the mean-first-passage-time (MFPT) for translocation of an arbitrary length and thereby calculate the length ejected as a

function of time using estimates of the spatially-varying ejection force from recent theories of phage packaging energetics. We find that the translocation times are 2 to 3 orders of magnitude faster than the diffusional time. We also treat the case of ejection into a volume comparable to the capsid size (mimicking, say, studies in which phage are made to eject into small vesicles that have been reconstituted with receptor protein [15, 102]) and find the ejection time dependence on the relative sizes of the phage capsid and the vesicle. In Section 4.4 we treat the further speed-up in translocation due to ideal ratcheting and reversible particle binding. We find that the simple ratcheting effect is small compared to that arising from the entropic force of reversible particle binding. The effect of reversible particle binding decreases the translocation time by another order of magnitude beyond that due to capsid pressure effects. We conclude in Section 4.5 with a discussion of related work by others, of additional contributions to ejection dynamics that will be studied in future theoretical work (in particular, the effect of RNA polymerase acting on the ejected DNA), and of experiments planned to test the various predictions made in the present work.

4.2 Various Mechanisms for Genome Injection

From an experimental perspective, it has been argued that there are a variety of mechanisms by which phage either passively push their genomes into the host cell or, alternatively, have it actively pulled into the cell [40, 16, 95, 103]. While the ejection in many phages like T4 and λ occurs in a single step, the ejection in other phages like T5 and $\phi 29$ occurs in more than one step with different ejection mechanisms operative in each step. The aim of this section is to provide an overview of the *in vitro* and *in vivo* studies on the ejection mechanisms in different phages.

4.2.1 *In vitro* Studies of Ejection Kinetics

The DNA ejection in λ and T5 phages is triggered by an outer membrane receptor protein that can be isolated. The receptor protein maintains its viability even if suspended in free solution or incorporated into liposomes, i.e., it triggers the DNA ejection from the corresponding phage even under such conditions [14]. This makes it possible to study the *in vitro* ejection behavior of these phages. Most other phages, on the other hand, have their ejection triggered by certain polysaccharides. These polysaccharides change their structure upon isolation, thus rendering them incapable of initiating the DNA ejection. This is the main reason why *in vitro* studies of the DNA ejection process from virions have been restricted to λ and $T5$ [103].

First, we consider the case of bacteriophage λ. In the experiment performed by Novick et al. [14], phage λ was suspended in a solution containing 10 mM $MgCl_2$ in the presence of vesicles reconstituted with LamB, the outer membrane receptor protein that triggers λ phage ejection. The λ phage attaches irreversibly to the vesicle with the help of LamB and injects its complete genome into

the vesicle. The vesicle is filled with a dye called Ethidium Bromide which fluoresces upon binding to the DNA. The saturation in the observed fluorescence was obtained in about a minute, which was concluded to be the ejection time. In its fully packed configuration, at this salt concentration, phage λ has an internal force of the order 10 pN on its genome [61, 28]. Since there is nothing else to bolster the injection, it is reasonable to assume that the DNA is passively ejected from the capsid into the vesicle as a result of the internal force, which biases the diffusive motion of the DNA through the phage tail. Though this experiment is extremely elegant, it must be pointed out that there are some problems in interpreting the results. It was pointed out by P. Grayson (personal communication) that the amount of Ethidium Bromide in the vesicles was insufficient to fully bind to the total DNA length of the phage, as a result of which, it is not possible to interpret the data as an unambiguous measure of ejection time. On the other hand, elegant single phage experiments conducted by P. Grayson in our lab have shown that under similar salt conditions, λ ejects its complete genome is around $10 - 15$ seconds.

The interaction of T5 virions with their receptor, FhuA, causes rapid ejection of the phage genome *in vitro* [15]. If FhuA is incorporated into lipsomes, the amount of DNA translocated from the phage head into the liposome interior is dependent on its volume. This is consistent with the idea that the forces in the phage virion drive DNA ejection until the resistive forces from the DNA already inserted into the liposome are balanced. Also, individual T5 phage have been observed by Mangenot et al. [104] to eject DNA at an extremely high rate of around 75kb/s. A fraction of the genomes ejected paused at distinct regions, which correlate well with sites of the major single-strand nicks on the T5 genome. The nicks supposedly provide an energetic barrier to the *in vitro* DNA ejection process.

4.2.2 *In vivo* Ejection Studies

The DNA ejection in phage λ occurs in a single step at a rate of around 0.5kb/s. The DNA ejection is supposedly effected by the internal pressure in the phage capsid. On the other hand, it was seen in the previous chapter that only 60% of the phage genome is ejected at around 3atm, the approximate osmotic pressure in the bacterial cell. This would mean that some other mechanism should aid the phage to eject the DNA into the cell. Unfortunately, the presence of such a mechanism has not been experimentally demonstrated.

In the case of T4, the phage adsorbs onto the bacterial membrane and binds to its receptor lipopolysaccharide, which triggers a contraction of the tail. The tail contraction helps puncture the outer membrane and brings its tip close to the cytoplasmic membrane [39, 105]. The 172 kbp DNA then crosses the membrane in about 30 seconds at 37 °C through a phage protein gp5, which forms a voltage gated channel across the membrane [40]. This represents an extremely high rate if around 6 kb/s, observed for DNA transport, and is significantly faster than if effected by enzymes [40].

Also, since the normal transcription times for the RNAP are of the order of minutes [27], 30 seconds seems to leave insufficient time for the enzymes to mediate infection. Further, it has been found experimentally that the phage does not internalize its DNA in the absence of a potential difference across the membrane [40]. This observation led to the speculation that the DNA injection is caused by the membrane potential. However, it was subsequently shown that the voltage serves to open the voltage-gated channel formed by the phage protein. Hence, it appears that DNA ejection in the T4 phage is governed by the tight internal packing of the DNA inside the capsid, resulting in a driving force tied to the free energy release when the DNA is liberated from the capsid.

Injection in the case of phage T7 is more complicated. T7 has a genome of about 40 kbp, and its capsid is icosahedral with a diameter of around 60 nm. It has an inner cylindrical core of about 28 nm $\times$ 10 nm formed of three proteins. Experimental data on T7 suggests that this phage first binds to the bacterial outer membrane. A signal is then passed through the phage tail and it releases some proteins from the capsid. This in turn triggers ejection of the cylindrical core, which penetrates the bacterial membrane and forms a channel for injection of the DNA. The internalization of the phage DNA is based upon a tripartite mechanism. First 850 bp of DNA, which has promoters for the *E. coli* RNA polymerase (RNAP), gets ejected by a proton motive force. The transcription due to the bacterial RNAP pulls out another 7 kbp of the phage DNA and leads to the manufacturing of T7 RNAP. The exposed DNA has promoters for T7 RNAP. The T7 RNAP then binds onto these promoters and internalizes the remaining DNA into the bacterial cell. The total time of injection for wild-type T7 is around 10 minutes at 30 °C [16, 106].

Phage T5 presents yet another example of the richness of the infection mechanisms adopted by bacteriophage. In this case, the genome length is roughly 86 kbp. As noted above, the phage binds to a cell surface receptor FhuA, which triggers the DNA ejection. The ejection process in T5 occurs in two steps. The first step transfer (FST), which involves 8% of the total DNA, is thought to be effected by the internal pressure. After the first step there is a pause for about 4 minutes (at 37 °C) during which time the proteins encoded by this part of the DNA are synthesized. Two of the proteins (A1 and A2) then transfer the remaining 92% DNA during a process called second step transfer (SST). The pause of 4 minutes is believed due to the fact that the FST DNA forms stem-and-loop structures that can jam the DNA and thus protect the viral DNA from the bacterial restriction system [40].

The ejection in $\phi 29$ phage is argued to be accomplished by the following two step process [95]. In the first step, about 65% of the DNA is injected into the cell, most likely by the high pressure inside the $\phi 29$ capsid [95, 11]. The genes associated with the first part of the ejected DNA are used to manufacture proteins and at least one protein, $P17$, participates in the molecular machinery that pulls the remaining DNA inside the bacterial cell [95]. The total time for the entire process is observed to be around half an hour.

Phage	Hypothesized Mechanism	Genome Length (kbp)	Ejection Time (sec)	Ejection Rate (kbp/sec)
λ	Pressure	48.5	60	0.8
T4	Pressure	169	30	5.6
T7	Enzyme	40	600[1]	0.06
T5	Pressure+Protein	121	360[2]	0.3
ϕ29	Pressure+Enzyme	19	1800	0.05

Table 4.1: Tabulation of different types of ejection behavior in different phages and their *average* rates of ejection. It can be seen that the phages show different types ejection mechanism, and a wide variation in the average ejection rates.

We thus have seen that the ejection behavior in bacteriophage follow a rich behavior pattern. A compilation of the rates and hypothesized mechanisms for different phages is made in Table. 4.1.

4.3 Kinetics of Ejection Driven by Packaging Force

As discussed in Section 5.1, we focus here on a chain which has been confined in a viral capsid and which is ejected from it through a hollow tail just big enough to accommodate its diameter. To elucidate the essentials of this ejection process we describe the translocation of the chain as a "diffusion-in-a-field" problem [108, 109, 110]. In the present case, involving the translocation of a linear polymer along its length, the diffusion coordinate is a scalar, i.e., the length of chain x that has been ejected from the tail of the virus. The external field is described by the potential energy $U(x)$ that gives rise to the force $F(x) = -dU(x)/dx$, pushing on the chain when a length x of it has been ejected. This force is due to the remaining chain length $L - x$ being confined inside the capsid and thereby subjected to strong self-repulsion ($U_{\rm rep}$) and bending ($U_{\rm bend}$). The corresponding potential $U(x) = U_{\rm rep}(L-x) + U_{\rm bend}(L-x)$ is the free energy calculated in recent theories of DNA packaging in viral capsids [61, 58, 28]. This energy is seen to decrease dramatically as ejection proceeds (i.e., as x increases), and so does the magnitude of its slope that constitutes the driving force for ejection.

One-dimensional dynamics of a diffusing particle in the presence of an external field is a classic problem in stochastic processes [111], and, as argued above, can be tailored to treat the translocation of phage DNA under the action of an ejection force $F(x) = -dU(x)/dx$. Accordingly, the probability $p(x,t)$ of finding a length x ejected at time t is given by the Fokker-Planck equation is

$$\frac{\partial p(x,t)}{\partial t} = \frac{\partial}{\partial x}\left(D\frac{\partial p(x,t)}{\partial x} + \frac{D}{k_B T}\frac{\partial U(x)}{\partial x}p(x,t)\right). \tag{4.3}$$

As part of this stochastic description of the translocation-under-a-force process, it is natural to define a mean-first-passage-time (MFPT), $t(x)$, that gives the average time it takes for a length x to be

ejected in the presence of the external field $U(x)$, namely [112]

$$t(x) = \frac{1}{D}\int_0^x dx_1 \exp\left(-\frac{U(x_1)}{k_BT}\right)\int_{x_1}^x dx_2 \exp\left(\frac{U(x_2)}{k_BT}\right). \tag{4.4}$$

It is useful to consider several limits of this general equation, the first corresponding to the familiar case of no external field. From $U \equiv 0$ the integrals in MFPT reduce trivially to $x^2/2D$, giving the expected diffusion time, $t(x) = x^2/2D$.

For the case of *constant* force, i.e., $U = -Fx + \text{constant}$, the integrals in MFPT can also be evaluated analytically, giving [99]

$$t_{\text{ConstantForce}}(x) = \frac{x^2}{D}\frac{\exp[-\beta Fx] + \beta Fx - 1}{(\beta Fx)^2}. \tag{4.5}$$

Here we have written β for $1/k_BT$ and taken $F = -dU(x)/dx > 0$ to denote the constant force *driving* translocation of the chain to the right (see Fig. 4.1). In Section 4.4 we will apply Eq. 4.5 *locally*, over each segment of length s associated with a binding site, to calculate the ideal ratcheting corrections to force-driven translocation. Note that simple and ratcheted diffusion are overwhelmed by force-driven translocation when $\beta FL \gg 1$ and $\beta Fs \gg 1$, respectively.

In the most general instance of spatially varying "external" field $U(x)$, as in the case of capsid-pressure-driven translocation, the integrals in Eq. 4.4 must be evaluated numerically. In this way we calculate $t(x)$ from Eq. 4.4 for the $U(x)$ determined from a recent treatment [61, 28] of the packaging energetics in phage capsids. This provides a one-to-one correspondence between each successive time $t(x)$ and the fraction of chain ejected $x(t)/L$ at that instant.

In Purohit *et al.* [61, 28] the DNA inside the phage capsid is assumed to be organized in a hexagonally packed inverse-spool. The potential $U(x)$ is expressed as a combination of the bending energy and the repulsive interaction between the DNA strands and is given by

$$\begin{aligned} U(x) &= U_{\text{rep}}(L-x) + U_{\text{bend}}(L-x) \\ &= \sqrt{3}F_0(L-x)(c^2+cd)\exp(-d/c) \\ &\quad + \frac{2\pi k_bT\xi}{\sqrt{3}d}\int_{R_{\text{in}}}^{R_{\text{out}}}\frac{N(r)}{r}dr. \end{aligned} \tag{4.6}$$

F_0 and c are experimentally determined constants [47] describing the interaction between neighboring DNA strands, ξ is the persistence length of DNA, d is the inter-strand spacing, R_{out} and R_{in} are the radius of the capsid and the inner radius of the DNA spool, respectively, and $N(r)$ is the number of hoops of DNA at a distance r from the spool axis. We are interested in finding the internal force on the phage genome as a function of genome length inside the capsid. We do so using Eq. 4.6 and simple geometrical constraints on the phage genome inside the capsid. The number of loops $N(r)$ in

Eq. 4.6 is given by $z(r)/d$, where $z(r) = (R_{\rm out}^2 - r^2)^{1/2}$ is the height of the capsid at distance r from the central axis of the DNA spool. The actual volume available for the DNA – $V(R_{\rm in}, R_{\rm out})$ – can be related to the genome length $L-x$ in the capsid and the inter-strand spacing d, giving an expression for $R_{\rm in}$ in terms of d, $R_{\rm out}$, and $L-x$. This relation can be substituted for $R_{\rm in}$ in Eq. 4.6, which then can be minimized with respect to d to give the equilibrium inter-strand spacing as a function of the genome length $L-x$ inside the capsid. In this way we determine the total packing energy as a function of genome length inside the capsid $(L-x)$ or as a function of the DNA length ejected x, i.e., $U(x)$. Using this result and Eq. 4.4 we can evaluate the MFPT, $t(x)$, for the DNA ejection in λ as a function of the length ejected. The corresponding fraction ejected, $x(t)/L$, is shown as a function of time in Fig. 4.2 with the label "no confinement".

The value of D can be estimated on the basis of this simple model by the following procedure. The experiment by Novick and Baldeschwieler [14] showed that in a buffer containing 10 mM of Mg^{+2} it took roughly 50 seconds for phage λ to completely eject its genome. The values for F_0 and c in buffers containing Mg^{2+} have been measured [47]. Since the values measured for 5mM and 25mM Mg^{2+} were not significantly different, we assume that the forces at 10mM will be identical, i.e., $F_0 = 12000$ pN/nm^2 and $c = 0.3$ nm. Using these values in Eq. 4.4 and numerically evaluating it for $x = L = 48500 \times 0.34$ nm we find the total time for λ to eject its genome of 48.5 kbp is $t \approx (10^5 \text{nm}^2/\text{D})$seconds. Then, since this value is experimentally estimated to be around 50 seconds [14], we infer that $D \approx 10^3 \text{nm}^2/\text{s}$. This is about 3 orders of magnitude smaller than the D estimated in Section 5.1, consistent with all the sources of dissipation that were left out of that estimate. Recent experiments on λ at the single phage level (P. Grayson, in progress) give ejection time of $10-15$ seconds. Hence, our estimate of D using the ejection time of 50 seconds [14] is fairly compatible with the more accurate single phage experiments. It should also be noted that D was the only unknown parameter in our model. With this estimate of D we are are left with no unknown parameters and are ready to make independent estimates.

An interesting application of our estimates is to the experiments in which viruses eject their DNA into lipid vesicles [40, 14, 15, 113]. Here lipid vesicles are reconstituted with the receptors recognized by the phage of interest and then mixed with a solution of the phage. The phage binds to the receptor and ejects its DNA into the vesicle. We argue that the amount of DNA ejected into the vesicle and the corresponding time depend on the radius of the vesicle. In particular, if the vesicle has a radius comparable to that of the viral capsid, there will be a build-up of pressure inside the vesicle due to the ejected DNA. Ultimately, the ejection process will come to a halt when the force on the DNA from the capsid equals the force from the vesicle side – this can be thought of similarly from the free energy perspective as a free energy minimizing configuration. Hence, the ejection will not, in general, be complete.

We can work out the ejection rate for this process as follows. If x is the length of genome ejected

into the vesicle, we denote the free energies of the DNA inside the viral capsid and the vesicle by $U_{\rm capsid}(L-x)$ and $U_{\rm vesicle}(x)$, respectively. The total free energy will be given by

$$U(x) = U_{\rm capsid}(L-x) + U_{\rm vesicle}(x). \tag{4.7}$$

As explained before, we already know $U_{\rm capsid}(L-x)$ (see Eq. 4.6); the expression for $U_{\rm vesicle}(x)$ can be obtained similarly by assuming that the vesicle is like a spherical capsid and that the DNA configuration inside is similar to that inside the viral capsid. Our assumed structure for the DNA in the vesicle is a highly idealized model, though we note that electron microscopy on such vesicles demonstrates that DNA within them can adapt highly ordered configurations [15]. In the limit where the vesicle radius is large compared to that of the phage capsid, we will recover the free injection result (DNA ejecting from phage into the surrounding solution).

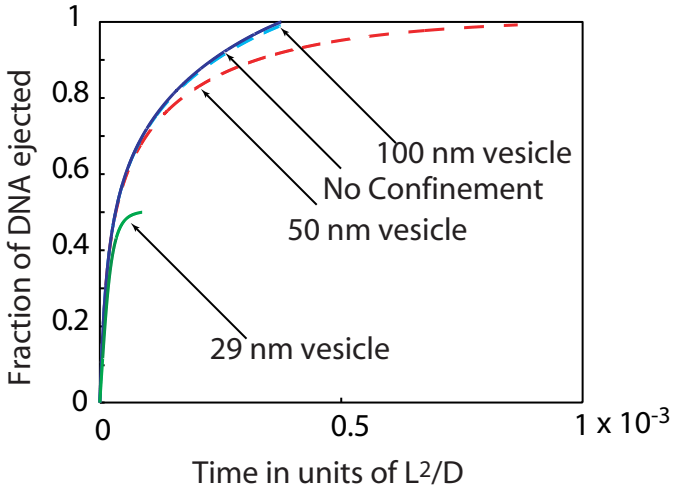

Figure 4.2: Ejection time for phage-λ injecting its genome into vesicles of radius 29, 50, and 100 nm. The capsid radius of the phage is 29 nm. It can be seen that the amount of DNA injection increases as the ratio of the vesicle radius to the capsid radius increases. On the time scale depicted here, there will be essentially no ejection due to pure diffusion (which takes place instead at times of order one in units of L^2/D).

The injection process will stop when the total free energy reaches a minimum, i.e., the total force on the DNA is zero. The time for DNA injection is given by Eq. 4.4. We have worked out the kinetics of the ejection for the bacteriophage λ (radius $\approx$ 29 nm) ejecting its genome into vesicles of radius $29, 50$, and 100 nm. The phage is taken to be suspended in a solution of Mg^{+2} ions, and similarly the vesicle, with concentration that approximately gives the same values for F_0 and c as discussed earlier. This yields a prediction for the kinetics of injection for different vesicle radii. It can be seen from Fig. 4.2 that when the size of the vesicle is comparable to the capsid size there is only a partial ejection of the DNA. When the vesicle size is almost twice the size of the capsid,

nearly the entire genome is ejected, except for the last part of the DNA, which takes "extra" time because of the resistance offered to it from the DNA inside the vesicle. Finally, when the vesicle is more than three times the size of the capsid, DNA gets completely ejected from the phage capsid as if there were no vesicle. It is interesting to note that in the initial stages of ejection all the curves for various vesicle sizes fall on one another because there is no resistance to the injection, but as the ejection proceeds each curve reflects a different resistance.

It is also possible that the arguments given above for *in vitro* ejection into vesicles could be relevant to thinking about ejection into the crowded environment of a bacterial cell [114, 115]. As a result of the crowding within the host bacterium, the viral DNA may be subject to confinement effects like those induced by vesicles.

4.4 DNA Ejection in the Presence of DNA Binding Proteins

The *E. coli* cell has as many as 250 types of DNA binding proteins [116]. Some fraction of these proteins likely bind either specifically or non-specifically to the phage genome as it enters the host bacterium. Accordingly, we consider what happens if the phage DNA is swarmed with binding proteins upon its entry into the host cell. Depending on the binding on/off rates, binding site density, and the strength of binding, we have a corresponding speed-up of the DNA injection into the bacterial cell. In this section we explore this effect and see how, in addition to the speed-up, it helps the phage inject its DNA against the osmotic pressure in the host cell.

Throughout the following analysis of particle binding effects, we assume that the chain is stiff on length scales (e.g. tens of nanometers for double-stranded DNA genomes) large compared to the size of the relevant binding particles (typically a few nanometers). We also assume that the binding particles are comparable in size to the distance between sites; for an estimate of Langmuir forces in the more general case of larger binding particles, see [101].

4.4.1 DNA Ejection due to the Ratchet Action.

Consider a scenario (as discussed in Section 5.1; $\tau_{\rm occ} \ll \tau_0 \ll \tau_{\rm unocc}$) in which host cell binding proteins *irreversibly* bind on to the DNA at a rate much faster than the translocation rate. In such a case, once a binding site is inside the cell, it is immediately occupied by a binding protein. If the protein stays bound long enough, compared to the translocation time, it will prevent thermal fluctuations from retracting the DNA back into the capsid. As a result, the DNA will diffuse only between consecutive binding sites instead of along its complete length. Depending on the spacing between the consecutive sites, it will bring about a speed-up in the translocation compared to when it is only force-driven [99].

For simplicity, we assume that the protein binding sites are uniformly distributed along the

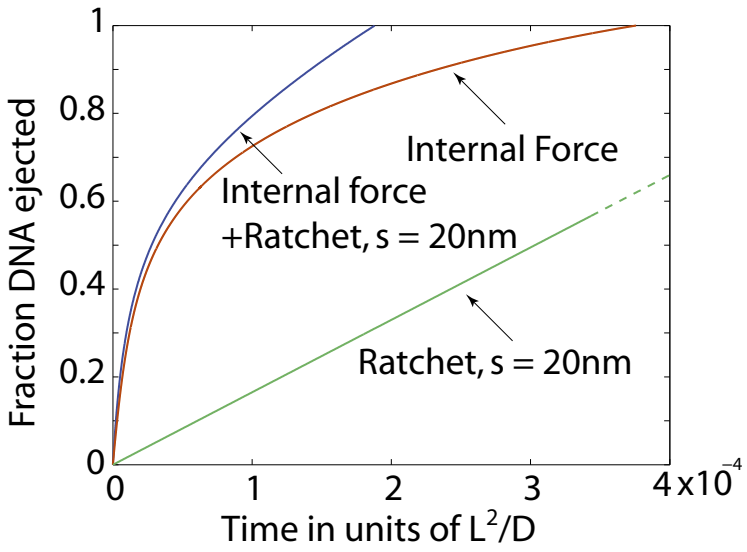

Figure 4.3: The fraction of DNA injected in phage λ as a function of time (in units of L^2/D) in the presence of binding particles that form a ratchet. The DNA injection purely due to the internal force is used as a benchmark, and the spacing between the binding sites $s = 20$ nm. It can be seen that the ratchet reduces the translocation time. The time required to internalize the genome solely by the ratcheting mechanism (see lower, straight line) is around twice the time taken for the purely internal force-driven mechanism.

length of the genome. If the distance between the consecutive binding sites, s, is small compared to genome length, i.e., $L \gg s$, we can assume that the internal force on the genome due to the packaged DNA is effectively constant, while the DNA chain is diffusing between the binding sites. In that case the MFPT, t_i, for the DNA to translocate the distance s between the binding sites $i-1$ and i is simply given by Eq. 4.5, with x replaced by s and F replaced by F_i. The internal force F is of course a varying function of ejected length x, but to a good approximation is constant over each interval of length s. The subscript i on the force F denotes this approximately constant force on the DNA chain when the translocation is taking place between the $i-1$ and i^{th} binding sites, i.e., when length $(i-1)s$ has been ejected.

The total translocation time for ejecting length x of the DNA is given by a sum over the MFPTs for all the sections of length s along the length x ejected. The MFPT as a function of x is given by

$$t(x)_{\text{Ratchet}+U(x)} = \sum_{i=1}^{x/s} t_i(F_i) \Big|_{\text{Eq. 4.5}}. \tag{4.8}$$

The corresponding plot for the fraction ejected, $x(t)/L$, as a function of time is shown in Fig. 4.3 for $s = 20$ nm: the ratcheting reduces the injection time by half as compared to when the ejection results exclusively from the internal force. From Eq. 4.5 it can be seen that the time will decrease exponentially as the spacing s decreases, but since s can not be smaller than the size of the binding

proteins, which is of the order of 10 nm, we have a lower bound on s. The important *qualitative* consequence of the ratchet will be seen (see Section 4.4.3) to be its helping with internalization of the complete phage genome against osmotic pressure when internal force alone is insufficient to carry it out.

4.4.2 Reversible Force From the Binding Proteins

Consider another extreme scenario (as discussed in Section 5.1; $\tau_{\rm occ}, \tau_{\rm unocc} \ll \tau_0$) where DNA injects into a reservoir of binding particles and the rate of translocation is slow compared to the time required for the particles to bind and unbind from the DNA. In this case, the binding proteins will come to equilibrium with the DNA. If in addition, the range of attraction, δ, of the binding sites with the proteins is comparable to the spacing s between the binding sites, there will be an adsorption force *pulling* on the DNA, given by [100](P. G. de Gennes, personal communication. Also, see Section 5.1),

$$\begin{aligned} F &= \frac{k_B T}{s} \ln \left\{ 1 + \exp\left(\frac{\epsilon + \mu}{k_B T} \right) \right\}. \\ &\approx \frac{\Delta G}{s}, \Delta G \gg k_B T. \end{aligned} \tag{4.9}$$

Here μ is the chemical potential maintained by the reservoir of binding proteins, ϵ is the binding energy of the proteins with the DNA, and $\epsilon + \mu = \Delta G (> 0)$ is the binding free energy for the proteins. This adsorption force is the 1D Langmuir pressure discussed in Section 5.1. The origin of this equation can be seen by a simple derivation [117]. Consider a stiff DNA segment of length l with binding sites seperated by spacing s. The total number of binding sites on the piece of DNA is, hence, $l/s = M$. The DNA is surrounded by binding proteins at chemical potential μ. The number of proteins that can bind to the DNA can vary from 0 to $l/s = M$. The grand partition function of the DNA and binding-proteins system is given by

$$\begin{aligned} \Xi &= \sum_{i=0}^{M} \frac{M!}{i!(M-i)!} \exp\left(\frac{i\epsilon + \mu}{k_B T} \right), \\ &= \left[1 + \exp\left(\frac{\epsilon + \mu}{k_B T} \right) \right]^M. \end{aligned} \tag{4.10}$$

The grand free energy is

$$G = -k_B T \ln \Xi = -M k_B T \ln \left[1 + \exp\left(\frac{\epsilon + \mu}{k_B T} \right) \right].$$

The force acting on the DNA will be given by

$$\begin{aligned} F &= -\frac{\partial G}{\partial l}, \\ &= -\frac{1}{s}\frac{\partial G}{\partial M}, \\ &= \frac{k_B T}{s} \ln\left[1 + \exp\left(\frac{\epsilon + \mu}{k_B T}\right)\right]. \end{aligned}$$

In the limit, where $\epsilon + \mu = \Delta G \gg k_B T$, we recover back Eq. 4.9 for the force. It may be noted that this is not the same as the ratcheting case because of the different time-scales (as noted in Section 5.1) involved in the two processes [101]. Even though $\Delta G \gg 0$, in this case we have $\tau_0 \gg \tau_{\rm occ}, \tau_{\rm unocc}$, which is different than when the ratcheting occurs ($\tau_{\rm occ} \gg \tau_0 \gg \tau_{\rm unocc}$). The langmuir force is a physical force acting on the DNA as opposed to the Brownian ratchet, which results only in the rectification of the motion.

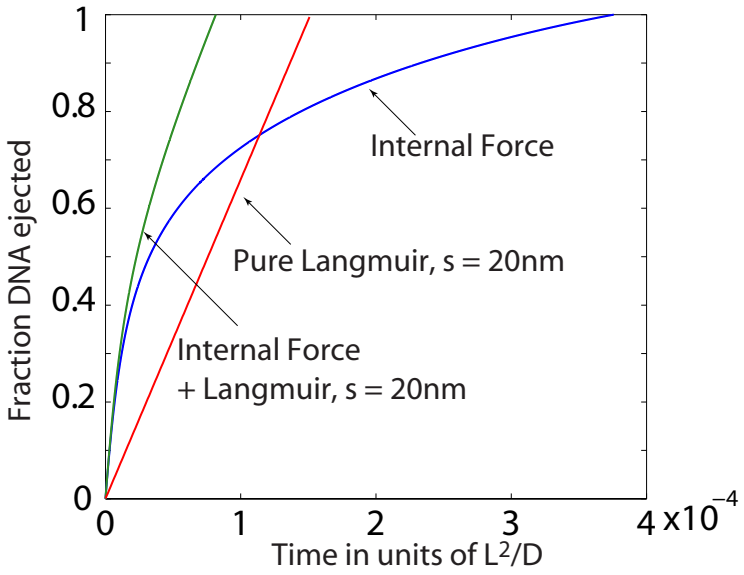

Figure 4.4: The fraction of DNA injected in phage λ in the presence of binding proteins that bind reversibly, as a function of time (in units of L^2/D.) The presence of reversible binding proteins result in a pulling Langmuir force (see text). This pulling force significantly enhances the DNA ejection rate over that of the purely force-driven mechanism, by almost a factor of ten.

In order to evaluate the MFPT we follow exactly the same process as in Section 4.3. The total force acting on the DNA is the sum of the internal pushing force and the external pulling Langmuir force. The total free energy involved with these two effects is given by $U(x) = U_{\rm capsid}(L - x) + \Delta G/s \times x$. The MFPT ($t(x)$) to inject x amount of DNA is then given by Eq. 4.4. We take a typical value of non-specific DNA-protein binding free-energy of $\Delta G = 8 k_B T$ [118]. The plot of DNA fraction ejected x/L against the corresponding ejection time $t(x)$ for $s = 20$ nm is shown in

Fig. 4.4. It can be seen that the Langmuir force speeds up the genome translocation by almost an order of magnitude. Not only that, but even if we do not have an internal force, this mechanism (see "Pure Langmuir" in Fig. 4.4) will inject the complete genome faster than the internal force-driven mechanism. This is because after about 50% ejection the internal force begins to drop below the constant value of the Langmuir force. Indeed, from Fig. 4.4, we see that it is at an ejected fraction of about 0.5 that the slope of the "Internal Force" curve drops below the constant slope (rate) of the "Pure Langmuir" plot.

The two cases we described are really two extreme cases for the DNA binding proteins. In reality the rate of binding and the equilibration times may not be very fast (compared to translocation times), and the translocation rates would lie somewhere in between the rates evaluated in this section; for these cases it is necessary to treat the dynamical coupling between particle binding and chain diffusion [100].

4.4.3 Binding Proteins Enable DNA Ejection Against Osmotic Pressure

Due to macromolecular crowding [114], the *E. coli* bacterium has internal osmotic pressures of about 3 atm [53]. The work of Evilevitch *et al.* [12] showed that for phage λ the ejection process can be partially/completely inhibited by an application of osmotic pressure. Hence, it appears that if the phage were to rely entirely on the driving force due to the packaged DNA to eject its genome, the time scale for full ejection would be prohibitively long. On the other hand, since we know that the genome *is* completely internalized, it seems likely that the particle-binding mechanisms described above may play a key role in *in vivo* DNA translocation. In this section we will see that the task can be accomplished by the Brownian ratchet and the 1D Langmuir force mechanism discussed in the preceding Sections 4.4.1 and 4.4.2.

To see how the Brownian ratchet can internalize the genome against the osmotic pressure, we use the following procedure. If the osmotic pressure in the host cell is $\Pi_{\rm Osmotic}$, the resisting force acting on the DNA can be approximated [58, 28] by $F_{\rm osmotic} = \Pi_{\rm Osmotic}\pi R_{\rm DNA}^2$, where $R_{\rm DNA}$ is the radius of the DNA (about 1nm). For an osmotic pressure of 3 atm, the osmotic force is then estimated to be around 1 pN. We can now replace the term F in Eq. 4.5 with $F_i - F_{\rm osmotic}$ to evaluate the MFPT, t_i for the injection of the DNA segment between binding sites, $i-1$ and i. This time t_i is then summed over all i, as in Eq. 4.8, to give the time $t(x)$ and hence $x(t)/L$. This fraction is plotted in Fig. 4.5 for the case of spacing $s = 20$ nm between binding sites, and for an osmotic pressure of 3 atm.

It can be seen from the figure (bottom curve) that the time required for internalizing the genome is comparable to the time it takes for phage to inject its genome purely by the internal force when there is no osmotic pressure. The internal force for λ (data not shown) at around 50% DNA ejection is approximately 1 pN, i.e., of the order of $F_{\rm osmotic}$. It can be seen from Fig. 4.5 that the slope of the

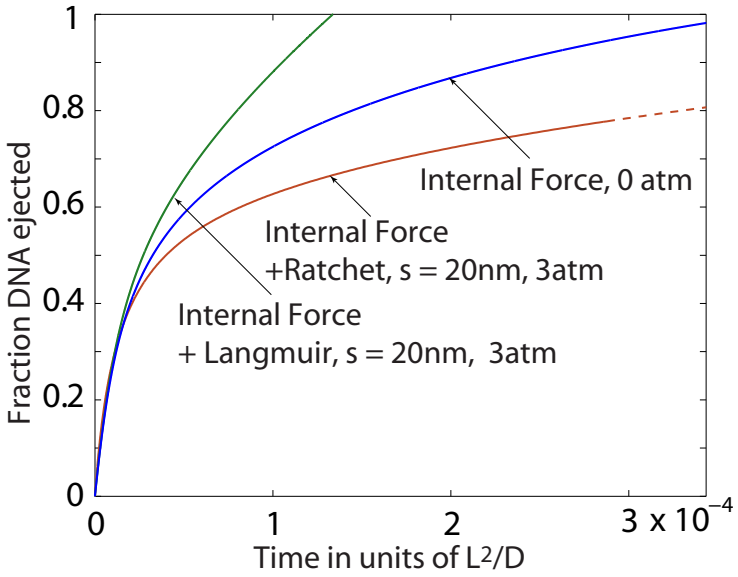

Figure 4.5: The fraction of DNA injected in phage λ as a function of time (in units of L^2/D) for the case in which there is a resistive force due to osmotic pressure. We compare the roles of the Langmuir force and the ratchet effect in ejecting the phage DNA against osmotic pressure. The spacing s is taken to be 20nm and the osmotic pressure in the cell is around 3atm. It can be seen that the Langmuir force easily pulls the DNA against this pressure. The DNA translocation by the Brownian ratchet requires a much longer time, but it still suceeds in pulling out the genome at time-scales not much longer than the ejection by internal force alone with zero osmotic pressure.

curve showing ejection in the presence of ratcheting and osmotic pressure starts decreasing at that percentage of ejection. The average force produced by a Brownian ratchet is $2k_BT/s \approx 0.4$pN for $s = 20$nm [99, 100]. At $60-70\%$ ejection the internal force is around 0.5pN; the total driving force is then approximately $0.5 + 0.4 = 0.9$ pN, which is almost the same as F_{osmotic}. This force hence works to eject the genome against the external osmotic force. When around 15% of the genome is left in the phage capsid, the internal force is almost zero. At this point there is only a small amount of the genome still to be ejected and a small differential of $F_{\text{osmotic}} - F_{\text{ratchet}} \approx 0.5$ pN to be worked against. This is accomplished by the Brownian motion of the DNA.

Now, take the case when, as discussed in Section 4.4.2, Langmuir force acts on the DNA. To include the effect of the osmotic pressure we have to subtract the osmotic force $F_{\text{osmotic}} = \Pi_{\text{Osmotic}}\pi R_{\text{DNA}}^2$ from the driving force $F_i + \Delta G/s$. The energy landscape associated with this force is simply $U(x) = U_{\text{capsid}}(L-x) + \Delta G/s \times x - \Pi_{\text{Osmotic}}\pi R_{\text{DNA}}^2 \times x$. We use this energy in Eq. 4.4 to obtain the MFPT $t(x)$. From this expression it is not too difficult to see that, so long as $(\Delta G/s - \Pi_{\text{Osmotic}}\pi R_{\text{DNA}}^2) \geq 0$, we will always have DNA ejection faster than or the same as that for the purely force driven non-osmotic pressure case. For the numbers we took in the preceding sections, $\Delta G/s = 8k_bT/s \approx 1.6pN$, which is greater than $F_{\text{osmotic}} \approx 1$pN. This implies that the phage would inject its genome faster than in the purely pressure-driven mechanism. The MFPT

$(t(x))$ is plotted in Fig. 4.5 when $s = 20\text{nm}$, $\Delta G = 8k_BT$, and $\Pi_{\text{Osmotic}} = 3\text{atm}$.

4.5 Discussion and Conclusion

This paper addresses the problem of the kinetics of phage injection and the various mechanisms responsible for it. We make use of the available experimental data, existing models for phage packaging, and classical Fokker-Planck theory to make predictions about translocation rates for phage DNA ejection. The key quantitative predictions described in this paper are:

- *Dependence of ejection rates on driving pressure.* As shown in Fig. 4.2, the driving force due to the packaged DNA speeds up the ejection process by $2-3$ orders of magnitude over free diffusion and thus is a major contributor to the process of injection. Also, in the *in vitro* setting, the smaller the vesicle into which ejection occurs, the smaller the amount of DNA injected. In addition, for genomes of the same size, the time required for the ejection of the DNA is larger than when into a bigger vesicle.

- *Dependence of ejection rates on the presence of irreversible DNA-binding proteins.* Ratcheting enhances the DNA ejection rate from the viral capsid. The speed-up is minor when compared to internal force-driven ejection (see Fig. 4.3), but as seen from Fig. 4.5 it is sufficient to pull out the genome against osmotic pressures of up to 3 atm found inside the bacterial cell.

- *Dependence of ejection rates on the presence of reversible binding proteins.* The reversible binding of proteins exerts a 1D Langmuir force on the DNA. It can be seen from Fig. 4.4 that the presence of this phenomenon significantly enhances the DNA ejection rate beyond that due to pressure in the viral capsid. From Fig. 4.5 it is clear that this force is sufficient to efficiently internalize the phage genome against osmotic pressures of up to 3 atm in the bacterium.

In bacteriophage T5 the DNA injection occurs in two steps. The first step transfer, which involves ejection of around 10% of the phage genome, is driven by the internal force [40]. There is then a brief pause when a protein is synthesized that is implicated in the degradation of the host chromosome, thereby freeing the large number of proteins that had been bound to it. These latter proteins are now available for binding to the injected portion of the phage genome and for pulling the remaining DNA into the cell via the ratcheting and Langmuir mechanisms.

Similar ideas to those proposed here might also prove useful in those cases where the viral genome is translocated as a result of the binding of motor proteins which themselves translocate along the DNA. One such example is the pulling force by the NTP-driven RNA polymerase (RNAP). RNAP is a very strong motor and can exert forces of up to 14 pN [119]. As described by Molineux and coauthors [16, 106], transcription by RNAP is the major mechanism for DNA injection from wild-type T7 into *E. Coli* and is an intriguing additional active mechanism that is of great interest to

treat theoretically as well. The calculations presented here call for a more systematic experimental analysis of the extent to which proteins bind onto phage DNA as the DNA enters the infected cell.

In this work we have analyzed various effects of DNA translocation on internal capsid pressure and "exterior" (cytoplasmic) binding proteins that can be tested by a variety of *in vitro* experiments involving phage ejection kinetics into synthetic vesicles and through membranes formed over holes in planar partitions. In these ways one can separately control the capsid pressures (by varying salt concentrations or genome length, for example) and the nature and concentration of DNA-binding proteins inside the capsid or on the other side of the membrane. In addition, it will be important to examine the role of these various mechanisms in determining the kinetics of genome delivery *in vivo*.

4.6 Appendix

4.6.1 Justification of the Expression for Steady-state First Passage Time

To measure the mean first passage time (MFPT) for a particle starting at an impenetrable wall at $x = 0$ and reach $x = L_0$, consider the following though experiment. Take an experimental system containing a large number M of non-interacting particles in a box of size L_0. Let the setup of the experiment be such that no sooner than a particle reaches L_0, it will be scooped and put back at $x = 0$. This is to ensure that the total number of particles in the box is constant, i.e., $\int_0^{L_0} p(x,t)dx = 1$. Here $p(x,t) = c(x,t)/M$ is the probability of finding a particle at position x at time t and $c(x,t)$ is the concentration of particles in the box. If t_i is the time after which a particle is seen to arrive at L_0 during the ith measurement, the mean-first passage time, by definition, will be given by

$$t_0 = \lim_{N\to\infty} \frac{\sum_{i=1}^{N} t_i}{N}, \tag{4.11}$$

where N in the denominator represents the total number of particles encountered during the time $\sum_{i=1}^{N} t_i$. Since the system is "non-driven," and the total number of particles in the system is constant, we will be into the steady state regime after some finite time t_k. Now, if we continue our measurement well beyond that time we can split the above equation as follows:

$$t_0 = \lim_{N\to\infty} \frac{\sum_{i=1}^{k} t_i + \sum_{j=k+1}^{N} t_j}{k + (N-k)} \tag{4.12}$$

Now, if we denote $\sum_{i=1}^{k} t_k$ as t, and $\sum_{i=k+1}^{N} t_i$ as T, the equation for MFPT becomes

$$\begin{aligned} t_0 &= \lim_{N\to\infty} \frac{t+aT}{k+(N-k)} && (4.13)\\ &= \lim_{N\to\infty} \frac{T}{(N-k)}\left(\frac{1+t'/T}{1+k/(N-k)}\right) && (4.14)\\ &= \lim_{N-k\to\infty} \frac{T}{(N-k)}. && (4.15) \end{aligned}$$

But the last equation is simply $1/j_0$, where j_0 is the constant steady-state flux. Thus the MFPT for a particle to start at $x = 0$, and reach $x = L_0$ is equal to the reciprocal of the steady state flux j_0.

That relation between the MFPT and the steady-state flux was a completely general result. We now wish to evaluate MFPT for the diffusion of a particle on an energy landscape $U(x)$. If we assume that this particle diffusion obeys a Fokker-Planck equation, the steady-state flux will be given by [112]

$$j_0 = -D\left(\frac{\partial p(x)}{\partial x} + \frac{1}{k_B T}\frac{\partial U(x)}{\partial x}\right). \tag{4.16}$$

This can be rewritten as

$$\frac{d}{dx}\left[p(x)\exp(\frac{U(x)}{k_B T})\right] = -\frac{j_0}{D}\exp\left(\frac{U(x)}{k_B T}\right). \tag{4.17}$$

Now, if we integrate this equation from the limits x to L_0, we will obtain

$$p(L_0)\exp\left(\frac{U(L_0)}{k_B T}\right) - p(x)\exp\left(\frac{U(x)}{k_B T}\right) = -p(x)\exp\left(\frac{U(x)}{k_B T}\right) = -\frac{j_0}{D}\int_x^{x_0}\exp\left(\frac{U(x)}{k_B T}\right). \tag{4.18}$$

We have used the fact that because we are interested in the MFPT, as described above, we absorb the particle soon as it reaches $x = L_0$, as a result of which $p(L_0) = 0$. Multiplying both sides of the above equation by $-\exp(-U(x)/k_B T)$ and integrating from 0 to L_0 we get

$$\frac{j_0}{D}\int_0^{L_0} dx \exp\left(-\frac{U(x)}{k_B T}\right)\int_x^{L_0}\exp\left(\frac{U(y)}{k_B T}\right)dy = \int_0^{L_0} p(x)dx = 1. \tag{4.19}$$

Upon rearrangement we get

$$t_0 = \frac{1}{j_0} = \frac{1}{D}\int_0^{L_0} dx \exp\left(-\frac{U(x)}{k_B T}\right)\int_x^{L_0}\exp\left(\frac{U(y)}{k_B T}\right)dy. \tag{4.20}$$

This is the precisely the equation (Eq. 4.4) used in Section 4.3 of the chapter.

4.6.2 Donnan Equilibrium Considerations When the Virus Injects DNA into the Vesicle

The difference between the vesicle and the viral capsid is that the viral capsid is permeable to the ions in the surrounding solution, while the vesicle is not. On the other hand, when we model the DNA inside the vesicle we use the same expression for the internal energy obtained from the experiments of Rau et al. [47], which essentially have free mobility of ions between the DNA condensate and the surrounding solution. How can we justify doing this? To do so we will first pretend that the vesicle is permeable to the surrounding ions. We then assume that the concentration of the ions inside the vesicle is as a result of Donnan equilibrium [120, 75] between the ions/DNA inside the vesicle and the ions in the surrounding solution. We then use a reverse process to find out what the concentration of the surroundings solution should be so that it is in equilibrium with the ions/DNA inside the vesicle, whose concentration is known.

Suppose the solute (corresponding to the experiments by Novick and Baldschwieler [14]) in the vesicle is $MgCl_2$. We first balance the chemical potentials of these ions inside the vesicle with with those in the surrounding solution. The chemical potential for the Cl^{-1} and Mg^{+2} ions inside the vesicle is given by

$$\mu_{\mathrm{Cl_I^{-1}}} = \mu^0_{\mathrm{Cl_I^{-1}}} - eV_{\mathrm{I}}[\mathrm{Cl_I^{-1}}] + \mathrm{RT}\ln\frac{[\mathrm{Cl_I^{-1}}]}{[\mathrm{Cl^{-1}}]_0} \text{ and} \tag{4.21}$$

$$\mu_{\mathrm{Mg_I^{+2}}} = \mu^0_{\mathrm{Mg_I^{+2}}} + 2eV_{\mathrm{I}}[\mathrm{Mg_I^{+2}}] + \mathrm{RT}\ln\frac{[\mathrm{Mg_I^{+2}}]}{[\mathrm{Mg^{+2}}]_0}, \tag{4.22}$$

where e is the charge of an electron, V_{I} is the effective potential inside the vesicle due to the ions, and $[\mathrm{Mg^{+2}}]_0$ and $[\mathrm{Cl^{-1}}]_0$ are the so called standard concentrations. Similar equations can be written for the ions outside the vesicle.

$$\mu_{\mathrm{Cl_O^{-1}}} = \mu^0_{\mathrm{Cl_O^{-1}}} - eV_{\mathrm{O}}[\mathrm{Cl_O^{-1}}] + \mathrm{RT}\ln\frac{[\mathrm{Cl_O^{-1}}]}{[\mathrm{Cl^{-1}}]_0}, \text{ and} \tag{4.23}$$

$$\mu_{\mathrm{Mg_O^{+2}}} = \mu^0_{\mathrm{Mg_O^{+2}}} + 2eV_{\mathrm{O}}[\mathrm{Mg_O^{+2}}] + \mathrm{RT}\ln\frac{[\mathrm{Mg_O^{+2}}]}{[\mathrm{Mg^{+2}}]_0}, \tag{4.24}$$

Since the chemical potentials of similar species are equal at equilibrium, equating Eq. 4.22 with Eq. 4.24 and Eq. 4.22 with Eq. 4.24, we obtain,

$$RT\ln[\mathrm{Cl_O^{-1}}] - \mathrm{eV_O} = RT[\mathrm{Cl_I^{-1}}] - \mathrm{eV_I} \text{ and} \tag{4.25}$$

$$RT\ln[\mathrm{Mg_O^{+2}}] + 2\mathrm{eV_O} = RT[\mathrm{Mg_I^{+2}}] + 2\mathrm{eV_I}. \tag{4.26}$$

Multiplying Eq. 4.25 and adding it to Eq. 4.26 we obtain,

$$[\mathrm{Mg}_{\mathrm{O}}^{+2}][\mathrm{Cl}_{0}^{-1}]^2 = [\mathrm{Mg}_{\mathrm{I}}^{+2}][\mathrm{Cl}_{\mathrm{I}}^{-1}]^2. \tag{4.27}$$

We also need to have charge neutrality both inside and outside the vesicle. This will give us

$$2[\mathrm{Mg}_{\mathrm{O}}^{+2}] = [\mathrm{Cl}_{\mathrm{O}}^{-1}], \tag{4.28}$$

$$z[\mathrm{DNA}] + [\mathrm{Cl}_{\mathrm{I}}^{-1}] = 2[\mathrm{Mg}_{\mathrm{I}}^{+2}]. \tag{4.29}$$

We can combine these expressions for the chemical potentials with that of the charge neutrality and get

$$4[\mathrm{Mg}_{\mathrm{O}}^{+2}]^3 = [\mathrm{Mg}_{\mathrm{I}}^{+2}](2[\mathrm{Mg}_{\mathrm{I}}^{+2}] - \mathrm{z[DNA]})^2, \tag{4.30}$$

where z is the negative charge on the DNA, which is 2 per bp. It can be seen from this equation that when the DNA concentration [DNA] is zero, there is no difference between the external and the internal concentration of the magnesium ions. When the DNA concentration increases the difference between the external and the internal concentration of the ions will increase. As a conservative estimate, we wish to find the highest possible concentration of the DNA inside the vesicle so that we get the maximum possible change in the external concentration. For that we take minimum vesicle radius 30 nm used in Section 4.3. The volume of this capsid will be 10^{-19} liters. The total charge on the 48.5 kbp λ DNA is $2 \times 48500 \sim 10^5$. Hence, the charge concentration due to the DNA in "molar units" M is $10^5/(10^{-19}N_A) \sim 2$M. Before the DNA entered into the vesicle the vesicle was charge neutral. To maintain that charge neutrality the DNA brings its own Mg^{+2} counterions with it into the vesicle. So if the concentration of Mg inside the vesicle before the entry of DNA is 10 mM, the concentration after the entry will be $z[\mathrm{DNA}]/2 + 10^{-2}$ M. Substituting this into Eq. 4.30 we obtain

$$\begin{aligned} 4[\mathrm{Mg}_{\mathrm{O}}^{+2}]^3 &= (z[\mathrm{DNA}]/2 + 10^{-2})(2(z \times [\mathrm{DNA}]/2 + 10^{-2}) - z[\mathrm{DNA}])^2\mathrm{M}^3 & (4.31) \\ \Longrightarrow [\mathrm{Mg}_{\mathrm{O}}^{+2}] &= (10^{-4}(z[\mathrm{DNA}]/2 + 10^{-2}))^{1/3}\mathrm{M}. & (4.32) \end{aligned}$$

We already evaluate the maximum value of z[DNA] and from this we find the concentration of $\mathrm{Mg}_{\mathrm{O}}^{+2}$ is approximately 50 mM. But we know from the experiments of Rau et al. [47] that within the range of 1mM-100mM for $\mathrm{Mg}_{\mathrm{O}}^{+2}$ the force measurements give almost the same results. So it would be safe to assume that vesicle is like the viral capsid and is permeable to ions (with the same salt strength in the surrounding).

Chapter 5

DNA Fluctuations in Nucleosomes

We saw in Chapter 1 that the eukaryotic genome is much longer than the characteristic size of a cell and needs to be compacted so as to fit inside the nucleus. In order to effect this compaction, the eukaryotic genome is organized into complex structures called nucleosomes, which consist of DNA tightly wrapped around four pairs of proteins called histones. In Chapter 1 we also saw that in order to perform important functions like gene expression, DNA repair, DNA replication, etc., different parts of the genome must be physically accessible to various proteins at different times. Since the eukaryotic DNA is effectively sequestered by virtue of packing within nucleosomes, at first thought it would seem that the genome is inaccessible, but it must be noted that the nucleosome is not a static structure, and it is highly possible that the genome accessibility is wrought out by the thermal fluctuations of the nucleosomal DNA involving its unwrapping and re-wrapping around the histone core. Although the *in vivo* case may be much more complicated, recent ingenious experiments [24, 22, 23] under *in vitro* conditions have demonstrated the role of these fluctuations and have measured the equilibrium constant and the rates for the DNA wrapping and the re-wrapping processes (see Fig. 1.3). In this chapter we model the DNA-histone system by taking into account the DNA bending elasticity and the DNA-histone interaction. We make predictions for the equilibrium constant associated with the wrapping and re-wrapping processes using the standard grand canonical ensemble of equilibrium statistical mechanics [26]. We also provide estimates of the DNA wrapping and re-wrapping rates using a Fokker-Planck description. In summary, we make quantitative predictions of these DNA fluctuations as a function of the length of the DNA under consideration with special reference to the probability of unwrapping the nucleosome by a given amount.

5.1 Introduction

In eukaryotic organisms the genome is organized in extremely compact structures called chromatin (see Fig. 1.2), which are themselves formed of a smaller scale structure called the nucleosome [27].

The nucleosome is built of a small piece of DNA–approximately 150 bp–wrapped around a structure that can be loosely thought of as a cylindrical disc formed of four pairs of histone proteins: H2A, H2B, H3 and H4 (see Fig. 1.2 and 5.1). There are two copies each of these four proteins, and their assembly is termed the histone core. The histone core can be modeled approximately as a cylinder of 6nm diameter with a height of around 6 nm. The DNA of around 150 bp is wrapped roughly 1.75 times around the histone core [27]. Two short pieces of approximately 50 bp each, called linker DNA, are present on either side to connect adjacent nucleosomes [27]. The radius of the DNA is around 2nm; taking that into account, the effective nucleosome diameter is the histone diameter plus the DNA thickness of 2nm and is around 10nm. In physiological conditions the persistence length of the DNA (described in Chapter 3) is around 50 nm, while the diameter of the histone core is around 10 nm. This means that the DNA is bent at length scales much shorter than its persistence length and, hence, the bending energy expended to form the nucleosome is really high. Fortunately, the energetically favorable interactions of the negatively charged DNA with the positively charged arginine and lysine residues of the histone core make up for the energy to be used up while bending the DNA to form a stable nucleosome.

We saw in Chapter 1 that the genome is segmented into a hundred to a thousand base pairs long sections called genes. Each gene has a code to synthesize various proteins that are composed of amino acids. The DNA code is converted into a messenger RNA (mRNA) code by an enzyme protein RNA polymerase (RNAP) in a process called "transcription." The mRNA code is then deciphered by transfer RNA (tRNA) to synthesize the corresponding amino acids and polymerize them to form various proteins by a process termed "translation." Thus, loosely speaking, the flow of genetic information is from DNA to mRNA to proteins. On the other hand, the real transcription process is not that straight forward. Each gene is preceded by a small segment of tens of base pairs called the promoter site, where RNAP is supposed to bind and start the mRNA transcription by translocating along the DNA. The rate of gene expression is proportional to the efficiency of the RNAP activity. The entire process of transcription, or gene expression, is regulated depending on the cellular environment. This gene regulation is effected by different regulatory proteins which bind at various places around the promoter to either enhance or suppress the activity of the RNAP. The genome is also required to be accessible to various proteins that carry on important processes like DNA replication and repair. In short, different parts of the DNA in this tightly packed nucleosome are supposed to be accessible to various proteins at different times. The question then is how do the proteins overcome the tight compaction and access the nucleosomal DNA to perform key genomic processes? It has been convincingly shown, in at least *in vitro* situations, that the nucleosomal DNA spontaneously unwraps from the histone core to transiently expose its binding sites to the corresponding proteins [24, 22, 23] and then re-wraps. This process happens constantly, and the efficiency of the protein binding depends on the times scales for unwrapping and rewrapping. In

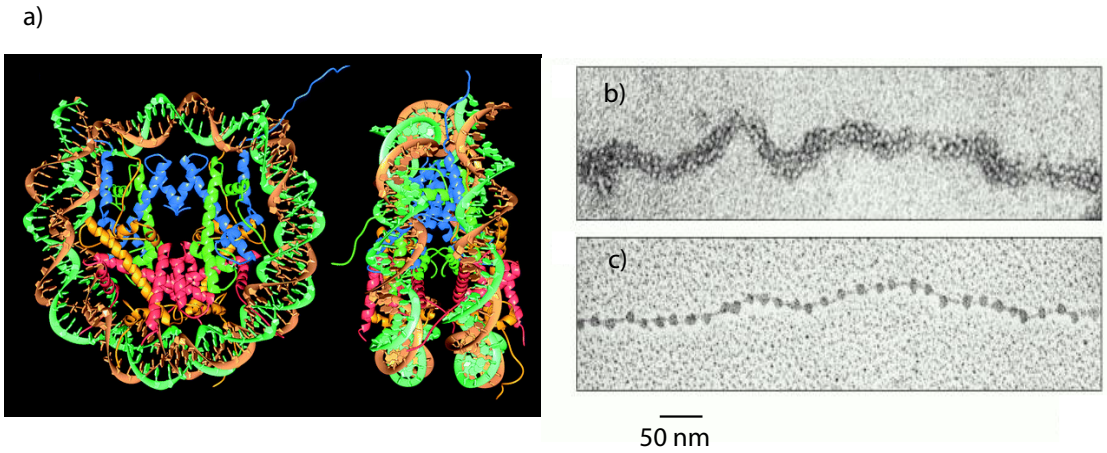

Figure 5.1: Structure of a nucleosome.a) High resolution X-ray diffraction structure of the complete nucleosome. Color-coding of proteins: H2A, orange; H2B, red; H3 blue; H4 green (figure from Luger et al. [121]. b) Electron micrograph of the condensed chromatin (figure from Alberts et al. [27].) c) Electron micrograph of chromatin that has been experimentally unpacked, or decondensed after isolation to show the nucleosomes (figure from Alberts et al. [27]).

addition to unequivocally demonstrating the feasibility of this particular mechanism of DNA access, the above mentioned experiments from Widom and co workers also measure the the rates for wrapping and rewrapping and the corresponding equilibrium constant. In this chapter we will address the measurements from these experiments and make new predictions to stimulate further experimentation.

The buried sites on the eukaryotic genome can be accessed by corresponding proteins via transient exposure of the nucleosomal DNA due to its unwrapping from the histone. The unwrapping can be effected by ATP-dependent nucleosome remodeling factors, which unwrap nucleosomal DNA, or drive nucleosomes to new locations along DNA. This mechanism, though experimentally observed, begs an explanation of how the remodeling factors know which nucleosomes to model. Similarly, increasing evidence suggests that remodeling factors are recruited to specific nucleosomes by site-specific DNA-binding proteins. This raises the question of how those DNA-biding proteins gain access to their target sites. Also, remodeling factors may not always be required to allow access to the nucleosomal DNA. Nucleosomes spontaneously undergo conformational fluctuations in which a stretch of their DNA transiently lifts off the histone surface, allowing free but transient access to proteins that would not otherwise be able to bind. The equilibrium constants describing this DNA accessibility are as large as–10^{-2} to 10^{-1} for sites located a short distance inside the nucleosome, decreasing to 10^{-4} to 10^{-5} for sites located near the middle of the nucleosome [24]. Studies by Li and Widom [22] using fluorescence resonance energy transfer (FRET) reveal that site exposure involves large increases in separation between a fluorescence donor on one end of the nucleosomal DNA and a fluorescence acceptor on the histone core (see Fig. 5.2). This implies that site exposure

occurs by progressive unwrapping of the nucleosomal DNA starting from one end of the nucleosome (see Fig. 5.2a).

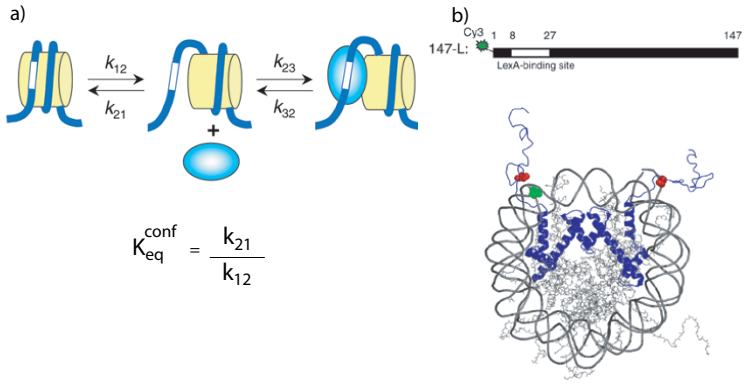

Figure 5.2: The experimental setting of Li et al. [23] addressed to by our theoretical model. a)The nucleosomal DNA undergoes transient thermal fluctuations, thereby unwrapping from the histone core and transiently exposing the binding site to the corresponding protein (LexA in this case). b) The experimental procedure by Li et al. [23] involves using a Cy3 FRET donor (green) attached to the end of the nucleosomal DNA. The binding site for LexA is situated close to the end. As can be seen, the DNA should unwrap at least 27bp to allow LexA binding. There are two Cy5 FRET acceptors (red) on two copies of H3 histone proteins (blue). When the LexA binds to the DNA the spacing between the Cy3 and Cy5 becomes large and the FRET loses efficiency. At saturating concentrations of LexA (see Section 5.2) the total FRET efficiency becomes minimally low. At such high concentrations of LexA the rate of decrease of FRET efficiency is related to the rate of LexA binding and provides the unwrapping rate k_{12} (figures from Li et al. [23]).

A consequence of this behavior of nucleosomes is that when nucleosomal DNA contains a target sequence for a site-specific DNA binding protein, the presence of the protein in the solution causes nucleosomes to respond by shifting their conformational equilibrium towards the exposed, unwrapped state. This unwrapping of the nucleosomal DNA allows stable binding by the protein. As a result a dynamic equilibrium is established between the wrapped state (W) and the unwrapped state without the binding protein (U) and between U and unwrapped state with the regulatory protein (UR) (see Fig. 5.2).

Widom and coworkers have obtained the the equilibrium constant $K_{\rm eq}^{\rm config}$ [24, 22] and the rate constants [23] for the DNA wrapping and rewrapping process shown in Fig. 5.2. We will formulate a simple model using statistical mechanics to obtain the the equilibrium constant $K_{\rm eq}^{\rm config}$ and supplement it with the Fokker-Planck equation to obtain the rate constants k_{12} and k_{21}, respectively, for the DNA unwrapping and re-wrapping. Using this simple model, we predict the equilibrium constant $K_{\rm eq}^{\rm config}$ as a function of z, the depth of the protein binding site from the edge of the DNA.

The organization of the chapter is as follows. In Section 5.2 we describe briefly the experiments we wish to address. We lay out the theoretical model in Section 5.3. We perform the required symbolic calculations in Section 5.4 and the corresponding numerical calculation in Section 5.5. We conclude the chapter with discussions and conclusions in Section 5.6.

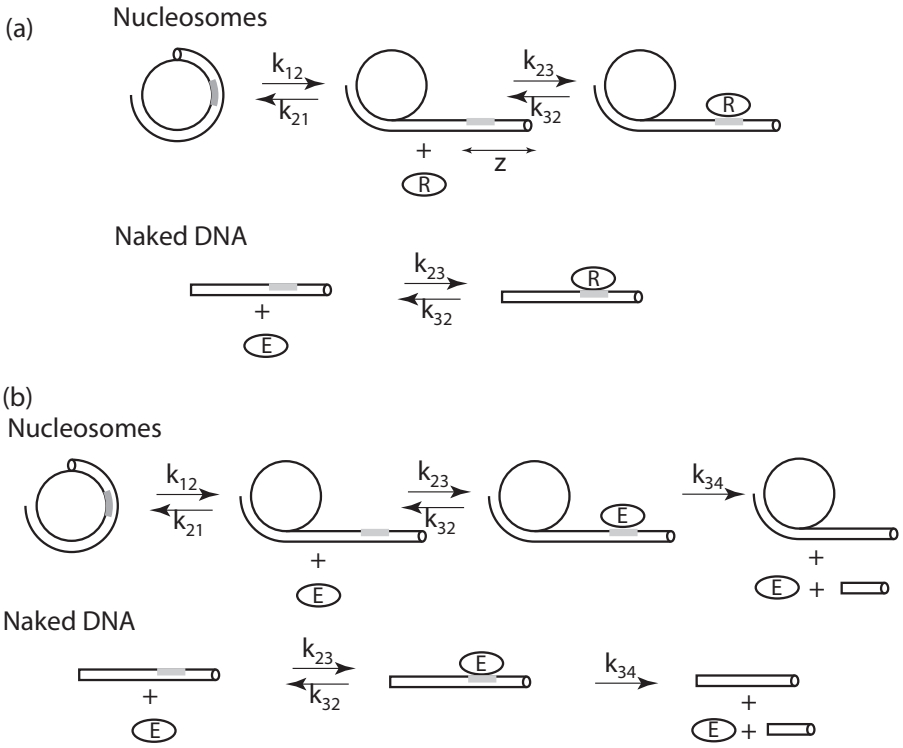

Figure 5.3: The idea behind the experiment by Polach and Widom [24] (figure adapted from Polach and Widom [24]).a) The mechanism hypothesized by Polach and Widom [24] for binding of a regulatory protein (R) to a specific DNA target sequence (gray) on the nucleosomal DNA. It was hypothesized that nucleosomes are dynamic structures, transiently exposing their DNA. In the exposed state, proteins can bind as though they were binding to naked DNA. The related rate constants are indicated. (b) In order to quantify the hypothesized equilibrium between the wrapped and the unwrapped states of the nucleosomes, Polach and Widom used a restriction enzyme binding to its recognition sequence (gray) in the place of regulatory protein (R). The restriction enzyme can catalyze the cleavage of DNA to yield detectable products. Rates of cleavage for nucleosomal DNA are compared with cleavage of naked DNA in identical solution conditions.

5.2 Brief Description of the Experiments to be Addressed

In the previous section we saw that the nucleosome is not a static structure where DNA is permanently wrapped around the histone octamer. The nucleosomal DNA undergoes spontaneous thermal fluctuations that result in its unwrapping and subsequent re-wrapping around the histone core. As mentioned earlier, we denote the unwrapped state as U and the wrapped state as W and assume that there is a dynamic equilibrium between the two states $W \underset{k_{12}}{\overset{k_{21}}{\rightleftharpoons}} U$ (also see Fig. 5.2). The rate constants k_{12} and k_{21} represent, respectively, the rate constants to switch from W to U (unwrapping) and from U to W (re-wrapping). This dynamic equilibrium between U and W gives rise to a configurational equilibrium constant $K_{\text{conf}} = (U)/(W) = k_{21}/k_{12}$ (also see Fig. 5.2). In this section we describe the two experiments performed to measure the equilibrium constant and the wrapping and rewrapping rates.

The first experiment we address is the experiment by Polach and Widom [24] that involves the measurement of $K_{\text{eq}}^{\text{config}}$ for the wrapped and unwrapped states (see Fig. 5.3). As seen in Fig. 5.3a, in the experiment by Polach and Widom [24] it is hypothesized that the nucleosomes (N) might be dynamic structures such that in the exposed state (S) regulatory proteins (R) may bind as though they were binding to the naked DNA. A simplifying assumption is made that sufficient nucleosomal DNA is exposed such that the rates and equilibria for binding to an exposed nucleosomal target sequence or to a naked DNA target is identical. With this assumption one can write down the following rate reaction:

$$N \underset{k_{12}}{\overset{k_{21}}{\rightleftharpoons}} S + R \underset{k_{23}}{\overset{k_{32}}{\rightleftharpoons}} RS, \tag{5.1}$$

for binding to a naked DNA target and

$$S + R \underset{k_{23}}{\overset{k_{32}}{\rightleftharpoons}} RS \tag{5.2}$$

for binding to a nucleosomal target. Binding of a regulatory protein to a nucleosomal target sequence will therefore occur with a net free energy change

$$\Delta G^0_{\text{net}} = \Delta G^0_{\text{conf}} + \Delta G^0_{\text{naked DNA}} \tag{5.3}$$

in which $\Delta G^0_{\text{naked DNA}}$ is the free energy change for the process shown in Eq. 5.2 and ΔG^0_{conf} is the free energy cost for site exposure. Only the value of $\Delta G^0_{\text{naked DNA}}$ was available for the experimenters, whereas the binding equilibrium is governed by ΔG^0_{net}.

If expressed in terms of equilibrium constants, a regulatory protein would bind to a nucleosomal

target sequence with an apparent binding constant (a detailed derivation in Section 5.4).

$$K_{\mathrm{d}}^{\mathrm{apparent}} = \frac{K_{\mathrm{d}}^{\text{naked DNA}}}{K_{\mathrm{eq}}^{\mathrm{conf}}}, \tag{5.4}$$

where $K_{\mathrm{d}}^{\text{naked DNA}}$ is the dissociation constant for naked DNA, which was measured in many studies prior to the current experiment, and $K_{\mathrm{eq}}^{\mathrm{conf}}$ is the equilibrium constant for the site exposure,

$$K_{\mathrm{eq}}^{\mathrm{conf}} = \exp\left(-\frac{\Delta G_{\mathrm{conf}}^{0}}{k_B T}\right). \tag{5.5}$$

The configuration equilibrium constant $K_{\mathrm{eq}}^{\mathrm{conf}}$ is expected to depend on the position of the target sequence within the nucleosome.

Polach and Widom [24] devised a sensitive assay to detect and quantify this equilibrium (see Fig. 5.3). They replaced the regulatory protein with a restriction enzyme (E), and constructed nucleosomes having a site at a known position in the particle, where the restriction enzyme (E) can bind. If the hypothesized conformational equilibrium existed, the restriction enzyme could bind and catalyze cleavage of the substrate to yield products (P) which can be detected by gel electrophoresis and quantified using a phosphorimager. Thus,

$$N \underset{k_{12}}{\overset{k_{21}}{\rightleftharpoons}} S + E \underset{k_{23}}{\overset{k_{32}}{\rightleftharpoons}} ES \overset{k_{34}}{\rightarrow} E + P \tag{5.6}$$

and

$$S + E \underset{k_{23}}{\overset{k_{32}}{\rightleftharpoons}} ES \overset{k_{34}}{\rightarrow} E + P \tag{5.7}$$

for nucleosomes and naked DNA, respectively. The kinetic analysis of the mechanisms in Eqs. 5.6 and 5.7 was performed as follows. Polach and Widom [24] experimentally monitored the loss of reactant nucleosomal DNA (D),

$$(D) = (N) + (S), \tag{5.8}$$

which dissappears according to a first order rate law with an observed rate constant k_{obs},

$$k_{\mathrm{obs}} = -\frac{1}{(D)}\frac{d(D)}{dt}. \tag{5.9}$$

They made what is called the steady-state approximation for S and ES to obtain

$$k_{\mathrm{obs}} = \frac{k_{34}(E)}{K_{\mathrm{m}}}\frac{k_{12}}{k_{12} + k_{21} + \frac{k_{34}(E)}{K_{\mathrm{m}}}} \tag{5.10}$$

with

$$K_{\rm m} = \frac{k_{32} + k_{34}}{k_{23}}. \tag{5.11}$$

This experiment obeyed a rapid confirmation pre-equilibrium limit:

$$k_{21} \gg k_{32}(E). \tag{5.12}$$

In this limit Eq. 5.10 reduces to

$$k_{\rm obs} = \frac{k_{34}(E)}{K_{\rm m}} \frac{K_{\rm eq}^{\rm conf}}{1 + K_{\rm eq}^{\rm conf}}. \tag{5.13}$$

For this experiment, $K_{\rm eq}^{\rm conf}$ is small ($\ll 1$), and the experiment was set up such that $(S) \ll K_{\rm m}$. The observed first order rate constant for the loss of reactant nucleosomal DNA (Eq. 5.13) then becomes

$$K_{\rm obs}^{\rm nucleosome} = \frac{k_{34}(E_0)}{K_{\rm m}} K_{\rm eq}^{\rm conf}. \tag{5.14}$$

Polach and Widom also performed separate experiments in which naked DNA is digested under identical conditions. The reactant naked DNA disappears with an apparent first order rate constant given by

$$K_{\rm obs}^{\rm naked\ DNA} = \frac{k_{34}(E_0)}{K_{\rm m}}. \tag{5.15}$$

Combining Eqs. 5.14 and 5.15 gives

$$K_{\rm conf}^{\rm conf} = \frac{k_{\rm obs}^{\rm nucleosome}/(E_0^{\rm nucleosome})}{k_{\rm obs}^{\rm naked\ DNA}/(E_0^{\rm naked\ DNA})}. \tag{5.16}$$

Thus, $K_{\rm conf}^{\rm conf}$ is obtained from all the experimental observables. Using this assay $K_{\rm conf}^{\rm conf}$ is obtained as a function of the depth of binding site z (see Fig. 5.3). Polach and Widom [24] obtain the values of $K_{\rm conf}^{\rm conf}$ for $z \approx 10, 45$, and 52bp. We will see in Section 5.5 that, we utilize these experimental results to obtain the free energy of binding of the DNA with the histone core.

The second experiment by Li et al. [23], which we wish to address is shown in Fig. 5.2. The experiment involved obtaining the unwrapping and rewrapping rates k_{12} and k_{21}, respectively (see Fig. 5.2). To find the rate k_{12} of the nucleosomal DNA to unwrap a length z off the histone the following strategy was used. Li et al. [23] engineered the nucleosomal DNA such that it had a binding site specific to the LexA repressor protein of *E. coli* at distance $z \approx 27$bp from one end of the DNA (see Fig. 5.2b). A donor dye Cy3 was attached to the end of the DNA, and a pair of Cy5 acceptors were fixed on the two copies of H3 histone proteins. When the nucleosomal DNA was

fully wrapped the distance between the donor Cy3 and the acceptor Cy5 was 2 nm and the FRET efficiency was very high. A very high concentration of LexA was then mixed with the nucleosomes such that the apparent rate of LexA binding to the nucleosomes k_{23}[LexA] was much larger than the rate of re-wrapping k_{21}. This step ensured that the LexA binds on to the DNA as soon as the binding site is exposed. Hence, the rate at which LexA binds on the DNA is almost equal to the rate k_{12} at which the binding site is exposed. When LexA binds to the DNA, due to steric hindrance the spacing between the donor Cy3 and the acceptor Cy5 becomes larger than 6nm, the characteristic FRET distance for Cy3-Cy5 dye pair. As a result, the FRET signal decreases at a rate almost equal to to the rate of LexA binding. By observing the rate corresponding to the decay of FRET signal, Li et al. [23] obtain the rate of LexA binding and, hence, the rate of DNA unwrapping k_{12}. To obtain the rate of rewrapping k_{21}, they utilize the value of $K_{\text{eq}}^{\text{config}}$ obtained from a previous experiment [22] performed under similar conditions and the fact that $K_{\text{eq}}^{\text{config}} = k_{12}/k_{21}$. The re-wrapping rate is, hence, $k_{21} = K_{\text{eq}}^{\text{config}}/k_{12}$. Li et al. [22] obtain k_{12} of around 4s^{-1}. The value of $K_{\text{eq}}^{\text{config}}$ under similar conditions was around 4.5×10^{-2} [22]. The re-wrapping rate, k_{21} was, hence, approximately obtained as 90s^{-1}. Li et al.also independently measure k_{12} and k_{21} using fluoresence correlation spectroscopy (FCS) and obtained their values to be around 3.6s^{-1} and 20s^{-1}, respectively. The values of rate constants obtained in this experiment corresponded to the depth of binding site, z, of around 30bp. In Section 5.3, we will obtain an expression for the rate constants with any arbitrary value of z.

5.3 Modeling the Nucleosome Unwrapping and Rewrapping process

We saw in Section 5.1 that the histone core of the nucleosome has a diameter of around 10nm. The persistence length of the DNA (see Chapter 3) in physiological salt conditions is around 50 nm. This means that the DNA has to be tightly bent around the nucleosome when it is in wrapped condition. As a result, similar to the case of bacteriophage, a significant amount of bending energy is to be paid to wrap the DNA around the nucleosome. The question now arises as to what provides the required energy? It turns out that there are favorable interactions between the negatively charged DNA and the surface of the histone, which is positively charged due to lysine and arginine residues [27]. This favorable interaction energy between the DNA and the histone core would want the DNA to be wrapped around the histone despite the high bending energy required to do so. We saw in Chapter 1 that there are around 12 contacts between the DNA and the histone. If we roughly ascribe a favorable binding free energy of $10k_BT$, a number common to such interactions (we will get better estimates in Section 5.5), to each contact, the total interaction free energy will be $F_{\text{binding}} = -100k_BT$. The

total bending energy of the fully wrapped DNA will be given by

$$F_{\text{bending}} = \frac{1}{2}\frac{\xi_p k_B T L}{R^2}, \tag{5.17}$$

where $L = 150$ bp is the total length of the DNA per nucleosome, $\xi_p = 50$ nm, and R nm is the radius of curvature of the wound DNA. The radius of the histone and the thickness of the wrapped DNA is around 3nm and 2nm, respectively. The effective radius of curvature of the DNA R is, hence, $3 + 1 = 4$nm. After substituting the required values, the bending energy of the completely wrapped nucleosome will be around $80k_BT$. The total energy of the wrapped DNA is hence $-120k_BT + 80k_BT = -40k_BT$. The negative sign shows that the binding is favorable and gives us an idea as to why it may be energetically favorable to form such a compact structure. It is mathematically convenient to convert the favorable binding energy in the units of binding energy per unit length. We represent it as γ, and $L \times \gamma = F_{\text{binding}}$. The total free energy of the nucleosome when length x of the DNA is unwrapped is given by

$$\begin{aligned} F(x) &= F_{\text{bending}}(x) + F_{\text{binding}}(x), \\ &= \frac{1}{2}\frac{\xi_p k_B T}{R^2}(L - x) + \gamma \times (L - x), \quad \text{and} \\ &= \left(\gamma + \frac{\xi_p k_B T}{2R^2}\right) \times (L - x). \end{aligned} \tag{5.18}$$

It may be noted that all of our free energies are with reference to the DNA that is completely unwrapped, with just one end (the center of the DNA for symmetry purposes) tied to the histone. We also make a somewhat bold assumption that the free energy of the DNA is linearly extensive with its length and that any loss of entropy of the DNA per unit length when it is wrapped around the histone can be absorbed into the coefficient γ. This assumption is usually valid for large systems (thermodynamic systems), but the length of DNA involved in our case is very small (150bp $\approx$ 50nm) and, hence, the linear extensivity of the free energy of the DNA with the unwrapped length is technically not perfect. Despite this shortcoming it would still be educational to see what the model has to offer.

5.4 The Equilibrium Constant and the Unwrapping and Rewrapping Rates as a Function of the Depth of the Buried Sites

In Section 5.2 we discussed briefly the experiment by Polach and Widom [24]. In this section we will formulate a model using statistical mechanics to provide us with the value of the configurational

equilibrium constant $K_{\text{eq}}^{\text{config}}$ as a function of z, the distance of the binding site from the edge of the nucleosomal DNA. To do so, consider a nucleosome with a specific binding site at a distance z from the nucleosome edge and surrounded by a reservoir of the corresponding binding proteins at chemical potential μ. We assume that the nucleosome/binding protein system has reached equilibrium. The binding protein can bind on the DNA only when the site at distance z is exposed. As discussed in Section 5.1, it was shown by Li and Widom [22] that the DNA sequentially unwraps from one end, as opposed to forming bubbles. As a result, the enumeration of the equilibrium states and, hence, the evaluation of the partition function becomes quite simple. The total number of microstates fall under two categories: (i) when the binding protein is not bound to the DNA; (ii) when the binding protein is bound to the DNA. Now, if we assume that the DNA unwraps only from one side, the amount of DNA exposed x can take values between 0 and L. Hence, the total number of possible microstates when the binding protein is not bound to the DNA is given by the values of x between 0 and L. The binding protein can bind on to the DNA only when at least z length of DNA is unwrapped. The total possible microstates when the binding protein is bound to the DNA is x between z and L. The partition function is the summation of the Boltzmann weights for all these microstates. The partition function [26] then can be written as

$$Z = \int_0^L \exp(-\bar{\alpha}(L-x))dx + \exp\left(\frac{\mu+\epsilon_{\text{bind}}}{k_BT}\right)\int_z^L \exp(-\bar{\alpha}(L-x))dx, \tag{5.19}$$

where $\bar{\alpha} = \alpha/k_BT$, $\alpha = \gamma + \xi_p k_BT/2R^2$ is as discussed in the previous section and ϵ_{bind} is the lowering of the energy when the protein binds to the binding site. The first integral in the partition function corresponds to the case when the protein isn't bound on the DNA, while the second integral corresponds to when at least length z of the DNA has unwrapped and the protein is bound on to the DNA. The extra exponential in the second integral involving sum of the chemical potential μ and the binding energy ϵ_{bind} is the effective binding free energy when the protein binds on to the DNA at $x = z$. The partition function can be easily evaluated as

$$Z = \frac{1}{\bar{\alpha}}\left(1 - \exp(-\bar{\alpha}L) + \exp\left(\frac{\mu+\epsilon_{\text{bind}}}{k_BT}\right)[1-\exp(-\bar{\alpha}(L-z))]\right). \tag{5.20}$$

The fraction of nucleosomes bound with the binding proteins is given by

$$\theta = \frac{\partial \ln Z}{\partial \mu} \quad \text{and} \tag{5.21}$$

$$= \frac{\frac{(R)}{(R_0)}\exp\left(\frac{\epsilon_{\text{bind}}}{k_BT}\right)[1-\exp(-\bar{\alpha}(L-z))]}{\left(1-\exp(-\bar{\alpha}L) + \frac{(R)}{(R_0)}\exp\left(\frac{\epsilon_{\text{bind}}}{k_BT}\right)[1-\exp(\bar{\alpha}(L-z))]\right)}. \tag{5.22}$$

We have used the standard ideal-solution result [122] that $\exp(\mu/k_BT) = (R)/(R_0)$, where, as in Section 5.2, (R) is the concentration of regulatory proteins in solution, while (R_0) is referred to as the standard concentration. As described in Section 5.2, the fraction of nucleosomes bound can also be expressed in terms of the equilibrium constant $K_{\rm d}^{\rm apparent}$, which gives the ratio of the product of concentrations of free proteins in solution (R) and unoccupied binding sites (S), to the concentration of binding sites occupied by regulatory proteins (RS):

$$K_{\rm d}^{\rm apparent} = \frac{[(N) + (S)](R)}{(RS)}. \tag{5.23}$$

The fraction of nucleosome bound by the proteins can be expressed in terms of concentrations of occupied and unoccupied sites as

$$\theta = \frac{(RS)}{(RS) + [(N) + (S)]}. \tag{5.24}$$

Using Eq. 5.23, we get

$$\theta = \frac{(R)/K_{\rm d}^{\rm apparent}}{1 + (R)/K_{\rm d}^{\rm apparent}}. \tag{5.25}$$

Comparing Eq. 5.22 with Eq. 5.25 we obtain

$$K_{\rm d}^{\rm apparent} = \frac{(R_0)}{\exp\left(\epsilon_{\rm bind}\right)} \frac{1 - \exp(-\bar{\alpha}L)}{1 - \exp(-\bar{\alpha}(L - z))}. \tag{5.26}$$

We can split this equilibrium constant into $K_{\rm naked}$ and $K_{\rm eq}^{\rm config}$, referring to the equilibrium constant just in the presence of the binding sites without the wrapping and unwrapping, and the equilibrium constant associated with simply the wrapping and unwrapping, respectively. As seen in Section 5.2 we can think of binding as occurring in two steps. The first step corresponds to a transformation of a binding site which is hidden by the presence of the histone to one that is exposed due to DNA unwinding. Since the concentration of exposed sites is (S), the equilibrium constant for this process is

$$\begin{aligned} K_{\rm eq}^{\rm config} &= \frac{(S)}{(N)} \quad \text{and} \\ \implies \frac{K_{\rm eq}^{\rm config}}{1 + K_{\rm eq}^{\rm config}} &= \frac{(S)}{(N) + (S)}. \end{aligned} \tag{5.27}$$

This equilibrium constant $K_{\rm eq}^{\rm config}$ is independent of the strength of the binding site and depends just on the histone-DNA energetics. The second step of the binding process is the binding of the

regulatory protein to an exposed binding site. The equilibrium dissociation constant in this case is

$$K_{\rm d}^{\rm naked\ DNA} = \frac{(R)(S)}{(RS)}. \tag{5.28}$$

Dividing Eq. 5.28 with Eq. 5.27 and comparing it with Eq. 5.23 we obtain

$$K_{\rm d}^{\rm apparent} = K_{\rm eq}^{\rm naked\ DNA} \frac{K_{\rm eq}^{\rm config} + 1}{K_{\rm eq}^{\rm config}}. \tag{5.29}$$

It may be noted that if $K_{\rm eq}^{\rm config} \ll 1$, the above equation reduces to Eq. 5.4 used by Polach and Widom [24]. It may also be noted that $K_{\rm eq}^{\rm naked\ DNA} = R_0/\exp(\epsilon_{\rm bind}/k_BT$. Hence, comparing Eq. 5.29 with Eq. 5.26 we obtain

$$\frac{K_{\rm eq}^{\rm config}}{1 + K_{\rm eq}^{\rm config}} = \frac{1 - \exp(-\bar{\alpha}(L-z))}{1 - \exp(-\bar{\alpha}L)} \quad \text{and} \tag{5.30}$$

$$\implies K_{\rm eq}^{\rm config} = \frac{\exp(\bar{\alpha}z) \times (\exp(\bar{\alpha}(L-z) - 1)}{(\exp(\bar{\alpha}z) - 1)}. \tag{5.31}$$

The above equation is easy to interpret. The nucleosomal DNA is in the wrapped state, W, when the binding site at distance z is not exposed, i.e., the nucleosome is in state W for $x < z$. The probability that this happens is the summation of the Boltzmann probabilities satisfying this condition,

$$\begin{aligned} p_{\rm W} &= \frac{1}{Z}\int_0^z \exp(-\bar{\alpha}(L-x))dx \quad \text{and} \\ &= \frac{\exp(-\bar{\alpha}L)}{\bar{\alpha}Z}(\exp(\bar{\alpha}z) - 1). \end{aligned} \tag{5.32}$$

On the other hand, when the binding site gets exposed, the nucleosome is in unwrapped state, U. This happens when $x \geq z$, i.e, $x \in [z, L]$. Hence, similar to the evaluation of $p_{\rm W}$ as done in Eq. 5.32, the probability that the nucleosome is unwrapped is

$$\begin{aligned} p_{\rm U} &= \frac{1}{Z}\int_z^L \exp(-\bar{\alpha}(L-x))dx \quad \text{and} \\ &= \frac{\exp(-\bar{\alpha}L)}{\bar{\alpha}Z} \exp(\bar{\alpha}z) \times (\exp(\bar{\alpha}(L-z) - 1). \end{aligned} \tag{5.33}$$

The configuration equilibrium constant is, hence, obtained by dividing Eq. 5.33 with Eq. 5.32:

$$K_{\rm eq}^{\rm conf} = \frac{p_{\rm U}}{p_{\rm W}} = \frac{\exp(\bar{\alpha}z) \times (\exp(\bar{\alpha}(L-z) - 1)}{\exp(\bar{\alpha}z) - 1}, \tag{5.34}$$

which is the same as that obtained in Eq. 5.27. We thus have obtained the equation for $K_{\rm eq}^{\rm config}(z)$ in terms of the microscopic parameters that involve the bending of the DNA and the DNA-histone interaction energy. In next section we will evaluate the numerical values of $K_{\rm eq}^{\rm config}(z)$ and compare

them with the experimental data of Polach and Widom [24]. Note that we have assumed that the unwrapping happens only from one end of the nucleosome. It will be shown in Appendix 5.7.1 that taking into account the unraveling of the DNA from both ends gives us almost the same result.

We now turn our attention towards obtaining the expressions for the rate constant k_{12} and k_{21}, as shown in Fig. 5.2 and Eq. 5.1. We first obtain an expression for k_{12}, the unwrapping process. To do so we will make a few assumptions:

1. For convenience we will assume that the DNA unwraps only from one end of the nucleosome. This may seem as a bit of a harsh assumption, but it is in accordance with the experimental conditions of Li et al. [23]. As explained in Section 5.2, Li et al. [23] used FRET to obtain the measurement of k_{12} by putting an acceptor dye Cy3 on one end of the DNA and two acceptor dyes Cy5 on the pair of histone protein H3. The FRET showed a signal loss only when the Cy3 end got separated from Cy5. Since there was no dye on the other end of the nucleosome, any amount of fluctuations of the DNA from the other end of the nucleosome would be immaterial in reducing the FRET signal. In short, the experimental conditions measured the fluctuations only from one end of the DNA. Of course, this is an experimental caveat in the sense that one can add a Cy5 dye also on the other end to characterize the fluctuations of that end. A more physical reasoning behind neglecting the fluctuations of the other end of the DNA is that if the binding site is closer to the first end of the DNA, it is much more unlikely for the binding protein to access that site by a fluctuation from the other end as compared to from the first end.

2. If x and $L - x$ are the lengths, respectively, of the unwrapped and the wrapped part of the DNA, we assume that the DNA is in local equilibrium for every x, i.e., the rate of unwrapping is slow compared to the local equilibration of the DNA-histone system. This assumption is to ensure that we can use the expression for free energy $F(x)$, as shown in Eq. 5.18.

3. The dynamics of DNA unwrapping obey a Fokker-Planck [111](also see Chapter 2) description. This means that we can model the unwrapping as the diffusion of DNA happening in the background of the free energy $F(x)$ in Eq. 5.18.

4. The rate constant k_{12} is equal to $1/\tau_{12}(x)$, where $\tau_{12}(x)$ is the mean-first-passage-time (MFPT) for the DNA to unwrap x nm of DNA. We have seen in Chapter 4 that, given a Fokker-Planck equation, the MFPT is easily obtained. We want to utilize this property of the Fokker-Planck equation. Also, MFPT seems to be the right description for the experimental measurement of k_{12}, where the unwrapping was defined as the first time that the FRET loses significant amount of its signal (see Section 5.2 for more details).

Let us now model the kinetics of the unwrapping process. As mentioned earlier, we assume that

the DNA is in local equilibrium for every segment of length x unwrapped, i.e., the free energy $F(x)$ is well defined. In that case, it is reasonable to model the unwrapping of the DNA as a diffusion-in-a-field problem. The diffusion variable here is the length x of the DNA unwrapped, and the external field is the free energy $F(x)$. Similar to the DNA ejection process in bacteriophage (see Chapter 4), the problem reduces to the Fokker-Planck equation. It involves $p(x,t)$, i.e., the probability that x length of DNA will unwrap in time t, and is given by

$$\frac{\partial p(x,t)}{\partial t} = D\left(\frac{\partial^2 p(x,t)}{\partial x^2} + \frac{1}{kT}\frac{\partial}{\partial x}\left(\frac{\partial F(x)}{\partial x}p(x,t)\right)\right). \tag{5.35}$$

In this equation the quantity D is the diffusion constant for the unwrapping DNA and signifies the "local" diffusion of the DNA. The MFPT (as in Chapter 4) is [112]

$$\tau_{12}(x) = \frac{1}{D}\int_0^x dx_1 \exp\left(\frac{F(x_1)}{kT}\right)\int_0^{x_1} dx_2 \exp\left(-\frac{F(x_2)}{kT}\right). \tag{5.36}$$

The integral is very easy to evaluate because in our model the free energy $F(x)$ (see Eq. 5.18) is linear in x. The expression for the MFPT as a function of x may be written as

$$\tau_{12}(z) = \frac{1}{k_{12}(z)} = \frac{1}{D}\int_0^z dx_1 \exp\left(\frac{\alpha x_1}{kT}\right)\int_0^{x_1} dx_2 \exp\left(-\frac{\alpha x_2}{kT}\right) \text{ and} \tag{5.37}$$

$$= \frac{1}{D}\left(\left(\frac{kT}{\alpha}\right)^2 \times (\exp\left(\frac{\alpha z}{kT}\right) - 1) - \frac{kT}{\alpha}z\right), \tag{5.38}$$

where $\alpha = \gamma + \xi kT/2R^2$ is the total free energy per unit length of the wrapped DNA. Thus we have obtained an expression for $k_{12}(x)$. In the experiment by Li *et al.* the value of re-wrapping rate k_{21} is found by using the relationship $k_{21} = k_{12}/K_{\text{eq}}$ and knowing $K_{\text{eq}}^{\text{config}}$ from [22]. We can use our model to make an estimate of k_{12} without referring to the equilibrium constant. To do so, we only need to replace α in Eq. 5.38 with $-\alpha$ because when the DNA re-wraps it undergoes the exact opposite process as of unwrapping. The expression for k_{21} is

$$\tau_{21}(z) = \frac{1}{k_{21}(z)} = \frac{1}{D}\left(\left(\frac{kT}{\alpha}\right)^2 \times (\exp\left(-\frac{\alpha z}{kT}\right) - 1) + \frac{kT}{\alpha}z\right). \tag{5.39}$$

The above estimate of re-wrapping relies on the additional assumption that, when the DNA re-wraps it does not do it haphazardly but retraces its original path.

We have seen in Section 5.1 that thermal fluctuations of the nucleosomal DNA is proposed as one of the methods, which explains how the binding sites on the genome are exposed to various proteins in order to perform many key genomic functions. The time window available for these proteins depends on the unwrapping and re-wrapping rates. Our theoretical expressions make falsifiable predictions about these time-scales and thus tell how feasible various genomic processes are depending on how

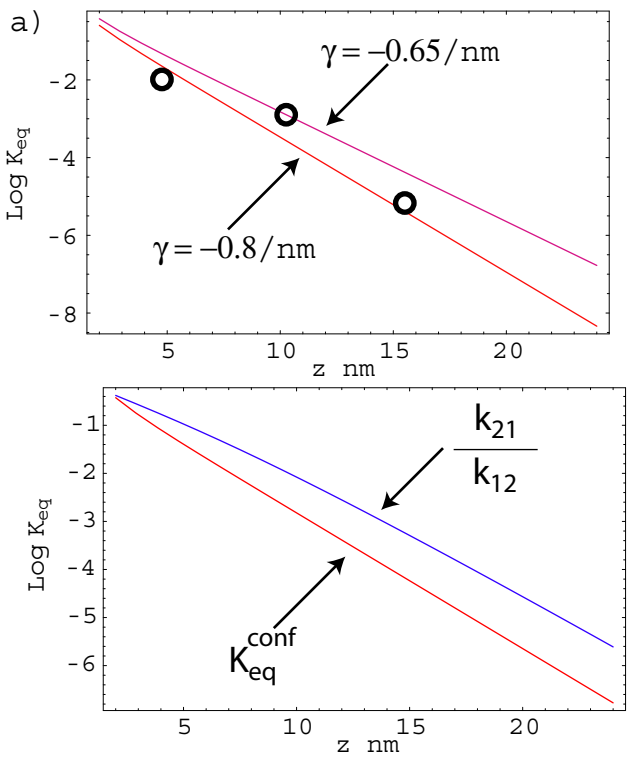

Figure 5.4: The configurational equilibrium constant predicted by the theoretical model. a)The configurational equilibrium constant $K_{\rm eq}^{\rm const}$ as a function of depth of the binding site z. Best fit is obtained to the experimental data (dots in the plot) when $\gamma = -0.65 k_B T$. b)The comparison of the Equilibrium constant obtained using Eq. 5.31 and the one obtained using Eqs. 5.38 and 5.39, k_{12}/k_{21}. There is a clear discrepancy between the two results. The discrepancy may be attributed to the fact that unlike the bistable energy landscape of the chemical reactions obeying, which obey the principle of detailed balance [123], the linear landscape $F(x)$ (see Eq. 5.18) does not admit clear cut definition of "states."

far into the nucleosome the binding sites are buried.

5.5 Numerical Estimates for $K_{\rm eq}^{\rm config}(z)$, $k_{12}(z)$, and $k_{21}(z)$

In the previous section we obtained the expressions for the configurational equilibrium constant $K_{\rm eq}^{\rm config}$, the rate of unwrapping k_{12}, and the rate of re-wrapping k_{21} as a function of the position z of the binding site from the end of the nucleosome. In this section we will insert the numerical values for various parameters, compare with the available experimental data, and make predictions for future experiments.

The parameters involved in the expressions of interest (Eqs. 5.31, 5.38 and 5.39) are the effective free energy of the nucleosome per unit length $\alpha = \gamma + \xi_p k_B T/2R^2$ and the diffusion constant D for the DNA. Upon using a canonical value of roughly $-10 k_B T$ per DNA-histone contact, we saw in Section 5.3 that the total DNA-histone interaction energy of the histone is around $-120 k_B T$,

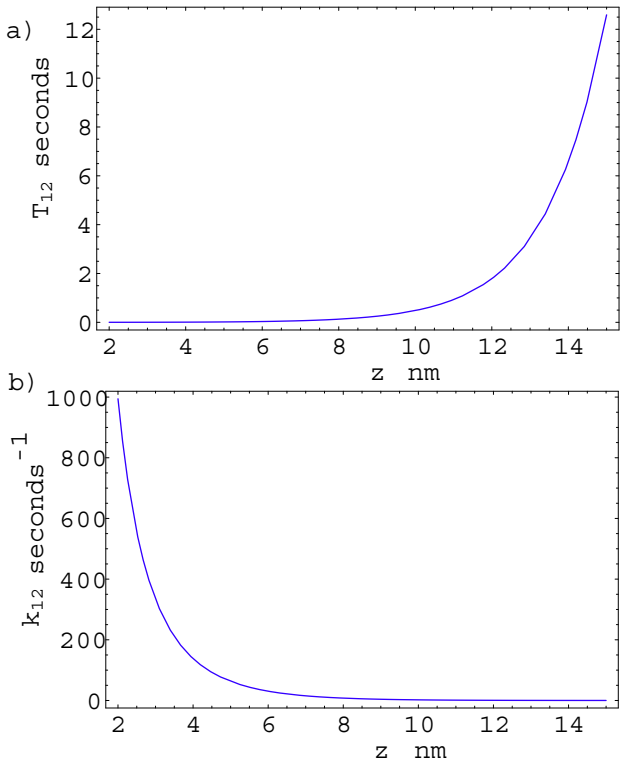

Figure 5.5: Theoretical prediction for kinetics of DNA unwrapping. (a) The plot of the unwrapping time $\tau_{12}(z)$ vs the depth of the binding site z. It can be seen from Eq. 5.38 that, the wrapping time increases exponentially with z. (b) The plot of the rate of unwrapping k_{12} vs the distance z of the binding site. The rate is given by $1/\tau_{12}(z)$, and it can be seen that the value of k_{12} decreases rapidly as the depth of the binding site z increases.

while the total bending energy is approximately $80k_BT$. The total length of the nucleosomal DNA is around 150bp, which is approximately 50nm. The value of the interaction free energy per unit length γ is, hence, around $-120k_BT/50 = 2.4k_BT$/nm. Similarly the bending energy per unit length of the nucleosome is $80k_B/50 = 1.6k_BT$/nm. The total nucleosomal free energy per unit length is, hence, $\alpha = -2.4k_BT + 1.6k_BT = 0.8k_BT$.

Using these values we can obtain $K_{\rm eq}^{\rm config}(z)$ using Eq. 5.31. The resulting value of $K_{\rm eq}^{\rm config}$ as a function of the depth of the binding site z is shown in Fig. 5.4a. It can be compared with the data from Polach and Widom [24] (see the points in Fig. 5.4a) and seen to match decently well with the values of equilibrium constant $K_{\rm eq}^{\rm config}$ they obtain. In order the get a better estimate of the nucleosomal free energy per unit length, α, we can make use of α from Eq. 5.31 as a parameter and obtain the value of α that gives a best fit to the experimental data of Polach and Widom [24]. The value of $\alpha \approx -0.65k_BT$ gives a best fit to the experimental data. The corresponding plot for $K_{\rm eq}^{\rm config}$ is shown in Fig. 5.4a.

After evaluating the configurational equilibrium constant, our next task is to make numerical estimates for k_{12} as given in Eq. 5.38. We have already made an estimate of α. The only unknown

left in the expression is the diffusion coefficient D of the unwrapping DNA. To make an estimate of D we make use of the experimental result from Li *et al.* [23] (see Section 5.2 for more details). They estimate τ_{12} for $z = 27$bp of around 250 milliseconds. Using this value for $z = 27\text{bp} \approx 9\text{nm}$ we obtain an unwrapping time $t_{12}(z = 9\text{nm})$ of $(800/D)\text{nm}^2 = 0.25$ seconds. This implies that the diffusion constant D is approximately $3.2 \times 10^3 \text{nm}^2/\text{second}$. We can use this value of D to make an estimate of the time and, hence, the rate required for the unwrapping of DNA for different values of z. The rate of unwrapping $k_{12}(z)$ is given by $1/\tau_{12}(z)$. The plots of z vs τ_{12} and z vs. $k_{12}(z)$ are shown, respectively, in Figs. 5.5a and 5.5b. Using the same value of D and Eq. 5.39 we can also make estimates of k_{21}. When z equal to 9 nm, the value of τ_{21} is obtained to be approximately 4 milliseconds. This is not within the range of $10 - 40$ milliseconds for re-wrapping as obtained by Li *et al.* [23]. Let us investigate why this might be so. The principle of detailed balance makes us expect that the configurational equilibrium constant $K_{\text{eq}}^{\text{config}}$ is equal to the ratio k_{12}/k_{21} of the unwrapping and the rewrapping rates. The plot of this ratio obtained from Eqs. 5.38 and 5.39 using $\gamma = -0.8kBT$ is shown as a function of the depth z of the binding site in Fig. 5.4. It can be seen that there is about an order of magnitude discrepancy between this ratio and the equilibrium constant obtained from Eq. 5.31. The reason for this discrepancy is not very clear, but we can think of at least two problems in the modeling that causes it:

1. We state that the DNA is in an unwrapped state if it unwraps a length greater than the depth z of the buried site, or else we call it to be in the wrapped state. The equilibrium constants for the dynamic equilibrium between two states is usually defined for bistable potentials with well defined energy wells. In such potentials there are two minimas corresponding to each state. The energy landscape for DNA diffusion along the nucleosome is linear (see Eq. 5.18) and, as a result, defining two states and the corresponding equilibrium constant is not technically correct.

2. We define rates k_{12} and k_{21}, respectively, to be the inverse of the MFPT t_{12} and t_{21} for unwrapping and re-wrapping the segment of the nucleosomal DNA of length z. As discussed above, since the "states" are not well defined, the corresponding MFPT may also not be rightly evaluated.

We also saw in Section 5.2 that Li et al. [23] obtained the value for k_{12} using the FRET measurement and used the previously obtained expression for $K_{\text{eq}}^{\text{config}}$ to obtain the value of k_{21} using the formula $k_{21} = K_{\text{eq}}^{\text{config}}/k_{12}$. Now, since our results for the ratio of the rate constants do not match with the directly obtained equilibrium constant, this discrepancy may also explain why the theoretically obtained value for $\tau_{21}(z = 9\text{nm})$ ($\approx 4\text{ms}$) is different from the experimentally obtained value ($\approx$ 20ms). The plots for re-wrapping rate and time, as a function of the depth z of the binding site, are shown in Fig. 5.6.

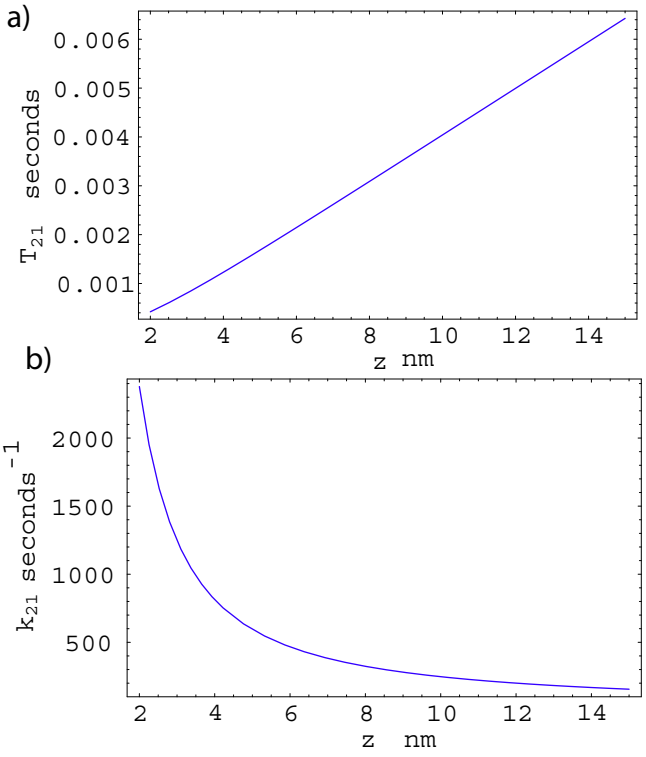

Figure 5.6: Theoretical predictions for the kinetics of DNA re-wrapping. a)The plot of DNA re-wrapping time τ_{21} vs length z of the DNA to be unwrapped . Since the total free energy per unit length, α, of the DNA is negative, it can be seen from Eq. 5.39 that the exponential term will be small compared to the remaining terms. From that expression and the plot it can be seen that the the re-wrapping time τ_{21} increases linearly with the depth of the buried site z. (b) The rate of re-wrapping k_{21} vs z. The rate is simply given by $1/\tau_{21}$.

5.6 Discussions and Conclusion

We saw in Section 5.1 that nucleosomal DNA is tightly packed and that there needs to be a mechanism to expose the DNA to the proteins performing key genomic functions. It was convincingly shown by Widom et al. [24, 22, 23] that, at least under *in vivo* conditions, the thermal fluctuations of the DNA is sufficient for this purpose. Actual numbers of the rate constants for DNA wrapping and unwrapping and the configurational equilibrium constants were also obtained. In this chapter we briefly discussed the experimental procedure for the corresponding experiments, approached the experimental data, and developed models based on statistical mechanics to explain the same.

The model made estimates for the equilibrium constant $K_{\text{eq}}^{\text{config}}$ as a function of the depth z of the binding site from the end of the nucleosome. We found that the generic value for the interaction free energy of $-10k_BT$ per DNA-histone contact along with the known values of the DNA persistence length and the size of the nucleosome were not too off from the experimentally obtained values of $K_{\text{eq}}^{\text{config}}$ (see Fig. 5.4a). We also obtained the value of nucleosome free energy per unit length, α, by using it as a free parameter to provide a best fit with the experimental values of $K_{\text{eq}}^{\text{config}}$ of Polach and Widom [24]. As can be seen from Fig. 5.4 the equilibrium constant steeply decreases with increasing z. This is as expected and is a reflection of the fact that with increasing amount of DNA to be unraveled, the unwrapping process is more and more rare. The value of α obtained was utilized to find k_{12} and k_{21}, the rate of unwrapping and re-wrapping, respectively, of the nucleosomal DNA as a function of depth of the binding site z by using Fokker-Planck equation applied to the aforementioned model. As expected, the rate constant k_{12} steeply drops as z increases because, as can be seen from Eq. 5.38, the time required to unwrap extra length of DNA increases exponentially. The rate k_{21}, on the other hand, decrease with increasing z, but the drop is not so sudden because, as can be seen from Eq. 5.39, since $\bar{\alpha}$ is negative, the exponential term becomes negligible and the rate constant drops as $1/z$.

We performed all the calculations assuming that the unwrapping and re-wrapping parameter x is continuous. On the other hand, the nucleosomal DNA contacts with the histone only at discrete points. It can however, be seen below (Section 5.7.2) that the discrete calculation gives almost the same results as its continuum counterpart. As far as the concerns with this simple models are concerned, we do not address the dependence of the unwrapping and re-wrapping rates on the salt concentration. The salt dependence of the DNA unwrapping will be reflected in the DNA-histone interaction free energy per units length γ. This dependence is studied experimentally by Tomschick *et al.* [124], and the model as it stands currently does not address this issue.

5.7 Appendix

5.7.1 DNA Fluctuations Involving Unravelling From Both Ends of the Nucleosome

In the main body of the chapter we assumed that the DNA unravels only from one end of the nucleosome and implicitly dealt with only with one half of the nucleosome. On the other hand, in the experimental conditions of Polach and Widom [24] there is no distinction between one end from the other. This would mean that the DNA should unwrap from both ends in the same way. In this section we perform a simple calculation to see if making this distinction changes our answer significantly.

Suppose that in addition to length x of DNA unwrapped from first end we also have length y, of the DNA from the other end. The free energy of the DNA-histone system will be a function of both x and y and can be easily generalized to give

$$\begin{aligned} F(x,y) &= F_{\text{bending}}(x) + F_{\text{binding}}(x), \\ &= \frac{1}{2}\frac{\xi_p k_B T}{R^2}(L-x-y) + \gamma \times (L-x-y), \text{ and} \\ &= \left(\gamma + \frac{\xi_p k_B T}{2R^2}\right) \times (L-x-y). \end{aligned} \tag{5.40}$$

The configurational equilibrium constant $K_{\text{eq}}^{\text{config}}$ is evaluated in the following fashion. The nucleosome is in the wrapped state, W, when the binding site at distance z from the first end is not exposed. This means that the amount of DNA unwrapped from the first end (x) should be less than z ($z < x$) and the amount of DNA unwrapped from the other end (y) should be less than $L - z$ ($y < L - z$). The probability of this happening is equal to the summation of the the Boltzmann probabilities over all the microstates satisfying this condition:

$$\begin{aligned} p_{\text{W}} &= \frac{1}{Z}\int_{x=0}^{z}\int_{y=0}^{L-z} \exp(-F(x,y)/k_B T)dydx, \\ &= \frac{1}{Z}\int_{0}^{z}\int_{0}^{L-z} \exp(-\bar{\alpha}(L-x-y))dydx, \text{ and} \\ &= \left(\frac{1}{\bar{\alpha}Z}\right)^2 \exp(-\bar{\alpha}L) \times (\exp(\bar{\alpha}z)-1) \times (\exp(\bar{\alpha}(L-z))-1). \end{aligned} \tag{5.41}$$

Here, Z is the partition function and is given by summing the Boltzmann weights over all possible

microstates.

$$\begin{aligned} Z &= \int_0^L \int_0^{L-x} \exp(-F(x,y)/k_BT)dydx, \\ &= \int_0^L \int_0^L \exp(-\bar{\alpha}(L-x-y)), \text{ and} \\ &= \exp(-\bar{\alpha}L)\left[\frac{\exp(\bar{\alpha}L)}{\bar{\alpha}} - \frac{\exp(\bar{\alpha})-1}{\bar{\alpha}^2}\right]. \end{aligned}$$

Since the nucleosomal DNA is either wrapped or unwrapped, the probability p_{U} is equal to $1 - p_{\mathrm{W}}$. Using Eqs. 5.41 and 5.42 we obtain

$$p_{\mathrm{U}} = \frac{\exp(-\bar{\alpha}L)}{Z}\left[\frac{L\exp(\bar{\alpha}L)}{\bar{\alpha}} - \frac{2\exp(\bar{\alpha}L) - \exp(\bar{\alpha}(L-z)) - \exp(\bar{\alpha}z)}{\bar{\alpha}^2}\right]. \tag{5.42}$$

The configurational equilibrium constant $K_{\mathrm{eq}}^{\mathrm{config}}$ is, hence, given by diving Eq. 5.42 with Eq. 5.41

$$K_{\mathrm{eq}}^{\mathrm{config}} = \frac{p_{\mathrm{U}}}{p_{\mathrm{W}}} = \frac{\bar{\alpha}L\exp(\bar{\alpha}L) - 2\exp(\bar{\alpha}L) + \exp(\bar{\alpha}(L-z)) + \exp(\bar{\alpha}z)}{(\exp(\bar{\alpha}z)-1)\times(\exp(\bar{\alpha}(L-z))-1)}. \tag{5.43}$$

5.7.2 DNA Fluctuations in Discrete Steps

In the previous section we assumed, for convenience, that the variable z for the burial depth of the binding site and the variable x for the unwrapped length are continuous variables. But, that is indeed not the case. In fact, it was seen in Section 5.3 that the DNA makes contact with the histone at 12 discrete places. Hence it would be more close to reality if we model the spontaneous fluctuations of the DNA in a discrete fashion. Let us first obtain the symbolic expressions. The nucleosome of length L makes contact with the histone at N different sites. If we assume that the sites are uniformly distributed, the spacing between the sites is $a = L/N$. In Section 5.3 the free energy of the DNA-histone system per unit length in units of k_BT is denoted by $\bar{\alpha}$. The free energy associated with length a, the spacing between the binding sites, is now denoted by Ω which equals $a \times \bar{\alpha}$. Since it was demonstrated by Li and Widom [22] that the nuclesome unwraps linearly without forming bubbles, the total number of allowed states is $N+1$. Suppose, the binding site for the protein is buried at the kth DNA-histone contact then the protein can bind if and only if atleast k sites are exposed. Hence, the nucleosome is in the wrapped state when the kth contact is not exposed. In this state the number of contacts exposed, i, can take values from 0 to $k-1$. As was done for the continuum model, the probability p_{W} that the DNA is in the wrapped state is given

by the sum of the Boltzmann weights over these states:

$$\begin{aligned} p_{\mathrm{W}} &= \frac{1}{Z}\sum_{i=0}^{k-1}\exp(-\Omega(N-i)), \\ &= \frac{\exp(-\Omega N)}{Z}\sum_{i=0}^{k-1}\exp(\Omega i), \text{ and} \\ &= \frac{\exp(-\Omega N)}{Z}\frac{\exp(\Omega k)-1}{\exp(\Omega)-1}. \end{aligned} \tag{5.44}$$

Here Z is the partition function, similar to the one evaluated for the continuum model. Since the total number of states possible in this model is $N+1$, evaluating Z would involve summing the Boltmann weights over all these states, i.e., $\sum_{i=0}^{N}\exp(-\Omega(N-i))$.

The nucleosome is in the unwrapped state when the protein can bind to the binding site, which happens when at least k sites are exposed. Thus, when the nucleosome is the unwrapped state, i can take values from k to N. The probability that the DNA is in the unwrapped state is, hence, given by

$$\begin{aligned} p_{\mathrm{U}} &= \frac{1}{Z}\sum_{i=k}^{N}\exp(-\Omega(N-i)), \\ &= \frac{\exp(-\Omega N)}{Z}\sum_{i=k}^{N}\exp(\Omega i), \text{ and} \qquad (5.45) \\ &= \frac{\exp(-\Omega N)}{Z}\frac{\exp(\Omega N+1)-\exp(\Omega k)}{\exp(\Omega)-1}. \qquad (5.46) \end{aligned}$$

Thus the configurational equilibrium constant $K_{\mathrm{eq}}^{\mathrm{config}}$ is given by dividing Eq. 5.46 with Eq. 5.44:

$$K_{\mathrm{eq}}^{\mathrm{config}} = \frac{p_{\mathrm{U}}}{p_{\mathrm{W}}} = \frac{\exp(\Omega N+1)-\exp(\Omega k)}{\exp(\Omega k)-1}. \tag{5.47}$$

This expression looks exactly like how the discretized version of the equilibrium constant, Eq. 5.31, obtained from the continuum model, works. It hence seems perfectly reasonable to use the continuum model.

Chapter 6

Statistical Mechanics From the Point of View of Information Theory

In Chapter 2 we had a brief overview of equilibrium statistical mechanics and the common methods used for systems that are far from equilibrium. We used a few of these approaches for equilibrium and non-equilibrium systems to make quantitative predictions about DNA packing and ejection in bacteriophage and the DNA fluctuations in nucleosomes. The rest of the thesis is dedicated to the application of the information-theoretical-maximum-entropy (maxent) methods to non-equilibrium systems. We saw in Chapter 2 that the entropy, S, of an equilibrium system involves the summation $S = -\sum_\nu p_\nu \ln p_\nu$ over all possible microstates ν. The maxent method puts an information theoretical spin on the thermodynamic entropy, wherein the entropy is interpreted as the information the experimenter has about the system [5, 6]. As will be seen later in this chapter, this particular outlook on the entropy makes it possible to write down an entropy for systems that are arbitrarily far from equilibrium. When the system is far from equilibrium, instead of writing the entropy over the *microstates* of the system, one defines it over *microtrajectories*. This trajectory entropy was introduced by E. T. Jaynes [6] and subsequently baptized by him as the Caliber [7]. The maximization of the caliber, subjected to physical constraints, provides the probabilities of the microtrajectories [6, 7, 8]. This methodology is called the "principle of maximum caliber" by Jaynes [7] (*please note that whenever we use the phrase "maxent" in relation to non-equilibrium systems we mean the "principle of maximum caliber"*).

Although the maxent methods for non-equilibrium systems are conceptually well understood [6, 7, 8, 125, 126, 127] and a few general properties of non-equilibrium systems (fluctuation theorem, non equilibrium detailed balance, etc.) are nicely derived from this formalism [128, 129, 130], we are not aware of its actual application to "specific" systems in an analytically tractable fashion. Our goal is to develop simple, analytically-tractable models for a few physical, chemical, and biological

systems and apply maxent methods to elucidate their behavior.

In this chapter we provide a brief introduction to the formalism of the maxent methods for equilibrium and non-equilibrium systems. In Chapter 7 we apply the apply maxent to a variation of the famous dog-flea model of the Ehrenfests [131] and derive transport equations for particle diffusion (Fick's law), heat diffusion (Fourier's law), momentum diffusion (Newton's law of viscosity), and chemical flux (rate equation). In Chapter 8 we develop simple microtrajectory models for biological problems like molecular motors and voltage gated ion channels and physical problems like the diffusion of a Brownian particle in dual optical traps, which is an analog of these biological examples. We then apply maxent to these models, subject to the external constraints, and obtain the probabilities of the microtrajectories.

6.1 Maxent for Equilibrium Statistical Mechanics

We discussed the conventional approach to equilibrium statistical mechanics in Chapter 2. In this section we focus on the information theoretic approach for equilibrium systems developed by Jaynes [5]. This approach does not invoke the conventional ergodic hyothesis, and as a result can be easily extended to non-equilibrium systems.

We saw in Chapter 2 that there are two levels of describing a "large" system, the microscopic description involving the degrees of freedom of all the constituent atoms and the macroscopic description specifying a small number of thermodynamic parameters like volume, temperature etc. For a given macrostate the system could be in multiple microstates, but since we can get experimentally "reproducible" behavior by simply tuning the "macro parameters" we need not delve too deeply into the microscopic description of the system. The convenient thing is to assign probabilities of finding the system in a particular microstate so as to obtain the mean values or the fluctuations of the macro quantities of interest.

The question now is how does one assign the probabilities? Jaynes proposes a completely information-theoretic derivation for the assignment of probabilities. He formulates the problem in the following fashion. Suppose that some quantity x can take on the values $(x_1, x_2, ..., x_n)$ where n can be finite or infinite and that the average values of several functions $f_1(x), f_2(x), ..., f_n(x)$ are given where $m < n$. The problem is to find the probability assignment $p_i = p(x_i)$ which satisfies the given data:

$$p_i \geq 0, \tag{6.1}$$

$$\text{`}\sum_{i=1}^{n} p_i = 1 \tag{6.2}$$

$$\sum_{i=1}^{n} p_i f_k(x_i) = \langle f_k(x) \rangle = F_k \quad k = 1, 2, ..., m \tag{6.3}$$

Since the number of equations m is less than the total number of variables n, this is clearly a problem of missing information and has no unique solution. To obtain a solution that is least biased with respect to the known constraints (Eqs. 6.1 and 6.3), Jaynes proposes a maximization of the "information measure" $S_I = \sum_i p_i \ln p_i$ introduced by Shannon. This quantity is known to have the properties of consistency and uniqueness which makes it the correct measure of the "amount of uncertainty" in a probability distribution. Thus, the scheme to obtain a distribution p_i involves maximization of the information theory entropy

$$S_I = -\sum_{i=1}^{n} p_i \ln p_i. \tag{6.4}$$

subject to Eqs. 6.1 and 6.3. The solution can be obtained by the method of Lagrange multipliers. The entropy subject to the constraints can be written as

$$S_I = -\sum_{i=1}^{N} p_i \ln p_i + \lambda_0 \sum_{i=1}^{N} p_i + \sum_{k=1}^{m} \lambda_k \sum_{i=1}^{N} f_k(x_i) p_i. \tag{6.5}$$

One can maximize this entropy by taking a differential and equating it to zero, i.e.,

$$\delta S_I = \sum_i (-1 - \ln p_i + \lambda_0 + \sum_{k=1}^{m} \lambda_k f_k(x_i)) \delta p_i = 0. \tag{6.6}$$

This implies that the probability p_i is given by

$$p_i = \exp(-\lambda_0 + 1) \exp(\sum_{k=1}^{m} \lambda_k f_k(x_i)). \tag{6.7}$$

The normalization condition implies that

$$\exp(-1 + \lambda_0) = \frac{1}{\sum_{i=1}^{N} \exp(\sum_{k=0}^{m} \lambda_k f_k(x_i))}. \tag{6.8}$$

The denominator on the right hand side (RHS) of the above equation is called the partition function and is denoted by $Z(\lambda_1, ..., \lambda_m)$. The probability of the microstate $p(i)$ is thus

$$p_i = \frac{\exp(\sum_{k=1}^{m} \lambda_k f_k(x_i))}{Z(\{\lambda_k\})}. \tag{6.9}$$

The Lagrange multipliers are obtained by noting that

$$\begin{aligned} \langle f_k \rangle &= \sum_{i=1}^{N} f_k(x_i) p_i, \\ &= \sum_i \underbrace{\frac{f_k x_i \exp(\sum_k \lambda_k f_k(x_i))}{\sum_j \exp(\sum_k \lambda_k f_k(x_j))}}_{Z(\lambda_1,\ldots,\lambda_m)}. \end{aligned} \tag{6.10}$$

It can be easily seen that the above equation can as well be written as

$$\langle f_k(x_i) \rangle = \frac{\partial}{\partial \lambda_i} Z(\lambda_1, ..., \lambda_m), \tag{6.11}$$

where k goes from 1 to m. The solution of these m equations will provide the Lagrange multipliers and give us the probabilities of the microstates. The variance of quantities can also be seen without much difficulty to be

$$\Delta f_k^2 = \langle f_k^2 \rangle - \langle f_k \rangle^2 = \frac{\partial^2}{\partial \lambda_k^2} \ln Z. \tag{6.12}$$

This was a completely general derivation without any reference to the nature of x and $f_k(x)$ and told us how to obtain a "least biased" distribution for an under constrained problem (or a problem with missing information). If we compare the probability distribution p_i and the partition function Z with those obtained in Chapter 2 for the canonical distribution, the mathematical similarities will be apparent. Specifically, let the energy levels of a system be $E(\alpha_1, \alpha_2, ...)$ where the external parameters α_i, may include the volume, strain tensor, electric field, etc. Then, if we are given only the average energy $\langle E \rangle$, the maxent probabilities are given by a special case of Eq. 6.9, which is the Boltzmann distribution if the Lagrange multiplier λ is equal to $1/k_B T$. Thus, the maximum entropy approach provides us with an information theoretic interpretation of equilibrium statistical mechanics without any reference to the ergodic properties of the system. It can also be shown that at thermodynamic equilibrium the information entropy S_I is the same as the experimental entropy S_E [5].

Jaynes approaches the probabilities in a Bayesian manner and maintains that the obtained probability p_i, more than anything else, represents the "belief" of the experimenter that the system is in microstate i. But how can the belief of an experimentalist dictate the course of an experiment? The answer lies in recognizing that we are concerned with the prediction of the "reproducible" macroscopic behavior. Whereas the macroscopic behavior is experimentally reproducible under the applied constraints, the microstates are not. That the macroscopic behaviour is reproducible under given constraints or experimental "knobs" implies that it is a characteristic of each of the vast number

of microstates compatible with those constraints. It, hence, follows that the vast majority of the microscopic details are irrelevant for the prediction of the macro quantities. When, the applications of the Jaynes procedure fails, the situation is informative because it signals the presence of new constraints that had not been taken into account.

The take away message of this section is that it is possible to interpret the entropy in an information theoretic manner and recover the results of equilibrium statistical mechanics. If we obtain a "reproducible" experiment by controlling certain "knobs," then the maximization of the information entropy subject to constraint imposed by the "knobs" will provide us with "least biased" estimates of the probabilities of the underlying microstates. In the equilibrium scenario the "knobs" are time independent. If we extend this logic by replacing the "time independent" constraint with "time dependent" constraints and replace the "microstates" with "microtrajectories," we should be able to have a general formulation for the systems that are far from equilibrium. That is the subject of the next section.

6.2 Non-equilibrium Statistical Mechanics

In the previous section we saw how an information theoretic interpretation of entropy reproduces the familiar results of statistical mechanics. Its extension to non equilibrium phenomena, on the other hand, is bound to be controversial. Hence, before we begin with the information theoretic description of non equilibrium statistical mechanics *a la* Jaynes, we want to clarify one thing. Though we are extremely intrigued by the elegance of Jaynes' approach, we do not hold so strong a opinion as Jaynes about its universality. We think that Jaynes' approach is extremely rational and promises a novel way to approach many non-equilibrium problems, especially in biology. Our approach towards the maxent formalism is primarily exploratory, and we wish to see if we can apply it to simple models and get insights into various interesting systems discussed in Chapters. 7 and 8.

In the previous section we were not at all insistent on the system being in equilibrium. The place, though, where we used the equilibrium fact was in the enumeration of the stationary microstates and putting time-independent constraints. Hence, in order to use maxent for reproducible non-equilibrium processes we need to put time-dependent constraints, and instead of using the stationary states use the time-dependent solution of the Schrodinger equation (Hamilton's equation for classical mechanics or for that matter, the microscopic evolution equation for any particular evolution we are interested in). Even though the actual solution of any problem can be very complicated, the philosophy remains as simple as that. We will give some demonstration of how the method can be applied to some specific problems using models of our choice. To summarize, the only(!) difference between the equilibrium and the non-equilibrium statistical mechanics, from the information theoretic perspective, is the application of time-dependent constraints and using microtrajectories

instead of microstates in the phase-space. Let us discuss this generalization.

In the previous section we had a time-independent microvariable x which could attain different values $x_1, ..., x_n$. Now consider a system that is not stationary, i.e., this variable x is a function of time t. If we consider a finite duration of time T, the variable $x(t)$ will have values $x_1(t), ..., x_n(t)$ for t between 0 and T. The experimental "knobs" $f_1(t), ..., f_m(t)$ are also time dependent and are given by

$$\sum_{i=1}^{n} f_k(x_i(t)) = \langle f_k(x(t)) \rangle = f_k(t) \quad k = 1, ..., M \quad t \in [0, T]. \tag{6.13}$$

Thus the time independent constraints in the previous section become time-dependent constraints. A little thought into Eq. 6.13 will tell us that the system evolves in the phase space x via individual microtrajectories $x_i(t)$. This microtrajectory $x_i(t)$ of duration T can be conveniently represented by Γ. Thus the entropy in this non-equilibrium case should be written over the microtrajectories, Γ, where Γ simply represents the time function $x_\Gamma(t)$ for t between 0 and T. The entropy becomes

$$S_I = -\sum_{\Gamma} p_\Gamma \ln p_\Gamma. \tag{6.14}$$

We now have to subject this entropy to the constraints given in Eq. 6.13. Since these constraints are for all values of time between 0 and T, the Lagrange multipliers corresponding to these constraints will be dependent on time. Taking into account all the constraints, the entropy over the trajectories can be written as

$$S_I = -\sum_{\Gamma} p_\Gamma \ln p_\Gamma + \lambda_0 \sum_{\Gamma} p_\Gamma + \sum_{\Gamma} \left(\sum_{k=1}^{M} \int_0^T \lambda_k(t) f_k^{(\Gamma)}(t) dt \right) p_\Gamma. \tag{6.15}$$

Using the standard procedure of maximizing the trajectory entropy, we will obtain

$$\delta S_I = \sum_{\Gamma} (-1 - \ln p_\Gamma + \lambda_0 + \sum_{k=0}^{m} \int_0^T \lambda_k(t) f_k^{(\Gamma)}(t)) \delta p_\Gamma = 0. \tag{6.16}$$

This implies that the probability of the trajectory is given by

$$p_\Gamma = \frac{1}{Z(\lambda_1(t), ..., \lambda_m(t))} \exp\left(\sum_{k=0}^{m} \int_0^T \lambda_k(t) f_k^{(\Gamma)(t)} \right), \tag{6.17}$$

where

$$Z = \exp(1 - \lambda_0) = \sum_{\Gamma} \exp\left(\sum_{k=0}^{m} \int_0^T \lambda_k(t) f_k^{(\Gamma)}(t) \right) \tag{6.18}$$

becomes a partition functional. Upon using the expression for p_Γ obtained in Eq. 6.17 the trajectory

entropy $-\sum_\Gamma p_\Gamma \ln p_\Gamma$ attains a maximum value of [8]:

$$S_I^{\max}(f_1(t), ..., f_m(t)) = Z + \lambda.A. \tag{6.19}$$

where $\lambda.A$ is a short form for the expression

$$\lambda.A = \sum_{k=0}^{m} \int_0^T \lambda_k(t) f_k(t). \tag{6.20}$$

This quantity $S_I^{\max}(f_1(t), ..., f_m(t))$ is called the time dependent caliber of the system and the principle of maximizing the trajectory entropy is called the "principle of maximum caliber" [7, 8]. The caliber is hypothesized to preside over the non-equilibrium statistical mechanics in the same way entropy rules the world of thermodynamic equilibrium.

We have presented a very simple general derivation of caliber formalism. Jaynes presents a more sophisticated version of this principle using a full fledged quantum mechanical operator theory and density matrices [6, 7, 8]. Even though we haven't presented the formalism with complete sophistication, the gist of the principle is captured. Jaynes uses this formalism to obtain Kubo formulas for transport coefficients without resorting to near equilibrium conditions [8]. Upon linearizing the full blown non-linear equations he obtains the Onsager reciprocal relations [7, 8].

If the underlying microtrajectory mechanics representing the evolution of a trajectory $\Gamma(\{x_i(t)\})$ is correct and the applied constraints correspond to the "knobs" whose control gives experimentally reproducible results, the principle of maximum caliber is expected to give correct predictions. The rationale behind why this method is expected to work is the same as why the maximum entropy method works for equilibrium statistical mechanics. The macroscopic behavior is experimentally reproducible under the applied constraints, while the microscopic path is not. The fact that the macroscopic behavior is reproducible under given constraints implies that it is characteristic of each of the vast number of microscopic paths compatible with those constraints. This implies that the vast majority of microscopic details are irrelevant to the prediction of macroscopic quantities. Jaynes' procedure of maximizing the information entropy S_I, subject only to the imposed constraints, effectively discards all of the irrelevant microscopic information.

6.3 Interpretation of the Lagrange Multipliers

In the previous two sections we saw how to apply the principle of maximum entropy to obtain the probabilities of the microstates and microtrajectories, respectively, when the system is in equilibrium

and non-equilibrium. It may be noted that the constraints on the system were always of the form

$$\langle A \rangle = \sum_{\nu} p_{\nu} A_{\nu} \tag{6.21}$$

when the system was in equilibrium and of the form

$$\langle A(t) \rangle = \sum_{\Gamma} p_{\Gamma} A_{\Gamma} \tag{6.22}$$

when the system was far from equilibrium. On the other hand, strange as it may seem, many a times we do not control these quantities. For example, when we obtained the canonical distribution in Section 1 we specified $\langle E \rangle$ as the applied constraint. On the other hand, it is a well know fact that what we can control experimentally is not the average energy but the Lagrange multiplier associated with it: the temperature. Similarly, in the non-equilibrium situation, most of the time we cannot control the flux, but only the driving force associated with it. By comparing these two different situations by the way of analogy we can say that the Lagrange multiplier associated with the "average" constraint is the driving force for that quantity and can be the experimentally controlled quantity. As we saw earlier, when the system is in equilibrium the information theoretic entropy S_I is the same as the thermodynamic entropy S_E. As a result, the relation of the Lagrange multiplier with the experimentally controlled quantity becomes apparent. On the other hand, since there is no such equivalent formalism for the systems arbitrarily far from equilibrium the exact interpretation of the multipliers is really difficult. For example, consider a simple case where we have a particle flux due to a time dependent external field. In that case we would specify the average flux $\langle J(t) \rangle$ as the applied constraint. We assume that the Lagrange multiplier that goes with this particle flux will be the driving force and will suggest experiments to probe the validity of our assumptions. On the other hand, its relationship with the experimentally controlled force parameter is not clear.

Despite these subtleties, we will apply the principle of maximum caliber to some simple models in Chapters 7 and 8 and elucidate our assumptions in more details.

Chapter 7

Simple Models for Systems Far from Equilibrium

[*Most of the work in this chapter appears in Ghosh et al. [132]*]

We describe a simple framework for the principles that underlie the dynamical laws of transport: Fick's law of diffusion, Fourier's law of heat flow, the Newtonian viscosity law, and the mass-action laws of chemical kinetics. In analogy with the way that the maximization of entropy over microstates leads to the Boltzmann distribution and predictions about equilibria, maximizing a quantity that E. T. Jaynes called "caliber" over all the possible *microtrajectories* leads to these dynamical laws. The principle of maximum caliber also leads to dynamical distribution functions that characterize the relative probabilities of different microtrajectories. A great source of recent interest in statistical dynamics has resulted from a new generation of single-particle and single-molecule experiments that make it possible to observe dynamics one trajectory at a time.

7.1 Introduction

We describe an approach to explain the principles that underlie the dynamical laws of transport of particles (Fick's law of diffusion), energy (Fourier's law of heat flow), momentum (the Newtonian law for viscosity)[133], and mass-action laws of chemical kinetics[123]. Recent experimental advances now allow for studies of forces and flows at the single-molecule and nanoscale level, representative examples of which may be found in References [134, 135, 136, 137, 11, 138, 35, 139]. For example, single-molecule methods have explored the packing of DNA inside viruses[11] and the stretching of DNA and RNA molecules [35, 139]. Similarly, video microscopy now allows for the analysis of trajectories of individual submicron size colloidal particles[140], and the measurement of single-channel currents has enabled the kinetic studies of DNA translocation through nanopores [134, 137].

One of the next frontiers in biology is to understand the "small numbers" problem: how does a biological cell function given that most of its proteins and nucleotide polymers are present in numbers

much smaller than Avogadro's number[141]? For example, one of the most important molecules, a cell's DNA, occurs in only a single copy. Also, it is the flow of matter and energy through cells that makes it possible for organisms to maintain a relatively stable form [2]. Hence, cells must be in this stable state far from equilibrium to function. Thus, many problems of current interest involve small systems that are out of equilibrium.

Our interest here is two-fold: to describe a physical foundation for the phenomenological macroscopic laws which describe the properties of averaged forces and flows and to obtain the dynamical fluctuations away from those average values for systems with small numbers of particles.

We start from the "principle of maximum caliber" first described by E. T. Jaynes [7]. It aims to provide the same type of foundation for the dynamics of systems with many degrees of freedom that the second law of thermodynamics provides for the equilibria of such systems. To illustrate the principle, we use a slight variant of one of the oldest and simplest models in statistical mechanics, the dog-flea or two urn model [142, 143, 131]. Courses in dynamics often introduce Fick's law, Fourier's law, and the Newtonian-fluid model as phenomenological laws, rather than deriving them from some deeper foundation. In analogy with the role of *microstates* as a basis for the properties of equilibria, we focus on *microtrajectories* as the basis for predicting dynamics.

One argument that might be leveled against the kind of framework we present here is that in the cases we consider it is not clear that it leads to anything different from what one obtains using conventional non-equilibrium thinking. On the other hand, restating the same physical result in different language often can provide a better starting point for subsequent reasoning. This point was well articulated by Feynman in his Nobel lecture [144]:

> "Theories of the known, which are described by different physical ideas may be equivalent in all their predictions and are hence scientifically indistinguishable. However, they are not psychologically identical when trying to move from that base into the unknown. For different views suggest different kinds of modifications which might be made and hence are not equivalent in the hypotheses one generates from them in one's attempt to understand what is not yet understood."

We begin with the main principle embodied in Fick's law. Why do particles and molecules in solution flow from regions of high concentration toward regions of low concentration? To keep it simple, we consider one-dimensional diffusion along a coordinate x. The diffusion is described by Fick's first law of particle transport [133, 123], which says that the average flux $\langle J \rangle$ is given in terms of the gradient of the average concentration $\partial \langle c \rangle / \partial x$ by

$$\langle J \rangle = -D \frac{\partial \langle c \rangle}{\partial x}, \tag{7.1}$$

where D is the diffusion coefficient. To clearly distinguish quantities that are dynamical averages

from those that are not, we indicate the averaged quantities explicitly by brackets, $\langle \ldots \rangle$. Before we describe the nature of this averaging and the nature of the dynamical distribution functions over which the averages are taken, we briefly review the standard derivation of the diffusion equation. We combine Fick's first law with particle conservation

$$\frac{\partial \langle c \rangle}{\partial t} = -\frac{\partial \langle J \rangle}{\partial x} \tag{7.2}$$

and obtain Fick's second law, which is also known as the diffusion equation:

$$\frac{\partial \langle c \rangle}{\partial t} = D \frac{\partial^2 \langle c \rangle}{\partial x^2}. \tag{7.3}$$

The solution of Eq. (7.3) subject to two boundary conditions and one initial condition gives $\langle c(x,t) \rangle$, the average concentration in time and space, and the average flux $\langle J(x,t) \rangle$ when no other forces are present. The generalization to situations involving additional applied forces is the Smoluchowski equation [123].

A simple experiment shows the distinction between *averaged* quantities and *individual microscopic realizations*. By using a microfluidics chip like that shown in Fig. 7.1(a), it is possible to create a small fluid chamber divided into two regions by control valves. The chamber is filled on one side with a solution containing a small concentration of micron-scale colloidal particles. The other region contains just water. The three control valves on top of that microfluidic chamber serve two purposes: The two outer ones are used for isolation so that no particles can diffuse in and out of the chamber, while the middle control valve provides the partition between the two regions. The evolution of the system is then monitored after the removal of the partition (see Fig. 7.1(b)). The time-dependent particle density is determined by dividing the chamber into a number of equal sized boxes in the long direction and by computing histograms of the numbers of particles in each slice as a function of time. This system is a colloidal solution analog of the gas diffusion experiments of classical thermodynamics. The corresponding theoretical model usually used is the diffusion equation. Figure 7.1(c) shows the solution to the diffusion equation as a function of time for the geometry of the microfluidics chip. The initial condition is a step function in concentration at $x = 200\,\mu$m at time $t = 0$.

We use this simple experiment to illustrate one main point. The key distinction is that the theoretical curves are very smooth, while there are very large fluctuations in the experimentally observed dynamics of the particle densities. The fluctuations are large because the number of colloidal particles is small, on the order of tens to hundreds. The experimental data shows that the particle concentration $c(x,t)$ is a highly fluctuating quantity. It is not well described by the standard smoothed curves that are calculated from the diffusion equation. Of course, when averaged over many trajectories or when particles are at high concentrations, the experimental data should approach the

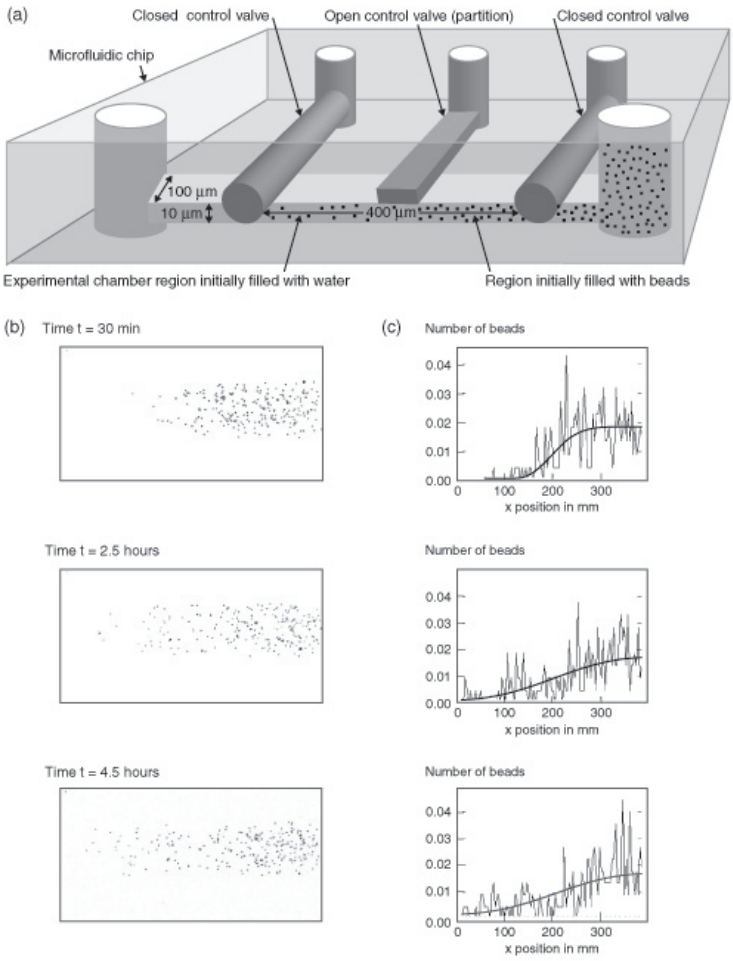

Figure 7.1: Colloidal free expansion setup to illustrate diffusion involving small numbers of particles. (a) Schematic of experimental setup. (b) Several snapshots from the experiment. (c) Normalized histogram of particle positions during the experiment. The solution to the diffusion equation for the microfluidic "free expansion" experiment is superposed for comparison.

smoothed curves that are predicted by the classical diffusion equation.

7.2 The Equilibrium Principle of Maximum Entropy

Because our strategy follows so closely the Jaynes derivation of the Boltzmann distribution law of equilibrium statistical mechanics [123, 5], we first show the equilibrium treatment. To derive the Boltzmann law, we start with a set of equilibrium microstates $i = 1, 2, 3, \ldots, N$ that are relevant to the problem at hand. Our aim is to calculate the probabilities p_i of these microstates in equilibrium.

We define the entropy S of the system as

$$S(\{p_i\}) = -k_B \sum_{i=1}^{N} p_i \ln p_i, \tag{7.4}$$

where k_B is Boltzmann's constant. The equilibrium probabilities, $p_i = p_i^*$ are those values of p_i that cause the entropy to be a maximum, subject to two constraints:

$$\sum_{i=1}^{N} p_i = 1, \tag{7.5}$$

which is a normalization condition that insures that the probabilities p_i sum to one, and

$$\langle E \rangle = \sum_i p_i E_i, \tag{7.6}$$

which says that the energies, when averaged over all the microstates, sum to the macroscopically observable average energy.

By using Lagrange multipliers λ and β to enforce the first and second constraints, respectively, we obtain an expression for the values p_i^* that maximize the entropy [123, 5]:

$$\sum_i [-1 - \ln p_i^* - \lambda - \beta E_i] = 0. \tag{7.7}$$

The result is that

$$p_i^* = \frac{e^{-\beta E_i}}{Z}, \tag{7.8}$$

where Z is the partition function, defined by

$$Z = \sum_i e^{-\beta E_i}. \tag{7.9}$$

After a few thermodynamic arguments, the Lagrange multiplier β can be shown to be equal to $1/k_B T$ [5]. This derivation, first given in this simple form by Jaynes [5], identifies the probabilities that are both consistent with the observable average energy and that otherwise maximize the entropy. Jaynes justified this strategy on the grounds that it would be the best prediction that an observer could make, given the observable mean energy, if the observer is ignorant of all else. Although this derivation of the Boltzmann law is now popular, its interpretation as a method of prediction rather than as a method of physics is controversial. Nevertheless, for our purposes here, it does not matter whether we regard this approach as a description of physical systems or as a strategy for making predictions.

We switch from the principle of maximum entropy to the principle of maximum caliber [7]. In

particular, rather than focusing on the probability distribution $p(E_i)$ for the various microstates, we seek $p[\{\sigma_i(t)\}]$, where $\sigma_i(t)$ is the ith microscopic trajectory of the system. Again, we maximize an entropy-like quantity obtained from $p[\{\sigma_i(t)\}]$ to obtain the predicted distribution of microtrajectories. If there are no constraints, this maximization results in the prediction that all the possible microtrajectories are equally likely during the dynamical process. In contrast, certain microtrajectories will be favored if there are dynamical constraints, such as may be specified in terms of the average flux.

7.3 Fick's Law from the Dog-Flea Model

We want to determine the diffusive evolution of particles in a one-dimensional system. The key features of this system are revealed by considering two columns of particles separated by a plane, as shown in Fig. 7.2. The left-hand column 1 has $N_1(t)$ particles at time t, and the right-hand column 2 has $N_2(t)$ particles. This system is a simple variant of the famous "dog-flea" model of the Ehrenfest's introduced in 1907 [142, 131]. Column 1 corresponds to dog 1, which has N_1 fleas on its back at time t, and column 2 corresponds to dog 2, which has N_2 fleas at time t. In the time interval between time t and $t+\Delta t$, a flea can either stay on its current dog or jump to the other dog. This model has been used extensively to study the Boltzmann H-theorem and to understand how the time asymmetry of diffusion processes arises from the underlying time symmetry in the laws of motion [145, 142, 131]. We use this model for a slightly different purpose. In particular, our aim is to take a well-characterized problem like diffusion and reveal how the principle of maximum caliber may be used in a concrete way.

First consider the equilibrium state of the dog-flea model. The total number of ways of partitioning the $(N_1 + N_2)$ fleas is

$$W(N_1, N_2) = \frac{(N_1 + N_2)!}{N_1! N_2!}. \tag{7.10}$$

The state of equilibrium is that for which the entropy, $S = k_B \ln W$, is a maximum. A simple calculation shows that the entropy is a maximum when the value $N_1 = N_1^*$ is as nearly equal to $N_2 = N_2^*$ as possible. In short, at equilibrium both dogs will have approximately the same number of fleas, in the absence of any bias.

Our focus here is on how the system reaches equilibrium. We discretize time into a series of intervals Δt. We define a dynamical quantity p, which is the probability that a particle (flea) jumps from one column (dog) to the other in any time interval Δt. Thus, the probability that a flea stays on its dog during the time interval is $q = 1 - p$. We assume that p is independent of the time t and that all the fleas and jumps are independent of each other.

In equilibrium statistical mechanics the focus is on the microstates. However, for dynamics we focus on *processes*, which at the microscopic level we call the microtrajectory. Characterizing the

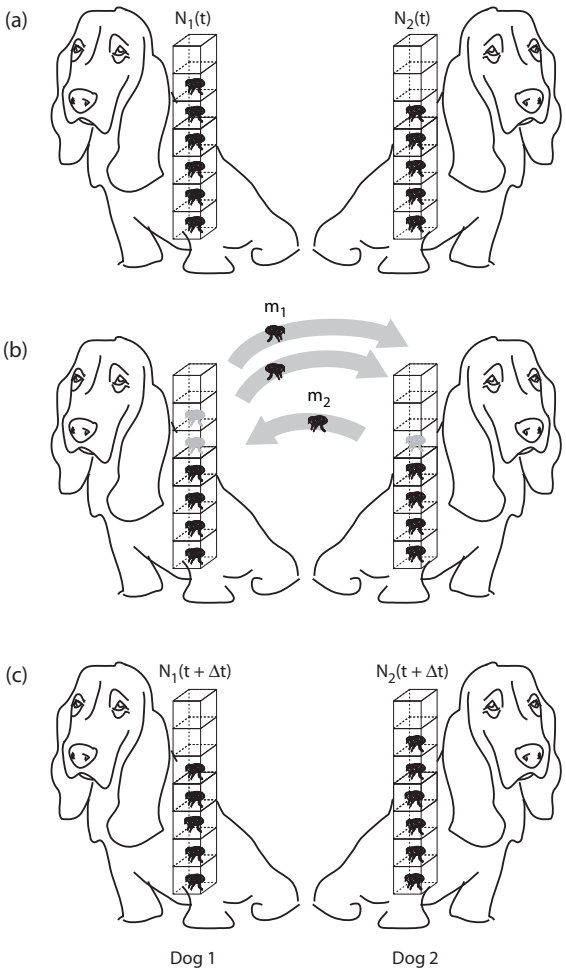

Figure 7.2: Schematic of the simple dog-flea model. (a) State of the system at time t. (b) A particular microtrajectory in which two fleas jump from the dog on the left and one flea jumps from the dog on the right. (c) Occupancies of the dogs at time $t + \Delta t$.

dynamics requires more than just information about the microstates; we must also consider the processes. Let m_1 represent the number of particles that jump from column 1 to 2 and m_2 represent the number of particles that jump from column 2 to 1 between time t and $t + \Delta t$. There are many possible values of m_1 and m_2: it is possible that no fleas will jump during the interval Δt, or that all the fleas will jump, or that the number of fleas jumping will be in between these limits. Each one of these different situations corresponds to a distinct microtrajectory of the system in this idealized dynamical model. We need a principle to tell us what number of fleas will jump during the time interval Δt at time t. Because the dynamics of this model is so simple, the implementation of the caliber idea is reduced to a simple exercise in enumeration and counting using the binomial distribution.

7.3.1 The Dynamical Principle of Maximum Caliber

The probability $W_d(m_1, m_2|N_1, N_2)$ that m_1 particles jump to the right and that m_2 particles jump to the left in a time interval Δt, given that there are $N_1(t)$ and $N_2(t)$ fleas on the dogs at time t, is

$$W_d(m_1, m_2|N_1(t), N_2(t)) = \underbrace{\left[p^{m_1} q^{N_1 - m_1} \frac{N_1!}{m_1!(N_1 - m_1)!}\right]}_{W_{d_1}} \underbrace{\left[p^{m_2} q^{N_2 - m_2} \frac{N_2!}{m_2!(N_2 - m_2)!}\right]}_{W_{d_2}}. \quad (7.11)$$

W_d counts microtrajectories in dynamics in the same spirit that W counts microstates for equilibrium. In the same spirit of the second law of thermodynamics, we maximize W_d over all the possible microtrajectories (that is, over m_1 and m_2) to predict the flux of fleas between the dogs. This maximization is the implementation of the principle of maximum caliber for this model. Maximizing W_d over all the possible processes (different values of m_1 and m_2) gives our prediction (right flux $m_1 = m_1^*$ and left flux $m_2 = m_2^*$) for the macroscopic flux that we should observe experimentally. (We follow the usual definition of flux, the number of particles transferred per unit time and per unit area. For simplicity, we take the cross-sectional area to be unity.)

Because the jumps of the fleas from each dog are independent, we find the predicted macroscopic dynamics by maximizing W_{d_1} and W_{d_2} separately or for convenience their logarithms:

$$\left.\frac{\partial \ln W_{d_i}}{\partial m_i}\right|_{N, m_i = m_i^*} = 0, \quad (i = 1, 2). \quad (7.12)$$

The application of Stirling's approximation to Eq. (7.11) gives

$$\ln W_{d_i} = m_i \ln p + (N_i - m_i) \ln q + N_i \ln N_i - m_i \ln m_i - (N_i - m_i) \ln(N_i - m_i). \quad (7.13)$$

We call $\mathcal{C} = \ln W_d$ the caliber. Maximizing $\mathcal{C}$ with respect to m gives

$$\frac{\partial \ln W_{d_i}}{\partial m_i} = \ln p - \ln q - \ln m_i^* + \ln(N_i - m_i^*) = 0. \quad (7.14)$$

This result may be simplified to yield

$$\ln\left(\frac{m_i^*}{N_i - m_i^*}\right) = \ln\left(\frac{p}{1 - p}\right), \quad (7.15)$$

which implies that the most probable jump number is simply given by

$$m_i^* = pN_i. \quad (7.16)$$

Because our probability distribution W_d is nearly symmetric about the most probable value of flux, the average number and the most probable number are approximately the same. Hence, the average

net flux to the right is

$$\langle J(t)\rangle = \frac{m_1^* - m_2^*}{\Delta t} = p\Big[\frac{N_1(t) - N_2(t)}{\Delta t}\Big] \approx -\frac{p\Delta x^2}{\Delta t}\frac{\Delta c(x,t)}{\Delta x}, \tag{7.17}$$

which is Fick's law for this simple model with the diffusion coefficient given by $D = p\Delta x^2/\Delta t$. We have rewritten $N_1 - N_2 = -\Delta c \Delta x$.

This approach gives us a simple explanation for why there is a net flux of particles diffusing across a plane down a concentration gradient: more microscopic trajectories lead downhill than uphill. It shows that the diffusion coefficient D is a measure of the jump rate p. This model does not assume that the system is near-equilibrium. For example, it does not utilize the Boltzmann distribution law, and thus it indicates that Fick's law should also apply far from equilibrium. We might have imagined that for very steep gradients, Fick's law might have been only an approximation and that diffusion is more accurately represented as a series expansion of higher derivatives of the gradient. But at least for the present model, Fick's law is a general result that emerges from counting microtrajectories. On the other hand, we would expect Fick's law to break down when the particle density becomes so high that the particles start interacting with each other, thus spoiling the assumption of independent particle jumps.

7.3.2 Fluctuations in Diffusion

We have shown that the most probable number of fleas that jump from dog 1 to dog 2 between time t and $t+\Delta t$ is $m_1^* = pN_1(t)$. The model also tells us that sometimes we will have fewer fleas jumping during this time interval and sometimes we will have more fleas. These variations are a reflection of the fluctuations resulting from the system following different microscopic pathways.

We focus now on predicting the fluctuations. To illustrate, we first construct a table of W_d, the different numbers of possible microtrajectories, for all the values of m_1 and m_2. To keep the illustration simple, we consider the special case $N_1(t) = 4$ and $N_2(t) = 2$. We also assume $p = q = 1/2$. Table 7.1 lists the multiplicities of all the possible routes of flea flow. A given entry tells us how many microtrajectories correspond to the value of m_1 and m_2.

m_1 \ m_2	0	1	2
0	1	2	1
1	4	8	4
2	6	12	6
3	4	8	4
4	1	2	1

Table 7.1: Trajectory multiplicity for the case where $N_1(t) = 4$ and $N_2(t) = 2$. Each entry in the table corresponds to the total number of trajectories for the particular values of m_1 and m_2.

Table 7.1 confirms our previous discussion. The dynamical process for which W_d is a maximum (12 microtrajectories in this case) occurs when $m_1^* = pN_1 = 1/2{\times}4 = 2$, and $m_2^* = pN_2 = 1/2{\times}2 = 1$. You can calculate the probability of this flux by dividing $W_d = 12$ by the sum of entries in Table 7.1, which is $2^6 = 64$, the total number of microtrajectories. The result, which is the fraction of all the possible microtrajectories that have $m_1^* = 2$ and $m_2^* = 1$, is 0.18. We have chosen an example in which the particle numbers are very small, so the fluctuations are large; they account for more than 80% of the flow. In systems with large numbers of particles, the relative fluctuations are much smaller.

Now look at the top right entry of Table 7.1. This entry says that there is a probability of 1/64 that both fleas on dog 2 will jump to the left, while no fleas will jump to the right, implying that the net flux for this microtrajectory is backward relative to the concentration gradient. We call these "bad actor" microtrajectories. In these cases, particles flow to increase the concentration gradient, not decrease it. At time t there are 4 fleas on the left dog and 2 on the right. At the next instant, $t + \Delta t$, all 6 fleas are on the left dog, and no fleas are on the right-hand dog.

Similarly, if you look at the bottom left entry of Table 7.1, you see a case of superflux: a net flux of 4 particles to the right, whereas Fick's law predicts a net flow of only 2 particles to the right. Table 7.1 illustrates that Fick's law is only a description of the average or most probable flow and that Fick's law is not always exactly correct at the microscopic level. However, such violations of Fick's law are of low probability, a point that we will make more quantitative in the following. Such fluctuations have been experimentally measured in small systems [146].

m_1 \ m_2	0
0	1
1	6
2	15
3	20
4	15
5	6
6	1

Table 7.2: Trajectory multiplicity for $N_1(t) = 6$ and $N_2(t) = 0$ when the system is far from macroscopic equilibrium.

We can elaborate on the nature of the fluctuations by defining the "potencies" of the microtrajectories. We define the potency to be the fraction of all the trajectories that lead to a substantial change in the macrostate. The potencies of trajectories depend on how far the system is from equilibrium. To see this, we continue our consideration of the simple system of 6 particles. The total number of microscopic trajectories available to this system at each instant in our discrete time picture is $2^6 = 64$. Suppose that at $t = 0$ all 6 of these particles are on dog 1. The total number of microscopic trajectories available to the system can be classified using m_1 and m_2, where in this

case $m_2 = 0$ because there are no fleas on dog 2 (see Table 7.2).

What fraction of all microtrajectories changes the occupancies of both dogs by more than some threshold value, say $\Delta N_i > 1$? In this case we find that 57 of the 64 microtrajectories cause a change greater than this value to the current state. We call these *potent* trajectories.

$m_1 \backslash m_2$	0	1	2	3
0	1	3	3	1
1	3	9	9	3
2	3	9	9	3
3	1	3	3	1

Table 7.3: Trajectory multiplicity for $N_1(t) = 3$ and $N_2(t) = 3$ when the system is at macroscopic equilibrium.

Now let us look at the potencies of the same system of 6 particles in a different situation, $N_1 = N_2 = 3$ when the system is in macroscopic equilibrium (see Table 7.3). In this case only the trajectories with (m_1, m_2) pairs given by (0,2), (0,3), (1,3), (2,0), (3,0), and (3,1) satisfy our criterion. Summing over all of these outcomes shows that just 14 of the 64 trajectories are potent in this case.

There are two key observations conveyed by these arguments. For a system far from equilibrium the vast majority of trajectories at that time are potent and move the system significantly away from its current macrostate. Also, when the system is near equilibrium, the vast majority of microtrajectories leave the macrostate unchanged. We now generalize from the tables to see when fluctuations will be important.

7.3.2.1 Fluctuations and Potencies

A simple way to characterize the magnitude of the fluctuations is to look at the width of the W_d distribution [123]. It is shown in standard texts that for a binomial distribution for which the mean and most probable value both equal $m_i^* = Np_i$, the variance is $\sigma_i^2 = N_i pq$. The variance characterizes the width. Moreover, if N_i is sufficiently large, a binomial distribution can be well-approximated by a Gaussian distribution:

$$\mathcal{P}(m_i, N_i) = \frac{1}{\sqrt{2\pi N_i pq}} \exp\Big(- \frac{(m_i - N_i p)^2}{2N_i pq}\Big), \tag{7.18}$$

a convenient approximation because it leads to simple analytic results. However, this distribution function is not quite the one we want. We are interested in the distribution of flux, $P(J) = P(m_1 - m_2)$, not the distribution of right-jumps m_1 or left-jumps m_2 alone.

Due to a remarkable property of the Gaussian distribution, it is simple to compute the quantity we want. If you have two Gaussian distributions, one with mean $\langle x_1 \rangle$ and variance σ_1^2 and the other

with mean $\langle x_2 \rangle$ and variance σ_2^2, then the distribution function, $P(x_1 - x_2)$ for the difference will also be a Gaussian distribution with mean $\langle x_1 \rangle - \langle x_2 \rangle$ and variance $\sigma^2 = \sigma_1^2 + \sigma_2^2$.

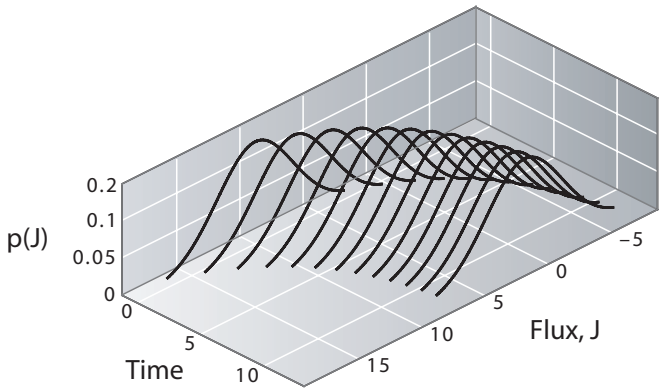

Figure 7.3: Schematic of the distribution of fluxes for different times as the system approaches equilibrium.

For our binomial distributions, the means are $m_1^* = pN_1$ and $m_2^* = pN_2$ and the variances are $\sigma_1^2 = N_1pq$ and $\sigma_2^2 = N_2pq$. Hence, the distribution of the net flux, $J = m_1 - m_2$ is

$$P(J) = \frac{1}{\sqrt{2\pi(pqN)}} \exp\Big(- \frac{(J - p(N_1 - N_2))^2}{2pqN} \Big), \tag{7.19}$$

where $N = N_1 + N_2$.

Figure 7.3 shows an example of the distributions of fluxes at different times using $p = 0.1$ and starting from $N_1 = 100, N_2 = 0$. We update each time step using an averaging scheme, $N_1(t + \Delta t) = N_1(t) - N_1(t)p + N_2(t)p$. Figure 7.3 shows how the mean flux is large at first and decays toward equilibrium, $J = 0$. This result could also have been predicted from the diffusion equation. Equally interesting are the wings of the distributions, which show the deviations from the average flux; these deviations are not predictable from the diffusion equation.

One measure of the importance of the fluctuations is the ratio of the standard deviation σ to the mean, $\sqrt{\sigma^2}/J$. In the limit of large N_1, $\sqrt{\sigma^2/J}$ reduces to

$$\sqrt{\frac{\sigma^2}{J}} = \sqrt{\frac{Npq}{(N_1 - N_2)p}} \sim N^{-1/2}. \tag{7.20}$$

In a typical bulk experiment, the particle numbers are large, of the order of Avogadro's number 10^{23}. In such cases the width of the flux distribution is exceedingly small, and it becomes overwhelmingly probable that the mean flux will be governed by Fick's law. However, within biological cells and in applications involving small numbers of particles, the variance of the flux can become significant. It

has been observed that both rotary and translational single motor proteins sometimes transiently step backward relative to their main direction of motion [112].

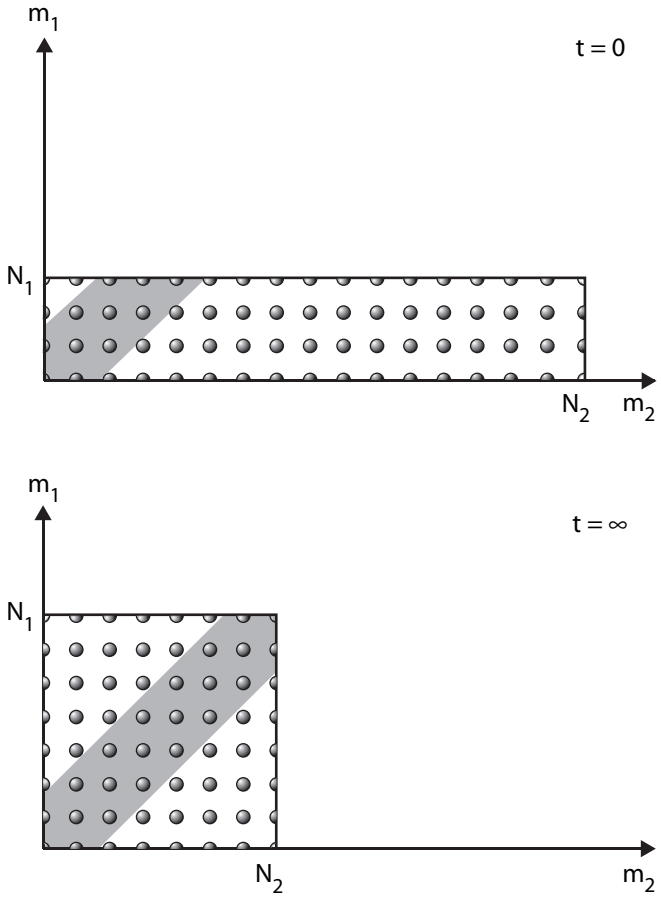

Figure 7.4: Schematic of which trajectories are potent and which are impotent. The shaded region corresponds to the impotent trajectories for which m_1 and m_2 are either equal or approximately equal and hence make relatively small change in the macrostate. The unshaded region corresponds to potent trajectories.

As a measure of the fluctuations, we now calculate the variance in the flux. It follows from Eq. (7.19) that $\langle J^2 \rangle = Npq$, where $N = N_1 + N_2$. Thus, we can represent the magnitude of the fluctuations as

$$\delta = \sqrt{\frac{\langle (\Delta J)^2 \rangle}{\langle J \rangle^2}} = \frac{\sqrt{Npq}}{pfN} \propto \frac{1}{f}\sqrt{\frac{q}{p}N^{-1}}, \tag{7.21}$$

where $N = N_1 + N_2$ is the total number of fleas and $f = (N_1 - N_2)/(N)$ is the normalized concentration difference. The quantity δ is also a measure of the degree of backflux. In the limit of large N, δ goes to zero. That is, the noise diminishes with system size. However, even when N is large, δ can still be large (indicating the possibility of back flux) if the concentration gradient, $N_1 - N_2$, is small.

$$\Phi_{\text{impotent}} \approx \int_{-h}^{h} dJ \frac{1}{\sqrt{2\pi Npq}} \exp\left(\frac{-(J-(N_1-N_2)p)^2}{2Npq}\right) \tag{7.22}$$

$$= \frac{1}{2}\left(\text{erf}\left[\frac{h+(N_1-N_2)p}{\sqrt{2Npq}}\right] + \text{erf}\left[\frac{h-(N_1-N_2)p}{\sqrt{2Npq}}\right]\right), \tag{7.23}$$

Another measure of fluctuations is potency. Trajectories that are not potent should have $|m_1 - m_2| \approx 0$ which corresponds to a negligible change in the current state of the system as a result of a given microtrajectory. In Fig. 7.4 the impotent microtrajectories are shown as the shaded band for which $m_1 \approx m_2$. We define impotent trajectories as those for which $|m_1 - m_2| \leq h$ ($h \ll N$). In the Gaussian model, the fraction of impotent trajectories is

$$\Phi_{\text{impotent}} \approx \int_{-h}^{h} dJ \frac{1}{\sqrt{2\pi Npq}} \exp\left(\frac{-(J-(N_1-N_2)p)^2}{2Npq}\right) \tag{7.24}$$

$$= \frac{1}{2}\left(\text{erf}\left[\frac{h+(N_1-N_2)p}{\sqrt{2Npq}}\right] + \text{erf}\left[\frac{h-(N_1-N_2)p}{\sqrt{2Npq}}\right]\right), \tag{7.25}$$

and corresponds to summing over the subset of trajectories that have a small flux. To keep it simple, we take $p = q = 1/2$ for which the probability distribution for the microscopic flux $m_1 - m_2$ is given by Eq. (7.19). The choice of h is arbitrary, and we choose h to be one standard deviation, $\sqrt{N/4}$. Figure 7.5 shows the potencies for various values of N_1 and N_2. When the concentration gradient is large, most trajectories are potent, leading to a statistically significant change of the macrostate, whereas when the concentration gradient is small, most trajectories have little effect on the macrostate.

As another measure of the fluctuations, let us now consider the "bad actors" (see Fig. 7.6). If the average flux is in the direction from dog 1 to dog 2, what is the probability that we will observe flux in the opposite direction (bad actors)? We use Eq. (7.19) for $P(J)$ to obtain

$$\Phi_{\text{badactors}} \approx \int_{-\infty}^{0} \frac{1}{\sqrt{2\pi Npq}} \exp\left(\frac{-(J-(N_1-N_2)p)^2}{2Npq}\right) \tag{7.26}$$

$$= \frac{1}{2}\left(1 - \text{erf}\left[\frac{(N_1-N_2)p}{\sqrt{2Npq}}\right]\right), \quad (N_2 > N_1), \tag{7.27}$$

which amounts to summing up the fraction of trajectories for which $J \leq 0$. Figure 7.7 shows the fraction of bad actors for $p = q = 1/2$. Bad actors are rare when the concentration gradient is large and highest when the gradient is small. The discontinuity in the slope of the curve in Fig. 7.7 at $N_1/N = 1/2$ is a reflection of the fact that the mean flux abruptly changes sign at that value.

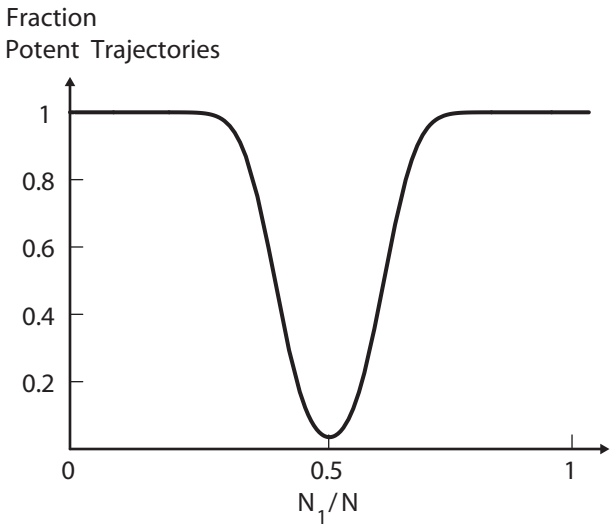

Figure 7.5: Illustration of the potency of the microtrajectories associated with different distributions of N particles on the two dogs. The total number of particles $N_1 + N_2 = N = 100$.

7.4 Fourier's Law of Heat Flow

Although particle flow is driven by concentration gradients according to Fick's law, $\langle J \rangle = -D\partial c/\partial x$, energy flow is driven by temperature gradients according to Fourier's law:[133]

$$\langle J_q \rangle = -\kappa \frac{\partial T}{\partial x}. \tag{7.28}$$

Here, J_q is the energy transferred per unit time and per unit cross-sectional area and $\partial T/\partial x$ is the temperature gradient that drives it. The thermal conductivity[133] κ plays the role that the diffusion coefficient plays in Fick's law.

To explore a simplified version of Fourier's law that depends only on particle transport, we return to the dog-flea model as described in Section 7.3. Now columns 1 and 2 can differ not only in their particle numbers, $N_1(t)$ and $N_2(t)$, but also in their temperatures, $T_1(t)$ and $T_2(t)$. For simplicity, we assume that each column is at thermal equilibrium and that each particle that jumps carries with it the average energy $\langle mv^2/2 \rangle = k_B T/2$ from the column it left. We again take the cross-sectional area to be unity. In this simple model all energy is transported by hot or cold molecules switching dogs. The average heat flow at time t is

$$\langle J_q \rangle = \frac{m_1^*}{\Delta t}(k_B T_1/2) - \frac{m_2^*}{\Delta t}(k_B T_2/2) = \frac{p k_B}{\Delta t}[N_1 T_1 - N_2 T_2], \tag{7.29}$$

where m_1^* and m_2^* are, as defined in Section 7.3.1, the numbers of particles jumping from each column

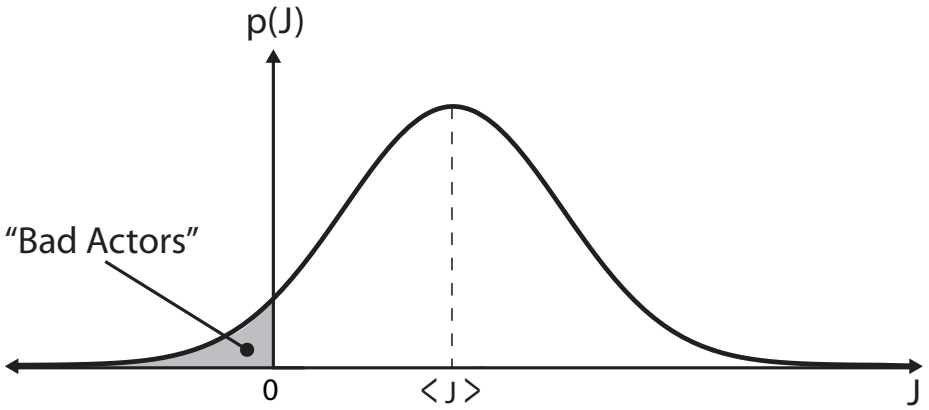

Figure 7.6: Illustration of the notion of bad actors. Bad actors are the microtrajectories that contribute net particle motion that has the opposite sign from the macroflux.

at time t. If the particle numbers are identical, $N_1 = N_2 = N/2$, then

$$\langle J_q \rangle = \frac{pk_B N}{\Delta t}(T_1 - T_2) = -\kappa \frac{\Delta T}{\Delta x}, \tag{7.30}$$

which is Fourier's law for the average heat flux for this two-column model. The model predicts that the thermal conductivity is $\kappa = (pk_B N \Delta x)/(\Delta t)$, which can be expressed in a more canonical form as $\kappa = pk_B n v_{\rm av} \Delta x$ in terms of the particle density $n = N/\Delta x$ and the average velocity, $v_{\rm av} = \Delta x/\Delta t$. Our model gives a value for the thermal conductivity similar to that found in the kinetic theory of gases [133], $\kappa = (1/3)k_B n v_{\rm av} \ell$, if Δx in our model corresponds to ℓ, the mean free path.

The factors of p and $1/3$ in our model and kinetic theory, respectively, can be reconciled by the following observation. Kinetic theory deals with the motion of particles in three dimensions so that each particle can move in 6 possible directions $(\pm x, \pm y, \pm z)$. As a result, only $1/6$ of the particles will contribute to the heat flux in our direction of interest. Also, on the plane of interest there are particles coming in from positive and negative directions. The factor of $1/6$ is increased by two to $1/3$. In contrast, in our model, the particles move with probability p or stay with probability $1 - p$. So the contribution to the flux comes from a fraction p of the particles. The origin of the numerical factors is thus clear.

The numerical factors of $1/3$ or p are not really important to the point we are trying to make. It is also not fair to read too much into this simple but illustrative model. The key point is that the simple model captures the main physical features of heat flow by appealing to the idea of summing over the weighted microtrajectories available to the system.

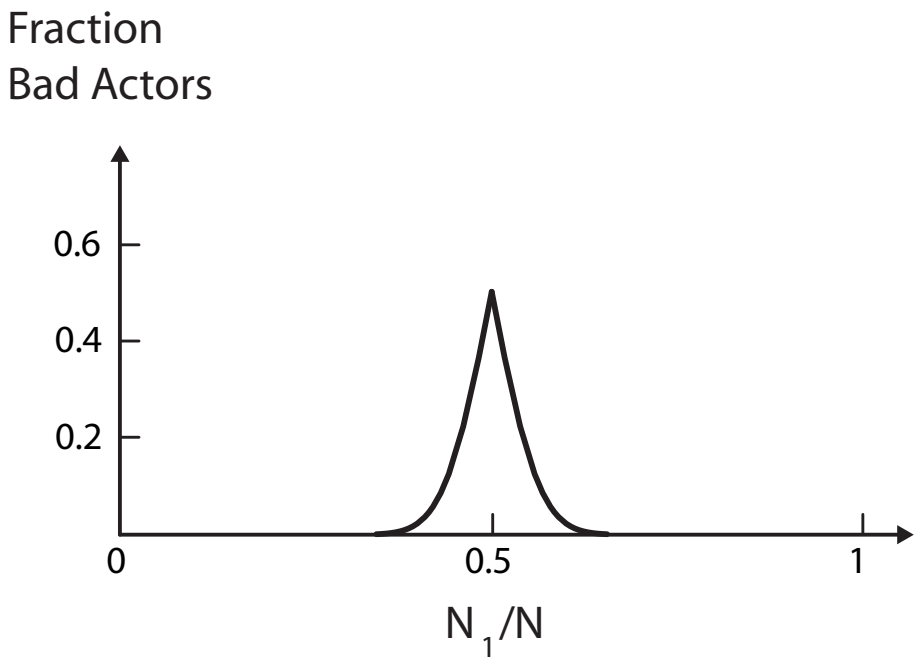

Figure 7.7: The fraction of all possible trajectories that go against the direction of the macroflux for $N = 100$. The fraction of bad actors is highest at $N_1 = N/2 = 50$.

7.5 Newtonian Viscosity

Another phenomenological law of gradient-driven transport is that of Newtonian viscosity [133]:

$$\tau = \eta \frac{dv_y}{dx}, \tag{7.31}$$

where τ is the shear stress that is applied to a fluid, dv_y/dx is the resultant shear rate, and the proportionality coefficient η is the viscosity of a Newtonian fluid. Whereas Fick's law describes particle transport and Fourier's law describes energy transport, Eq. 7.31 describes the transport (in the x-direction from the top moving plate toward the bottom fixed plate) of linear momentum in the y-direction (parallel to the plates) (see Fig. 7.8). In the same spirit as our simplified treatment of Fourier's law, the dog-flea model can be used as the basis of a particle transfer version of momentum transport. Suppose each particle in column 1 of Table 7.1 carries momentum mv_{y_1} along the y-axis and m_1^* particles hop from column 1 to 2 at time t, carrying with them some linear momentum. As before, we consider the simplest model for which every particle carries the same average momentum from the column it leaves to its destination column.

The flux J_p is the amount of y-axis momentum that is transported from one plane to the next

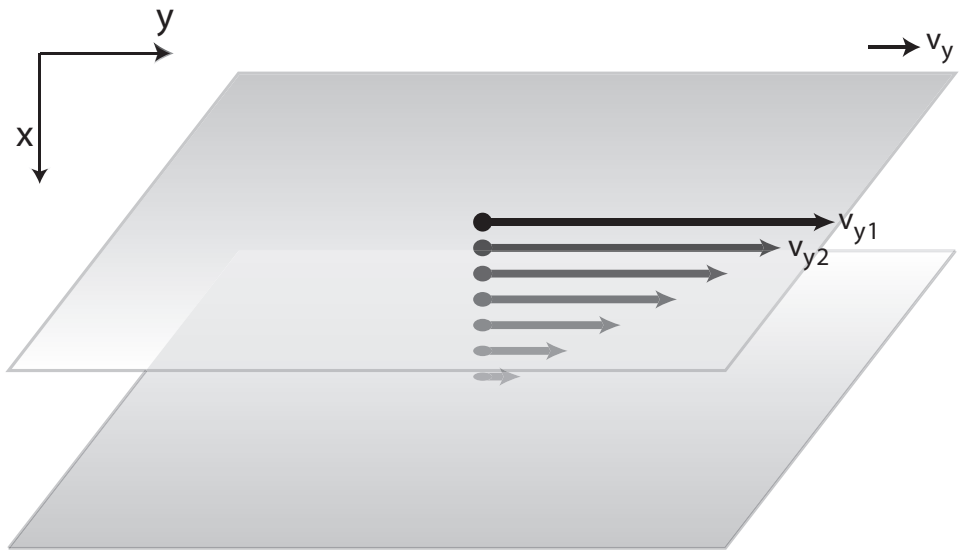

Figure 7.8: Illustration of Newton's law of viscosity. The fluid is sheared with a constant stress. The fluid velocity decreases continuously from its maximum value at the top of the fluid to zero at the bottom. There is thus a gradient in the velocity which can be related to the shear stress in the fluid.

in the x-direction per unit area:

$$\langle J_p \rangle = \frac{m_1^*}{\Delta t}(m v_{y_1}) - \frac{m_2^*}{\Delta t}(m v_{y_2}) = \frac{pm}{\Delta t}\left[N_1 v_{y_1} - N_2 v_{y_2}\right]. \tag{7.32}$$

If the number of particles is the same in both columns, $N/2 = N_1 = N_2$, Eq. 7.32 simplifies to

$$\langle J_p \rangle = \frac{pmN}{\Delta t}[v_{y_1} - v_{y_2}] = \eta \frac{\Delta v_y}{\Delta x}, \tag{7.33}$$

which is the Newtonian law of viscosity for this two-column model. The viscosity is predicted by this model to be $\eta = (pmN\Delta x)/(\Delta t)$. If we convert this result to the more canonical form, we have $\eta = pmnv_{\rm av}\Delta x$, where $n = N/\Delta x$ is the particle density and $v_{\rm av} = \Delta x/\Delta t$ is the average velocity. This form is equivalent to the value given by the kinetic theory of gases [133], $\eta = (1/3)mn\ell v_{\rm av}$, if Δx from our model equals ℓ. The numerical factors of $1/3$ and p in the kinetic theory and our model, respectively, have the same origin as discussed in in the context of heat flow. Note that this simple model based on molecular motions will clearly not be applicable to complex fluids where the underlying molecules possess internal structure.

7.6 Chemical Kinetics Within the Dog-Flea Model

Let us now look at chemical reactions using the dog-flea model. Chemical kinetics can be modeled using the dog-flea model when the fleas have preference for one dog over the other. Consider the reaction

$$A \underset{k_r}{\overset{k_f}{\rightleftharpoons}} B. \tag{7.34}$$

The time-dependent average concentrations $[A](t)$ and $[B](t)$ are often described by chemical rate equations [123]

$$\frac{d[A]}{dt} = -k_f[A] + k_r[B] \text{ and} \tag{7.35a}$$

$$\frac{d[B]}{dt} = k_f[A] - k_r[B], \tag{7.35b}$$

where k_f is the average conversion rate of an A to a B, and k_r is the average conversion rate of a B to an A. These rate expressions describe only average rates; they do not give the distribution of rates. Some As will convert to Bs faster than the average rate $k_f[A]$ predicts, and some will convert more slowly. Again we use the dog-flea model and consider the average concentrations and the fluctuations in concentrations. A particularly fruitful area for applications of the $A \rightleftharpoons B$ dynamics considered here is to problems involving molecular motors and ion channels.

We assume that dog 1 represents chemical species A and dog 2 represents chemical species B. The net chemical flux from 1 to 2 is given by $J_c = m_1^* - m_2^*$. What is different about our model for these chemical processes as compared to our previous situations is that now the intrinsic jump rate from column 1 (species A), p_1, is different than the jump rate from column 2, p_2. This difference reflects the fact that a forward rate can differ from a backward rate in a chemical reaction. We assume that the fleas have a different escape rate from each dog. Fleas escape from dog 1 at rate p_1, and fleas escape from dog 2 at rate p_2. Maximizing W_d gives $m_1^* = N_1 p_1$ and $m_2^* = N_2 p_2$, so the average flux (which is almost the same as the most probable flux because of the approximately symmetric nature of the binomial distribution) at time t is

$$\langle J \rangle = N_1 p_1 - N_2 p_2 = k_f[A] - k_r[B], \tag{7.36}$$

which is just the standard mass-action rate law expressed in terms of the mean concentrations. The mean values satisfy detailed balance at equilibrium ($\langle J \rangle = 0$ implies that $N_2/N_1 = p_1/p_2 = k_f/k_r$).

More interesting than the behavior of the mean chemical reaction rate is the behavior of the fluctuations. For example, if the number of particles is small, then even when $k_f[A] - k_r[B] > 0$, indicating an average conversion of As to Bs, the reverse can happen occasionally. When will these fluctuations be large? As in Section 7.3, we first determine the probability distribution of the flux

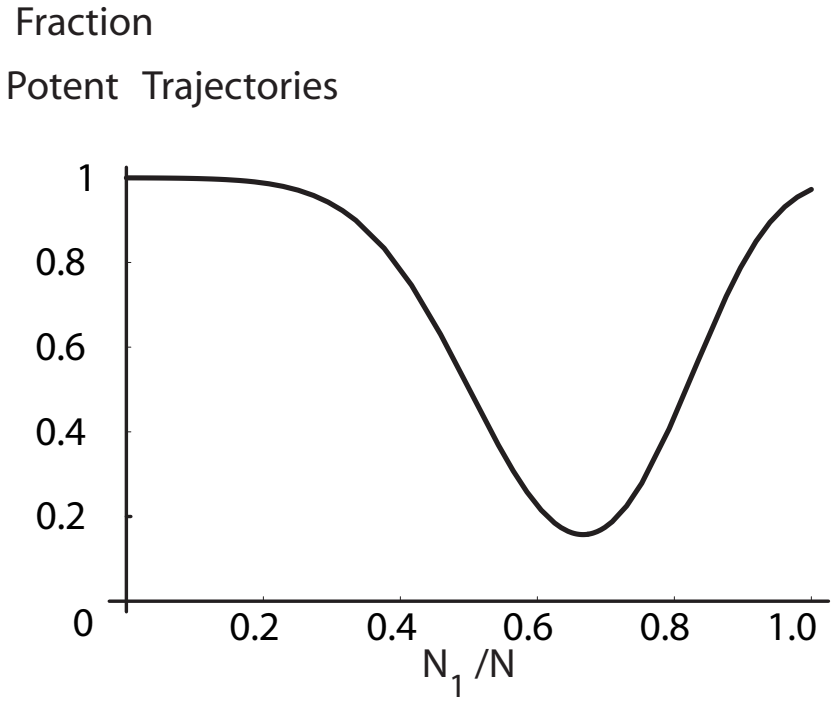

Figure 7.9: The fraction of potent trajectories Φ_{potent} as a function of N_1/N for $N_1+N_2 = N = 100$, and $p_1 = 0.1$ and $p_2 = 0.2$. The minimum value of the potency does not occur at $N_1/N = 0.5$, but at $N_1/N = 0.66$. This value of N_1/N also corresponds to its equilibrium value given by $p_2/(p_1+p_2)$.

J. In this case, the probability distribution becomes

$$P(J) = \frac{1}{\sqrt{2\pi(p_1q_1N_1 + p_2q_2N_2)}} \exp\Big(- \frac{(J - (N_1p_1 - N_2p_2))^2}{2(p_1q_1N_1 + p_2q_2N_2)}\Big). \tag{7.37}$$

We use this flux distribution function to consider the fluctuations in the chemical reaction. The relative variance in the flux is

$$\frac{\langle(\Delta J)^2\rangle}{\langle J\rangle^2} = \frac{\sqrt{N_1p_1q_1 + N_2p_2q_2}}{N_1p_1 - N_2p_2}. \tag{7.38}$$

As before, the main message is that when the system is not yet at equilibrium (that is, the denominator is nonzero), macroscopically large systems will have negligibly small fluctuations. The relative magnitude of the fluctuations scales approximately as $N^{-1/2}$. Let us also look at the potencies of microtrajectories as another window into the fluctuations. If we use Eq. (7.25) with p_1 and p_2, we

find that the fraction of trajectories that is impotent is

$$\Phi_{\text{impotent}} \approx \int_{-h}^{h} dJ \frac{1}{\sqrt{2\pi(N_1p_1q_1+N_2p_2q_2)}} \exp\left(\frac{-(J-(N_1p_1-N_2p_2))^2}{2(N_1p_1q_1+N_2p_2q_2)}\right) \text{ and} \quad (7.39)$$

$$= \frac{1}{2}\left(\text{erf}\left[\frac{h+(N_1p_1-N_2p_2)}{\sqrt{2(N_1p_1q_1+N_2p_2q_2)}}\right] + \text{erf}\left[\frac{h-(N_1p_1-N_2p_2)}{\sqrt{2(N_1p_1q_1+N_2p_2q_2)}}\right]\right). \quad (7.40)$$

For $N_1 + N_2 = N = 100$ and $p_1 = 0.1$ and $p_2 = 0.2$, $\Phi_{\text{potent}} = 1 - \Phi_{\text{impotent}}$ is shown in Fig. 7.9 as a function of N_1/N.

7.7 Derivation of the Dynamical Distribution Function from Maximum Caliber

We have used the binomial distribution function W_d as the basis for our treatment of stochastic dynamics. The maximum caliber assumption is that if we find the value of W_d that is a maximum with respect to the microscopic trajectories, this value will give the macroscopically observable flux. We now restate this assumption more generally in terms of the probabilities of the trajectories.

Let $P(i)$ be the probability of a microtrajectory i during the interval from time t to $t + \Delta t$. A microtrajectory is a specific set of fleas that jump; for example microtrajectory $i = 27$ might be the case for which fleas 4, 8, and 23 jump from dog 1 to 2. We take as a constraint the average number of jumps, $\langle m \rangle$, the macroscopic observable. The quantity $m_i = 3$ in this case indicates that trajectory i involves 3 fleas jumping. We express the caliber $\mathcal{C}$ as

$$\mathcal{C} = \sum_i P(i) \ln P(i) - \lambda \sum_i m_i P(i) - \alpha \sum_i P(i), \quad (7.41)$$

where λ is the Lagrange multiplier that enforces the constraint of the average flux and α is the Lagrange multiplier that enforces the normalization condition that the $P(i)$s sum to one. Maximizing the caliber gives the populations of the microtrajectories,

$$P(i) = e^{-\alpha - \lambda m_i}. \quad (7.42)$$

Note that the probability $P(i)$ of the ith trajectory depends only on the total number m_i of the jumping fleas. Also, all trajectories with the same m_i have the same probabilities. In the same way that it is sometimes useful in equilibrium statistical mechanics to switch from microstates to energy levels, we now express the population $P(i)$ of a given microtrajectory in terms of $\rho(m)$, the fraction of all the microtrajectories that involve m jumps during this time interval,

$$\rho(m) = g(m)Q(m), \quad (7.43)$$

where $g(m) = N!/[m!(N-m)!]$ is the density of trajectories with flux m (in analogy with the density of states for equilibrium systems) and $Q(m)$ is the probability $P(i)$ of microtrajectory i with $m_i = m$. In other words, i denotes a microtrajectory (a specific set of fleas jumping) and m denotes a microprocess (the number of fleas jumping). The total number of is associated with a given m is $g(m)$. It can also be easily seen that

$$\sum_i P(i) \qquad = \sum_{m=0}^{N} g(m)Q(m) = \sum_{m=0}^{N} \rho(m) = 1 \text{ and} \tag{7.44}$$

$$\langle m \rangle \quad = \sum_i m_i P(i) = \sum_{m=0}^{N} m g(m) Q(m) = \sum_{m=0}^{N} m\rho(m). \tag{7.45}$$

Thus the distribution of jump-processes written in terms of the jump number m is

$$\rho(m) = \frac{N!}{m!(N-m)!} e^{-\alpha} e^{-\lambda m}. \tag{7.46}$$

The Lagrange multiplier α can be eliminated by summing over all trajectories and requiring that $\sum_{m_i=0}^{N} \rho(m_i) = 1$, that is,

$$e^{\alpha} = \sum_m^N g(m) e^{-\lambda m} = \sum_m^N \frac{N!}{m!(N-m)!} e^{-\lambda m} = (1 + e^{-\lambda})^N. \tag{7.47}$$

We combine Eqs. (7.46) and (7.47) to obtain

$$\rho(m) = \frac{N!}{m!(N-m)!} \frac{e^{-\lambda}}{1 + e^{-\lambda}}. \tag{7.48}$$

If we now let

$$p = \frac{e^{-\lambda}}{1 + e^{-\lambda}}, \tag{7.49}$$

we obtain

$$p^m = \frac{e^{-\lambda m}}{[1 + e^{-\lambda}]^m} \tag{7.50}$$

and

$$(1-p)^{N-m} = \frac{1}{[1 + e^{-\lambda}]^{N-m}}. \tag{7.51}$$

If we combine Eqs. (7.48), (7.50), and (7.51), we find the simple form

$$\rho(m) = \frac{N!}{m!(N-m)!} p^m (1-p)^{(N-m)}, \tag{7.52}$$

which appears in Eq. (7.11) and which we have used throughout this paper.

7.8 Onsager Reciprocity Relations For a Modified Dog-Flea Model

In Chapter 2 we briefly discussed about the Onsager reciprocal relations, which relates the coupling between two different types of fluxes. We also briefly mentioned in Chapter 6 that these relations fall out naturally from the maximum caliber principle [7, 8]. In this section we explore the simplest dynamical model in which there is a coupling of two different types of flows that can be explored both near equilibrium and far from equilibrium. Our model is a variant of the earlier used dog-flea model, which we will use to treat the problem of coupled dynamical flows by the application of the principle of maximum caliber.

7.8.1 The hot-dog model and the principle of maximum caliber

As before, consider dogs 1 and 2 with N_1 and N_2 fleas, respectively, at time t. The fleas here are of two types: the *ground-state* fleas (GS) or the *excited-state* fleas (ES). The ES fleas are higher in energy than GS fleas by an amount ϵ. A flea can be in one of the four possible states: $1_{\rm GS}, 1_{\rm ES}, 2_{\rm GS}$, or $2_{\rm ES}$, depending on whether it sits on dog-1 or dog-2 and if it is in GS or ES. The fleas on dog-1 are at temperature T_1, and those on dog-2 at temperature T_2 (see Figure 7.10). As the present model differs from the simpler Dog-Flea model in our inclusion of thermal excitation, we call this the Hot Dog (HD) Model.

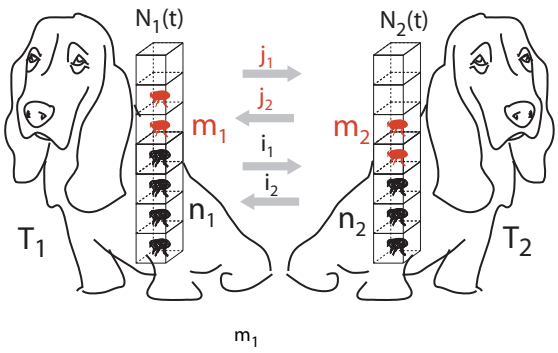

Figure 7.10: Schematic of the simple 2-state "hot-dog" model. On each dog the fleas can be in two states, the excited state (ES) and the ground state (GS). The total number of fleas in the ES of dog-1 and dog-2 (red fleas) are m_1 and m_2, respectively, while the total number of fleas in the GS of dog-1 and dog-2 (black fleas), respectively, are n_1 and n_2 respectively. The red fleas are greater in energy than the black fleas by an amount ϵ. The temperatures of the fleas on dog-1 and dog-2 are T_1 and T_2, respectively.

The occupancy number of the fleas in each state are denoted by the following convention:

- m_1 ES fleas are on Dog 1.

- n_1 GS fleas are on Dog 1.
- m_2 ES fleas are on Dog 2.
- n_2 GS fleas are on Dog 2.

The total number of fleas on dog-1 and dog-2 are, respectively, given by

$$N_1 = n_1 + m_1 \tag{7.53}$$

and

$$N_2 = n_2 + m_2. \tag{7.54}$$

Further, the GS and ES fleas are in thermal equilibrium on each dog, i.e, for dog-1

$$\frac{m_1}{n_1} = \exp(-\epsilon/kT_1) \tag{7.55}$$

and for dog-2

$$\frac{m_2}{n_2} = \exp(-\epsilon/kT_2). \tag{7.56}$$

We wish to obtain equations for the transport of fleas between the two dogs. A flea on a given dog can jump onto another dog within a time interval Δt according to a few simple rules:

- In the time-interval Δt a flea can either stay put on its current dog, or jump to the other dog.
- In the case of a jump, an ES (GS) flea remains an ES (GS) flea within the time-interval Δt.
- A flea can change its thermal state only after it has arrived on a dog, where it then equilibrates rapidly (compared to the jump rate) between the ES and the GS.
- The *intrinsic jump rate* and *intrinsic stay rate* is p and $1 - p$, respectively, for the fleas.

We now adopt Jaynes' principle of maximum caliber for computing the dynamics of the model. To evaluate the space of trajectories for the model we introduce the following variables:

- i_1 fleas jump from the GS of dog-1 to the GS of dog-2.
- j_1 fleas jump from the ES of dog-1 to the ES of dog-2.
- i_2 fleas jump from the GS of dog-2 to the GS of dog-1.
- j_2 fleas jump from the ES of dog-2 to the ES of dog-1.

The rest of the fleas stay put on their respective dogs. Thus, a given combination of (i_1, j_1, i_2, j_2) defines a trajectory Γ of duration Δt for the model. As in the previous sections, we maximize the entropy over the possible trajectories. We subject subject the entropy to two constraints:

1. **Average particle flux constraint**: The particle flux can be resulted by the flux of both ES and GS particles. The average particle flux is $\sum_\Gamma p_\Gamma (i_1 + j_1 - i_2 - j_2)$.

2. **Average heat-flux constraint**: Since the heat flux is possible only by the motion of ES fleas, the average heat flux is $\sum_\Gamma p_\Gamma \epsilon (j_1 - j_2)$.

As explained in the previous sections, we now evaluate the intrinsic jump-rate prior:

- The prior for the jump of i_i GS particles from dog-1 to dog-2 is $p^{i_1}(1-p)^{(n_1 - i_1)}$.
- The prior for the jump of j_1 ES particles from dog-1 to dog-2 is $p^{j_1}(1-p)^{(m_1 - j_1)}$.
- The prior for the jump of i_2 GS particles from dog-1 to dog-22 is $p^{i_2}(1-p)^{(n_2 - i_2)}$.
- The prior for the jump of j_2 ES particles from dog-1 to dog-2 is $p^{j_2}(1-p)^{(m_2 - j_2)}$.

The total probability prior for the trajectory will be a product of all these expressions. The caliber for the process can now be written as

$$\begin{aligned}\mathcal{C} &= \sum_\Gamma p_\Gamma \ln \left(\frac{p_\Gamma}{p^{i_1}(1-p)^{(N_1 - i_1)} p^{j_1}(1-p)^{(m_1 - j_1)} p^{i_2}(1-p)^{(N_2 - i_2)} p^{j_2}(1-p)^{(m_2 - j_2)}} \right) \\ &\quad - \lambda_e \sum_\Gamma p_\Gamma \epsilon (j_1 - j_2) - \lambda_d \sum_\Gamma p_\Gamma (i_1 + j_1 - i_2 - j_2),\end{aligned}$$

where Γ corresponds to the combination (i_1, i_2, j_1, j_2). The multipliers λ_d and λ_e correspond to the "average particle flux" and the "average heat flux," respectively. The partition function can be evaluated as

$$\begin{aligned}Z &= (1 - p + p\exp(\lambda_d + \epsilon\lambda_e))^{m_1} (1 - p + p\exp(\lambda_d))^{n_1} (1 - p + p\exp(-\lambda_d - \epsilon\lambda_e))^{m_2} \times ... \\ &\times (1 - p + p\exp(-\lambda_d))^{n_2} \qquad (7.57)\end{aligned}$$

The average flux of fleas is given by

$$\langle J_d \rangle = \frac{\partial \ln Z}{\partial \lambda_d}. \qquad (7.58)$$

while the average flux of heat is given by

$$\langle J_e \rangle = \frac{\partial \ln Z}{\partial \lambda_e} \qquad (7.59)$$

Thus,

$$\begin{aligned}\langle J_d\rangle &= \frac{m_1 p\exp(\lambda_d+\epsilon\lambda_e)}{1-p+p\exp(\lambda_d+\epsilon\lambda_e)}+\frac{n_1 p\exp(\lambda_d)}{1-p+p\exp(\lambda_d)}-\frac{m_2 p\exp(-\lambda_d-\epsilon\lambda_e)}{1-p+p\exp(-\lambda_d-\epsilon\lambda_e)}\ldots \\ &- \frac{n_2 p\exp(-\lambda_d)}{1-p+p\exp(-\lambda_d)} \end{aligned} \tag{7.60}$$

and

$$\langle J_e\rangle = \frac{m_1 p\epsilon\exp(\lambda_d+\epsilon\lambda_e)}{1-p+p\exp(\lambda_d+\epsilon\lambda_e)}-\frac{m_2 p\epsilon\exp(-\lambda_d-\epsilon\lambda_e)}{1-p+p\exp(-\lambda_d-\epsilon\lambda_e)}. \tag{7.61}$$

Within the limitations of our model, these expressions for flux are completely general and apply arbitrarily far from equilibrium. As explain in Chapter 6, we interpret the Lagrange multipliers λ_d and λ_e as the driving forces for the particle and the heat diffusion, respectively.

7.8.2 Proving the Onsager Reciprocal Relations

The reasons for choosing this particular model here are:

1. It applies not just near equilibrium, but rather, we can get exact expressions for its behavior over the full nonequilibrium range, including far from equilibrium.

2. We believe that this is the very simplest microscopic model for coupled flow dynamics, which is essential if we want to study the reciprocal relations.

We first consider the behavior of the model near equilibrium, which has been the main focus of much of the past work with the reciprocal relations [25]. The average flux of particles, $\langle J_d(\lambda_d,\lambda_e)\rangle$ and the average flux of energy, $\langle J_e(\lambda_d,\lambda_e)\rangle$, can each be expressed as a function of the two Lagrange multipliers, λ_d and λ_e, that represent forces acting on the system (see below). We expand around $\lambda_d = 0$ and $\lambda_e = 0$ to obtain:

$$\langle J_d\rangle = \langle J_d(0,0)\rangle + \left.\frac{\partial\langle J_d\rangle}{\partial\lambda_d}\right|_{0,0}\lambda_d + \left.\frac{\partial\langle J_d\rangle}{\partial\lambda_e}\right|_{0,0}\lambda_e \tag{7.62}$$

$$\langle J_e\rangle = \langle J_e(0,0)\rangle + \left.\frac{\partial\langle J_d\rangle}{\partial\lambda_d}\right|_{0,0}\lambda_d + \left.\frac{\partial\langle J_e\rangle}{\partial\lambda_e}\right|_{0,0}\lambda_e. \tag{7.63}$$

Written in the Onsager form, we have

$$\langle J_d\rangle = \langle J_d(0,0)\rangle + L_{11}\lambda_d + L_{12}\lambda_e \tag{7.64}$$

and

$$\langle J_e \rangle = \langle J_e(0,0) \rangle + L_{21}\lambda_d + L_{22}\lambda_e. \tag{7.65}$$

The virtues of the maximum caliber principle here are: (1) that it makes deriving the reciprocal relations very simple and (2) it shows the direct resemblance of the reciprocal relations of dynamics to Maxwell's relations of equilibrium thermodynamics [25]. From equations 7.58 and 7.59, we have

$$L_{12} = \left.\frac{\partial \langle J_d \rangle}{\partial \lambda_e}\right|_{0,0} = \left.\frac{\partial^2 \ln Z}{\partial \lambda_e \partial \lambda_d}\right|_{0,0} \tag{7.66}$$

and

$$L_{21} = \left.\frac{\partial \langle J_e \rangle}{\partial \lambda_d}\right|_{0,0} = \left.\frac{\partial^2 \ln Z}{\partial \lambda_d \partial \lambda_e}\right|_{0,0} \tag{7.67}$$

Thus, due to the equality of mixed derivatives, it can be seen from Eqs. 7.66 and 7.67 that $L_{12} = L_{21}$.

Within the present model, the Onsager reciprocal relation, $L_{12} = L_{21}$, also holds arbitrarily far from equilibrium. This is readily obtained from the following Maxwell-like relationship:

$$L_{12} = \frac{\partial \langle J_d \rangle}{\partial \lambda_e} = \frac{\partial^2 \ln Z}{\partial \lambda_e \partial \lambda_d} \tag{7.68}$$

and

$$L_{21} = \frac{\partial \langle J_e \rangle}{\partial \lambda_d} = \frac{\partial^2 \ln Z}{\partial \lambda_d \partial \lambda_e} \tag{7.69}$$

7.8.3 Obtaining the Driving Forces for the Model

In the previous section we provided a simple derivation of the Onsager reciprocal relations. Here, we will evaluate the corresponding kinetic coefficients in terms of the parameters of the underlying microscopic model. Using Eq. 7.60, we have

$$\begin{aligned} L_{11} = \left.\frac{\partial \langle J_d \rangle}{\partial \lambda_d}\right|_{0,0} &= m_1 p - m_1 p^2 + n_1 p - n_1 p^2 + m_2 p - m_2 p^2 + n_2 p - n_2 p^2 \\ &= p(1-p)(m_1 + n_1 + m_2 + n_2) = 2p(1-p)(N_1 + N_2), \\ &= 2p(1-p)N, \end{aligned} \tag{7.70}$$

where we have used $N_1 + N - 2$ to be equal to N, the total number of fleas on dog-1 and dog-2 combined. Now, to evaluate L_{12} we use Eq 7.61 to obtain

$$L_{12} = \left.\frac{\partial \langle J_d \rangle}{\partial \lambda_e}\right|_{0,0} = \epsilon p(1-p)(m_1 + m_2). \tag{7.71}$$

We saw earlier that L_{12} equals L_{21} and hence do not need to evaluate it separately. To obtain L_{22}, we use equation 7.61:

$$L_{22} = \left.\frac{\partial\langle J_e\rangle}{\partial\lambda_e}\right|_{0,0} = \epsilon^2 p(1-p)(m_1+m_2). \tag{7.72}$$

Thus we have obtained the values of the kinetic coefficients for our simple hot-dog model.

7.9 Summary and Comments

We have shown how to derive the phenomenological laws of nonequilibrium transport, including Fick's law of diffusion, Fourier's law of heat conduction, the Newtonian law of viscosity, and the mass-action laws of chemical kinetics from a simple physical foundation. We used the dog-flea model for describing how particles, energy, or momentum can be transported across a plane. Using a variant of the dog-flea model we also obtained Onsager reciprocal relations describing the coupling between the particle diffusion and the heat diffusion. We combined this simple model with the principle of maximum caliber, a dynamical analog of the principle of maximum entropy for the laws of equilibrium. For dynamics we focus on microtrajectories rather than microstates and maximize a dynamical entropy-like quantity, subject to an average flux constraint. In this way, maximizing the caliber is the dynamical equivalent of minimizing a free energy for predicting equilibria. A particular value of this approach is that it also gives us fluctuation information, not just averages. In diffusion, for example, sometimes the flux can be a little higher or lower than the average value expected from Fick's law. These fluctuations can be important for biology and nanotechnology, where the numbers of particles can be very small and therefore where there can be significant fluctuations in rates, around the average.

Chapter 8

The Dynamics of Two-state Systems

In the previous chapter we introduced Jaynes' principle of maximum caliber and discussed how it can be utilized to model systems far from equilibrium. When we have a classical (or a quantum) system with a well defined Hamiltonian, the maximum caliber formalism gives us the time-evolution of macro-variables. It would have been extremely gratifying if that were the end of the story. On the other hand, the major drawback of writing down an exact description (classical or quantum) is that not only is it almost impossible to analytically solve the problem, but the exact solution of even an approximate model is rare. Fortunately, we saw in Chapter 6 that the maximum caliber principle need not be restricted to such full blown description. In fact, we can develop our own simple models to describe a particular system of interest.

Consider, for example, the case of the Ising model in equilibrium statistical mechanics, which was introduced to describe magnetic phase transition [26]. Although the relation of this model with the actual quantum model describing the evolution of quantum spins is evident, the Ising model is still a coarse-grained approximation to the underlying reality. Despite the drastic coarse-graining, the Ising model has been truly instrumental in modeling critical phenomena and has provided an insightful description of disparate systems such as the lattice gases and binary mixtures [26]. This particular argument is just to drive home the point that simple coarse-grained models are capable of providing insight into problems. The lack of generality of these models is made up for by the interesting physics they produce for specific cases [147]. Like the Ising model, such models are also capable of generating analogies with seemingly unrelated problems. Our goal is to capitalize on this observation and develop simple coarse-grained models for a few representative non-equilibrium systems. Once we specify the underlying microscopic dynamics and the macroscopic constraints, as explained in Chapter 6, the maximum caliber principle provides us with a recipe to obtain the probabilities of the micro-trajectories. A concern that needs to be answered is about the appropriateness of the model and the underlying microscopic dynamics. Also, since we coarse-grain our model, the constraints

that may have been obvious in the complete classical (or quantum) setting may have a very different coarse-grained form. But this is not too much of a price to pay, considering the fact that we obtain nice closed-form solutions from these coarse-grained models. In this chapter, we will study a few problems with coarse-grained microscopic dynamics.

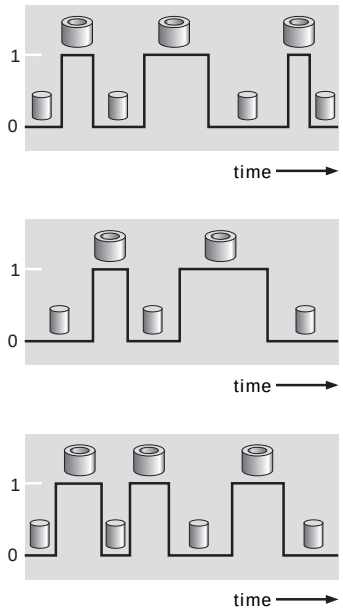

Figure 8.1: Description of the microtrajectories for the two-state system $A \leftrightarrow B$. For mathematical convenience, the time is discretized into time steps of Δt, which can be thought of as the time-resolution of the corresponding experiment.

Certain physical systems have dynamics with a signature quantity, which assumes a set of discrete values as a function of time. The discreteness of these values is intrinsically related to the internal states of the system. For example, in the case of ion channels, the ion channels are either closed or open. The ion-current flowing through the channel either has a finite value or is zero when the channel is open or closed, respectively. The ion-current hence represents the state of the ion channel. We can represent the temporal states of such physical systems with such finite-state time trajectories (see Fig. 8.1). The principle of maximum caliber can then be applied to these trajectories in order to obtain their probabilities. These probabilities in turn can be used to quantify the dynamics of the physical system they represent.

The outline of this chapter is as follows. In Section 8.1 we discuss the class of two state trajectories in which the system stays in state-1 for a certain time period and then permanently switches to state-2. In particular, we discuss the application of the maximum caliber principle to this class of trajectories in order to explain the dynamics of processive molecular motors. In Section 8.2 we discuss another class of two-state trajectories where the system continuously switches between states-1 and 2. We then apply the maximum caliber principle over this set of trajectories to elucidate the

dynamics of opening and closing of ion channels when the applied voltage can be time-dependent. Section 8.2.1 discusses an experiment, currently in progress in our lab, on the diffusion of a Brownian particle in dual-laser traps. The experiment is expected (as a test ground) to check our ideas on the application of the maximum caliber principle to the class of two state trajectories.

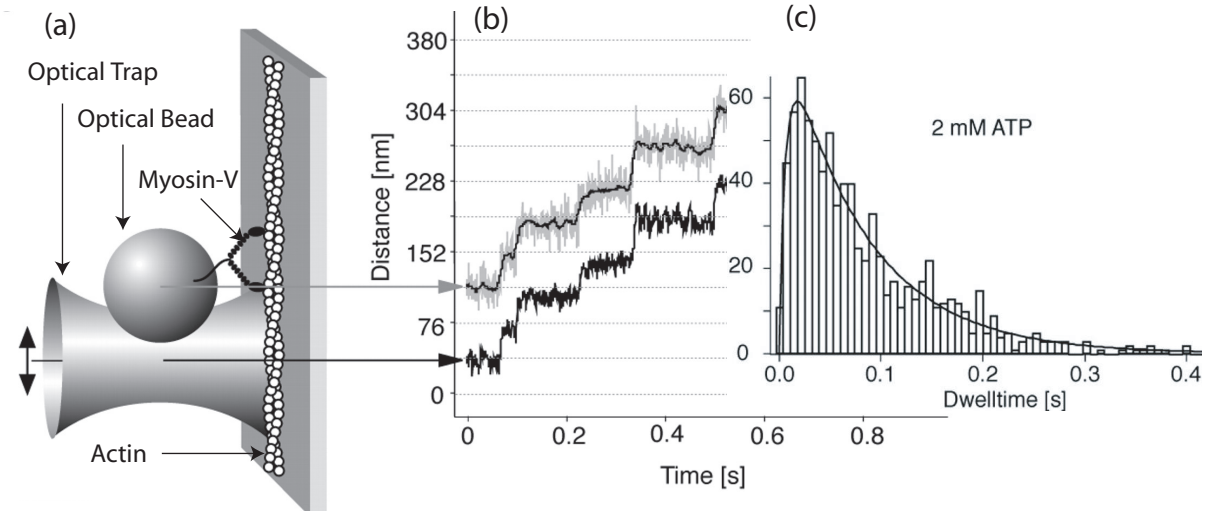

Figure 8.2: Measurements of myosin-V motor dynamics. (a)The molecular motor myosin-V moves over actin by consuming ATP. An optical bead is attached to the myosin molecule. The bead is then held in an optical trap and a force is exerted on myosin. (b) The motion of myosin-V occurs in a series of steps of around 38 nm, an experimental observable. The transition from 1 to 0, as described in Fig. 8.3, corresponds to the step taken by the motor. (c) Myosin-V waits for a certain amount of time τ before taking a step. The waiting time distribution is a way of summarizing the behavior of different separate trajectories and transitions. The stepping behavior depends on the ATP concentration and on the applied force (figure taken from Rief et al. [136]).

8.1 Two State System With Single Step Trajectories

We begin with the class of systems (see Fig. 8.2) whose time-trajectories exhibit the type of behavior as shown in Fig. 8.3. These systems show a microscopic behavior that can be categorized as two-state dynamics of the form $A \rightarrow B$. The transformation of A into B is microscopically irreversible in the sense that every microscopic trajectory of this two-state system, as shown in Fig. 8.3, shows a permanent jump from state A to state B after a certain time τ. This time is called the waiting time for the process. A classic example of such behavior is the process of radioactive decay, where a radioactive material A emits a particle and gets converted into B. In the biological setting such behavior is also seen in the case of processive molecular motors, for example [112]. Take the case of the molecular motor myosin-V. As briefly discussed in Chapter 1, this motor moves along actin fibers in the cells by consuming ATP molecules. The motor moves along actin in distinct steps (see

Fig. 8.2). This stepping process is stochastic, with each step taking place independently of the earlier ones. The behavior of each step is, thus, similar to that described in Fig. 8.3. Myosin-V waits for a certain waiting time τ before taking the step. Now, as is shown in Fig. 8.2, the waiting time τ for such processes is not a deterministic quantity and has a probabilistic distribution $p(\tau)$. Often, the observed distribution for such processes is the so called exponential distribution given by

$$p(\tau) = \frac{1}{\tau_0} \exp\left(-\tau/\tau_0\right). \tag{8.1}$$

It can be seen by direct integration that the mean life-time $\langle\tau\rangle$ is given by,

$$\begin{aligned} \langle\tau\rangle &= \int_0^\infty \tau \times \frac{1}{\tau_0} \exp\left(-t/\tau_0\right) d\tau. \\ &= \tau_0. \end{aligned} \tag{8.2}$$

Thus, the quantity τ_0 is the mean life-time of the process. This quantity is also termed the half-life period of the process.

One of the most elementary derivations using the maxent methods is that of the exponential distribution. Suppose the only thing we know about the process is the mean life time $\langle\tau\rangle = \tau_0$ then what can we say about the probability distribution $p(\tau)$ for the allowed waiting times τ? To answer that question, we write down the information entropy $S = -\int_0^\infty p(\tau) \ln p(\tau) d\tau$ and maximize it, subject to the applied constraint $\langle\tau\rangle = \int_0^\infty \tau p(\tau) d\tau = \tau_0$. For this purpose, we use the method of Lagrange multipliers as demonstrated in Chapter 6. We thus maximize the following expression

$$S = -\int_0^\infty p(\tau) \ln p(\tau) d\tau + \lambda \int_0^\infty p(\tau) d\tau - \mu \int_0^\infty \tau p(\tau) d\tau. \tag{8.3}$$

Here, the second integral is the normalizing constraint to ensure that $\int_0^\infty p(\tau) d\tau = 1$, while the last constraint corresponds to the mean life time constraint. To maximize this expression we take a differential δS of S and make it equal to zero. Thus

$$\delta S = \int_0^\infty \left[(-1 - \ln p(\tau)) + \lambda + \mu\right] \delta p(\tau) d\tau = 0. \tag{8.4}$$

Since this expression is valid for arbitrary functions $p(\tau)$ it means that the integrand equals zero, i.e.,

$$\begin{aligned} -1 - \ln p(\tau) + \lambda + \mu\tau &= 0, \\ \implies p(\tau) &= \exp(-1 + \lambda) \times \exp(\mu\tau). \end{aligned} \tag{8.5}$$

Using the normalizing constraint, $\int_0^\infty p(\tau)dt = 1$, we obtain

$$\exp(-1+\lambda) \times \frac{1}{\mu} = 1.$$

Using this value in Eq. 8.5 we obtain

$$p(\tau) = \mu \times \exp(-\mu\tau). \tag{8.6}$$

Using the second constraint $\int_0^\infty t \times p(\tau) = \tau_0$ and performing the simple integral we can see that $\mu = 1/\tau_0$. The distribution then is the same as in Eq. 8.1. Thus, we have obtained the standard exponential distribution using maxent with just the mean time constraint.

We can solve this same problem by using the trajectory entropy (or the caliber) approach as explained in Section 6. Indeed, the calculation performed above can be entirely reinterpreted as resulting from summing over all the possible microscopic trajectories of the system. The set of trajectories for this $A \to B$ is as shown in Fig. 8.3. Since τ, the *waiting time* after which the system moves from state A to state B (represented by 1 and 0, respectively), distinguishes one trajectory from the other, the trajectory is completely represented by τ. Consider all such trajectories ranging in duration from $\tau = -$ to $\tau = T$. To keep the notation clear, let us denote each such trajectory by τ. With the application of proper constraints, the principle of maximum caliber will provide us with the probabilities of the microtrajectories. We also saw in the previous paragraph that each microtrajectory Γ is represented by the corresponding waiting time τ. Hence, knowing the probabilities of micro trajectories we can find the distribution of waiting times τ for the system. The waiting time constraint is given as

$$\langle\tau\rangle = \sum_\tau \tau p_\tau, \tag{8.7}$$

where τ is the waiting time associated with the trajectory τ. The caliber S of the system is given by writing the entropy over its trajectories, i.e., $S = -\sum_\tau p_\tau \ln p_\tau$. The caliber S subject to the mean time constraint Eq. 8.7:

$$S = -\sum_\tau p_\tau \ln p_\tau + \lambda \sum_\tau p_\tau - \mu \sum_\tau \tau p_\tau. \tag{8.8}$$

As in the earlier case, the constraint associated with the multiplier λ is the normalization constraint, while the constraint associated with the multiplier μ is the average waiting time constraint. Upon

differentiating and putting $\delta S = 0$, we obtain

$$\begin{aligned} \delta S &= \sum_{\tau}(-1 - \ln p_\tau + \lambda - \mu\tau p_\Gamma = 0, \text{ and} \\ \implies p_\tau &= \exp(-1+\lambda) \times \exp(-\mu\tau). \end{aligned} \tag{8.9}$$

Using the standard procedure as shown in the previous example, we obtain,

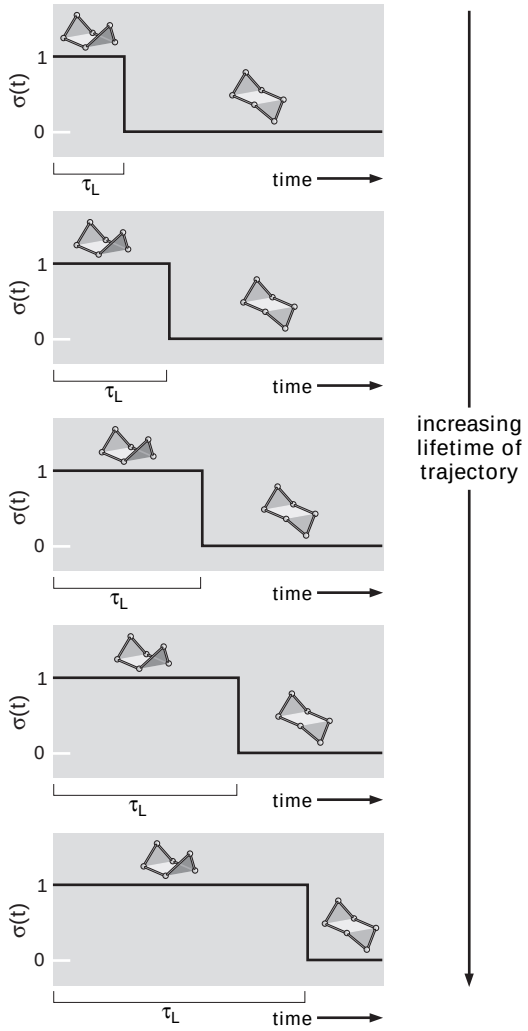

Figure 8.3: Description of the microtrajectories for the two-state system $A \rightarrow B$. The system makes a transition from state 1 to state 0 after a time τ_{L}.

$$\exp(-1+\lambda) = \frac{1}{\sum_\tau \exp(-\mu\tau)}. \tag{8.10}$$

The term in the denominator is *like* the partition function Z we saw in equilibrium statistical mechanics. We have deliberately used the phrase *like partition function* because the partition function involves the sum over microstates, while this involves sum over trajectories. But just to limit the no-

tations and terminologies, unless stated otherwise, we will refer to this sum as the partition function. Using Eqs. 8.9 and 8.10, the probability of a trajectory τ is

$$p_\tau = \frac{\exp(-\mu\tau)}{\sum_\tau \exp(-\mu\tau)}. \tag{8.11}$$

Since τ assumes continuous values between 0 and L, it is convenient to convert the sum in the denominator of the above equation to an integral, $\int_0^\tau$. Upon converting to an integral, the partition function $Z(\mu) = \sum_\Gamma \exp(\mu\tau)$ can be evaluated as

$$Z(\mu) \quad = \quad \int_0^\infty \exp(-\mu\tau)d\tau = \frac{1}{\mu}, \tag{8.12}$$

where we have taken $\mu < 0$. Converting the summation for the mean time $\langle\tau\rangle$ in Eq. 8.7 to an integral, we obtain

$$\begin{aligned} \langle\tau\rangle &= \mu\int_0^\infty \tau\exp(-\mu\tau), \\ \implies \mu &= \langle\tau\rangle, \end{aligned} \tag{8.13}$$

which is, of course, the same result we obtained earlier. Despite the simplicity, this calculation gives us a very good insight into how we can formulate a physical model with trajectories and apply the principle of maximum caliber. As will be seen later in this section, even with this very simple model we can apply time-dependent constraints and, hence, can model the problems with time-dependence.

In both the calculations performed so far we modeled processes of the form $A \to B$. It is quite possible that there is an intermediate state C such that the actual process is $A \to C \to B$ with waiting times τ and t, respectively. In such a case there might be two observables, i.e., the mean time τ_0 for $A \to B$, and t_0 for the process $C \to B$. We can follow the procedure used in Eq. 8.3. The probability distribution, $p(t,\tau)$, for observing a waiting time of τ and t, respectively, for the processes $A \to C$, and $C \to B$ will have two variables. Similar to equation Eq. 8.3 we write down the entropy, but now subject to two constraints $\langle\tau\rangle = \tau_0$, and $\langle t\rangle = t_0$. The entropy is

$$\begin{aligned} S &= -\int_0^\infty\int_0^\infty p(t,\tau)\ln p(t,\tau)dtd\tau + \lambda\int_0^\infty\int_0^\infty p(t,\tau)dtd\tau \\ &+ \mu_1\lambda\int_0^\infty\int_0^\infty tp(t,\tau)dtd\tau + \mu_2\lambda\int_0^\infty\int_0^\infty \tau p(t,\tau)dtd\tau. \end{aligned} \tag{8.14}$$

Upon maximizing the entropy by the standard method used earlier, we obtain

$$p(t,\tau) = \exp(-1+\lambda)\times\exp(\mu_1 t + \mu_2\tau). \tag{8.15}$$

Performing simple integrations as before we can see that $\exp(-1+\lambda) = \mu_1 \times \mu_2$, $\mu_1 = -1/t_0$ and

$\mu_2 = 1/\tau_0$. The probability distribution $p(t,\tau)$ will, hence, be

$$p(t,\tau) = \frac{1}{t_0\tau_0}\exp\left(-\frac{t}{t_0} - \frac{\tau}{\tau_0}\right). \tag{8.16}$$

Thus, using these two constraints, we have obtained the probability distribution $p(t,\tau)$ when there is one intermediate state. Now comes the interesting question: what if we want to overlook the intermediate state C and straightaway evaluate the probability distribution for the waiting time $t+\tau$, which we call $t_{\text{effective}}$, the time required to switch from state A to state B? To evaluate this distribution $P(t_{\text{effective}})$ we will have to integrate $p(t,\tau)$ over all the times t and τ such that for a given t, the value of τ is $t_{\text{effective}} - t$. Thus, t can take all the values from 0 to $t_{\text{effective}}$, and τ is simply $t_{\text{effective}} - t$. This amounts to evaluating the following integral

$$\begin{aligned} P(t_{\text{effective}}) &= \int_0^{t_{\text{effective}}} p(t, t_{\text{effective}} - t)dt \text{ and} \\ &= \frac{1}{t_0 - \tau_0}\left[\exp\left(-\frac{t_{\text{effective}}}{t_0}\right) - \exp\left(-\frac{t_{\text{effective}}}{\tau_0}\right)\right]. \end{aligned} \tag{8.17}$$

Thus, we obtain the probability distribution for the effective rate $t_{\text{effective}}$ of switching from $A \to B$. The relevance of this particular distribution will be clear in context of the experiment on myosin-V by Rief et al. [136]. The experiment consists of applying a known resistive force on myosin-V, which is suspended in a given concentration of ATP (see Fig. 8.2). The distribution of the dwell times of myosin-V are obtained under different values of resisting force and ATP concentration. Loosely speaking, Rief et al. obtained a dwell time distribution that can be fitted to two exponentials with two characteristic rate constants, $k_1 = 1/t_0$, and $k_2 = 1/\tau_0$, as shown in Eq. 8.17.

Now, let us see if we can address this problem by applying the maximum caliber principle to the trajectories shown in Fig. 8.3. We already saw that the waiting time distribution for a process $A \to C \to B$ can be described by two exponentials (Eq. 8.17). To apply the external constraints, we note that there are two controlled "knobs" in the experiment by Rief et al. [136] to give "reproducible" results for the dwell times distribution. The first knob is the externally applied resistive force, while the second "knob" is the ATP concentration of the medium. At the given resolution of the experiment, the intermediate states can only be inferred and not directly observed. What can be observed experimentally is the stepping of the motor, which happens precisely as shown in Fig. 8.3. Thus we have all necessary information about the experimental process. As seen before, the experiment by Rief et al.involves applying a constant load on myosin-V. We can imagine designing an experiment with a loading that is a function of time. In this general situation, with a prescribed time-dependent loading and ATP concentration we write down the external constraints as follows:

1. **Average Displacement Constraint**: As seen in Fig. 8.2, the molecular motor myosin-V is

subjected to an external force. In the most general case the external loading may be time-dependent. As seen earlier, the applied force is the "knob" controlled by the experimentalist. Hence, keeping in spirit with the maxent formalism as explained in Chapter 6, we can put a time dependent average displacement and interpret the corresponding time-dependent Lagrange multiplier as being proportional to the applied time-dependent force. The average displacement up to the step size s ($s \approx 38$ nm for myosin-V) at a given time t will be

$$\langle d(t) \rangle = \sum_{\Gamma} \sigma_{\Gamma}(t) p_{\Gamma}, \tag{8.18}$$

where $\sigma(t)$ is as shown in Fig. 8.3. It may be noted that since we are taking into account the most general driving force possible, we need to apply this average displacement constraint at all time instants of the trajectory. This average displacement multiplied by the applied force $F(t)$ and the step size s will give us the dissipated work. Hence, this constraint can be alternately viewed as the average dissipation constraint.

2. **The consumption constraint**: The second "knob" controlled in the experiment is the ATP concentration. In order to move, myosin-V has to consume energy by burning ATP molecules. The rate at which it burns the ATP molecules depends on the ATP concentration in the surrounding medium. If the consumption of one ATP molecule has a certain energy ϵ associated with it, the consumption rate for the trajectory Γ with a waiting time of τ is ϵ/τ. We hence put the consumption rate as the second constraint. The mean consumption rate is given by

$$\langle C \rangle = \sum_{\Gamma} \frac{\epsilon}{\tau} p_{\Gamma}. \tag{8.19}$$

The Lagrange multiplier that goes with this consumption rate must be a function of the ATP concentration.

We have seen in Chapter 2 that when the system is in equilibrium, there is no net energy flux, which in turn implies that the energy consumption equals the energy dissipation. It may be noted that, since our time trajectories (as shown in Fig. 8.3) are *microscopically irreversible*, i.e., they do not go back to state 1 from state 0, this state of equilibrium is automatically dismissed from consideration. This microscopic irreversibility manifests itself in the experimental conditions as the irreversible consumption of ATP.

We have based our model completely on macroscopic observables and control parameters. However, since the model is extremely coarse-grained, we cannot be completely sure that the underlying dynamics is correct and that the constraints have the proper form. Also, as we discussed in Chapter 6 the interpretations of the Lagrange multipliers are not unequivocally clear. On the other hand, starting from the choice of the trajectories to the choice of constraints, we neither swayed from any

experimental observation nor made any unwarranted assumptions. Thus, if a scheme for proper interpretation of the Lagrange multipliers is obtained, this scheme would, indeed, be a very powerful predictive tool.

With all these ideas in mind, similar to what we did in Eq. 8.8, let us write down the caliber for the problem. Consider all possible trajectories of some arbitrary duration T that is greater than the duration of the experiment. The caliber, or the trajectory entropy of the system, is

$$S = -\sum_{\tau} p_\tau \log p_\tau + \lambda \sum_{\tau} p_\tau - \alpha \sum_{\tau} \frac{\epsilon}{\tau} p_\tau - \sum_{\tau} \left(\int_0^T \mu(t')\sigma_\tau(t')dt' \right) p_\tau. \tag{8.20}$$

As discussed in Chapter 6 and earlier in this chapter, the Lagrange multiplier associated with a generalized displacement may be interpreted as a force. Hence, the multiplier $\mu(t)$ can be interpreted as Force$(t) \times s$, where s is the step-size for the motor. The other Lagrange multiplier α that goes with the ATP consumption will, in general, depend on the ATP concentration. To obtain the probabilities p_τ of the trajectories, we take a differential and put $\delta S = 0$. We obtain

$$p_\tau = \exp(-1+\lambda) \exp\left(-\frac{\alpha}{\tau} - \int_0^T \mu(t')\sigma_\tau(t)dt' \right) \text{ and} \tag{8.21}$$

$$= \exp(-1+\lambda) \exp\left(-\frac{\alpha}{\tau} - \int_0^\tau \mu(t')dt' \right). \tag{8.22}$$

The partition function will be given by

$$Z(\alpha, \{\mu(t)\}) = \frac{1}{\exp(-1+\lambda)} = \sum_{\tau} \exp\left(-\frac{\alpha}{\tau} - \int_0^\tau \mu(t')dt' \right). \tag{8.23}$$

For mathematical convenience, we can replace the summation over Γ in Eq. 8.23 with an integral $\int_0^T$. The partition function will then be

$$Z(\alpha, \{\mu(t)\}) = \int_0^T d\tau \exp\left(-\frac{\alpha\epsilon}{\tau} - \int_0^\tau \mu(t')dt' \right) \tag{8.24}$$

The probability density that the time for conversion of the given species into another species is τ is given by,

$$p_\tau = \frac{\exp(-\frac{\alpha\epsilon}{\tau} - \int_0^\tau \mu(t')dt')}{\int_0^T d\tau \exp(-\frac{\alpha}{\tau} - \int_0^\tau \mu(t')dt')} \tag{8.25}$$

As noted before, T is the upper time limit for the process. For mathematical convenience, we can take $T \to \infty$. The simplest case is when $\mu(t)$ is some constant μ, and so the probability becomes

$$p_\tau = \frac{\exp(-\frac{\alpha\epsilon}{\tau} - \mu\tau)}{\int_0^\infty d\tau \exp(-\frac{\alpha}{\tau} - \mu\tau)}. \tag{8.26}$$

We can compare these results with the experimental observations of Rief et al. [136] for the distribution of dwell times, τ in our case, during forward stepping for myosin molecules under constant forcing and in the presence of ATP molecules. Rief et al. [136] fit Eq. 8.17 to their experimental data with using t_0 and τ_0 as the parameters. We fit Eq. 8.26 to the experimental data by using α and μ as parameters. The results of these fits are shown in Fig. 8.4.

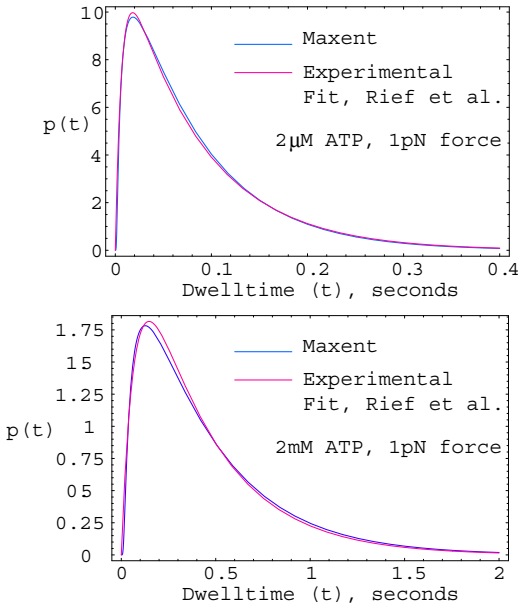

Figure 8.4: The probability distribution of dwell times(s) for the forward stepping of myosin compared with the experimental data of Rief et al. [136]. Reif et al. [136] fit their experimental observation using Eq. 8.17 with t_0 and τ_0 as the fitting parameters. (a) This experimental data corresponds to 2μM ATP concentration and a force of 1pN. Reif et al. [136] obtain a fit to the experimental data with $1/t_0 = 12.8\text{s}^{-1}$ and $1/\tau_0 = 2.7\text{s}^{-1}$. We obtain a fit by using Eq. 8.26 with $\alpha = 0.0045$ s, and 13.3/sec. (b) This experimental data corresponds to 2mM ATP concentration and a force of 1pN. Reif et al. [136] obtain a fit to the experimental data with $1/t_0 = 12.5\text{s}^{-1}$ and $1/\tau_0 = 150.0\text{s}^{-1}$. We obtain a fit by using Eq. 8.26 with $\alpha = 0.0042$ sec and 2.3/sec.

8.1.1 Discussion

In the previous section we solved the problem of waiting-time distribution of myosin-V under conditions used by Rief et al. [136]. We obtained the parameters α and μ (the Lagrange multipliers in our model) that give the best fit to the waiting times in Rief et al. [136]. The question that naturally arises is: We put the *average displacement* and *power consumption* as the constraints in the problem, but ultimately use μ and α, the respective Lagrange multipliers, as the *controllable parameters* of the problem. How can we justify this? It is not possible to get a rigorous argument for this, but we can work in terms of analogies to make this plausible. Note that in the case of the early days of statistical mechanics the situation was similar. One really only had results for the ideal gas, and there the meaning of parameters was clear. We are in similar early stages and as yet

there are analogies and hints to go by, but there is nothing that we have already found that gives the same general framework that exists in classical thermostatics. As explained in Chapter 6, take the case of the canonical ensemble of equilibrium statistical mechanics. The applied constraint is, $\langle E \rangle$, the average energy. On the other hand, what is experimentally controlled is $\beta = 1/k_B T$. We carry this procedure over to the non-equilibrium case, where we put the *ensemble average* as the constraint, but act as if we can control the Lagrange multiplier. It may also be possible that the Lagrange multipliers μ and α in our case have a universal constraint like Boltzmann's constant, k_B, in the case of the canonical ensemble [148].

Another question that arises in this context is about the number of constraints versus the number of unknowns. The unknown in this case is $p(\tau)$, the probability distribution of the waiting time τ. The number of unknowns is the total allowed values of τ, which is the set of all numbers between 0 and the total duration of the trajectory T. The number of constraints is equal to the number of "average displacement" constraints plus the total number of "consumption" constraints. It can be seen from Eq. 8.18 that the total number of "average displacement "constraints is the same as the total number of unknowns $p(\tau)$. The additional consumption constraint shown in Eq. 8.19 makes the total number of constraints more than the number of unknowns. It, thus, seems that the problem is over-determined, apparently making the application of maximum caliber principle redundant. On the other hand, since the set of real numbers between 0 and T is "uncountable," it does not really make sense to enumerate the total "number" of unknowns and the total "number" of constraints. Thus, there is a bit of a dilemma here. However, it may be noted that in the case where μ is constant, i.e, the applied loading is time-independent, this complexity clearly does not arise. The problem is only when we look at the most general case of a time-dependent force and we do not have a clear answer to the problem.

8.2 Microscopically Reversible Two-state Systems

In the previous section we discussed the two-state problem with irreversible microtrajectories using the waiting time distribution for myosin-V as a case study. Consider another extremely rich class of two-state systems in which the system switches back and forth between two states $A \leftrightharpoons B$. The trajectories for this type of system are shown in Fig. 8.1. The states A and B can be converted into numbers represented by 1 and 0, respectively. A particularly interesting instance of this kind of behavior comes from the ion-current flow in voltage gated ion channels. The ion channel can be in two macroscopically observable possible states, open or closed (see Fig. 8.5a,c). When the ion channel is open, a certain amount of ion-current flows through the channel. On the other hand, when the ion channel is closed, the value of current reduces to zero. The flow of current in the potassium ion channel (K-channel) is shown in Fig. 8.5a,c. A variety of experiments, called "patch-

clamp" experiments can be performed for such voltage-gated ion channels. Loosely speaking, the experiment involves isolating an ion channel and measuring the current through the channel by

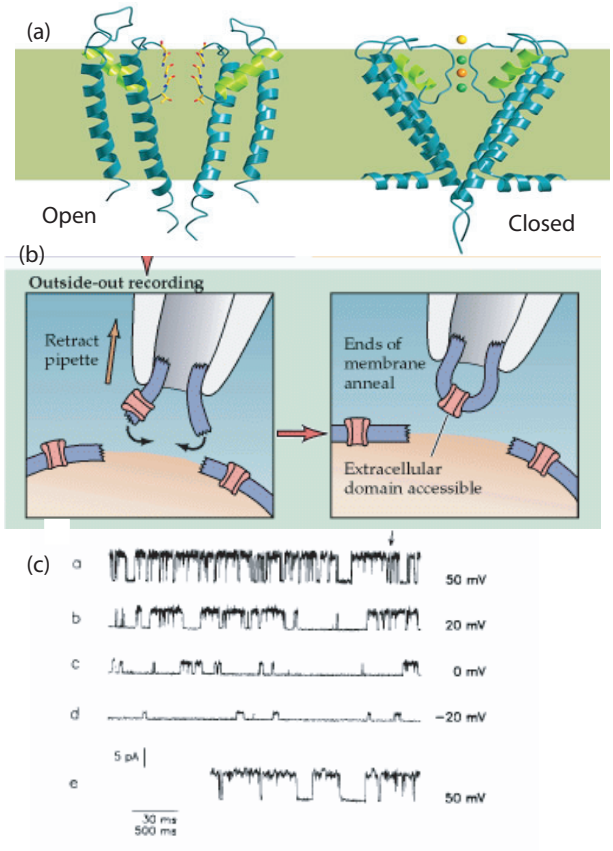

Figure 8.5: Observing time traces for current in ion channels. a)The voltage-gated potassium ion channel. When the channel is open there is a current flow through it. When the channel is closed, the current flow is zero. b) Schematic of a patch-clamp experiment. The ion channel is isolated and subjected to an external voltage. The resulting ion-current is then measured. (c) The time trace for the ion-current in the patch-clamp experiment under different applied voltages. The ion-current observation shows similar binary behavior as can be seen in Fig. 8.1 (figure from Llano et al. [149]).

applying a voltage across it. The ion channel opens and closes due to thermal fluctuations. When the ion channel is closed no current is observed, while a fixed current is observed when it is open. The time traces for the ion-current obtained by using a patch-clamp experiment are shown in Fig. 8.5c. It is not possible to differentiate between two time traces obtained under different voltage conditions by a cursory observation. On the other hand, the statistics of various quantities, for example dwell times in either open or closed states, will differ markedly depending on the applied voltage. The time-traces for ion-current by using a patch-clamp experiment under different voltage conditions are shown in Fig. 8.5c. It may be noted that the open and the closed states of ion channels may have several substates (see Fig. 8.8), but for the sake of simplicity we choose to neglect them.

The class of trajectories described in Fig. 8.1 need not be restricted to ion channels. Consider the force pulling experiment performed on the stem-loop structure of RNA [150] (see Fig. 8.6). The RNA molecule exists in two different states (see Fig. 8.6 for more details), stem-loop structure and linear structure. Due to the thermal fluctuations, the molecule constantly switches between these two states, giving rise to the type of time-trajectories shown in Fig. 8.1. If an external force is applied to the molecule, there is a change in the energy landscape that connects the two states, and this leads to different probabilities of the microscopic realizations, depending on the magnitude of the force. If we make the external loading time-dependent, the microscopic realizations will have further different probabilities. Another example is the hopping of a Brownian bead between two optical traps placed close to one another [98, 151]. Upon transmission, a beam of laser light transfers its momentum and, hence, exerts force on optically transparent beads [152]. The amount of force exerted depends on the bead diameter, bead opacity, the intensity and the frequency of the light. The forces on the optical bead are shown in Fig. 8.7a. If we bring two such optical traps close to one another, the bead will diffuse between two potential wells and its position will show the type of behavior seen in Fig. 8.1 (see Fig. 8.7b for more details). Depending on the energy depth for the two wells and the energy difference between them, the probabilities of observing a certain micro-trajectory will vary. As in the case of the RNA pulling experiment, if the barriers and the energy differences are time-dependent, we may see an interesting hopping behavior that can be characterized by the principle of maximum caliber. Hence, there are quite a few systems that exhibit such two-state behavior. Not only that, but it is also possible to measure the time-trajectories of the relevant quantities and obtain their probabilities. For example, the experimental observations made by pulling on the RNA structure under extreme non-equilibrium conditions (as shown in Fig. 8.6a) has lead to the verification of Jarzynksi's equality and the fluctuation theorem (described in Chapter 2) and to the recovery of the folding free energies of RNA [35, 153]. A fluctuation theorem for a two-state system with non-thermal noise was also recently verified [154]. Since the microtrajectories govern the overall macroscopic dynamics of a non-equilibrium system, if the probabilities of the microtrajectories (as shown in Figs. 8.5c, 8.6, and 8.7) are obtained, we essentially obtain the soul of the system. These probabilities can be used to obtain the dwell times and time-correlation functions of the concerned variables, obtain the free energy landscape by using fluctuation theorem, etc. Since it is possible to measure such micro-trajectories for a number of small systems, it is our goal to have theoretical results of the probabilities of such microtrajectories and other quantities of interest like the dwell times, time-correlation functions, etc., under extreme conditions of non-equilibrium loading.

As a particular case, let us take the case of ion-current in voltage gated ion channels, as shown in Fig. 8.5. Loosely speaking, the ion channel exists in two states: open or closed, but as shown in Fig. 8.8 even within these open and closed states there are different sub-states. The most common way of describing the dynamics of the opening and closing of ion channels is by using the standard

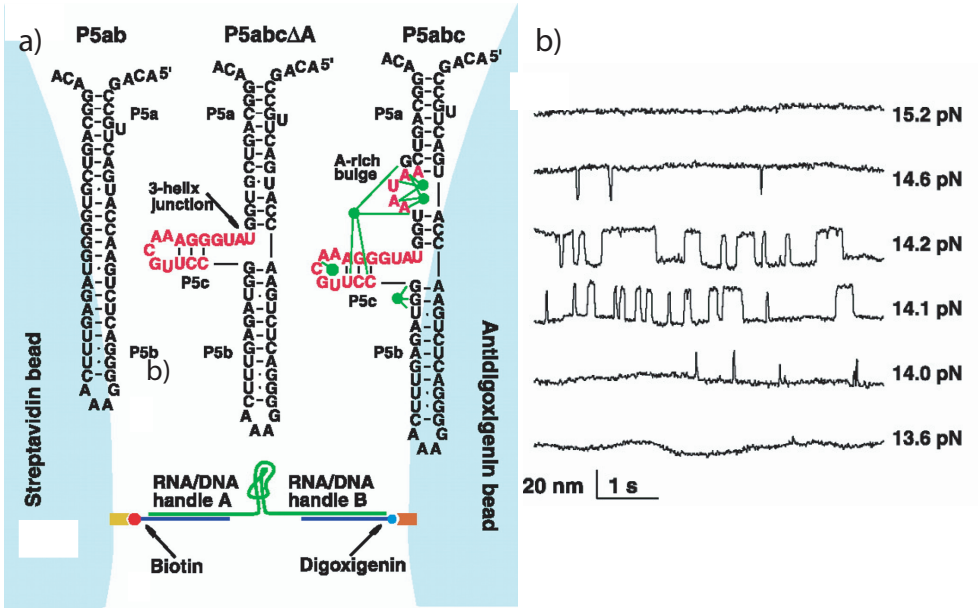

Figure 8.6: Force pulling experiments on mRNA. (a) The RNA exists in two states: (1) stem-loop structure and (2) straight structure. The RNA molecule is attached between 2μm beads (blue) with *sim*500-base pair RNA:DNA hybrid handles. The mRNA alternates between these two states because of the thermal fluctuations. (b) Different types of representative time trajectories are obtained upon application of the external load (figure from Liphardt et al. [150].

rate theory operating on an energy landscape, as shown in Fig. 8.8 [155]. Despite the successes of such theories, we still wish to apply the maximum caliber principle to the class of trajectories shown in Fig. 8.1. Other than seeking an alternative to the already existing theories, our main purpose behind doing this exercise is to see if the application of maximum caliber method to simple model gives us good insight into important non equilibrium problems. As described in Chapter 6, the maximum caliber principle is supposed to be a general principle that holds even for systems extremely far from equilibrium. Obtaining concrete predictions for, say, the probabilities of the trajectories with this principle will increase our confidence in the maximum caliber principle in general and its application to simple models in particular. As explained earlier, there are many interesting developments in the field of single particle methods that involve measuring time-trajectories under different time-dependent loading (see, especially, Section 8.2.1). We think that some of the ideas in this chapter would be a novel way of addressing such experiments and are capable of generating predictions to stimulate further experimentation. Despite bringing this to the attention of the reader, we do not claim to have all the answers, and our attempts are small strides towards the bigger goal.

In order to apply the maximum caliber principle, we proceed in an almost similar way as we did in the previous section with one difference. The trajectory in Section 8.1 was continuous in time. In this case, for mathematical convenience we discretize the time interval in units of Δt, where Δt can be considered as the time resolution behind acquiring the data. Let the total duration of

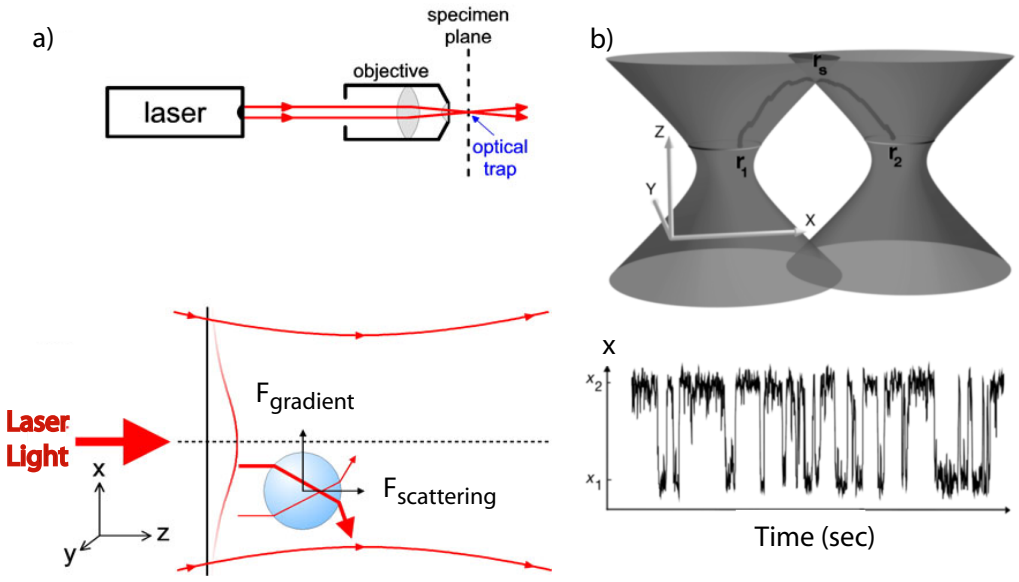

Figure 8.7: Trapping Brownian particle in a dual laser trap. (a)The laser is used to exert optical force on transparent beads. Upon the passage of the laser light through the beads a scattering force and a restoring force act on the bead. When the restoring force is larger than the scattering force, a stable optical trap is formed [152]. (b) When a bead is trapped between two optical traps very close to each other, it alternates between them and gives trajectories of the type shown in Fig. 8.1 [151] (Figure (b) taken from McCann et al. [151]).

any trajectory be $T = N\Delta t$. Since at each time step σ can be either 0 or 1, the total number of trajectories is 2^N. An individual realization is represented by Γ. In the previous section Γ was a label for a general trajectory with waiting time τ (see Fig. 8.3). In this section Γ is a numerical label for a given realization of the microtrajectory, and Γ can assume values between 1 and 2^N. Keeping this in mind, we now start identifying the constraints on the system.

When a certain voltage is applied across an ion channel, one sees time traces of current as in Fig. 8.5c, which are similar to the types of time trajectories illustrated in Fig. 8.1. If the ions channel is open, i.e., in state 1, the ion-current is a constant value i_0. On the other hand, when the ion channel is closed, i.e., in state 0, there is no current flow. It has also been observed for the voltage gated ion channels that when the applied voltage is zero, the channel is almost always closed, giving practically zero value for the ion-current. The channel begins to open more and more with increasing voltage. Finally, at saturating voltage the ion channel is almost always open, giving a steady current of i_0. This relation between the applied voltage and the ion-current makes it reasonable to assume that the voltage is one of the "knobs" for the process. We thus take applied voltage as our constraint. As we have explained in Chapter 6 and done previously in Section 8.1, this would mean that we provide the mean ion-current as a constraint and interpret the Lagrange multiplier associated with the constraint as being proportional to the applied voltage V. In the most general case, the applied

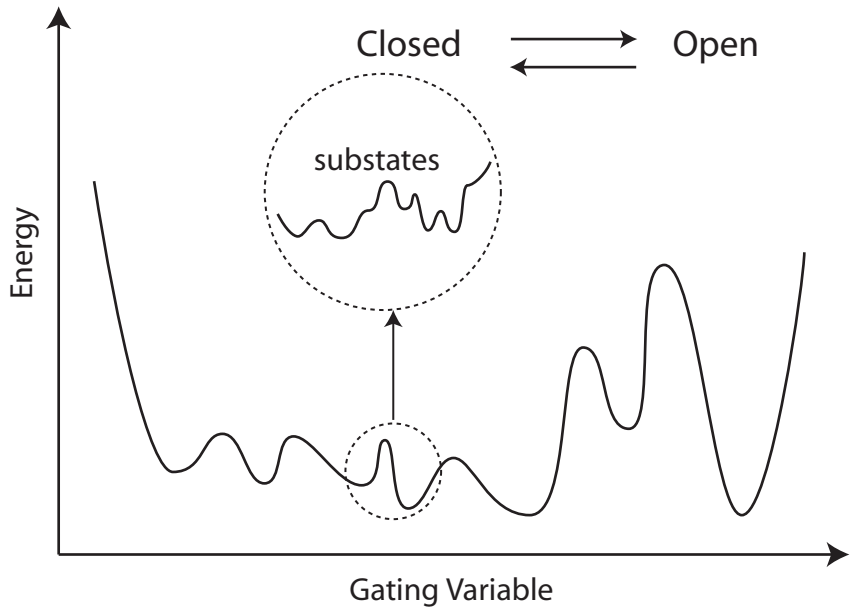

Figure 8.8: Schematic of the energy landscape for an ion channel. It can be seen that within every state there are different substates (figure adapted from Goyshuk and Hanggi [155].)

voltage can be a function of time. Similar to the case of the myosin-V in Section 8.1, this would mean applying the average current constraint at every instant of time. The mathematical form of this constraint will be

$$\langle i(t) \rangle = \sum_{\Gamma} \sigma_{\Gamma}(t) p_{\Gamma}. \tag{8.27}$$

Here, p_{Γ} is the probability of a particular microtrajectory Γ, and $\sigma(t)$, as shown in Fig. 8.1, is either 1 or 0. Though formalistically it does not make too much of a difference, the average current $\langle i(t) \rangle$ in Eq. 8.27 is up to a numerical factor i_0, the actual value of the current that flows when the channel is open. Note that, t is the discretized time and assumes value from 1 to N, where $N\Delta t = T$ is the total duration of the trajectory. It is interesting to observe that the product of the applied voltage $V(t)$ with the observed current $\langle i(t) \rangle$ is the power consumption that occurs in the ion channel. As a result, the average current constraint can also be identified as a power consumption constraint. Just to repeat what we said earlier, even though the applied voltage $V(t)$ is the controlled parameter, we specify average current as the constraint. As was seen in Chapter 6, the Lagrange multiplier that goes with the observed flux is interpreted as the driving force. Since the applied voltage is the driving force, the Lagrange multiplier that goes with the current flux $\langle i(t) \rangle$ will be interpreted as being "proportional" to the applied voltage $V(t)$.

Let us now write down the caliber of the system subject to this constraint:

$$S = -\sum_{\Gamma} p_{\Gamma} \ln p_{\Gamma} + \lambda \sum_{\Gamma} p_{\Gamma} + \sum_{\Gamma} \sum_{t=1}^{N} \mu(t) \sigma_{\Gamma}(t) p_{\Gamma}. \tag{8.28}$$

Using the standard procedure of maximizing the entropy we obtain

$$p_{\Gamma} = \exp(-1+\lambda) \exp\left(\sum_{i=1}^{N} \mu(t) \sigma_{\Gamma}(t) \right). \tag{8.29}$$

Using the fact that the sum of the probabilities over the complete set of trajectories $\{\Gamma\}$ equals one, i.e., $\sum_{\Gamma} p_{\Gamma} = 1$, we will get $\exp(-1+\lambda) = 1/Z(\{\mu(t)\})$. Here, $Z(\{\mu(t)\})$ is the partition function. Following the usual procedure we get

$$Z(\{\mu(t)\} = \sum_{\Gamma} \exp\left(\sum_{t=1}^{N} \mu(t) \sigma_{\Gamma}(t) \right). \tag{8.30}$$

The Lagrange multiplier $\mu(t)$ that goes with the average current constraint is interpreted as being proportional to the applied time-dependent voltage $V(t)$. Let us take a special case when the voltage is constant, i.e, $\mu(t) = \mu$. In that case, the partition function can be written as

$$\begin{aligned} Z(\{\mu(t)\} &= \sum_{\Gamma} \exp\left(\sum_{t=1}^{N} \mu \sigma_{\Gamma}(t) \right), \text{ and} \\ &= \sum_{\sigma(1)=0}^{1} \cdots \sum_{\sigma(N)=0}^{1} \exp\left(\mu \sum_{t=1}^{N} \sigma(t) \right). \end{aligned}$$

Since all the σ's are independent of each other this sum is straightforward to evaluate and the partition function is, hence, given by the product of the sum over individual $\sigma(t)$. The sum over each $\sigma(t)$ is given by $\exp(\mu \times 1) + \exp(\mu \times 0)$, which equals $\exp(\mu) + 1$. The partition function, hence, becomes

$$Z(\{\mu\}) = (\exp(\mu) + 1)^N. \tag{8.31}$$

The probability of an individual trajectory is, hence,

$$p_{\Gamma} = \frac{\exp\left(\mu \sum_{t=1}^{N} \sigma_{\Gamma}(t) \right)}{(\exp(\mu)+1)^N}. \tag{8.32}$$

Since σ is either 0 or 1, $\sum_{t=1}^{N} \sigma_{\Gamma}(t)$ is equal to the total number of 1's in a given trajectory Γ, j_{Γ}.

Thus, the probability of a trajectory Γ can also be given as

$$p_\Gamma = \frac{\exp(\mu j_\Gamma)}{(1+\exp(\mu))^N}. \tag{8.33}$$

The value of the average current over the entire duration of the trajectory is

$$\langle I \rangle = \sum_\Gamma \sum_{t=1}^{N} \sigma_\Gamma(t) p_\Gamma. \tag{8.34}$$

As noted in Chapter 6, it can be conveniently written as

$$\langle I \rangle = \frac{\partial Z(\mu)}{\partial \mu}$$

and can be evaluated as

$$\langle I \rangle = \frac{N \exp(\mu)}{1+\exp(\mu)}. \tag{8.35}$$

Note that the average current at any time instant, $\sum_\Gamma \sigma_\Gamma(t) p_\Gamma$, is independent of time t, and will be given by

$$i_{\text{av}} = \left\langle \frac{I}{N} \right\rangle = \frac{\exp(\mu)}{1+\exp(\mu)}. \tag{8.36}$$

In the above expression $\langle i \rangle = i_{\text{av}}$ is the average current at a given instant and is given by $\langle I/N \rangle$. Let us examine this expression a bit. When $\mu \to \infty$, $i_{\text{av}} \to 1$. Thus, as expected, when the voltage is very high the average current is 1, i.e, the ion channel is open all the time. When $\mu \to -\infty$, $i_{\text{av}} \to 0$, i.e., for extremely negative voltage, the ion-current is zero. This is a bit puzzling because we expect the ion-current to be equal to zero when the voltage is zero [156]. This fact can be reconciled by noting that the ion channel already has a high intrinsic negative voltage. Hence the quantity μ is the combination of the externally applied voltage $V(t)$ and the intrinsic base voltage $-V_0$ ($V_0 > 0$ and $V_0 \to \infty$). So the multiplier μ is proportional to $V(t) - V_0$. Hence when $\mu = -V_0 \to \infty$, there is no extrinsic voltage, and the channel is almost always closed, giving $i_{\text{av}} = 0$.

When the ion channel switches from close to open and vice-versa, certain energy needs to be dissipated. The total number of such switches (0 to 1 and vice-versa) for a given microtrajectory is given by

$$N_{\text{switch}}(\Gamma) = \sum_{t=1}^{N} (\sigma_\Gamma(t+1) - \sigma_\Gamma(t))^2.$$

It may be noted that the summand in the summation above is 1 when $\sigma_\Gamma(t+1) \neq \sigma_\Gamma(t)$, i.e., when

there is a switch from open to close or vice-versa; it is zero otherwise. This summation, hence, gives us the total number of switches for a given micro-trajectory. The average number of switches is, hence,

$$\langle N_{\rm switch}\rangle = \sum_{\Gamma}\sum_{t=1}^{N}(\sigma_\Gamma(t+1)-\sigma_\Gamma(t))^2 p_\Gamma. \tag{8.37}$$

Using the above analysis, let us obtain the average value of total number of switches $\langle N_{\rm switch}\rangle$. The total number of switches is given by Eq. 8.37. The average number of switches is, hence,

$$\begin{aligned}\langle N_{\rm switch}\rangle &= \sum_{\Gamma}\sum_{t=1}^{N-1}\sigma_\Gamma(t+1)-\sigma_\Gamma(t))^2 p_\Gamma, &(8.38)\\ &= \sum_{\Gamma}\sum_{t=1}^{N-1}(\sigma_\Gamma(t+1)+\sigma_\Gamma(t)-2\sigma_\Gamma(t)\sigma_\Gamma(t+1))p_\Gamma. &(8.39)\end{aligned}$$

Here we have used the fact that since σ_Γ is either 0, or 1, $\sigma_\Gamma^2=\sigma_\Gamma$. Now, from Eq. 8.32 we note that the value of $\langle\sigma(t)\rangle$ is independent of t and is nothing but $i_{\rm av}$ (see Eq. 8.36). From Eq. 8.32 it can also be seen that $\sigma(t)$ is independent of $\sigma(t')$ for $t\neq t'$. This time independence and uncorrelation means that $\langle\sigma(t)\sigma(t')\rangle$ equals $\langle\sigma(t)\rangle\langle\sigma(t')\rangle$, which evaluates out to $i_{\rm av}^2$. Using this fact, we can continue from Eq. 8.39 to obtain

$$\begin{aligned}\langle N_{\rm switch}\rangle &= \sum_{t=1}^{N-1}2(N-1)i_{\rm av}(1-i_{\rm av})\\ &\approx 2Ni_{\rm av}(1-i_{\rm av}) \quad \text{for large N.}\end{aligned} \tag{8.40}$$

Substituting the expression for $i_{\rm av}$ from Eq. 8.36, we obtain

$$\begin{aligned}\langle N_{\rm switch}\rangle &= 2Ni_{\rm av}\times(1-i_{\rm av}),\\ &= 2N\left(\frac{\exp(\mu)}{\exp(\mu)+1}\right)\times\left(1-\frac{\exp(\mu)}{\exp(\mu)+1}\right), \text{ and}\\ &= \frac{2N\exp(\mu)}{(\exp(\mu)+1)^2}.\end{aligned} \tag{8.41}$$

It can be seen that $\langle N_{\rm switch}\rangle = 0$ when $\mu\to\infty$ (ion channels stay open all the time), or when $\mu\to-\infty$ (the ion channels stay closed all the time). It is interesting to compare the relative values of the total current over the entire trajectory, i.e, the total time for which the ion channel stays open and the total number of switches that happen during the duration of the trajectory. The simplest way of comparing that is to estimate the ratio of average total current $\langle I\rangle$ (Eq. 8.35) with the average

number of switches $\langle N_{\rm switch}\rangle$ (Eq. 8.41). From Eqs. 8.35 , 8.36, and 8.41 we obtain

$$\begin{aligned}\frac{\langle I\rangle}{\langle N_{\rm switch}\rangle} &= \frac{Ni_{\rm av}}{2Ni_{\rm av}(1-i_{\rm av})},\\ &= \frac{1}{2(1-i_{\rm av})}, \text{ and}\\ &= \frac{1+\exp(\mu)}{2}. \end{aligned} \tag{8.42}$$

It would be really interesting to obtain the probability distribution, $p(N_{\rm switch})$, for the the total number of switches, but it is not possible to get a closed form solution for the same, unless $\mu = 0$. On the other hand, when N is large it can be shown that the $k^{\rm th}$ moment, $\langle N_{\rm switch}^k\rangle$, of $N_{\rm switch}$ evaluates out to $\langle N_{\rm switch}\rangle^k$. The probability distribution $p(N_{\rm switch})$ can then be shown to be given by $\delta(N_{\rm switch} - \langle N_{\rm switch}\rangle)$. The quantity $p(N_{\rm switch})$ can, of course, be evaluated numerically. When $N = 15$, the distribution $p(N_{\rm switch})$ for different values of μ, is shown in Fig. 8.9. It is interesting to note that $p(N_{\rm switch}(\mu))$ is the same as $p(N_{\rm switch}(-\mu))$. This observation can be explained as follows. From Eq. 8.33 it can be noted that

$$\begin{aligned} p_\Gamma &= \frac{\exp(\mu j_\Gamma)}{(1+\exp(\mu))^N}\\ &= \frac{\exp(-\mu(N-j_\Gamma))}{(1+\exp(-\mu))^N}. \end{aligned} \tag{8.43}$$

Thus, the probability of a trajectory Γ when the ion channel under voltage μ is open j_Γ times is the same as the probability of its complementary trajectory Γ' when the ion channel under voltage $-\mu$ is closed j_Γ number of times. But it may be noted that the number of switches, $N_{\rm switch}$, for both trajectories is the same. It, hence, follows that $p(N_{\rm switch}(\mu))$ must be equal to $p(N_{\rm switch}(-\mu))$.

In Section 8.1 we evaluated the probability distribution of the dwell times for the molecular motors. We can evaluate the waiting time distributions $p(k_{\rm o})$ and $p(k_{\rm c})$ of the the dwell time k for the ion channel in the open and the closed state, respectively. The analytic solution is again very difficult to find. Within every trajectory Γ, let the ion channel be open (closed) o_k^Γ (c_k^Γ) number of times for a duration of k. The probability $p(k_{\rm o})$ is given by

$$p(k_{\rm o}) = \frac{\sum_\Gamma o_k^\Gamma p_\Gamma}{\sum_\Gamma \sum_{k=0}^N o_k^\Gamma p_\Gamma}. \tag{8.44}$$

Similarly, $p(k_{\rm c})$ is given by

$$p(k_{\rm c}) = \frac{\sum_\Gamma c_k^\Gamma p_\Gamma}{\sum_\Gamma \sum_{k=0}^N c_k^\Gamma p_\Gamma}. \tag{8.45}$$

A glance at Eqs. 8.33, 8.44, and 8.45 will reveal that $p(k_{\rm c}(\mu))$ is equal to $p(k_{\rm o}(-\mu))$, i.e., the waiting

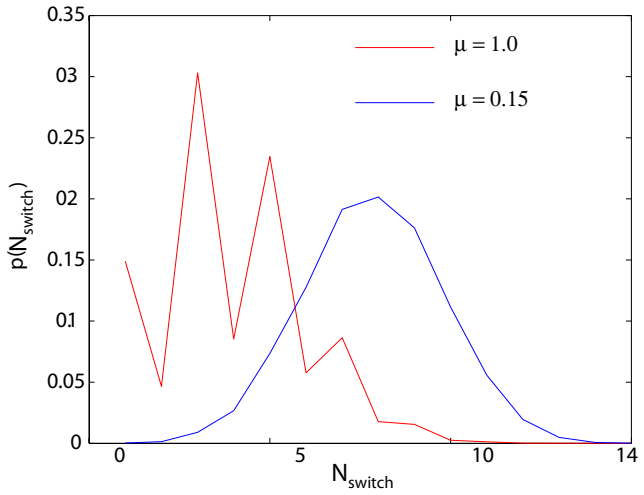

Figure 8.9: The plot for $p(N_{\text{switch}})$ as a function of the number of switches N_{switch} for different values of μ. When μ is small (0.15), the probability distribution is centered around $Ns = N/2$. When μ is large (1.0), the probability distribution shifts towards $Ns < N/2$, thus making the number of kinks less likely. There are bumps in $p(N_{\text{switch}})$ when $\mu = 1.0$, maybe, because $N = 15$ is not a very large number and thus the discrete nature of $p(N_{\text{switch}})$ is more prominent.

time distribution for the channel to be in open state under voltage μ is the same as the waiting time distribution for the channel to be in closed state under voltage $-\mu$. The dwell time distributions $p(k_{\text{c}})$ and $p(k_{\text{o}}(\mu))$ are shown in Fig. 8.10 for different values of μ.

From Eq. 8.33 it can be seen that the probability p_Γ of a given trajectory depends solely on j_Γ, the total number of times the ion channel is open. Hence, the two trajectories, for example, as shown in Fig. 8.11 with the same j_Γ will have the same probability. This seems counterintuitive, and it seems that we may need to have another constraint. This constraint can be identified as the "average number of switches" constraint.

In general the energy that is dissipated when the system switches from 1 to 0 should be different from when it switches from 0 to 1. But, for the time-being, let us assume that the energy is the same and denoted by ϵ. This quantity is expected to be conjugate with the total number of switches and, hence, should be proportional to the Lagrange multiplier α that would go with $\langle S \rangle$.

If it happens that this switching energy ϵ is a function of time, we should replace the average total number of switches constraint with the constraint specifying the average number of instantaneous switches,

$$\langle N_{\text{switch}}(t) \rangle = \sum_\Gamma \sum_{t=1}^{N} (\sigma_\Gamma(t+1) - \sigma_\Gamma(t))^2 p_\Gamma. \tag{8.46}$$

Since the total number of switching events determine the amount of energy dissipated by the ion channel, this constraint can also be called the "average dissipation constraint." This constraint

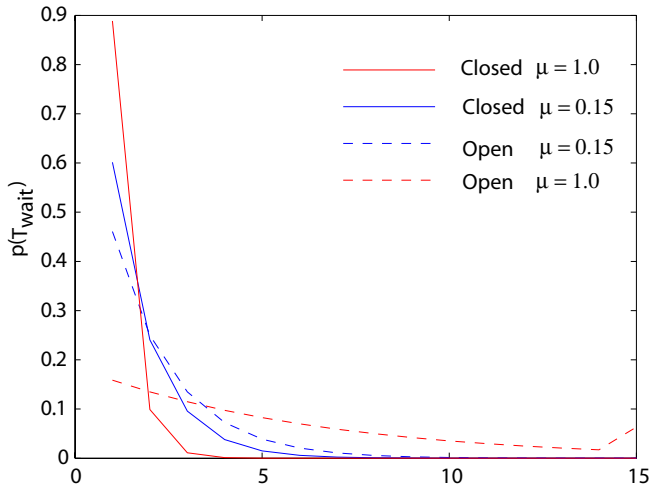

Figure 8.10: The plot of waiting times for opening and closing of ion channels for two different applied voltages μ. As expected. When μ is small (0.15) the waiting times k_o and k_c for the channel to be, respectively, in the open and the closed state are almost the same. When μ is large, as expected, the probability that the ion channel is always closed is very large.

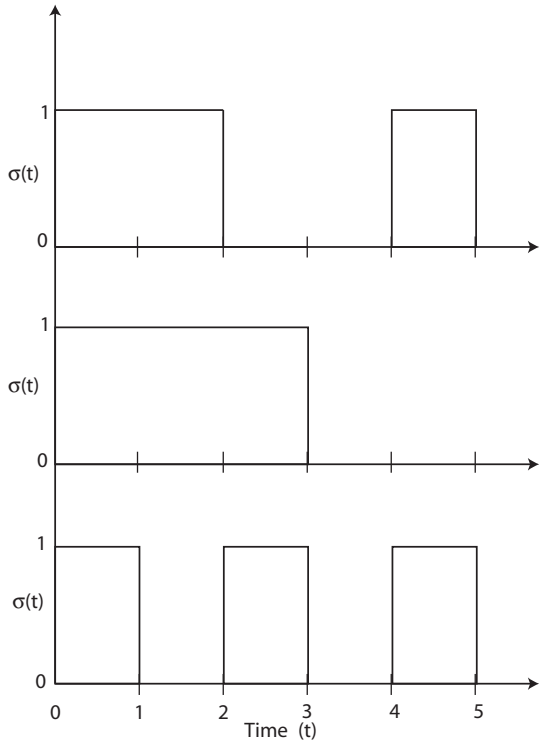

Figure 8.11: Three different types of trajectories with the same total duration of time. When only the "average current" constraint is applied the probabilities of all these trajectories will be the same (see Eq. 8.33). On physical grounds, this seems implausible, and this necessitate the addition of the second constraint.

with the average number of switches may seem to be a bit contrived, but, as will be explained in Section 8.2.1, it is certainly possible to emulate it under laboratory conditions.

Utilizing these two constraints, we write the caliber of the system:

$$S = -\sum_{\Gamma} p_\Gamma \ln p_\Gamma + \lambda \sum_{\Gamma} p_\Gamma - \sum_{t=1}^{N} \sum_{\Gamma} \alpha(t)(\sigma_\Gamma(t+1) - \sigma_\Gamma(i))^2 p_\Gamma + \sum_{t=1}^{N} \sum_{\Gamma} \mu(t)\sigma_\Gamma(t) p_\Gamma. \quad (8.47)$$

Upon maximizing the entropy by following the procedure in the previous section, we will obtain

$$p_\Gamma = \exp(-1+\lambda) \exp\left(-\sum_{t=1}^{N} \alpha(t)(\sigma_\Gamma(t+1) - \sigma_\Gamma(t))^2 + \sum_{i=1}^{N} \mu(t)\sigma_\Gamma(t) \right). \quad (8.48)$$

Again, using the fact that the sum of the probabilities over the complete set of trajectories $\{\Gamma\}$ equals one, i.e., $\sum_\Gamma p_\Gamma = 1$, we will get $\exp(-1+\lambda) = 1/Z(\{\alpha(t), \mu(t)\})$. Here, $Z(\{\alpha(t), \mu(t)\})$ is the partition function. Following the usual procedure (see Chapter 6) we get

$$Z = \sum_{\Gamma} \exp\left(-\sum_{t=1}^{N-1} \alpha(t)(\sigma_\Gamma(t+1) - \sigma_\Gamma(t))^2 + \sum_{i=1}^{N} \mu(t)\sigma_\Gamma(t) \right). \quad (8.49)$$

We can map this to the 1-D Ising two-spin problem with near-neighbor interactions. Because the Ising model is well studied in the literature [26], it may be possible to exploit the available results on the Ising model. The 1-D Ising model is comprised of spins that can take values ± 1. The σ in our model, on the other hand, can assume values of either 0 or 1. We can have a one-to-one mapping between s and σ by noting that

$$\sigma = \frac{1}{2}(s+1); s = \pm 1. \quad (8.50)$$

On substituting σ with s we will get,

$$\sum_{t=1}^{N-1} \alpha(t)(\sigma_\Gamma(t+1) - \sigma_\Gamma(t))^2 + \sum_{i=1}^{N} \mu(t)\sigma_\Gamma(t), \quad (8.51)$$

$$= \sum_{t=1}^{N-1} \alpha(t) \left(\frac{1}{2}(1+s_\Gamma(t)) - \frac{1}{2}(1+s_\Gamma(t+1)) \right)^2 + \sum_{i=1}^{N} \mu(t) \left(\frac{1}{2}(1+s_\Gamma(t)) \right), \text{ and}$$

$$= \sum_{t=1}^{N-1} \frac{\alpha(t)}{4} \left(s_\Gamma(t)^2 + s_\Gamma(t+1)^2 - 2 s_\Gamma(t) s_\Gamma(t+1) \right) + \sum_{t=1}^{N} \left(\frac{\mu(t)}{2} + \frac{\mu(t) s_\Gamma(t)}{2} \right). \quad (8.52)$$

Note that since s equals ± 1, s^2 will always be equal to one. With this fact, Eq. 8.52 becomes,

$$\begin{aligned} & \sum_{t=1}^{N-1} \frac{\alpha(t)}{4} \left(2 - 2 s_\Gamma(t) s_\Gamma(t+1)\right) + \sum_{t=1}^{N} \left(\frac{\mu(t)}{2} + \frac{\mu(t) s_\Gamma(t)}{2} \right), \text{ and} \\ = & -\sum_{t=1}^{N-1} \frac{\alpha(t)}{2} s_\Gamma(t) s_\Gamma(t+1) + \sum_{t=1}^{N} \frac{\mu(t)}{2} s_\Gamma(t) + \underbrace{\sum_{t=1}^{N-1} \frac{\alpha(t)}{2} + \sum_{t=1}^{N} \frac{\mu(t)}{2}}_{\text{constant}}. \end{aligned} \tag{8.53}$$

The constants are not important because they will be eliminated since they appear both in the numerator and the denominator. Equation 8.51 thus reduces to Eq. 8.53 upon mapping from σ to s. Since Eq 8.51 was the argument in the exponential in Eq. 8.49, the partition function reduces to

$$\begin{aligned} Z &= \sum_{\Gamma} \exp\left[\sum_{t=1}^{N-1} \frac{\alpha(t)}{2} s_\Gamma(t) s_\Gamma(t+1) + \sum_{t=1}^{N} \frac{\mu(t)}{2} s_\Gamma(t) \right], \text{ and} \\ &= \sum_{s_1=\pm 1} \ldots \sum_{s_N=\pm 1} \exp\left[\sum_{t=1}^{N-1} \frac{\alpha(t)}{2} s_t s_{t+1} + \sum_{t=1}^{N} \frac{\mu(t)}{2} s_t \right], \end{aligned} \tag{8.54}$$

and the probability distribution p_Γ becomes

$$p_\Gamma = \frac{1}{Z(\{\mu(t), \alpha(t)\})} \exp\left[\sum_{t=1}^{N-1} \frac{\alpha(t)}{2} s_\Gamma(t) s_\Gamma(t+1) + \sum_{t=1}^{N} \frac{\mu(t)}{2} s_\Gamma(t) \right]. \tag{8.55}$$

This particular formulation is exactly analogous to the 1-D Ising model with space-varying magnetic field and coupling constant [26]. The Lagrange multiplier μ that goes together with the average current can be interpreted as the applied voltage, while the multiplier that goes with the coupling terms may be interpreted as the energy dissipation to switch from 1 to 0 or vice-versa. The closed form solution for the problem is available only when α and μ are constants. Even then, if the boundary conditions are not periodic (which they are not in our case), the closed form solution of the partition function becomes extremely cumbersome. We can numerically obtain the probability distributions for N_{switch} and the dwell times when $\alpha \neq 0$. Though the distributions will, in general, depend on the values of $\alpha(t)$ and $\mu(t)$, the basic idea is as simple as that. In the remainder of the chapter we will discuss an experiment, currently in progress in our lab, to test these ideas.

8.2.1 Two State Trajectories Using Dual Laser Traps

Earlier we saw the complete derivation for the probability distribution of the trajectories for the ion channels. On the other hand, we had a problem with interpreting the Lagrange multipliers and relating them to the experimental observables. In this section we will describe an experiment, currently underway in our lab, that can shed some light on these issues.

The predictions obtained for ion channels are generic for any two-state system and can be applied

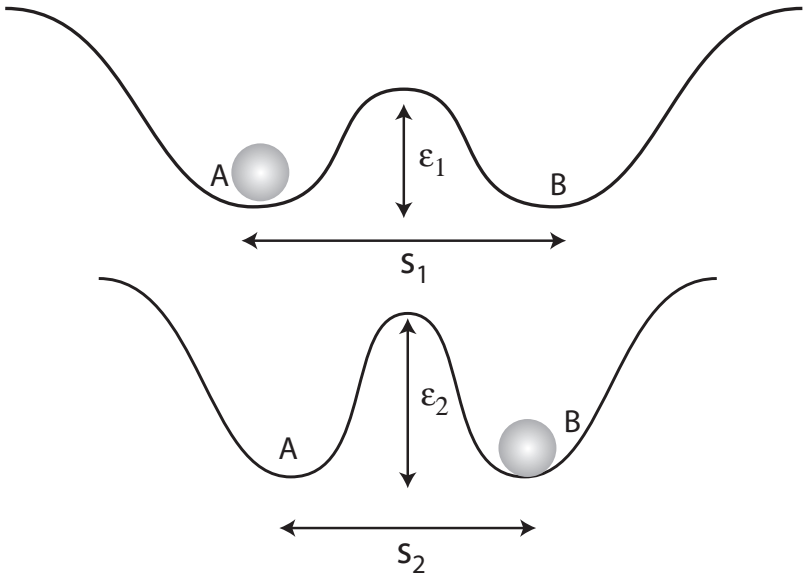

Figure 8.12: Schematic of the energy-landscape experienced by the Brownian particle. When the bead is in the proximity of energy well A (B) it is taken to be in state-1 (state-2). The energy barrier ϵ for the dual-trap can be controlled by changing the spacing between the traps.

to the diffusion of a Brownian particle in dual-optical traps (see Fig. 8.7). A single optical trap is obtained by focusing one laser beam using a microscope objective(see Fig. 8.7a). Depending on the intensity and the frequency of the laser light, the Brownian particle is trapped in an approximately harmonic landscape. If instead of focusing just one laser beam we focus on two laser beams very close to each other, the Brownian particle is trapped in a combined energy landscape with two energy wells [98, 151] (see Figs. 8.7b, and 8.12b). The Brownian particle then hops between the two energy wells describing a trajectory shown in Fig. 8.7b [151]. The energy wells represent the state of the Brownian particle. The Brownian particle is taken to be in state-1 and 2 when it is in energy wells A and B, respectively.

In order to switch from state-1 to state-2, the Brownian particle has to hop over the energy barrier by expending an ϵ amount of energy (Fig. 8.12). This seems to be the equivalent to the switching of the ion channels from the open state to close state, or vice-versa. We can thus relate the energy barrier ϵ to the parameter α in our formalism (see Eq. 8.55). The energy barrier between the traps can be controlled by controlling the spacing between the traps (see Fig. 8.12) and the intensity of the laser light. The barriers can also be made time-dependent by changing the spacing between the traps with time (see Fig. 8.12). The time-dependent energy barrier $\epsilon(t)$ can then be related to the time-dependent Lagrange multiplier $\alpha(t)$ (see Eq. 8.55).

Let us now make a very simple, experimentally verifiable prediction to check the relation of the Lagrange multiplier α with the energy barrier ϵ between the energy wells. If there is no external driving force on the particle μ should be equal to zero. This scenario can be experimentally achieved

when the two laser beams are identical and the spacing between the traps is constant, providing an energy barrier of ϵ. We can now obtain the theoretical probability distribution, $p(N_{\rm switch})$, for the number of switches using Eq. 8.55. In Eq. 8.55, if $s_\Gamma(t)$ is not equal to $s_\Gamma(t)$, we say that a switch has occurred. Since s can be either $+1$ or -1, the product $s_\Gamma(t)s_\Gamma(t+1)$ is -1 in the case of a switch and $+1$ otherwise. As a result, the sum $\sum_{t=1}^{N-1} s_\Gamma(t)s_\Gamma(t+1)$ can be written as

$$\begin{aligned}\sum_{t=1}^{N-1} s_\Gamma(t)s_\Gamma(t+1) &= -N_{\rm switch} + [(N-1) - N_{\rm switch}] \text{ and} \\ &= (N-1) - 2N_{\rm switch}. \end{aligned} \tag{8.56}$$

The partition function Eq. 8.54, hence, can be written as

$$\begin{aligned} Z &= \sum_\Gamma \exp\left[\frac{\alpha}{2}\sum_{t=1}^{N-1} s_\Gamma(t)s_\Gamma(t+1)\right], \\ &= \sum_\Gamma \exp(\alpha(N-1)/2 - \alpha N_{\rm switch}), \text{ and} \qquad (8.57) \\ &= \sum_{N_{\rm switch}=0}^{N-1} \Omega(N_{\rm switch}) \exp(\alpha(N-1)/2 - \alpha N_{\rm switch}), \qquad (8.58) \end{aligned}$$

where $\Omega(N_{\rm switch})$ is the total number of microtrajectories with the number switching events equal to $N_{\rm switch}$. $\Omega(N_{\rm switch})$ can be easily evaluated by observing the following. A trajectory Γ is determined by the time history of s, i.e., $\Gamma \equiv s_1, s_2, ..., s_N$. If s_1 is given, then the trajectory is uniquely determined by a sequence of $s_t s_{t+1}$. Hence, if the total number of switches is $N_{\rm switch}$, the total possible arrangements of all these switches is given by $\binom{N-1}{N_{\rm switch}}$. Since s_1 can take two values, ± 1, $\Omega(N_{\rm switch})$ is

$$\Omega(N_{\rm switch}) = 2\binom{N-1}{N_{\rm switch}}. \tag{8.59}$$

Hence, the partition function is given by,

$$\begin{aligned} Z &= \sum_{N_{\rm switch}=0}^{N-1} \Omega(N_{\rm switch}) \exp(\alpha(N-1)/2 - \alpha N_{\rm switch}), \\ &= 2\exp(\alpha(N-1)/2) \sum_{N_{\rm switch}=0}^{N-1} \binom{N-1}{N_{\rm switch}} \exp(-\alpha N_{\rm switch}), \\ &= 2\exp(\alpha(N-1)/2)(1+\exp(-\alpha))^{(N-1)}. \end{aligned} \tag{8.60}$$

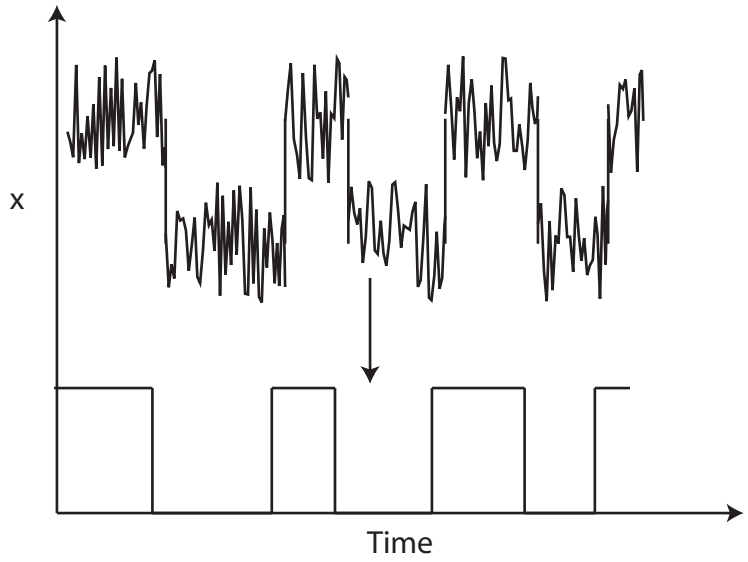

Figure 8.13: Typical data for the position of the Brownian bead versus time. The data can then be converted into binary form, where the Brownian particle is either in state 1 or state 0.

The probability $p(N_{\rm switch})$ is hence given by

$$\begin{aligned} p(N_{\rm switch}) &= \frac{1}{Z}\Omega(N_{\rm switch})\exp(\alpha(N-1)/2-\alpha N_{\rm switch}), \\ &= \binom{N-1}{N_{\rm switch}}\frac{\exp(-\alpha N_{\rm switch})}{(1+\exp(-\alpha))^N}. \end{aligned} \tag{8.61}$$

Thus we have a closed form expression for $p(N_{\rm switch})$.

On the experimental front, we can observe the diffusion of the Brownian particle in the dual-laser traps via video microscopy. The camera can take images at around 60 frames per second, so Δt corresponding to our Caliber expressions is equal to 1/60 seconds. We can then analyze the images to obtain the position x of the Brownian particle as a function of time (as shown in Fig. 8.7b and 8.13). Two things need to be (and can be) done. First, the histogram for the position of the beads can be obtained, i.e., the probability distribution $p(x)$ can be experimentally obtained. But, the probability is related to the energy landscape by

$$p(x) \sim \exp\left(-\frac{E(x)}{k_B T}\right). \tag{8.62}$$

Thus by knowing $p(x)$ the energy landscape $E(x)$ can be obtained. By knowing the energy landscape the barrier ϵ can be easily evaluated.

Knowing the position history $x(t)$ of the beads, the data can be converted into the binary form of 1s and 0s (see Fig. 8.13). If the bead is near the energy well A (B), it can be classified as being in state-1 (0). From this modified data, one can obtain the probability distribution $p(N_{\rm switch})$ for

the number of switching events. The experimental $p(N_{\rm switch})$ can then be fitted to Eq. 8.61 using α as a parameter. By changing the spacing between the traps and modifying the laser intensity, one can obtain different values for ϵ. The same analysis can be repeated to obtain α as a function of ϵ. Once we know how α is related to ϵ further experiments with time varying $\epsilon(t)$ can be done to check the predictions obtained by using the method of maximum caliber. D. Wu and E. Seitaridou in our lab are currently involved in the dual-laser trap experiment in our lab, and we hope to shortly have the results from the experiment.

In addition to changing the barrier, we can also also add a time-dependent external loading and, hence, can emulate the theoretical use of the time-varying Lagrange multiplier $\mu(t)$. Getting a closed form expression in the presence of both μ and α is difficult, but we can always resort to numerical calculations to compare experimental results with the theoretical predictions.

8.3 Discussions

In Section 8.2 we used the class of trajectories shown in Fig. 8.1 to explain the dynamics of opening and closing of ion channels. We started by applying a simple constraint of "average current." We then used the principle of maximum caliber to obtain the probabilities of the trajectories. The Lagrange multiplier corresponding to the "average current" was interpreted as an applied voltage. We also obtained the probability distribution $p(N_{\rm switch})$ for the number of switching events $N_{\rm switch}$ (see Fig. 8.9) and the probability distribution $p(k_{\rm o})$ and $p(k_{\rm c})$ of the waiting time k for the ion channel to be in the open and closed states, respectively (Fig. 8.10). Because of the complication shown in Fig. 8.11, the need of a second constraint with an "average switch number" was demonstrated. The Lagrange multiplier that went with this constraint was identified as the energy dissipated per switch from open to closed state, and vice-versa. We then obtained the expression for the probability p_Γ. Finally, in Section 8.2.1 we described an experiment with dual-laser traps to check the predictions made with the principle of maximum caliber and obtain a relationship between the Lagrange multipliers and the experimentally controlled parameters.

Bibliography

[1] B. Alberts. The cell as a collection of protein machines. *Cell*, 92:291–4, 1998.

[2] D. Kondepudi and I. Prigogine. *Modern thermodynamics:From heat engines to dissipative structures*. John Wiley and sons, 1998.

[3] M. LeBellac, F. Mortessagne, and G. G. Batrouni. *Equilibrium and Non-equilibrium thermodynamics*. University Press, Cambridge, UK, 2004.

[4] D. Ruelle. Conversations on nonequilibrium physics with an extraterrestrial. *Phys. Today*, 57(5):48–53, 2004.

[5] E. T. Jaynes. Information theory and statistical mechanics. In R. D. Rosenkrantz, editor, *E. T. Jaynes: Papers on probability, statistics and statistical physics*, chapter 1. Kluver academic publishers, 1957.

[6] E. T. Jaynes. Where do we stand on maximum entropy? In R. D. Rosenkrantz, editor, *E. T. Jaynes: Papers on probability, statistics and statistical physics*, chapter 10. Kluver academic publishers, 1978.

[7] E. T. Jaynes. The minimum entropy production principle. In R. D. Rosenkrantz, editor, *E. T. Jaynes: Papers on probability, statistics and statistical physics*, chapter 14. Kluver academic publishers, 1980.

[8] E. T. Jaynes. Macroscopic predictions. In H. Haken, editor, *Complex systems–operational approaches*, page 254. Springer-Verlag, 1985.

[9] S. J. Flint, L. W. Enquist, R. M. Krug, V. R. Racaniello, and A. M. Skalka. *Principles of Virology*. ASM Press, Washington, DC, 2000.

[10] E. S. Luria, J. E. Darnell, D. Baltimore, and A. Campbell. *General Virology*. John Wiley and Sons, Inc., 1978.

[11] D. E. Smith, S. J. Tans, S. B. Smith, S. Grimes, D. L. Anderson, and C. Bustamante. The bacteriophage $\phi 29$ portal motor can package DNA against a large internal force. *Nature*, 413:748, 2001.

[12] A. Evilevitch, L. Lavelle, C. M. Knobler, E. Raspaud, and W. M. Gelbart. Osmotic pressure inhibition of DNA ejection from phage. *Proc. Natl. Acad. Sci. USA*, 100:9292–9295, 2003.

[13] P. D. Grayson, A. Evilevitch, M. M. Inamdar, P. K. Purohit, C. M. Knobler, R. Phillips, and W. M. Gelbart. Effect of genome length on the internal pressure of bacteriophage lambda capsids. *Virology*, in press, 2006.

[14] S. Novick and J. Baldeschwieler. Fluorescence measurement of the kinetics of DNA injection by bacteriophage λ into liposomes. *Biochemistry*, 27:7919–7924, 1988.

[15] J. Bohm, O. Lambert, A. Frangakis, L. Letellier, W. Baumeister, and J. Rigaud. FhuA-mediated phage genome transfer into liposomes: A cryo-electron tomography study. *Curr. Biol.*, 11:1168–1175, 2001.

[16] I. J. Molineux. No syringes please, ejection of phage T7 DNA from the virion is enzyme driven. *Mol. Microbiol.*, 40:1–8, 2001.

[17] M. E. Cerritelli, N. Cheng, McC. E. Pherson A. H. Rosenberg, F. P. Booy, and A. C. Steven. Encapsidated conformation of bacteriophage T7 DNA. *Cell*, 91:271, 1997.

[18] W. C. Earnshaw and S. C. Harrison. DNA arrangement in isometric phage heads. *Nature*, 268:598–602, 1977.

[19] S. Kanamaru, P. G. Leiman, V. A. Kostyuchenko, P. R. Chipman, V. M. Mesyanzhinov, F. Arisaka, and M. G. Rossmann. Structure of the cell-puncturing device of bacteriophage T4. *Nature*, 415:553, 2002.

[20] Y. Tao, N. H. Olson, W. Xu, D. L. Anderson, M. G. Rossmann, and T. S. Baker. Assembly of a tailed bacterial virus and its genome release studied in three dimensions. *Cell*, 95:431, 1998.

[21] A. A. Simpson, Y. Tao, P. G. Leiman, M. O. Badasso, Y. He, P. J. Jardine, N. H. Olson, M. C. Morais, S. Grimes, D. L. Anderson, T. S. Baker, and M. G. Rossmann. Structure of the bacteriophage ϕ29 DNA packaging motor. *Nature*, 408:745, 2000.

[22] G. Li and J. Widom. Nucleosomes facilitate their own invasion. *Nat. Struct. and Mol. Biol.*, 11:763–769, 2004.

[23] G. Li, M. Levitus, J. Widom, and C. Bustamante. Rapid spontaneous accessibilty of nucleosomal dna. *Nat. Struct. Mol. Biol.*, 12(1):46–43, 2005.

[24] K. J. Polach and J. Widom. Mechanism of protein access to specific dna sequences in chromatin: a dynamic equilibrium model for gene regulation. *J Mol Biol*, 254(2):130–49, 1995.

[25] H. B. Callen. *Thermodynamics and an introduction to thermostatics*. Wiley, second edition, 1985.

[26] R. K. Pathria. *Statistical Mechanics*. Butterworth-Heinemann, 2nd edition edition, 1996.

[27] B. Alberts, D. Bray, J. Lewis, M. Raff, K. Roberts, and J. Watson. *Molecular biology of the cell*. Garland, NY, 1994.

[28] P. Purohit, M. Inamdar, P. Grayson, T. Squires, J. Kondev, and R. Phillips. Forces during bacteriophage DNA packaging and ejection. *Biophys. J.*, 88:851–866, 2005.

[29] M. M. Inamdar, W. M. Gelbart, and R. Phillips. Dynamics of DNA ejection in bacteriophage. *To be published in Biophys. J.*, 2006.

[30] M. Doi. *Introduction to polymer physics*. Clarendon Press, February 1996.

[31] N. G. van Kampen. *Stochastic processes in physics and chemistry*. Elsevier, 1982.

[32] Chris Jarzynski. Nonequilibrium equality for free energy differences. *Phys. Rev. Lett.*, 78(14):2690–2691, 1997.

[33] C. Jarzynski. Equilibrium free energy difference from nonequilibrium: A master equation approach. *Phys. Rev. E*, 56:5018–5035, 1997.

[34] Chris Jarzynski. Nonequilibrium work theorem for a system strongly coupled to a thermal environment. *J. Stat. Mech.: Theor. Exp.*, pages 1–13, 2004.

[35] J. Liphardt, S. Dumont, S. B. Smith, I. Tinocho, and C. Bustamante. Equilibrium information from nonequilibrium measurements in an experimental test of Jarzynski's equality. *Science*, 296:1832–1835, 2002.

[36] G. Crooks. *Excursions in statistical dynamics*. PhD thesis, University of California, Berkeley, 1999.

[37] Denis J. Evans and Debra J. Searles. The fluctuation theorem. *Adv. Phys.*, 51(7):1529–1585, 2002.

[38] T. S. Baker, N. H. Olson, and S. D. Fuller. Adding the third dimension to virus life cycles: Three-dimensional reconstruction of icosahedral viruses from cryo-electron micrographs. *Microbiol. and Mol. Bio. Rev.*, 63:862, 1999.

[39] P. G. Leiman, S. Kanamaru, V. V. Mesayanzhinov, F. Arisaka, and M. G. Rossmann. Structure and morphogenesis of bacteriophage T4. *Cell. Mol. Life Sci.*, 60:2356–2370, 2003.

[40] Lucienne Letellier, Pascale Boulanger, Laure Plançon, Pierre Jacquot, and Monica Santamaria. Main features on tailed phage, host recognition and DNA uptake. *Frontiers in Bioscience*, 9:1228–1339, 2004.

[41] D. Endy, D. Kong, and J. Yin. Intracellular kinetics of a growing virus: A genetically structured simulation for simulation for the growth of bacteriophage T7. *Biotech. Bioeng.*, 55:375–389, 1997.

[42] A. Hershey and M. Chase. Independent functions of viral protein and nucleic acid in growth of bacteriophage. *J. Gen. Physiol.*, 36(1):39–56, 1952.

[43] H. Echols. *Operators and promoters: The story of molecular biology and its creators*. University of California Press, Berkeley,California, 2001.

[44] M. Ptashne. *Genetic switch: Phage lambda revisited*. Cold Spring Harbor Laboratory, 2004.

[45] V. S. Reddy, P. Natarajan, B. Okerberg, K. Li, K. V. Damodaran, R. T. Morton, and C. L. Brooksand J. E. Johnson. Virus particle explorer (VIPER), a website for virus capsid structures and their computational analyses. *Virology*, 75:11943, 2001. The Viper website can be found at `http://mmtsb.scripps.edu/viper/viper.html`.

[46] M. Feiss, R. A. Fisher, M. A. Crayton, and C. Egner. Packaging of the bacteriophage λ chromosome: Effect of chromosome length. *Virology*, 77:281–293, 1977.

[47] D. C. Rau, B. Lee, and V. A. Parsegian. Measurement of the repulsive force between polyelectrolyte molecules in ionic solution: hydration forces between parallel DNA double helices. *Proc. Natl. Acad. Sci. USA*, 81(9), 1984.

[48] H. Shibata, H. Fujisawa, and T. Minagawa. Characterization of the bacteriophage T3 DNA packaging reaction in vitro in a defined system. *J. Mol. Biol.*, 196:845–851, 1987.

[49] National Center For Biotechnology Information. Entrez genomes. Online at `http://www.ncbi.nlm.nih.gov/`, 2004.

[50] T. Dokland and H. Murialdo. Structural transitions during maturation of bacteriophage lambda capsids. *J. Mol. Biol.*, 223, 1993.

[51] World Health Organization. Smallpox. Fact sheet online at `http://www.who.int/mediacentre/factsheets/smallpox/en/`, 2004.

[52] B. La Scola, S. Audic, C. Robert, L. Jungang, X. de Lamballerie, M. Drancourt, R. Birtles, and D. Raoult J.-M. Claverie. A giant virus in amoebae. *Science*, 299:2033, 2003.

[53] F. Neidhardt, editor. *Escherichia Coli and Salmonella Typhimurium*. ASM Press, 1996.

[54] R. Y. Young. Bacteriophage lysis: Mechanism and regulation. *Microbiol. Rev.*, 56(3):430–481, 1992.

[55] A. Evilevitch, M. Castelnovo, C. Knobler, and W. Gelbart. Measuring the force ejecting DNA from phage. *J. Phys. Chem. B*, 108(21):6838–6843, 2004.

[56] S. C. Riemer and V. A. Bloomfield. Packaging of DNA in bacteriophage heads: Some considerations on energetics. *Biopolymers*, 17:785, 1978.

[57] J. Kindt, S. Tzlil, A. Ben-Shaul, and W. Gelbart. DNA packaging and ejection forces in bacteriophage. *Proc. Natl. Acad. Sci. USA*, 98:13671, 2001.

[58] S. Tzlil, J. Kindt, W. Gelbart, and A. Ben-Shaul. Forces and pressures in dna packaging and release from viral capsids. *Biophys. J.*, 84:1616–1627, 2003.

[59] J. Arsuaga, R. K. Tan-Z., M. Vazquez, D. W. Sumners, and S. C. Harvey. Investigation of viral DNA packaging using molecular mechanics models. *Biophys. Chem.*, 101–102:475–484, 2002.

[60] T. Odijk. Statics and dynamics of condensed DNA within phages and globules. Submitted, 2003.

[61] P. K. Purohit, J. Kondev, and R. Phillips. Mechanics of DNA packaging in viruses. *Proc. Natl. Acad. Sci. USA*, 100(6):3173–3178, 2003.

[62] V. A. Parsegian, R. P. Rand, N. L. Fuller, and D. C. Rau. Osmotic stress for the direct measurement of intermolecular forces. *Methods in Enzymology*, 127:400–416, 1986.

[63] D. C. Rau and V. A. Parsegian. Direct measurement of the intermolecular forces between counterion-condensed DNA double helices. *Biophys. J.*, 61:246, 1992.

[64] T. Odijk and F. Slok. Nonuniform Donnan equilibrium within bacteriophages packed with DNA. *J. Phys. Chem. B*, 107(32):8074–8077, 2003.

[65] D. Marenduzzo and C. Micheletti. Thermodynamics of DNA packing inside a viral capsid: The role of DNA intrinsic thickness. *J. Mol. Biol.*, 330(3):485–492, 2003.

[66] K. E. Richards, R. C. Williams, and R. Calendar. Mode of DNA packing within bacteriophage heads. *J. Mol. Biol.*, 78:255, 1973.

[67] F. P. Booy, W. W. Newcomb, B. L. Trus, J. C. Brown, T. S. Baker, and A. C. Steven. Liquid-crystalline, phage-like packing of encapsidated DNA in herpes-simplex virus. *Cell*, 64(5):1007–1015, 1991.

[68] W. M. Gelbart, R. F. Bruinsma, P. A. Pincus, and V. A. Parsegian. DNA inspired electrostatics. *Physics Today*, pages 38–44, September 2000.

[69] T. Odijk. Hexagonally packed DNA within bacteriophage T7 stabilized by curvature stress. *Biophys. J.*, 75:1223–1227, 1998.

[70] W. S. Klug and M. Ortiz. A director field model of DNA packaging in viral capsids. *J. Mech. Phys. Sol.*, 51(10):1815–1847, 2003.

[71] L. Black. DNA packaging in dsDNA bacteriophage. In R.Calendar, editor, *The Bacteriophages*, volume 2, chapter 5, pages 321–363. Plenum Press, 1988.

[72] J. LaMarque, T. Le, and S. Harvey. Packaging double-helical DNA into viral capsids. *Biopolymers*, 73:348–355, 2004.

[73] Steven B. Smith, Laura Finzi, and Carlos Bustamante. Direct mechanical measurements of the elasticity of single dna molecules by using magnetic beads. *Science*, 258:1122–1126, 1992.

[74] J. Bednar, P. Furrer, V. Katritch, A. Z. Stasiak, J. Dubochet, and A. Stasiak. Determinition of DNA persistence length by cryo-electron microscopy. seperation of static and dynamic contributions to the apparent persistence length of DNA. *J. Mol. Biol.*, 254:579–594, 1995.

[75] P. Nelson. *Biological Physics: Energy, Information, Life*. W. H. Freeman & Co., 2003.

[76] A. P. Lyubartsev and L. Nordenskiöld. Monte carlo simulation study of ion distribution and osmotic pressure in hexagonally oriented DNA. *Journal of Physical Chemistry*, 99, 1995.

[77] T. Odijk. On the statistics and dynamics of confined or entangled stiff polymers. *Macromolecules*, 16(8):1340–1344, 1983.

[78] H. H. Strey, V. A. Parsegian, and R. Podgornik. Equation of state for DNA liquid crystals: Fluctuation enhanced electrostatic double layer repulsion. *Phys. Rev. Lett.*, 78(5):895–898, 1997.

[79] K. Iwasaki, B. L. Trus, P. T. Wingfield, N. Cheng, G. Campusano, V. B. Rao, and A. C. Steven. Molecular architecture of bacteriophage T4 capsid: Vertex structure and bimodal binding of the stabilizing accessory protein, Soc. *Virology*, 271:321–333, 2000.

[80] R. Lata, J. F. Conway, N. Cheng, R. L. Duda, R. W. Hendrix, W. R. Wikoff, J. E. Johnson, H. Tsuruta, and A. C. Steven. Maturation dynamics of a viral capsid: Visualization of transitional intermediate states. *Cell*, 100:253–263, 2000.

[81] E. Raspaud, M. O. de la Cruz, J. L. Sikorav, and F. Livolant. Precipitation of DNA by polyamines: A polyelectrolyte behavior. *Biophys. J.*, 74(1):381–393, 1998.

[82] P. K. Purohit, J. Kondev, and R. Phillips. Force steps in viral DNA packaging? *J. Mech. Phys. Sol.*, 51(11):2239–2257, 2003.

[83] L. D. Landau and E. M. Lifshitz. *Fluid Mechanics*. Butterworth-Heinemann, NY, USA, 2 edition, 1987.

[84] I. Gabashvili and A. Grosberg. Dynamics of double stranded DNA reptation from bacteriophage. *J. Biomol. Struc. Dyn.*, 9(5):911–919, 1992.

[85] F. Tama and C. L. Brooks. The mechanism and pathway of pH induced swelling in cowpea chlorotic mottle virus. *J. Mol. Biol.*, 318:733–747, 2002.

[86] A. Cordova, M. Deserno, W. M. Gelbart, and A. Ben-Shaul. Osmotic shock and the strength of viral capsids. *Biophys. J.*, 85:70–74, 2003.

[87] M. Castelnovo, R. K. Bowles, H. Reiss, and W. M. Gelbart. Osmotic force resisting chain insertion in a colloidal suspension. *Euro. Phys. J. E*, 10:191, 2003.

[88] A. Evilevitch, M. Castelnovo, C. M. Knobler, and W. M. Gelbart. Measuring the force ejecting DNA from phage. *Journal of Physical Chemistry B*, 108(21):6838–6843, 2004.

[89] R. de Vries. Flexible polymer-induced condensation and bundle formation of DNA and F-actin filaments. *Biophys. J.*, 80:1186–1194, 2001.

[90] T. Odijk. Protein-macromolecule interactions. *Macromolecules*, 29:1842–1843, 1996.

[91] Nicholas L. Abbot, Daniel Blankschtein, and T. Alan Hatton. Protein partitioning in two-phase aqueous polymer systems. 2. on the free energy of mixing globular colloids and flexible polymers. *Macromolecules*, 25(15):3917–3931, 1992.

[92] A. Yu. Grosberg and A. R. Khokhlov. *Statistical Physics of Macromolecules*. American Institute of Physics, 1994.

[93] P.-G. de Gennes. *Scaling concepts in polymer physics*. Cornell University Press, Ithaca, NY, 1979.

[94] Derek Marsh. Scaling and mean-field theories applied to polymer brushes. *Biophysical Journal*, 86:2630–2633, 2004.

[95] V. Gonzales-Huici, M. Salas, and J. Hermoso. The push-pull mechanism of bacteriophage ϕ29 DNA injection. *Mol. Microbiol.*, 52(2):529–540, 2004.

[96] T. Odijk. Statics and dynamics of condensed DNA within phage and globules. *Phil. Trans. Roy. Soc. A*, 362(1820):1497–1517, 2004.

[97] R. Metzler and P. G. Dommersnes. Helical packaging of semiflexible polymers in bacteriophages. *Eur. Biophys. J.*, 33(6):497–505, 2004.

[98] Adam Simon and Albert Libchaber. Escape and synchronization of a brownian particle. *Phys. Rev. Lett.*, 68:3375–3378, 1992.

[99] C. S. Peskin, G. M. Odell, and G. F. Oster. Cellular motions and thermal fluctuations: The Brownian ratchet. *Biophys. J.*, 65:316–324, 1993.

[100] R. Zandi, D. Reguera, J. Rudnick, and W. Gelbart. What drives the translocation of stiff chains? *Proc. Natl. Acad. Sci. USA*, 100:8649–8653, 2003.

[101] T. Ambjornsson and R. Metzler. Chaperone-assisted translocation. *Phys. Biol.*, 1:77–88, 2004.

[102] L. Letellier, L. Planon, M. Bonhivers, and P. Boulanger. Phage DNA transport across membranes. *Res. Microbiol.*, 150(8):499–505, 1999.

[103] Ian J. Molineux. Fifty-three years since hershey and chase; much ado about pressure but which pressure is it? *Virology*, 344(1):221–229, 2006.

[104] S. Mangenot, M. Hochrein, J. Radler, and L. Letellier. Real-time imaging of dna ejection from single phage particles. *Curr Biol*, 15(5):430–5, 2005.

[105] M. Rossmann, V. Mesayanzhinov, F. Arisaka, and P. Leiman. The bacteriophage T4 DNA injection machine. *Curr. Opin. Struct. Biol.*, 14:171–180, 2004.

[106] P. Kemp, M. Gupta, and I. J. Molineux. Bacteriophage T7 DNA ejection into cells is initiated by an enzyme-like mechanism. *Molecular Microbiology*, 53(4):1251–1265, 2004.

[107] L. Letellier, P. Bouolanger, M. de Frutos, and P. Jacquot. Channeling phage DNA through membranes: from in vivo to in vitro. *Res. Microbiol.*, 154:283–287, 2003.

[108] W. Sung and P. J. Park. Polymer translocation through a pore in a membrane. *Phys. Rev.*, 77:783–787, 1996.

[109] David K. Lubensky and David R. Nelson. Driven polymer translocation through a narrow pore. *Biophys. J.*, 77:1824–1838, 1999.

[110] M. Muthukumar. Polymer translocation through a hole. *J. Chem. Phys.*, 111:10371–10374, 1999.

[111] N. G. van Kampen. *Stochastic processes in physics and chemistry.* Elsevier Science publishers, Amsterdam, 1992.

[112] J. Howard. *Mechanics of motor proteins and the cytoskeleton.* Sinauer Associates Inc., 2001.

[113] A. Graff, M. Sauer, P. van Gelder, and W. Meier. Virus-assisted loading of polymer nanocontainer. *Proc. Natl. Acad. Sci. USA*, 99:5064–5068, 2002.

[114] S. B. Zimmerman and A. P. Minton. Macromolecular crowding: biochemical, biophysical, and physiological consequences. *Annu. Rev. Biophys. Biomol. Struct.*, 22:27–65, 1993.

[115] K. Luby-Phelps. Cytoarchitecture and physical properties of cytoplasm: volume, viscosity, diffusion, intracellular surface area. *Int. Rev. Cytol.*, 192:189–221, 2000.

[116] K. Robison, A. M. McGuire, and G. M. Church. A comprehensive library of DNA-binding site matrices for 55 proteins applied to the complete Escherichia coli K12 genome. *J. Mol. Biol.*, 284:241–254, 1998.

[117] Terrell L. Hill. *An Introduction to Statistical Thermodynamics*. Dover Publications, NY, 1986.

[118] M. Shea and G. K. Ackers. The O_R control system of bacteriophage λ: A physical-chemical model for gene regulation. *J. Mol. Biol.*, 181:211–230, 1985.

[119] M. Wang, M. Schnitzer, H. Yin, R. Ladnick, J. Gelles, and S. Block. Force and velocity measured for single molecules of RNA polymerase. *Science*, 282:902–907, 1998.

[120] J. Israelachvili. *Intermolecular and surface forces: With application to colloidal and biological systems*. Academic Press, second edition, 1992.

[121] K. Luger, A. W. Mder, R. K. Richmond, D. F. Sargent, and T. J. Richmond. Crystal structure of the nucleosome core particle at 2.8 a resolution. *Nature*, 389(6648):251–60, 1997.

[122] David Chandler. *Introduction to Modern Statistical Mechanics*. Oxford University Press, 1987.

[123] K. Dill and S. Bromberg. *Molecular driving forces: statistical thermodynamics in chemistry and biology*. Garland Science, New York, 2003.

[124] M. Tomschik, H. Zheng, K. van Holde, J. Zlatanova, and S. Leuba. Fast, long-range, reversible conformational fluctuations in nucleosomes revealed by single-pair fluorescence resonance energy transfer. *Proc. Nat. Acad. Sci.*, 9:3278–3283, 2005.

[125] B. Robertson. Equations of motion in non-equilibrium statistical mechanics. *Phys. Rev.*, 144:151–161, 1966.

[126] B. Robertson. Projection operators using maximum entropy methods. In R. D. Levine and M. Tribus, editors, *The maximum entropy formalism*. MIT press, 1978.

[127] W. T. Grandy. Principle of maximum entropy and irreversible processes. *Phys. Rep.*, 62:176–266, 1980.

[128] R. Dewar. Information theory explanation of the fluctuation theorem, maximum entropy production and self-organized criticality in non-equilibrium stationary states. *J. Phys. A*, 36:631–641, 2003.

[129] R. C. Dewar. Maximum entropy production and the fluctuation theorem. *J. Phys. A*, 38:L371–L381, 2005.

[130] R. M. L. Evans. Detailed balance has a counterpart in non-equilibrium steady states. *J. Phys. A*, 38:293–313, 2005.

[131] Gerard G. Emch and Chuang Liu. *The logic of thermostatical physics*. Springer-Verlag, NY, 2002.

[132] K. Ghosh, K. Dill, M. Inamdar, E. Seitaridou, and R. Phillips. Teaching the principles of statistical dynamics. *Am. J. Phys.*, 74:123–133, 2006.

[133] F. Reif. *Fundamentals of statistical and thermal physics*. McGraw-Hill, NY, 1965.

[134] J. Kasianowicz, E. Brandin, D. Branton, and D. Deamer. Characterization of individual polynucleotide molecules using a membrane channel. *Proc. Nat. Acad. Sci. USA*, 93:13770–13773, 1996.

[135] H. P. Lu, L. Xun, and X. S. Xie. Single molecule enzymatic dynamics. *Science*, 282:1887, 1998.

[136] M. Reif, R. S. Rock, Amit D. Mehta, M. S. Mooseker, R. E. Cheney, and J. A. Spudich. Myosin-V stepping kinetics:A molecular model for processivity. *Proc. Nat. Acad. Sci.*, 97:9482–9486, 2000.

[137] A. Meller, L. Nivon, and D. Branton. Voltage-driven DNA translocations through a nano-pore. *Phys. Rev. Lett.*, 86(15):3435–3438, 2001.

[138] H. Li, W. A. Linke, A. F. Oberhauser, M. Carrion-Vazquez, J. G. Kerkvliet, H. Lu, P.E. Marszalek, and J. M. Fernandez. Reverse engineering of the giant muscle protein. *Nature*, 418:998–1002, 2002.

[139] C. Bustamante, Z. Bryant, and S. B. Smith. Ten years of tension: single-molecule DNA mechanics. *Nature*, 421:423–427, 2003.

[140] E. R. Dufresne, D. Altman, and D. G. Grier. Brownian dynamics of sphere in a slit pore. *Europhys. Lett.*, 53:264–270, 2001.

[141] B. Alberts, D. Bray, A. Johnson, J. Lewis, M. Raff, K. Roberts, and P. Walter. *Essential Cell Biology: An Introduction to the Molecular Biology of the Cell*. Garland Publishing, New York, July 1997.

[142] M. Klein. Entropy and the Ehrenfest urn model. *Physica*, 22:569–575, 1956.

[143] V. Ambegaokar and A. Clerk. Entropy and time. *Am. J. Phys.*, 67(12):1068–1073, 1999.

[144] R. P. Feynman. Nobel lecture in physics, 1965. In *Nobel Lectures in Physics: 1901–1995*. World Scientific Publishing Co., 1998.

[145] M. Kac. Paper. *Amer. Math. Monthly*, 54:369, 1947.

[146] G. M. Wang, E. M. Sevick, E. Mittag, D. J. Searles, and D. J. Evans. Experimental verification of the fluctuation theorem. *Phys. Rev. Lett.*, 89:050601, 2002.

[147] William Silvert. Complexity. *J. Biol. Sys.*, 4:585–591, 1996.

[148] H. Haken. Application of the maximum information entropy principle to self-organizing systems. *Z. Phys. B–Condensed Matter*, 61:335–338, 1985.

[149] I. Llano, C. K. Webb, and F. Bezanilla. Potassium conductance of the squid giant axon. single-channel studies. *J Gen Physiol*, 92(2):179–96, 1988.

[150] J. Liphardt, B. Onoa, S. B. Smith, I. Tinocho Jr, and C. Bustamante. Reversible unfolding of single RNA molecules by mechanical force. *Science*, 292:733–7, 2001.

[151] Lowell L. McCann, Mark Dykmann, and Brage Golding. Thermally activated transitions in a bistable three-dimensional optical trap. *Nature*, 402:785–787, 1999.

[152] K. C. Neuman and S. M. Block. Optical trapping. *Rev. Sci. Inst.*, 75:2787–2809, 2004.

[153] D. Collin, F. Ritort, C. Jarzynski, S. B. Smith, I. Tinocho Jr, and C. Bustamante. Verification of the Crooks fluctuation theorem and recovery of RNA folding energies. *Nature*, 437:231–234, 2005.

[154] S. Schuler, T. Speck, C. Teitz, J. Wrachtrup, and U. Seifert. Experimental test of the fluctuation theorem for a driven two-level system. *Phys. Rev. Lett.*, 94:180602–1–4, 2005.

[155] I. Goychuk and P. Hanggi. Ion channel gating: a first-passage time analysis of the kramers type. *Proc Natl Acad Sci U S A*, 99(6):3552–6, 2002.

[156] B. Hille. *Ion channels of excitable membranes*. Sinauer Associates, third edition, 2001.